

Interfacial Debonding From a Sandwiched Elastomer Layer

By

Bikramjit Mukherjee

Dissertation submitted to the faculty of Virginia Polytechnic Institute and State University in
partial fulfillment of the requirements of the degree of

Doctor of Philosophy

In

Engineering Mechanics

Romesh C. Batra, Co-chair

David A. Dillard, Co-chair

Robert B. Moore

Douglas P. Holmes

Slimane Adjerid

Peyton L. Hopson

April 29, 2016
Blacksburg, VA, USA

Keywords: Cohesive Zone Model (CZM), Traction-Separation (TS) Relation, Adhesion,
Elastomeric Adhesive, Interfacial Debonding, Adhesion-Induced Instability, Wavy
Debonding, Fracture Mechanics, Confinement, Preferential Debonding, Pull-off Force,
Demolding

© 2016, Bikramjit Mukherjee

Interfacial Debonding From a Sandwiched Elastomer Layer

(Bikramjit Mukherjee)

ABSTRACT

The problem of a thin elastomeric layer confined between two stiff adherends arises in numerous applications such as microelectronics, bio-inspired adhesion and the manufacture of soft biomedical products. A common requirement is that the debonding of the elastomeric layer from the adherends be controlled to avoid undesirable failure modes. This level of control may necessitate understanding the collective role of the interfacial adhesion, material properties, part geometries, and loading conditions on the debonding. Analytical and numerical approaches using the finite element method and a cohesive zone model (CZM) for the interfacial debonding are used in this dissertation to delineate the role of the afore-mentioned parameters on the initiation and propagation of debonding for both rigid and non-rigid adherends.

Extensively studied in the dissertation is the debonding of a semi-infinite relatively stiffer adherend from an elastomer layer with its other surface firmly bonded to a rigid base. The adherend is pulled upwards by applying normal displacements either on its entire unbonded surface or on the edge of its part overhanging from the elastomer layer. The adherend and the elastomeric layer materials are assumed to be linear elastic, homogeneous and isotropic and the elastomer is assumed to be incompressible. Viscoelasticity of the elastomer is considered in the first part of the work. Plane strain deformations of the system with a bilinear traction-separation (TS) relation in the CZM are analyzed. Two non-dimensional numbers, one related to the layer confinement and the other to the interfacial TS parameters, are found to determine if debonding initiates at interior points in addition to at corner points on the adherend/elastomer interface, and if adhesion-induced instability is exhibited. This work is extended to axisymmetric problems in which debonding can take place at both interfaces. Motivated by an industrial demolding problem, numerical experiments are conducted to derive insights into preferential debonding at one of the two interfaces, including for curved adherends. Results reported herein should help engineers design an elastomer layer sandwiched between two adherends for achieving desired failure characteristics.

Dedicated to my parents

Acknowledgements

This dissertation signifies the culmination of the last five and a half years of my graduate research. I am indebted to a large number of individuals, without whose help and support this would never be possible.

At the very outset, I express my deepest gratitude to my advisors, Dr. Romesh C. Batra and Dr. David A. Dillard, for the training they have imparted to me over the course of my graduate work. We met on a regular basis to discuss progress on research. The brainstorming sessions not only catalyzed my progress but helped me grow as a researcher. Many thanks are owed to them for giving me independence in my approach and trusting me. I thank them for critiquing my work and helping me hone my technical communication skills. I am indebted to them for giving me countless opportunities to learn and grow while sharing their knowledge and expertise with me. It is impossible to overstate my gratitude to them for investing their time and effort in my success.

I would like to thank my committee members Dr. Robert B. Moore, Dr. Douglas P. Holmes, Dr. Slimane Adjerid and Dr. Peyton L. Hopson for serving my committee, asking insightful questions and advising me whenever needed.

I am immensely thankful to the Department of Engineering Science and Mechanics (ESM) for giving me the opportunity to pursue my graduate studies here. I feel grateful to ESM and the Department of Biomedical Engineering and Mechanics (BEAM) for awarding me the graduate teaching assistant (GTA) positions which not only mitigated my financial burden but also offered me the valuable experiences of teaching and mentoring undergraduate students. I am deeply grateful to Dr. Scott Case and Dr. Mark Stremmer for offering me the position of an instructor of *Mechanics of Deformable Bodies* in spring 2015. This proved to be a tremendously valuable experience for me.

I would like to thank Lisa Smith, Mellissa Nipper, Linda Taylor, Paul Sibert, Ann Merrie Bracken and Cristina Rosa Castaner for their help with administrative issues during my graduate studies.

I am thankful to Tim Tomlin and Mark Warbeck for helping me with issues related to using ABAQUS on the Linux computer cluster.

I thank the Institute of Critical Technology and Applied Sciences (ICTAS) for the use of its facilities and the Macromolecules and Interfaces Institute (MII) for fostering

interdisciplinary research in the adhesion area. Many thanks go to Tammy Jo for helping with my travel to the annual Adhesion Society meetings. I do appreciate her inviting me for a talk in the MII technical review, 2015.

I thank my lab-mates (current/previous), Qian Li, Ahmad Rezaei Mojdehi, Md. Shahriar Khandaker, Ivan Vu, Shantanu Ranade, Leo Guan, and Geoffrey Tizard for making my time in the lab memorable. Thanks are owed to them for all the stimulating discussions on topics ranging from science and minute details of research to life in general. I owe a special mention to Orkun Kaymakci who worked with me on an industrial project in the initial two years of my research. It was fun collaborating with him as I kick-started my graduate research.

I am grateful to a large number of my fellow Hokies from Kolkata whose company made me feel the warmth of my hometown. I will carry with me sweet memories of the time I spent with them in Blacksburg. Many thanks go to Arnab Gupta, Surya Deb, Debomoy Sen, Wrik Mallik, Souvik Pal, Souvick Chatterjee, Krishnashis Chatterjee, Shibarata Naik, Suvojit Ghosh, Anupam Pandey, Subhradeep Roy, Debarati Basu, Bireswar Laha, Poulomi Laha and Arnab Roy and Saikat Basu. I am indebted to Abhijit Sarkar and Shreya Mitra for bearing with me during my tough times and more importantly, their friendship.

This culmination would never be possible without the support, love and blessings from my family. I take this opportunity to thank my parents, Mr. Pijush Kumar and Mrs. Debjani Mukherjee, for their blessings and the sacrifices they made in order to raise me and help me chase my dreams. No words can express my gratitude to my father for taking care of my ailing mother back home and taking many responsibilities off my shoulder. I thank my elder sister, Mrs. Satarupa Bhattacharya, for her affection and all her prayers for me. Thanks are owed to my brother-in-law, Dr. Deepanjan Bhattacharya, for being a friend, philosopher and guide. I am indebted to him for many things including his helping me with the graduate school application process six years ago. The weekend trips to their place in Tennessee and the quality time I spent with them and their little ones (Rishi and Rihan) mark a significant portion of my last five and a half years in the US. Amongst many others in my extended family, I would like to thank my uncles Mr. Somnath Mukherjee, Mr. Haraprasad Chatterjee, Dr. Sankar Ganguly and Dr. Somnath Ganguly, my aunt, Mrs. Sharmila Mukherjee, and my cousins Miss Somdutta and Miss Somrita Mukherjee for their respective roles in my journey. As I finish writing my Doctoral dissertation, I feel grateful to my uncle, Mr. Somnath

Mukherjee, for teaching me English. Thanking my family is never complete without acknowledging the blessings of my late grandparents, Mr. Sailesh Kumar and Mrs. Gauri Rani Mukherjee (paternal), and Mrs. Rani Pathak (maternal).

I thank my friend-turned-wife Debolina for her love and constant support through thick and thin in all my endeavors. I am deeply grateful to her for bearing with me with steadfast patience and taking over many domestic responsibilities over the last few months. I express my sincere appreciation to my parents-in-law, Mr. Somnath Gupta and Mrs. Rekha Gupta for their affection, support and encouragement. A special mention is owed to the four-legged member of our family, Kuttu, for teaching us unconditional love.

Last but not the least, I thank the domestic helpers (Tumpa, Sopna, Sheela, Sobita, and Rupa) back in India, who, led by my father, are working together to help my mother with her ongoing struggle with a degenerative brain disease. Their tireless service mitigates a great source of my anxiety on a daily basis.

Table of contents

1	<i>Introduction</i> -----	1
	References.....	6
2	<i>Debonding of Confined Elastomeric Layer using Cohesive Zone Model</i> -----	9
	Abstract.....	9
	List of symbols.....	10
	2.1 Introduction.....	12
	2.2 Analytical approach	14
	2.2.1 Problem formulation.....	14
	2.2.2 Results and discussion	22
	2.3 Debonding of elastomeric layer from a rigid adherend by the FEM.....	27
	2.3.1 Approach	27
	2.3.2 Results and discussion	29
	2.4 Analysis of 3D deformations for peeling of a flexible plate off a soft elastomeric layer by the FEM.....	34
	2.4.1 Approach	34
	2.4.2 Results and discussion	36
	2.5 Conclusions.....	40
	Acknowledgements.....	41
	Appendix A.....	41
	Appendix B.....	42
	Appendix C.....	42
	References.....	45
3	<i>Effect of confinement and interfacial adhesion on peeling of a flexible plate from an elastomeric layer</i> -----	48
	Abstract.....	48
	3.1 Introduction.....	49
	3.2 Formulation of the problem	53
	3.3 Numerical Solution of the Problem.....	56
	3.3.1 Approach	56
	3.4 Results and discussion	57
	3.4.1 Choice of Parameters.....	57
	3.4.2 Analysis of interfacial tractions with no damage allowed at the interface	58
	3.4.3 Analysis of damage growth and debonding	62
	3.4.4 Debonding at both interfaces of the interlayer	77
	3.5 Conclusions.....	81
	Acknowledgments.....	82

Appendix D.....	82
Appendix E.....	86
Appendix F.....	87
References.....	88
4 <i>Analysis of edge debonding in peeling of a thin flexible plate from an elastomer layer</i>	-----92
Abstract.....	92
4.1 Introduction.....	93
4.2 Problem description and analysis.....	95
4.2.1 Governing Equations.....	97
4.2.2 Approximate solution of the governing equations.....	98
4.3 Results and discussion.....	102
4.4 Conclusions.....	108
4.5 Acknowledgments.....	109
References.....	109
5 <i>On preferential debonding during demolding of a sandwiched elastomeric layer----</i>	111
Abstract.....	111
5.1 Introduction.....	112
5.2 Problem description and computational approach.....	115
5.3 Results and discussion.....	123
5.3.1 Effect of the FE mesh.....	123
5.3.2 Flat molds of different flexural rigidities.....	125
5.3.3 Molds as portions of a hemisphere.....	133
5.3.4 Increasing temperature of the flat molds differentially.....	138
5.3.5 Limitations of the present analysis.....	145
5.4 Conclusions.....	146
Acknowledgements.....	147
Appendix H.....	147
Appendix I.....	149
Understanding bridging of a soft organogel layer by numerical simulations.....	149
References.....	154
6 <i>Conclusions -----</i>	156
6.1 Summary:.....	156
6.2 Future directions:.....	159
6.2.1 Wavy/undulatory debonding:.....	159
6.2.2 Three-dimensional (3D) effects:.....	159
6.2.3 Flexible plate on elastomeric foundation:.....	160
6.2.4 Debonding evolution in the demolding problem:.....	160

References.....	161
Appendix J	162
J.1 Sample input file for debonding of a rigid semi-infinite block (Chapter 2)	162
J.2 Sample input file for peeling of a flexible plate (Chapter 3).....	164
J.3 Sample input file for axisymmetric debonding problem (Chapter 5).....	167

List of figures

Figure 1.1: A schematic sketch of the wavy debonding phenomenon studied in Chapter 2.....	3
Figure 2-1: Schematic sketch of the problem studied. The width W (normal to the page, not shown) is large enough to justify studying plane strain deformations in the xz -plane.	14
Figure 2-2: A bilinear traction-separation relation	16
Figure 2-3: The plot of function $f(hk)$. The implication is that a sinusoidal solution with wavenumber k is possible when $\alpha h / \mu \geq 6.22$. Note that f is a positive valued function of hk	20
Figure 2-4: For $m = 3$, the dimensionless growth rate versus the dimensionless wave number (a) for different values, labelled in the figure, of ϕ in $[\phi_{c1}, \phi_{c2})$ and (b) for $\phi(=41.25) > \phi_{c2}$. Results in Fig. (a) imply that larger the value of ϕ , faster is the growth rate and wider is the range of the growing wavenumbers. However, the fastest growth rate always corresponds to the wavenumber of wavelength $2.96h$. Results in Fig. (b) show that for two indicated wavenumbers perturbations grow infinitely fast while for wavenumbers lying between them they decay due to their negative growth rates.	24
Figure 2-5: Contours in the wavenumber- ϕ plane of the normalized growth rate $\tilde{\omega}$ of perturbations for $m=3$. Values of $\tilde{\omega}$ are indicated on the contours. These plots imply that a sinusoidal perturbation of wavenumber hk will decay in regions <i>I</i> and <i>III</i> and grow in region <i>II</i>	25
Figure 2-6: Effect of m : (a) elastic limit with two possible wavenumbers, (b) three regions for $m=1$, and (c) three regions with a wider region <i>II</i> for $m=5$	26
Figure 2-7: Details of the FE mesh and boundary conditions. Applied zero tractions in directions of the unconstrained displacement components are not shown.	29
Figure 2-8: Deformed and undeformed configurations when a wavy debonding is predicted by the model. The FE mesh is shown only on the undeformed configuration. The gap between the adherend and the interlayer is due to the displacement jump at the interface. Debond occurs only when this jump exceeds its prescribed limiting value.	31
Figure 2-9: The map illustrating that the quantity T_c^2 / G_c must exceed approximately $4.15E_\infty / h$ for a wavy debond to ensue. This plot was generated for $m = 3, \tau = 10^{-5} s$, and $\dot{\Delta} = 1 mm / s$	31
Figure 2-10: Evolution of the contact opening for $m = 3$ and (a) $\phi = 8.25(\phi_{c1} < \phi < \phi_{c2})$ and (b) $\phi = 41.25(\phi > \phi_{c2})$. Variables in the plot are: $\bar{\delta} = \delta / \delta_f$ and $\bar{x} = 2x / L$. The deformation shown is multiplied by 5 for ease in visualization. Plots correspond to the central portion of the interface of non-dimensional length 1. Deformed configurations are for the interface portion of non-dimensional length 0.66.....	32
Figure 2-11: Effect of ϕ on the dominant wavelength (normalized by thickness) of the debonding undulation	33

Figure 2-12: The FE mesh and boundary conditions with zero tractions along unconstrained displacement components not exhibited	36
Figure 2-13: Two main types of debond front predicted by the simulations: debond front (a) with or (b) without fingerlike undulations. In these images, the bonded and the debonded regions are shown by plotting the damage variable, $\bar{d} = \frac{\delta_f (\delta - \delta_c)}{\delta (\delta_f - \delta_c)}$ defined for the region corresponding to segment AB of the TS relation (for segment OA, $\bar{d} = 0$). The value of \bar{d} equals 1 over the debonded region (represented by red color) and varies from 0 to 1 over the region which is yet to debond (represented by blue color). Whether or not undulation is exhibited at the debond front depends on the plate bending rigidity, the viscoelastic properties and the thickness of the interlayer, temperature, pulling rate and values of the TS parameters.....	38
Figure 2-14: Contour plots of contact opening at three values of the applied displacement when the plate rigidity $D = 21Nm$ and the interlayer thickness $h = 250 \mu m$. For easy visualization, deformations are exaggerated by a factor of 10 and by a factor of 12 for the cross-section AA' illustrating wavy debonding.	39
Figure 2-15: Dependence of the (a) dominant wavelength, λ , of the fingerlike pattern on the interlayer thickness, h , and (b) the fingers length, l_{finger} , on the length scale $(D / \mu)^{1/3}$ when $h = 250 \mu m$. As shown in (a) fingerlike debonding is not predicted when $D = 2.1Nm$ and $h = 750 \mu m$. However, a larger value of D causes fingerlike debonding. The linear fit of the data points shown in (b) agrees with the linear fit of experimental results of Ghatak and Chaudhury [9], $l_{finger} = 0.2(D / \mu)^{1/3} - 0.16$. The intercepts are not important since undulatory debond fronts do not occur for small values of $(D / \mu)^{1/3}$	39
Figure 3-1: Schematic sketches of (a) a probe-tack configuration, and (b) a flexible plate peeled from a thin elastomeric layer bonded to a fixed rigid base.....	50
Figure 3-2: Schematic sketch of the problem studied.....	53
Figure 3-3: Bilinear traction-separation relation between the interfacial normal traction and the jump (contact-opening) in the interface normal displacement. Also included is a plot of the variation of the damage variable as a function of the contact-opening.....	56
Figure 3-4: The FE mesh and the boundary conditions on the region whose plane-strain deformations are analyzed.....	57
Figure 3-5: (a) A schematic sketch of the deformed shape of the specimen; the computed (b) interfacial normal traction (T_n) and (c) the interfacial tangential traction (T_s) as functions of the distance x from the corner point B for different levels of confinement, α ($\mu = 5MPa$). Note that these results correspond to a very high value of the interfacial strength to prevent debonding at the interface....	60
Figure 3-6: Comparison of present results with those from the literature for $\alpha = 3$ and $\alpha = 5$ (for $\mu = 5 MPa$). Note that these results correspond to a very high value of the interfacial strength to prevent debonding at the interface.....	61

- Figure 3-7: Non-dimensional location of the internal peak as a function of the confinement level. Note that these results correspond to a very high value of the interfacial strength to prevent debonding at the interface. 62
- Figure 3-8: For $\alpha = 3, \phi = 0.1$, distributions of the non-dimensional normal traction ($\bar{T}_n = T_n / T_c$) and the damage variable (D) at the interface as a function of the non-dimensional distance (X) measured from point B at increasing values of the non-dimensional applied displacement (Δ_A). The deformed configurations, shown on the left, have been exaggerated by a factor of 5. This is an example of the type-1 debonding mechanism shown in Figure 3-13. The inset included in the top figure illustrates the TS relation used and the variation of D as a function of $\delta (> \delta_c)$ normalized by δ_f . The insets included in the third and the fourth figures illustrate the variation of D on magnified scales. 66
- Figure 3-9: For $\alpha = 100, \phi = 4$, distributions of the non-dimensional normal traction (\bar{T}_n) and the damage variable (D) at the interface as a function of the non-dimensional distance (X) measured from point B at increasing values of the non-dimensional applied displacement (Δ_A). The deformed configurations, shown on the left, have been exaggerated by a factor of 25. This is an example of the type-2 debonding mechanism exhibited in Figure 3-13. The inset included in the top figure illustrates the TS relation used and the variation of D as a function of $\delta (> \delta_c)$ normalized by δ_f . The inset included in the third figure illustrates the variation of D on a scale from 0.99 to 1. 67
- Figure 3-10: For $\alpha = 100, \phi = 5$, distributions of the non-dimensional normal traction (\bar{T}_n) and the damage variable (D) at the interface as a function of the non-dimensional distance (X) measured from point B at increasing values of the non-dimensional applied displacement (Δ_A). The deformed configurations, shown on the left, have been exaggerated by a factor of 25. This is an example of the type-3 debonding mechanism displayed in Figure 3-13. The inset included in the top figure illustrates the TS relation used and the variation of D as a function of $\delta (> \delta_c)$ normalized by δ_f . The inset included in the third figure illustrates the variation of D on a scale from 0.99 to 1. 68
- Figure 3-11: For $\alpha = 100, \phi = 50$, distributions of the non-dimensional normal traction (\bar{T}_n) and the damage variable (D) at the interface as a function of the non-dimensional distance (X) measured from point B at increasing values of the non-dimensional applied displacement (Δ_A). The deformed configurations, shown on the left, have been exaggerated by a factor of 25. This is an example of the type-4 debonding mechanism evinced in Figure 3-13. The inset included in the top figure illustrates the TS relation used and the variation of D as a function of $\delta (> \delta_c)$. The inset included in the third figure illustrates the variation of D on a scale from 0.999999 to 1. 69
- Figure 3-12: On a semi-log plot, computed average spacing between the internal debonds normalized by the interlayer thickness as a function of ϕ when $\alpha = 100, \beta^{-1} = 1 \text{ mm}$ and $a_0 = 2.83 \text{ mm}$ 70
- Figure 3-13: Computed mechanisms of damage growth/debonding in the $\alpha\phi$ - plane. Values of other parameters are: $a_0 = 2.83 \text{ mm}$, and $\beta^{-1} = 1 \text{ mm}$ 70

Figure 3-14: Non-dimensional load vs. non-dimensional displacement for $\phi / \alpha = 1$. Values of other parameters are: $a_0 = 2.83 \text{ mm}$, and $\beta^{-1} = 1 \text{ mm}$ 73

Figure 3-15: (a) Non-dimensional load versus non-dimensional tip-displacement plots for $\alpha = 100$ and three values of ϕ . Deformed shapes (exaggerated by a factor of 20) corresponding to points **a, b, c** and **d** are included in the right figure. Values of other parameters are: $a_0 = 2.83 \text{ mm}$, and $\beta^{-1} = 1 \text{ mm}$; (b) Plots of X-coordinate of the debond tip as a function of the applied non-dimensional tip-displacement for $\phi = 250$, and 1000. 74

Figure 3-16: Dependence of the non-dimensional pull-off force on the non-dimensional number ϕ / α 75

Figure 3-17: (a) The configuration analyzed ; snapshots (exaggerated by a factor of 100) of the interfacial debonding for (b) $\alpha = 8$, (c) $\alpha = 2$ and (d) $\alpha = 10$, and the same values of the TS parameters at both interfaces corresponding to $\phi = 4$ when vertical displacement is monotonically increased at point A. The total length of each plate in the numerical simulations is taken to be 50 mm . Values of other parameters are: $a_0 = 2.83 \text{ mm}$, and $\beta^{-1} = 1 \text{ mm}$ 79

Figure 3-18: Snapshots of debond growth (exaggerated by a factor of 100) when the assembly is pre-cooled homothermally by -2°C followed by a vertical displacement applied at point A while the displacement components at the bottom surface of the lower mold equal zero. The coefficients of thermal expansion are assumed to be $7 \times 10^{-5} / ^\circ \text{C}$ and $6 \times 10^{-4} / ^\circ \text{C}$ for the two molds and the interlayer materials, respectively. The pre-cooling stage is simulated by inputting $\Delta T = -2^\circ \text{C}$ and no thermal effects are simulated for the mechanical loading stage. These results are for a confinement level of $\alpha = 8$ and equal values of TS parameters at both interfaces corresponding to $\phi = 4$. Values of other parameters are: $a_0 = 2.83 \text{ mm}$, $\mu = 5 \text{ MPa}$, and $\beta^{-1} = 1 \text{ mm}$. Both molds have identical values of material parameters. 80

Figure 4-1: Sketch of (a) the problem studied, and (b) various zones near the debond tip B after it has moved in the \tilde{x} direction by the distance $a - a_0$. Also schematically plotted are variations of the peel stress (normal traction) and the corresponding contact opening (displacement jump) along the \tilde{x} -axis... 96

Figure 4-2: A bilinear TS relation..... 97

Figure 4-3: For three values of the non-dimensional applied displacement, Δ_A , distributions of the non-dimensional (a) plate deflection and (b) peel stress (T/T_c) on the global horizontal axis $\tilde{X} = \beta\tilde{x}$. For $\Delta_A = 4.0$, the three regions around a debond are marked in (b) 105

Figure 4-4: Non-dimensional debond length as a function of the applied non-dimensional displacement. 105

Figure 4-5: Non-dimensional CZ size, the plate deflection at the debond tip and the plate slope at the debond tip versus the non-dimensional applied displacement. The dashed lines represent results prior to the initiation of debonding..... 105

Figure 4-6: (a) The CZ size at debond initiation versus η_s for three values of the initial overhang length A_0 (solid lines) and versus A_0 for two values of η_s (dashed lines). (b) Peel stress distribution at $\Delta_A = 4.0$ and the size of the tensile region near the debond tip as a function of the debond length given by Ghatak et al.'s [8] solution. 106

Figure 4-7: Non-dimensional load versus the applied non-dimensional displacement. The dashed lines represent results prior to the initiation of debonding. 106

Figure 4-8: For $A_0 = 2.83$, the peak load (pull-off force) as a function of the non-dimensional number ψ on a log-log scale. 108

Figure 5-1: Schematics of a demolding process for fabrication of an ophthalmic lens made of an organogel. ... 112

Figure 5-2: Schematic sketches of (a) the desired failure mode of separation from one interface and the undesired modes of separation (b) from the wrong interface and (c) from both interfaces resulting in 'bridging'. 113

Figure 5-3: Schematic of the problem studied. 116

Figure 5-4: The bilinear TS relation. 119

Figure 5-5: The FE meshes 1 and 2 used, respectively, for analyzing stresses over interfaces without (FE mesh 1) and with (FE mesh 2) the possibility of damage initiation and propagation. 123

Figure 5-6: Distributions of the peel stress (a) over the upper interface for FE meshes 1 and 2, and (b) near the upper interface corner for FE meshes 1 and 3 plotted on a log-log scale. $\alpha_1 = 10, \eta = 0.2, \beta_1^{-1} = 1mm, \mu = 5MPa, \Delta T_1 = \Delta T_2 = \Delta T_{elas} = 0$, and $\delta_0 = 4\mu m$ 124

Figure 5-7: Comparison of the non-dimensional interfacial opening computed with FE meshes 1 and 2 for following values of parameters: $\alpha_1 = 10, \eta = 0.7, \phi = 3, \beta_1^{-1} = 1mm, \Delta T_1 = \Delta T_2 = \Delta T_{elas} = 0, \Delta_0 = 2.35$ 125

Figure 5-8: Distributions of the computed interfacial (a) peel and (b) shear stress at interface points close to the free edge of the interlayer for three values of η when $\alpha_1 = 10, \mu = 20 MPa, \beta_1^{-1} = 1mm$, and $\delta_0 = 4\mu m$. The inset in (b) illustrates directions of the positive interfacial traction components. To facilitate comparison in (b), the shear stress at the bottom interface is multiplied by -1. Deformed shapes (exaggerated by a factor of 100) are illustrated in (c) for the three values of η . These results are for interfaces that are yet to damage. 127

Figure 5-9: Distributions of the interfacial peel stress (a) for three values of η when $\alpha_1 = 10$, (b) for three values of α_1 when $\eta = 1$, (c) distributions of the interfacial shear stress for three values of η when $\alpha_1 = 10$; (d) variations of the magnitude of internal peak peel stress at the upper interface as a function of η for three values of α_1 and the % difference, Ω , between the magnitudes of internal peaks at the two interfaces (Ω is plotted on the vertical axis on the right hand side). For illustration in (c), the shear stress at the bottom interface is multiplied by -1. The plot of hydrostatic tension on the upper interface is included in (a). 128

Figure 5-10: Snapshots of computed deformed shapes for the flat mold assembly at indicated values of the applied non-dimensional displacements for (a) $\eta = 1$, (b) $\eta = 2$, (c) $\eta = 0.7$, and (d) $\eta = 0.5$ when

$\alpha_1 = 10$. The applied displacements at debonding initiation differ among these cases due to the change in the overall confinement when η is varied.	131
Figure 5-11: Debonding mechanisms on the $\alpha_1\alpha_2$ – plane for the flat mold assembly. Results correspond to the indicated values of $\eta = \alpha_2 / \alpha_1$ when $\alpha_1 = 5, 10$ and 20 , and $\alpha_2 = 5, 10$ and 20	132
Figure 5-12: For $\alpha_1 = 10, \eta = 1, \beta_1^{-1} = 1mm, \mu = 5MPa$ and $\delta_0 = 4\mu m$, and prior to the initiation of damage, distributions of the computed interfacial peel and shear stresses close to the free edge of the interlayer for one flat and for four curved mold assemblies. For the flat mold assembly the horizontal axis corresponds to the horizontal distance X measured from the axis of symmetry and for the curved cases it corresponds to the angular position, γ in degrees, measured from the axis of symmetry. A log scale is used on the vertical axis. The shear stress on the lower interface is multiplied with -1 to facilitate comparison of the opening shear.....	135
Figure 5-13: For $\alpha_1 = 10, \eta = 1, \beta_1^{-1} = 1mm, \mu = 5MPa$ and $\delta_0 = 4\mu m$, and prior to the initiation of damage through-the-thickness variation of $\varepsilon_{\theta\theta}$ for one flat and four curved molds with their radii of curvatures, r_1 , indicated in the plots. The angular positions at which through-the-thickness variations are plotted correspond with those of the interlayer edge. The distance z_0 is measured from the mid-surface (upper mold: $r = r_1 - t_1 / 2$, and Lower mold $r = r_1 + h + t_2 / 2$) of each mold.	136
Figure 5-14: For $\alpha_1 = 10, \eta = 1, \beta_1^{-1} = 1mm, \mu = 5MPa$ and $\delta_0 = 4\mu m$, and prior to the initiation of damage, distributions of the computed peel stress for $r_1 = 10mm$ (a) close to the free surface of the interlayer, and (b) over the entire interface for $\eta = 0.2, 0.5$ and 1 . The corresponding plots of the interfacial shear stress are shown in (c) and (d). For illustration in (c) and (d), the shear stress at the bottom interface is multiplied by -1. The plot of the hydrostatic pressure on the upper interface is included in (b) for $\eta = 1$	137
Figure 5-15: Debonding mechanisms on the $\alpha_1\alpha_2$ – plane for the curved mold assembly with $r_1 = 10mm$ and $\eta = \alpha_2 / \alpha_1$	138
Figure 5-16: For $\alpha_1 = 10, \beta_1^{-1} = 1mm, \mu = 5MPa$ and $\Delta T_1 = 4^\circ C$, and no damage allowed at the two interfaces, distributions of the interfacial peel and shear stresses after preheating (Figs. I and II), and of the interfacial peel and shear stresses upon applying $\delta_0 = 4\mu m$ with and without preheating (Figs. III and IV). The three columns correspond to results for (a) $\Delta T_2 = 2^\circ C$, (b) $\Delta T_2 = 1^\circ C$ and (c) $\Delta T_2 = 0^\circ C$	141
Figure 5-17: Computed distributions of peel stresses after application of $\delta_0 = 4\mu m$ at the (a) upper and the (b) lower interfaces at different levels of heating of the upper mold while the difference of temperature between the upper and the lower mold stays constant at $3^\circ C$ except for the black lines which correspond to no pre-heating. The values of other input parameters are: $\alpha_1 = 10, \beta_1^{-1} = 1mm, \mu = 5MPa$. These results are obtained when damage is not allowed at the interfaces.	142

Figure 5-18: Snapshots illustrating evolution of debonding for $\Delta T_1 = 4^\circ C$, and (a) $\Delta T_2 = 3^\circ C$ and (b) $\Delta T_2 = 1^\circ C$	144
Figure 5-19: Debonding mechanisms ‘map’ on the $\Delta T_2 \Delta T_1$ -plane for the curved mold-assembly when $\alpha_1 = 10$ and $\eta = 1$	144
Figure C 1: For $\phi = 8.25$, sensitivity to the FE mesh of (a) the dimensionless reaction force ($\bar{P} = R/T_c \tilde{A}$) vs. the dimensionless displacement, $\bar{\Delta}$, applied at a rate of 1 mm/s when $m = 3$, and (b) the dimensionless interfacial contact opening when $\Delta = 0.54$	43
Figure C 2: For $\phi = 41.25$, sensitivity to the FE mesh of (a) the dimensionless reaction force vs. dimensionless displacement applied at a rate of 1 mm/s when $m = 3$, and (b) the dimensionless interfacial contact opening when $\Delta = 1.67$	44
Figure D 1: For $\alpha = 8, \beta^{-1} = 1mm, a_0 = 2.83mm$, sensitivity to the FE mesh of (a) distribution of the peel stress at the interface (yet to damage) when $\delta_A = 1\mu m$, and (b) distribution of the contact opening when $\phi = 4, \Delta_A = 3.634$	83
Figure D 2: For $\alpha = 100, \phi = 4, \beta^{-1} = 1mm$, sensitivity to the FE mesh of (a) the non-dimensional peel stress distribution for $\Delta_A = 0.7$, and (b) the non-dimensional load-displacement variation until $\Delta_A = 0.7$. This represents a type-2 debonding as illustrated in Figure 3-9.	84
Figure D 3: For $\alpha = 100, \phi = 5, \beta^{-1} = 1mm$, sensitivity to the FE mesh of (a) the non-dimensional peel stress distribution for $\Delta_A = 1.2$, and (b) the non-dimensional load-displacement variation until $\Delta_A = 1.2$. This represents type-3 debonding as illustrated in Figure 3-10.	84
Figure D 4: For $\alpha = 100, \phi = 50, \beta^{-1} = 1mm$, sensitivity to the FE mesh of (a) the non-dimensional peel stress distribution for $\Delta_A = 0.85$, and (b) the non-dimensional load-displacement variation until $\Delta_A = 0.85$. This represents a type-4 debonding as illustrated in Figure 3-11.	85
Figure E 1: Computed energy histories for mesh-1, and $\alpha = 25, \phi = 4, \beta^{-1} = 1mm, \mu = 5MPa, T_c = 0.04MPa$, and $a_0 = 2.83mm$. The out-of-plane dimension (width) is taken to be 1 mm when computing the total energy. As discussed in Section 3.4, the dip in the load-displacement plot corresponds to the initiation of internal debonding.	86
Figure F 1: Snapshots of interfacial dimensionless contact opening for $\phi = 4$, and 5 and confinement levels of $\alpha = 25$, and 2, when the lateral surfaces of the interlayer are prevented to deform in the y-direction but those of the plate are free. The bottom right figure corresponds to $\alpha = 25$ and $\phi = 5$ when the lateral surfaces of both the plate and the interlayer are restrained in the y-direction.....	88

Figure H 1: Schematic sketch of the configuration of Anderson et al.'s cone test[17].....	148
Figure I 1: The computational domain	150
Figure I 2: The bi-linear traction separation law	151
Figure I 3: Separation behavior at different separation speeds and -20°C, shown at 1 mm separation	152
Figure I 4: Separation behavior at different temperatures at 10 mm/s separation speed, shown at 1 mm separation.....	152
Figure I 5: Frames showing the growth and propagation of bridge at -20°C and 10 mm/s separation speed	153
Figure I 6: Contours of maximum principal stresses on the deformed shapes of the interlayer at -20°C and 10 mm/s separation speed.....	153

List of tables

Table 2-1: Qualitative evidence of the time-temperature equivalence in predictions from the model	33
Table 2-2: Effect of the TS parameters (for plate rigidity = 2.1 Nm, interlayer thickness = 250 μm , and pulling rate = 1 mm/s), which evince that wavy undulations vanish when the interfacial softening is increased relative to the interlayer stiffness (lower effective stiffness at a higher temperature due to viscoelasticity).....	40
Table 3-1: Effect of confinement and adhesion on the pull-off force	76
Table 5-1: Illustration of opening and closing at the edge due to the sign of the shear stress	114
Table 5-2: Sensitivity of computed predictions of debonding to a prescribed strength/fracture energy bias (lower interface stronger than the upper interface) when $\alpha_1 = 10$, and $\eta = 0.4$. The biases are expressed in terms of % difference.	132
Table 5-3: Sensitivity of computed predictions of debonding to a prescribed strength/fracture energy bias (lower interface stronger than the upper interface) $\alpha_1 = 10$, and $\eta = 0.7$. The biases are expressed in terms of % difference.	133
Table 5-4: Sensitivity of debonding to a prescribed strength/fracture energy bias (lower interface stronger than the upper interface) when $\alpha_1 = 10$, and the level of heating is varied.	145
Table B 1: Values of material parameters in the Prony series at the reference temperature of 45°C [45].....	42
Table D 1: The FE meshes used [†]	82
Table H 1: Summary of computed predictions of debonding in a cone test	148
Table I 1: The Prony series parameters	150

1 Introduction

Understanding the mechanics of interfacial debonding of an elastomeric layer sandwiched between two adherends is of widespread interest due to its relevance in science and technology. The research presented in this dissertation was essentially initiated by the need to identify key factors governing a soft ophthalmic lens demolding process [1]. However, the reported outcomes are envisioned to be useful in contexts of a number of other applications. Examples include durability of sealants[2], ensuring integrity of the elastomer interlayer in laminated safety glasses[3], restricting potential delamination in flip-chip packaging [4], ease of ink release in transfer printing processes[5-7], engineering antifouling such as of barnacles to ship-hulls [8, 9], and in the rapidly growing field of bio-inspired adhesion [10, 11]. Dictated by the application, interfacial debonding of a sandwiched layer is to be either prevented or facilitated under stress. For example, a sealant should be designed so that the nucleation of new debonds and growth of pre-existing interfacial flaws are prevented. On the other hand, release applications, such as successful demolding during lens fabrication or the release of an ink layer from a substrate in a transfer printing process[6], must be engineered to facilitate damage-free debonding from an interface. Tunable adhesion may be pivotal to the success of applications such as Gecko-inspired adhesives[12], which are designed to have a high resistance to debonding in shear but low resistance in the normal direction. Regardless of the varying application-specific requirements, the common underlying need is to achieve control of the interfacial debonding. This motivates the need to understand the collective role of the geometric, material, and interfacial adhesion parameters on the mechanics of debonding.

Previous research [13-20] on debonding of a sandwiched elastomeric interlayer suggests that even in the presence of an external debond, debonding may nucleate over the interior of the interface/bondline to relieve the imposed lateral constraint when the interlayer thickness is small enough relative to a characteristic length scale. Research has shown that locations of the nucleation sites [18] and the average spacing between multiple internal debonds [19] could be predicted for smooth interfaces as functions of geometric lengths. This suggests the importance of capturing, in a mechanistic analysis, debond initiation regardless of the presence of pre-existing defects.

The traditional linear elastic fracture mechanics (LEFM) approach for analyzing debonding is based on the premise that a pre-existing debond/crack begins to grow under

applied stress when the change in the potential energy per unit growth of crack area, termed as the energy release rate (ERR), exceeds a critical value [21]. This critical value is known as the fracture energy. The intensity of singular stress fields that may occur near a bi-material crack tip [22-25] can be related to the ERR to assess the resistance to debonding. Besides being unsuitable for capturing debond nucleation at a defect-free interface, the LEFM approach is not amenable to a strict continuum mechanics analysis since the latter cannot accommodate the creation of two points from one point as necessitated by debonding/cracking. A maximum stress (strength) criterion seems to be helpful at first sight but is not sufficient because it (i) may predict spurious results when stresses are singular, (ii) does not correctly account for experimentally measured energy required to create two new surfaces, and (iii) cannot predict experimentally observed defect-size-dependence of the measured global results such as the failure load [21, 26]. A cohesive zone model (CZM) approach, introduced conceptually by Dugdale [27] and Barenblatt [28] and later coupled with a finite element analysis of concrete fracture by Hillerborg et al. [29], helps to bridge the gap between the LEFM and the strength-based approach by circumventing limitations of each. A CZM approach can model evolution of damage and debonding occurring at a stressed interface. This is achieved by prescribing *a-priori* a relation between the surface traction vector and the displacement jump vector (separation) between two adjoining interfacial points conceived to be connected by zero-length springs. Such a relation is commonly known as a traction-separation (TS) relationship. Enforcing a TS relation makes the approach amenable to a continuum analysis and suppresses traction singularities via the prescribed peak tractions. One motivation of using a TS relation is to lump the collective influence of small-scale dissipative processes which contribute to the interfacial damage accumulation leading to debonding. The shape of a TS relation, in particular, the prescribed critical separation values can be tailored [30] to capture these mechanisms occurring over various length scales. The CZM approach has been successfully used to simulate a large range of interfacial as well as bulk fracture problems [31-39]. Recognizing its ease of use in studying adhesive debonding of elastomers, a CZM with a bilinear TS relation has been used throughout this dissertation.

This dissertation is written in manuscript-format and consists of four papers (one published article, one in review, one ready for submission and one in preparation for submission for publication in peer-reviewed journals), included here as Chapters 2-5. Brief outlines of each of these four chapters are listed below.

Chapter 2

This chapter analyzes the well-known wavy/undulatory debonding [40] phenomenon that occurs when an elastomeric layer, sandwiched between two stiff adherends, debonds from one adherend. A schematic sketch of the phenomenon is shown in Figure 1.1. We advance the reported understanding of the problem [19, 20, 40-43] by employing a TS relation for the elastomer/adherend interface. The problem is first analyzed for a semi-infinite elastomer layer debonding from a rigid adherend. A combination of stability analysis of linear equations governing plane strain deformations of the system and the finite element method (FEM) leads to the conclusion that the competition between interfacial softening (captured by CZM) and the elastic deformation of the film triggers a wavy debonding process. A non-dimensional parameter in terms of the CZM parameters and the viscoelastic properties, and its lower limit are found to provide a necessary condition for wavy debonding to occur. We have augmented the concept further, at least qualitatively, in the context of fingerlike debonding phenomenon[44] by analyzing three-dimensional deformations and progressive debonding that occurs in a peel test involving a flexible adherend. However, it is found that whether or not fingerlike debonding occurs depends also on the rigidity of the plate dictated by the modulus and thickness of the elastomer layer. The outcome of this work is hoped to be of value from a materials design perspective as well as in view of modeling debonding process of elastomeric materials.

This work has recently appeared in the *International Journal of Adhesion and Adhesives*. ([doi:10.1016/j.ijadhadh.2015.12.006](https://doi.org/10.1016/j.ijadhadh.2015.12.006))

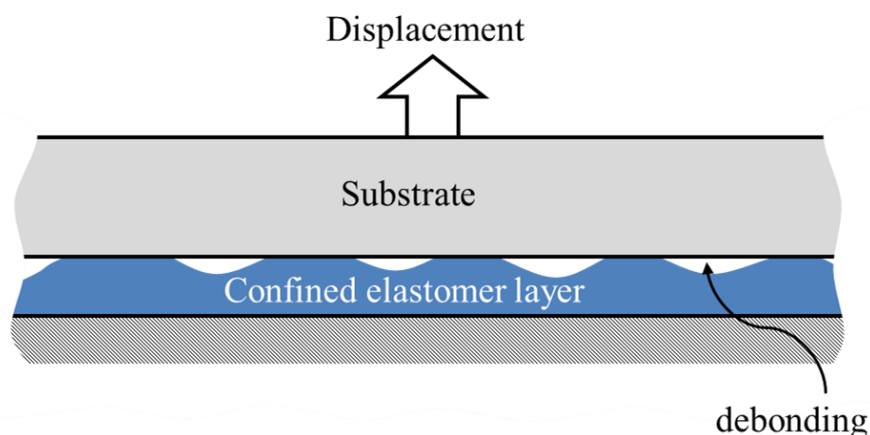


Figure 1.1: A schematic sketch of the wavy debonding phenomenon studied in Chapter 2

Chapter 3

Motivated by the finding in Chapter 2 that whether or not a fingerlike debonding ensues during peeling of a flexible plate is dictated by both the interfacial adhesion and the rigidity of the plate for an elastomer layer of given modulus and thickness, this chapter investigates the role of the coupling between the geometric and material parameters, and the interfacial adhesion on debonding characteristics of an elastomeric layer when an overhanging flexible plate is pulled off from it. The deformations are approximated as plane strain, and the FEM is used to solve for the deformations. Our computed results reveal the collective effects of the two non-dimensional variables: the confinement parameter, which was also identified by previous investigators [20, 44, 45], and the adhesion parameter found from the work reported in Chapter 2. The roles played by these two parameters on the interfacial debonding mechanisms and on the maximum load in the load-displacement history are delineated through numerical experiments. Results reported here advance our current understanding of the peeling phenomenon, may help in developing predictive models for complex manufacturing processes involving separation of confined elastomeric layers, shed light on the global behavior such as the pull-off force as a function of geometric confinement and interfacial adhesion and its transition from a strength-dominated regime to a fracture-energy dominated regime, and may help in determining the TS parameters for the interface between an elastomer layer and a stiff adherend

Results of several additional numerical experiments in which the elastomer can debond from both adherends provide insights into controlling of adhesive debonding in order to improve process yield in industrial fabrication of soft elastomeric products such as ophthalmic lenses. This is investigated in greater detail in Chapter 5.

Chapter 4

An outcome of the numerical experiments conducted in Chapter 3 is that for interlayers that are not sufficiently confined, damage initiates at the edge of the interface, forms a process zone (cohesive zone (CZ)), and then propagates with a CZ at its front upon continued loading. This debonding mechanism is investigated in this chapter using the CZM and a semi-analytical method built on the approaches of Dillard [46] who analyzed bending of a flexible plate resting on an elastomeric foundation and Ghatak et al. [47] who later extended Dillard's work by using an LEFM approach to relate the propagating crack length to the work of adhesion. The key outcome of the present work is a non-dimensional parameter

in terms of the plate flexibility, the modulus and thickness of the elastomeric layer and the TS parameters, which is shown to govern the interfacial peel stress distribution, debond length and the reaction force under a chosen normalization scheme. It is also shown that the pull-off force transitions from a strength-dominated regime (LEFM invalid) to a fracture energy-dominated regime (LEFM valid) as the value of this parameter gradually increases.

Chapter 5

The research work reported in Chapter 5 is closely related to an industrial demolding process used to fabricate an ophthalmic lens. A key processing step during the fabrication is the separation of an elastomeric (organogel) layer sandwiched between two flexible molds. The demolding process involves prying open the flexible mold-assembly by a displacement-controlled loading and is engineered for interfacial separation to occur preferentially from one desired mold interface. With the use of molds made of the same material in a practical manufacturing line, the demolding process runs the risk of causing debonding from the wrong interface and/or both interfaces, resulting in an erratic separation process that can damage the product. Motivated by the suspicion that edge peeling could be biased towards one interface by increasing the amount of opening shear towards the edge of that interface, the primary goals of this chapter are to study the roles of (i) the relative flexibilities of the two molds, (ii) the curvature when the interlayer is in the shape of a portion of a hemisphere, and (iii) preheating the assembly differentially prior to mechanical loading in causing debonding to occur preferentially at a desired interface. We use the FEM to analyze axisymmetric deformations of a simple configuration consisting of an elastomeric layer of uniform thickness with its two surfaces adhered to two overhanging flexible molds that are subjected to normal displacements near the edges of the overhangs. Results of numerical experiments suggest that (i) debonding occurs preferentially from the edge of the interface between the elastomer and the more flexible mold; however, internal debonding may ensue and grow on the other interface when the molds are rigid enough depending on the modulus and the thickness of the elastomeric layer, (ii) for a curved assembly, edge debonding is inherently biased, for the considered normal loading conditions, to the interface corresponding with the inner surface of the interlayer and (iii) preferential debonding can be engineered by preheating the assembly differentially; however, a differential large enough dictated by the absolute level of heating may cause internal debonding. Sensitivities of the predicted debonding mechanisms to prescribed biases in the TS parameters are assessed. The outcomes

of this work may be useful in engineering similar demolding processes to achieve a desired separation process.

References

- [1] Larsen, H.-O., *Mold for making contact lenses, either the male or female mold sections being relatively more flexible*. Patent No. 4640489. 1987
- [2] Dillard, D.A., et al. *Seals and sealants in PEM fuel cell environments: Material, design, and durability challenges*. in *ASME 2004 2nd International Conference on Fuel Cell Science, Engineering and Technology*. 2004. American Society of Mechanical Engineers.
- [3] Chabal, J. and R.G. Rieser, *Laminated safety windshields*. U.S. Patent 3881043. 1975
- [4] Uddin, M., M. Alam, Y. Chan, and H. Chan, *Adhesion strength and contact resistance of flip chip on flex packages—effect of curing degree of anisotropic conductive film*. *Microelectronics Reliability*, 2004. **44**(3): p. 505-514.
- [5] Kim-Lee, H.-J., A. Carlson, D. Grierson, J. Rogers, and K. Turner, *Interface mechanics of adhesiveless microtransfer printing processes*. *Journal of Applied Physics*, 2014. **115**(14): p. 143513.
- [6] Carlson, A., A.M. Bowen, Y. Huang, R.G. Nuzzo, and J.A. Rogers, *Transfer printing techniques for materials assembly and micro/nanodevice fabrication*. *Advanced Materials*, 2012. **24**(39): p. 5284-5318.
- [7] Tucker, M.B., D. Hines, and T. Li, *A quality map of transfer printing*. *Journal of Applied Physics*, 2009. **106**(10): p. 103504.
- [8] Chung, J.Y. and M.K. Chaudhury, *Soft and hard adhesion*. *The Journal of Adhesion*, 2005. **81**(10-11): p. 1119-1145.
- [9] Hui, C.-Y., R. Long, K.J. Wahl, and R.K. Everett, *Barnacles resist removal by crack trapping*. *Journal of The Royal Society Interface*, 2011. **8**(59): p. 868-879.
- [10] Bartlett, M.D. and A.J. Crosby, *Scaling normal adhesion force capacity with a generalized parameter*. *Langmuir*, 2013. **29**(35): p. 11022-11027.
- [11] Glassmaker, N.J., A. Jagota, C.-Y. Hui, W.L. Noderer, and M.K. Chaudhury, *Biologically inspired crack trapping for enhanced adhesion*. *Proceedings of the National Academy of Sciences*, 2007. **104**(26): p. 10786-10791.
- [12] Crosby, A.J., M. Bartlett, A.B. Croll, and D.J. King, *High capacity easy release extended use adhesive devices*. U.S. Patent 20140030490. 2014
- [13] Anderson, G., K. DeVries, and M. Williams, *Mixed mode stress field effect in adhesive fracture*. *International Journal of Fracture*, 1974. **10**(4): p. 565-583.
- [14] Mowery, C.L., A.J. Crosby, D. Ahn, and K.R. Shull, *Adhesion of thermally reversible gels to solid surfaces*. *Langmuir*, 1997. **13**(23): p. 6101-6107.
- [15] Webber, R.E., K.R. Shull, A. Roos, and C. Creton, *Effects of geometric confinement on the adhesive debonding of soft elastic solids*. *Physical Review E*, 2003. **68**(2): p. 021805.
- [16] Crosby, A.J., K.R. Shull, H. Lakrout, and C. Creton, *Deformation and failure modes of adhesively bonded elastic layers*. *Journal of Applied Physics*, 2000. **88**(5): p. 2956-2966.
- [17] Creton, C., J. Hooker, and K.R. Shull, *Bulk and interfacial contributions to the debonding mechanisms of soft adhesives: extension to large strains*. *Langmuir*, 2001. **17**(16): p. 4948-4954.
- [18] Ghatak, A., L. Mahadevan, J.Y. Chung, M.K. Chaudhury, and V. Shenoy, *Peeling from a biomimetically patterned thin elastic film*. *Proceedings of the Royal Society of*

- London. Series A: Mathematical, Physical and Engineering Sciences, 2004. **460**(2049): p. 2725-2735.
- [19] Chaudhury, M.K., A. Chakrabarti, and A. Ghatak, *Adhesion-induced instabilities and pattern formation in thin films of elastomers and gels*. The European Physical Journal E, 2015. **38**(7): p. 1-26.
- [20] Adda-Bedia, M. and L. Mahadevan, *Crack-front instability in a confined elastic film*. Proceedings of the Royal Society A: Mathematical, Physical and Engineering Science, 2006. **462**(2075): p. 3233-3251.
- [21] Griffith, A.A., *The phenomena of rupture and flow in solids*. Philosophical transactions of the royal society of london. Series A, containing papers of a mathematical or physical character, 1921. **221**: p. 163-198.
- [22] Suo, Z. and J.W. Hutchinson, *Interface crack between two elastic layers*. International Journal of Fracture, 1990. **43**(1): p. 1-18.
- [23] Hutchinson, J.W. and Z. Suo, *Mixed mode cracking in layered materials*. Advances in applied mechanics, 1992. **29**(63): p. 191.
- [24] Hutchinson, J.W., *Mixed mode fracture mechanics of interfaces*. Metal and Ceramic interfaces, 1990: p. 295-306.
- [25] Anderson, T.L., *Fracture mechanics: fundamentals and applications*. 2005: CRC press.
- [26] Inglis, C.E., *Stresses in a plate due to the presence of cracks and sharp corners*. Proceedings of the Institute of Naval Architects, 1913.
- [27] Dugdale, D., *Yielding of steel sheets containing slits*. Journal of the Mechanics and Physics of Solids, 1960. **8**(2): p. 100-104.
- [28] Barenblatt, G.I., *The mathematical theory of equilibrium cracks in brittle fracture*. Advances in applied mechanics, 1962. **7**(1): p. 55-129.
- [29] Hillerborg, A., M. Mod er, and P.-E. Petersson, *Analysis of crack formation and crack growth in concrete by means of fracture mechanics and finite elements*. Cement and concrete research, 1976. **6**(6): p. 773-781.
- [30] Sills, R. and M. Thouless, *Cohesive-length scales for damage and toughening mechanisms*. International Journal of Solids and Structures, 2015. **55**: p. 32-43.
- [31] Rahul-Kumar, P., A. Jagota, S. Bennison, S. Saigal, and S. Muralidhar, *Polymer interfacial fracture simulations using cohesive elements*. Acta materialia, 1999. **47**(15): p. 4161-4169.
- [32] Rahulkumar, P., A. Jagota, S. Bennison, and S. Saigal, *Cohesive element modeling of viscoelastic fracture: application to peel testing of polymers*. International Journal of Solids and Structures, 2000. **37**(13): p. 1873-1897.
- [33] Blackman, B., H. Hadavinia, A. Kinloch, and J. Williams, *The use of a cohesive zone model to study the fracture of fibre composites and adhesively-bonded joints*. International Journal of Fracture, 2003. **119**(1): p. 25-46.
- [34] Chandra, N., H. Li, C. Shet, and H. Ghonem, *Some issues in the application of cohesive zone models for metal–ceramic interfaces*. International Journal of Solids and Structures, 2002. **39**(10): p. 2827-2855.
- [35] Li, S., M. Thouless, A. Waas, J. Schroeder, and P. Zavattieri, *Use of mode-I cohesive-zone models to describe the fracture of an adhesively-bonded polymer-matrix composite*. Composites Science and Technology, 2005. **65**(2): p. 281-293.
- [36] Song, S.H., G.H. Paulino, and W.G. Buttlar, *A bilinear cohesive zone model tailored for fracture of asphalt concrete considering viscoelastic bulk material*. Engineering Fracture Mechanics, 2006. **73**(18): p. 2829-2848.

- [37] Wang, J., *Cohesive zone model of intermediate crack-induced debonding of FRP-plated concrete beam*. International journal of solids and structures, 2006. **43**(21): p. 6630-6648.
- [38] Nguyen, T. and S. Govindjee, *Numerical study of geometric constraint and cohesive parameters in steady-state viscoelastic crack growth*. International journal of fracture, 2006. **141**(1-2): p. 255-268.
- [39] Alfano, M., F. Furguele, A. Leonardi, C. Maletta, and G. Paulino, *Mode I fracture of adhesive joints using tailored cohesive zone models*. International journal of fracture, 2009. **157**(1-2): p. 193-204.
- [40] Ghatak, A., M.K. Chaudhury, V. Shenoy, and A. Sharma, *Meniscus instability in a thin elastic film*. Physical Review Letters, 2000. **85**(20): p. 4329.
- [41] Shenoy, V. and A. Sharma, *Pattern formation in a thin solid film with interactions*. Physical review letters, 2001. **86**(1): p. 119.
- [42] Sarkar, J., A. Sharma, and V. Shenoy, *Adhesion and debonding of soft elastic films: Crack patterns, metastable pathways, and forces*. Langmuir, 2005. **21**(4): p. 1457-1469.
- [43] Mönch, W. and S. Herminghaus, *Elastic instability of rubber films between solid bodies*. EPL (Europhysics Letters), 2001. **53**(4): p. 525.
- [44] Ghatak, A. and M.K. Chaudhury, *Adhesion-induced instability patterns in thin confined elastic film*. Langmuir, 2003. **19**(7): p. 2621-2631.
- [45] Vilmin, T., F. Ziebert, and E. Raphaël, *Simple View on Fingering Instability of Debonding Soft Elastic Adhesives*. Langmuir, 2009. **26**(5): p. 3257-3260.
- [46] Dillard, D., *Bending of plates on thin elastomeric foundations*. Journal of applied mechanics, 1989. **56**(2): p. 382-386.
- [47] Ghatak, A., L. Mahadevan, and M.K. Chaudhury, *Measuring the work of adhesion between a soft confined film and a flexible plate*. Langmuir, 2005. **21**(4): p. 1277-1281.

2 Debonding of Confined Elastomeric Layer using Cohesive Zone Model

Bikramjit Mukherjee^a, David A. Dillard^{a*}, Robert B. Moore^b and Romesh C. Batra^a

^aDepartment of Biomedical Engineering and Mechanics, M/C 0219

^bDepartment of Chemistry, M/C 0212

Virginia Polytechnic Institute and State University
Blacksburg, Virginia 24061, USA

(The material of this chapter has appeared as an article in *International Journal of Adhesion and Adhesives*; doi:10.1016/j.ijadhadh.2015.12.006)

Abstract

Wavy or undulatory debonding is often observed when a confined/sandwiched elastomeric layer is pulled off from a stiff adherend. Here we analyze this debonding phenomenon using a cohesive zone model (CZM). Using stability analysis of linear equations governing plane strain quasi-static deformations of an elastomer, we find (i) a non-dimensional number relating the elastomer layer thickness, h , the long term Young's modulus, E_∞ , of the interlayer material, the peak traction, T_c , in the CZM bilinear traction-separation (TS) relation, and the fracture energy, G_c , of the interface between the adherend and the elastomer layer, and (ii) the critical value of this number that provides a necessary condition for undulations to occur during debonding. For the elastomer modeled as a linear viscoelastic material with the shear modulus given by a Prony series and a rate-independent bilinear TS relation in the CZM, the stability analysis predicts that a necessary condition for a wavy solution is that $T_c^2 h / G_c E_\infty$ exceed 4.15. This is confirmed by numerically solving governing equations by the finite element method (FEM). Lastly, we use the FEM to study three dimensional deformations of the peeling (induced by an edge displacement) of a flexible plate from a thin elastomeric layer perfectly bonded to a rigid substrate. These simulations predict progressive debonding with a fingerlike front for sufficiently confined interlayers when the TS parameters qualitatively satisfy the constraint found from the stability analysis of the plane strain problem.

Keywords: Fingerlike instability, wavy or undulatory debond front, cohesive zone model (CZM), elastomeric interlayer, debonding

* Corresponding author, Email: dillard@vt.edu, Tel.: +1- 540-231-4714, Fax: +1- 540-231-9187

List of symbols

Symbols	Meaning
A	Hamaker constant for van der Waals interaction
\mathbf{B}	Left Cauchy-Green tensor
d	Distance between an elastic film and an approaching contactor
\bar{d}	Damage variable
D	Bending rigidity of the flexible plate
E	Young's modulus of the elastomeric interlayer
h	Thickness of the elastomeric interlayer
i	$= \sqrt{-1}$
K	Slope of the rising part of the straight line in the bilinear traction-separation law
k	Wavenumber of the x - dependent part of the perturbation to the stream function and the hydrostatic pressure.
m	Ratio of the modulus of the spring in the spring-dashpot link to the long-time modulus for the 1-term Prony series
p	Hydrostatic pressure not related to strains for incompressible materials
R	Reaction force on the rigid adherend
T	Normal traction at the interface
t	Time
u, v, w	Displacement components along x , y and z directions, respectively
x, y, z	Axes of the rectangular Cartesian coordinate system when the index i of the system x_i has values 1, 2 and 3, respectively
α	Magnitude of the slope of the falling part of the straight line portion of the bilinear traction-separation relation
Δ	Applied vertical displacement to the upper adherend
δ	Displacement jump at the interface, also called the contact opening
λ	Dominant wavelength of debonding undulation
μ	Shear modulus of the elastomeric interlayer
Ψ	Stream function introduced to define displacement components u and w
ω	Growth rate of a perturbation
a_1, a_2	Material constants in the constitutive equation used to model finite strain viscoelasticity
a_T	Shift factor relating the relaxation time at temperature T to that at the reference temperature
C_1, C_2	Constants in the Williams- Landel-Ferry (WLF) equation for a_T
$E_\infty (= 3\mu_\infty)$	Long term Young's modulus ($=3 \times$ long-term shear modulus) of the viscoelastic material
$E_0 (= 3\mu_0)$	Instantaneous Young's modulus ($=3 \times$ instantaneous shear modulus) of the viscoelastic material
F_t	Deformation gradient
G_c	Fracture energy
g_R	Relaxation function normalized by the instantaneous modulus of the viscoelastic material
K	$= K_I$

$K_{I,II,III}$	Initial slopes in the TS relations for the debonding modes <i>I,II</i> and <i>III</i>
$K_{softening}$	$= T_c^2 / G_c$
$K_{elastic}$	$= E_\infty / h$
l_{finger}	Length of a finger
p^{nh}	Non-homogeneous perturbation to the hydrostatic pressure
T_c	Peak value of the normal traction at the interface
x_i	Axes of the rectangular Cartesian coordinate system
δ_c	Critical displacement jump when damage initiates
δ_f	Displacement jump at the initiation of debonding/separation
ε_{ij}	Components of the infinitesimal strain tensor
μ_i	Shear modulus of the i^{th} term in the generalized Maxwell model used to define the relaxation function of the viscoelastic model.
μ_R	Relaxation function for the elastomeric interlayer when modeled as a linear viscoelastic material
σ_{ij}	Components of the stress tensor
τ_i	Characteristic relaxation time of the i^{th} element of the generalized Maxwell model
ϕ_{c1}	The lower limit of ϕ for debonding instability
ϕ_{c2}	The value of ϕ beyond which region III sets in
ψ^{nh}	Non-homogeneous perturbation of the stream function
\tilde{A}	Area of the interlayer initially bonded to the rigid adherend
\tilde{P}	z -dependent part of the hydrostatic pressure perturbation
\tilde{T}	Temperature
\tilde{T}_{REF}	Reference temperature
$\frac{\partial}{\partial x_i}$	Partial derivative (with respect to x_i) operator
\bar{x}	Distance along the x axis normalized by the half width of the rigid adherend
$\dot{\Delta}$	Rate of the applied vertical displacement to the upper adherend
$\bar{\delta}$	Contact opening normalized by δ_f
$\tilde{\psi}$	z - dependent part of the stream function perturbation
$\tilde{\omega}$	The growth rate ω normalized by $1/\tau_1$

2.1 Introduction

Systems consisting of a soft elastic or viscoelastic layer confined between two stiff substrates occur in numerous industrial applications. One example is manufacturing of bio-implants, which may involve mechanically demolding a soft polymer layer sandwiched between two relatively stiff molds [1]. A frequently observed phenomenon is the occurrence of contact undulations when a stiff layer is separated from the soft layer under tensile tractions. Classical examples include the formation of ripples when a contactor approaches an elastic film bonded to a fixed base [2-4], and wavy debonds in peel [5] and probe tack tests [6-8]. Experimentally, the characteristic spacing, λ , between two adjacent undulation peaks has been found [2, 9] to scale linearly ($\lambda \approx 3 - 4h$) with the thickness h of the confined interlayer while being independent of the interfacial adhesion properties. The linear stability analyses and energy arguments [10-13] have been used to show that undulations result from the competition between the strain energy of the system acting as a stabilizing influence, and the energy associated with the interfacial forces (such as van der Waals forces) acting as a destabilizing influence. These approaches give a threshold value of the interaction energy for the onset of instability. For example, it was shown [10, 14] that the condition $\frac{A}{6\pi d^4} \geq \frac{2E}{3h}$ is necessary for the onset of contact instabilities when a rigid contactor is gradually brought close to an elastic film of thickness h and Young's modulus E , where A is the effective Hamaker constant for van der Waals interactions and d the gap between the contactor and the film at the onset of instabilities. Other examples include [15] morphological changes in an elastic film caused by an applied electric field. Combined experimental and linear stability approaches have helped identify a threshold value of the effective voltage as a function of the film stiffness.

As debonding ensues at the interface between an adhesive and an adherend, multiple nonlinear processes such as cavitation and fibrillation may occur at the debonding site. These involve different length scales and contribute to the overall energy dissipation during the creation of the two new surfaces. In a cohesive zone model (CZM) [16, 17], the collective influences of these small-scale mechanisms are lumped together into a traction-separation (TS) relation. In this approach the adjoining points on the two sides of an interface are conceived to be connected by a spring of zero length that begins softening with extension (separation) after reaching a critical extension and subsequently breaks upon reaching a larger

limiting value of the extension. In a typical TS relation, it is assumed that the energy associated with the softening process is irrecoverable, i.e., upon unloading from extension between the critical and the limiting values, the spring stiffness remains constant at the reduced value. At the limiting extension value, the area under the TS curve equals the critical fracture energy (G_c) of the interface whose value is generally derived from the test data. Works cited above addressing the interplay between the destabilizing contact interaction, and the stabilizing elastic deformations of a film and the concomitant debonding instability suggest that the threshold for undulatory separation can be modeled by a TS relation. Hui et al. [18] illustrated this in the event of debonding between two blocks made of the same material.

In order to understand the mechanics of the peeling and demolding processes, researchers have often relied on numerical simulations. Since the use of the CZM coupled with the finite element method (FEM) by Hillerborg et al. [19] to study fracture problems, significant progress has been made in modeling interfacial debonding/delamination of a polymer interlayer [20-23]. However, there has been limited research [8, 24, 25] on capturing progressive interfacial debonding undulations using the CZM. The formation of debonding undulations (such as fingering in a peeling problem) adds to the complexity of the mechanics of the demolding process. The development of a tool for capturing such phenomena is important for delineating the debonding process and improving our understanding of the associated mechanics. The focus of our work is to identify the role of the TS, the material and the geometric parameters in causing undulatory debonding.

The rest of the paper is organized as follows: In Section 2.2, we present a linear stability analysis of plane strain deformations of an elastomeric layer debonding from a rigid adherend pulled vertically outward. We find a non-dimensional parameter in terms of the TS and the elastic film parameters that must exceed a critical value for debonding to exhibit an undulatory morphology. In Section 2.3, we analyze the two-dimensional (2D) problem by the FEM to provide details of the debonding evolution and confirm the necessary condition derived by the linear stability analysis. In Section 2.4, we use the FEM to analyze a practical problem, namely 3D deformations when a flexible plate is peeled off a confined elastomeric layer bonded to a rigid substrate. This necessitates introducing another non-dimensional parameter in terms of the plate bending stiffness and elastomer properties. We correlate results of this problem with our learnings from Sections 2.2 and 2.3. Conclusions are summarized in Section 2.5.

2.2 Analytical approach

2.2.1 Problem formulation

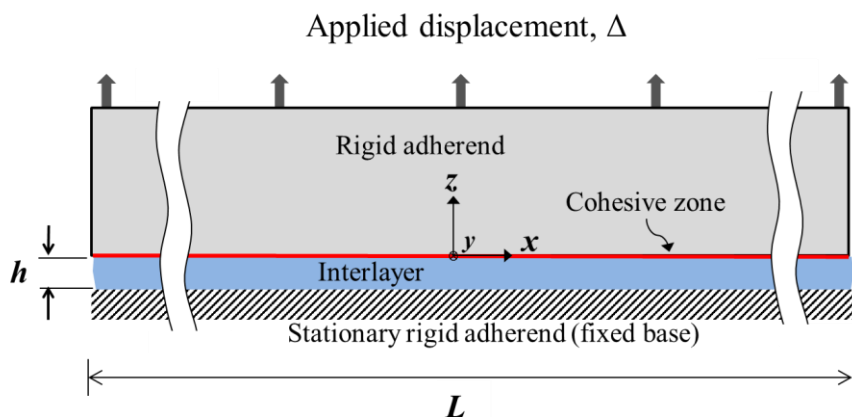


Figure 2-1: Schematic sketch of the problem studied. The width W (normal to the page, not shown) is large enough to justify studying plane strain deformations in the xz -plane.

We investigate the initiation of wavy debonding using a CZM when a rigid smooth adherend bonded to the upper surface of an elastomeric layer is pulled upwards while its lower surface stays perfectly bonded to the rigid support. Our analysis is essentially similar to those of [Shenoy and Sharma \[10\]](#) and [Huang et al. \[14\]](#) who used a linear stability approach to study instabilities in an elastic layer triggered by van der Waals forces when a rigid probe is brought near the layer. However, we use a TS relation to simulate debonding between the elastomeric layer and the upper rigid adherend. The configuration studied is schematically shown in Figure 2-1. The perfect bonding between the lower stationary rigid adherend and the elastomer layer is modeled by constraining to zero displacements of points on the bottom surface of the interlayer. We assume that the interlayer material is isotropic, incompressible, homogeneous and linear elastic/viscoelastic. The problem is first analyzed for a linear elastic interlayer, and subsequently for a viscoelastic layer. For the assumed form of the solution using the separation of variables with evolution in time represented by a sine (or cosine) function, the constitutive relation for a linear viscoelastic material reduces to that of a linear elastic material with the shear modulus depending upon a solution variable.

2.2.1.1 Linear elastic material

The constitutive equation for an incompressible, homogeneous and isotropic linear elastic material is $\sigma_{ij} = -p\delta_{ij} + 2\mu\varepsilon_{ij}$, where σ_{ij} is the stress tensor (i, j and k correspond to x, y , and z , respectively), ε_{ij} the strain tensor for infinitesimal deformations, p the

hydrostatic pressure not related to strains, and μ the shear modulus of the interlayer material. Recalling the strain-displacement relation, $\varepsilon_{ij} = \frac{1}{2} \left(\frac{\partial u_i}{\partial x_j} + \frac{\partial u_j}{\partial x_i} \right)$, the incompressibility constraint, $\varepsilon_{xx} + \varepsilon_{yy} + \varepsilon_{zz} = 0$, and assuming zero body force and negligible inertial effects the equilibrium equations $\frac{\partial \sigma_{ij}}{\partial x_j} = 0$ (repeated index j is summed over x , y , and z) reduce to the following Navier's equations.

$$\begin{aligned} \frac{\partial p}{\partial x} &= \mu \left(\frac{\partial^2 u}{\partial x^2} + \frac{\partial^2 u}{\partial z^2} \right) \\ \frac{\partial p}{\partial z} &= \mu \left(\frac{\partial^2 w}{\partial x^2} + \frac{\partial^2 w}{\partial z^2} \right) \end{aligned} \quad (2-1)$$

Here and below we denote the displacement components u_x and u_z as u and w , respectively. Perfect bond with the fixed lower rigid adherend is incorporated by setting u and w equal to zero at the lower interface of the interlayer. For thin confined infinitely wide incompressible films under tension, the shear stress over the central region is negligible, e.g., see [Lindsey et al. \[26\]](#). Thus, boundary conditions are:

$$\begin{aligned} \text{Fixed base: } & u(x, -h) = w(x, -h) = 0 \\ \text{Surface tractions: } & \begin{cases} \sigma_{zz}(x, 0) = -p(x, 0) + 2\mu \frac{\partial w}{\partial z}(x, 0) = T(\delta) \\ \sigma_{xz}(x, 0) = \mu \left(\frac{\partial w}{\partial x}(x, 0) + \frac{\partial u}{\partial z}(x, 0) \right) = 0 \end{cases} \end{aligned} \quad (2-2)$$

The interfacial normal traction T is related to the displacement jump $\delta = \Delta - w(x, 0)$ by the TS relation that characterizes the interface between the interlayer and the upper adherend. Here Δ is the vertical displacement of the upper rigid adherend. We have tacitly assumed that the region of interest is far removed from the edges $x = \pm \frac{L}{2}$ and boundary conditions at these edges, not specified in Eq. (2-2), do not affect deformations in the interior.

2.2.1.1.1 Description of cohesive zone behavior at the interface

We consider a bilinear TS relation [27] for the interface, illustrated in Figure 2-2, and given by Eq. (2-3). That is, the traction first increases linearly with the displacement jump, commonly termed the contact opening/separation, over the region OA. Point A denotes initiation of damage/softening beyond which the traction decreases affinely with an increase in the contact opening (line AB). Should unloading occur at point M, the traction follows the path MO. Subsequent reloading occurs along the path OMB.

$$T(\delta) = \begin{cases} K\delta & (0 \leq \delta \leq \delta_c) \\ \frac{T_c}{\delta_f - \delta_c}(\delta_f - \delta) & (\delta_c \leq \delta \leq \delta_f) \\ 0 & (\delta_f \leq \delta) \end{cases} \quad (2-3)$$

Point B signifies complete separation at a point on the interface. The energy release rate at debonding (i.e., the fracture energy) equals the area of the triangle OAB. That is,

$$\mathcal{G}_c = \frac{1}{2} T_c \delta_f \quad (2-4)$$

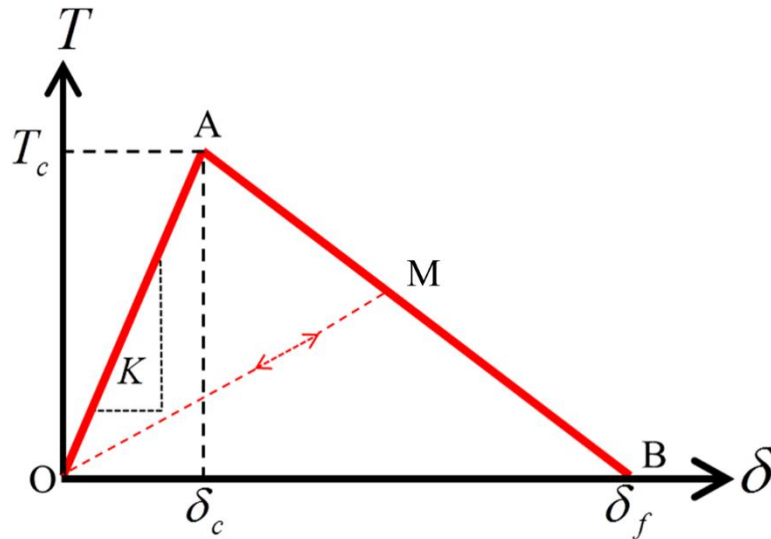


Figure 2-2: A bilinear traction-separation relation

A complete description of the bilinear TS relation involves specifying the initial slope K , the peak traction T_c and the fracture energy \mathcal{G}_c . In general, the value of K must be large

enough to not significantly alter the effective stiffness of the system and prevent interpenetration under compression. A very large value of K can make the system matrices ill-conditioned when the problem is analyzed by the FEM. While \mathcal{G}_c can be obtained directly from test data [28, 29], finding values of parameters, T_c and δ_c , is difficult. An indirect method, frequently employed [22, 30], is to iteratively find values of these parameters which, when used in numerical simulations, can predict reasonably well the experimental load-displacement traces. Recently, the digital image correlation [31] and the interferometry techniques [32] have been used to measure the TS parameters.

2.2.1.1.2 Homogeneous solution

We note that the homogeneous solution $u=0, w=0, p=\text{constant}$ satisfies equilibrium equations (2-1) and boundary conditions (2-2) for $T(\delta)=p$. The corresponding stresses are $\sigma_{zz}=\sigma_{xx}=\sigma_{yy}=-p$ and $\sigma_{zx}=0$. The pressure p , found from Eqs. (2a) and (3a), is given by Eq. (2-5). This homogeneous solution implies that pulling the upper adherend upwards will stretch the fictitious CZ springs while the interlayer will not deform.

$$p = \begin{cases} -K\Delta & (0 \leq \Delta \leq \delta_c) \\ -\frac{T_c}{\delta_f - \delta_c}(\delta_f - \Delta) & (\delta_c \leq \Delta \leq \delta_f) \\ 0 & (\delta_f \leq \Delta) \end{cases} \quad (2-5)$$

2.2.1.1.3 Non-homogeneous solution

We now explore the possibility of a non-homogeneous solution of the boundary value problem defined by Eqs. (2-1)–(2-3). For the deformation to identically satisfy the incompressibility constraint, we write displacements in terms of a stream function ψ as

$$u = \frac{\partial \psi}{\partial z}, w = -\frac{\partial \psi}{\partial x} \quad (2-6)$$

where ψ is a twice continuously differentiable function of x and z . In order to find necessary conditions for the instability of the homogeneous solution $\psi = \text{constant}$ and $p = \text{constant}$ (defined by Eq. (2-5)), we perturb it by adding to it the non-homogeneous field:

$p^{nh}(x, z) = e^{ikx} \tilde{p}(z)$ and $\psi^{nh}(x, z) = e^{ikx} \tilde{\psi}(z)$. Here the superscript nh stands for non-homogeneous, $i = \sqrt{-1}$, and k represents the wavenumber of the perturbation¹. The perturbed form, when substituted into equilibrium equation (2-1), yields the following system of ordinary differential equations (ODEs).

$$\begin{aligned} \mu \left(\frac{d^3 \tilde{\psi}}{dz^3} - k^2 \frac{d\tilde{\psi}}{dz} \right) - k\tilde{p} &= 0 \\ i\mu k \left(-\frac{d^2 \tilde{\psi}}{dz^2} + k^2 \tilde{\psi} \right) - \frac{d\tilde{p}}{dz} &= 0 \end{aligned} \quad (2-7)$$

The ODEs (2-7) have the solution

$$\begin{aligned} \tilde{p}(z) &= \cosh(kz)A_1 + ik^2\mu \sinh(kz)A_2 - i\mu \sinh(kz)A_4 \\ \tilde{\psi}(z) &= \frac{\left[\begin{aligned} &i(-kz \cosh(kz) - \sinh(kz))A_1 + k^2\mu(2\cosh(kz) - kz \sinh(kz))A_2 + \\ &2k\mu \sinh(kz)A_3 + k\mu z \sinh(kz)A_4 \end{aligned} \right]}{2k^2\mu} \end{aligned} \quad (2-8)$$

where constants A_1, \dots, A_4 of integration are determined from the boundary conditions.

Recalling that Δ is not perturbed, $\delta = \Delta - w(x, 0) = \Delta + ike^{ikx}\tilde{\psi}(0)$. In terms of the non-homogeneous z -dependent terms, boundary conditions (2-2) become:

$$\text{Fixed base: } \tilde{\psi}(-h) = \frac{d\tilde{\psi}}{dz}(-h) = 0 \quad (2-9a,b)$$

¹ The assumed perturbation, in the form of separation of variables with the complex x -dependent term, implies a sinusoidal variation in x -direction of wave-number k . Any perturbation can be considered for finding necessary conditions. However, finding sufficient conditions is more challenging.

$$\text{Top face} \quad : \quad \begin{cases} \tilde{p}(0) + 2\mu k \frac{d\tilde{\psi}}{dz}(0) + \alpha k \tilde{\psi}(0) = 0 \\ \frac{d^2\tilde{\psi}}{dz^2}(0) + k^2\tilde{\psi}(0) = 0 \end{cases} \quad (9c,d)$$

where

$$\alpha = \begin{cases} -K & (0 \leq \delta \leq \delta_c) \\ \frac{T_c}{\delta_f - \delta_c} & (\delta_c \leq \delta \leq \delta_f) \\ 0 & (\delta_f \leq \delta) \end{cases} \quad (2-10)$$

We assume that δ is increased monotonically during the debonding process. Two constants in solution (2-8) are evaluated from boundary conditions (2-9a,b). Enforcing the remaining boundary conditions (2-9a,b) we obtain the eigenvalue problem $[C]\{A\} = \{0\}$ that has a non-trivial solution if and only if $\det[C] = 0$. This gives the following equation for k of which we seek real roots.

$$f(hk) - \frac{\alpha h}{\mu} = 0 \quad (2-11)$$

where $f(hk) = \frac{2hk(1 + e^{2hk})^2 + 8e^{2hk}(hk)^3}{e^{4hk} - 4hke^{2hk} - 1}$. Roots of Eq. (2-11) depend upon values of the

TS parameters through their dependence upon α , the interlayer thickness h , and the shear modulus, μ , of the interlayer material. The function f versus hk , plotted in Figure 2-3, has

the minimum value 6.22. Thus Eq. (2-11) has real roots only if $\frac{\alpha h}{\mu} \geq 6.22$ and α is positive.

Eq. (2-10) implies that the separation, δ , must have values greater than δ_c and at most equal to δ_f .

For $\frac{\alpha h}{\mu} > 6.22$, one real root of Eq. (2-11) is less than 2.12 and the other greater than

2.12. The perturbed solution can be expressed as a linear combination of these two solutions. It is possible that the two perturbations will grow at different rates.

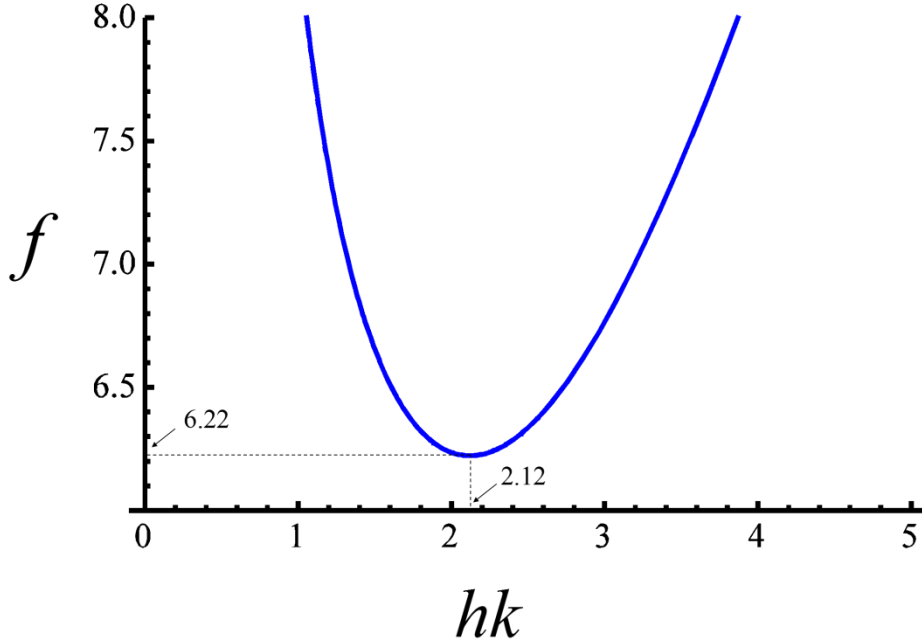


Figure 2-3: The plot of function $f(hk)$. The implication is that a sinusoidal solution with wavenumber k is possible when $\alpha h / \mu \geq 6.22$. Note that f is a positive valued function of hk .

2.2.1.2 Linear viscoelastic material

For a linear viscoelastic interlayer we assume the following constitutive relation.

$$\sigma_{ij}(x, z, t) = -p(x, z, t)\delta_{ij} + \int_0^t 2\mu_R \left(\frac{t-s}{a_T} \right) \frac{\partial \varepsilon_{ij}(x, z, s)}{\partial s} ds \quad (2-12)$$

Here $\varepsilon_{ij}(x, z, t) = 0$ for $t \leq 0$, t is the present value of time and μ_R is the relaxation function expressed as Prony series [33], $\mu_R(t) = \mu_\infty + \sum_{i=1}^n \mu_i e^{-\frac{t}{\tau_i}}$. Here μ_i and τ_i denote, respectively, the shear modulus and the relaxation time. For discussion later, the dependence of τ_i upon the temperature² \tilde{T} is included; i.e., $\tau_i(\tilde{T}) = \tau_i(\tilde{T}_{REF})a_T$, where the thermal shift

² We introduce the tilde (\sim) notation to distinguish temperature from traction but use the conventional notation a_T for the thermal shift factor.

factor a_T is given by the Williams-Landel-Ferry (WLF) equation:

$$\log_{10}(a_T) = \frac{-C_1(\tilde{T} - \tilde{T}_{REF})}{C_2 + \tilde{T} - \tilde{T}_{REF}},$$

C_1 and C_2 are constants, and \tilde{T}_{REF} is the reference temperature

[33]. The temperature is assumed to be uniform in the interlayer and stay constant during its deformations. Furthermore, for simplicity, we assume that the TS parameters are independent of the temperature and the loading rate.

2.2.1.2.1 Homogeneous solution:

We note that the trivial solution $u = 0, w = 0, p = \text{constant}$ satisfies governing equations for a viscoelastic layer provided that values of the TS parameters are independent of the rate of increase of $\Delta, \dot{\Delta}$.

2.2.1.2.2 Non-homogeneous solution

We add to homogeneous fields the perturbation $p^{nh}(x, z, t) = e^{ikx} \tilde{p}(z) e^{\omega t}$ and $\psi^{nh}(x, z, t) = e^{ikx} \tilde{\psi}(z) e^{\omega t}$. The real part of ω gives the growth rate of perturbations. The perturbation will grow (decay) if the real part of ω is positive (negative). Although perturbations are time-dependent, we ignore inertia forces in equations of motion because the time of interest is much larger than that taken by an elastic wave to travel through the interlayer thickness (see Appendix A). Substitution of the perturbed field into Eq. (2-12) gives

$$\sigma_{ij} = -p\delta_{ij} + 2\bar{\mu}\varepsilon_{ij} \quad (2-13)$$

where $\bar{\mu} = \mu_\infty + \sum_{i=1}^N \frac{\mu_i \omega \bar{\tau}_i a_T}{1 + \omega \bar{\tau}_i a_T}$. Eq. (2-13) is the constitutive equation of the linear elastic material with shear modulus $\bar{\mu}$. For one-term Prony series (i.e., Zener's model), $i=1$, and we set $\bar{\tau}_i = \bar{\tau}$, $\bar{\mu} = \mu_\infty + \frac{\mu_1 \tilde{\omega}}{1 + \tilde{\omega}}$ where $\tilde{\omega} = \omega \bar{\tau} a_T$. Replacing μ by $\bar{\mu}$ in Eq. (2-11) and solving the resulting equation for $\tilde{\omega}$, we get

$$\tilde{\omega} = \frac{\phi - f}{mf + f - \phi} \quad (2-14)$$

where we have set $\phi = \frac{\alpha h}{\mu_\infty}$ and $m = \frac{\mu_1}{\mu_\infty}$. We call ϕ the CZM control parameter; it equals the ratio of the interfacial softening stiffness relative to the effective long-term stiffness (modulus to thickness ratio) of the interlayer and signifies the potential importance of the former relative to the latter. Eq. (2-10) implies that α equals the magnitude of the slope of line AB (softening stiffness) in [Figure 2-2](#).

2.2.2 Results and discussion

We recall that the function f given after Eq. (2-11) is positive-valued (see [Figure 2-3](#)), $m > 0$ for a viscoelastic elastomer, and $\phi > 0$ since α , h and μ_∞ are positive. Then for the growth rate $\tilde{\omega}$ to be real and positive, the following inequalities must hold since the numerator and the denominator of the expression on the right hand side of Eq. (2-14) cannot be simultaneously negative.

$$f < \phi < (m+1)f \quad (2-15)$$

Eq. (2-14) and inequalities (2-15) suggest that the fastest growing wavelength corresponds to the minimum value of $f(hk)$ which is independent of values assigned to the CZM parameters and the interlayer material. Either by setting $\frac{df}{d(hk)} = 0$ or from [Figure 2-3](#), we get $hk = 2.12$, $f(hk) = 6.22$. We call values of variables for $k = 2.12/h$ critical and denote them by a subscript c . Thus $\lambda_c = (2\pi/k) = 2.96h$, and for this value of hk , $\frac{d^2 f}{d(hk)^2} > 0$. Between two critical values, $\phi_{c1} \approx 6.22$ and $\phi_{c2} \approx 6.22(1+m)$, the growth rate $\tilde{\omega}$ of perturbations is positive for all wavenumbers lying between roots of $f(hk) = \phi$, as shown in [Figure 2-4a](#) in which we have plotted the growth rate as a function of the wavenumber for values of ϕ in the range $[\phi_{c1}, \phi_{c2})$. Thus the interaction parameter ϕ must

exceed the threshold ϕ_{c1} for a spatial sinusoidal perturbation to grow. Beyond the upper critical value, ϕ_{c2} , of ϕ the growth rate becomes negative for wavenumbers lying between the two roots of $f(hk) = \frac{\phi}{m+1}$, as illustrated in Figure 2-4b in which we have plotted the growth rate as a function of wavenumber for a $\phi > \phi_{c2}$. Contours in the wave number- ϕ plane of the normalized growth rate $\tilde{\omega}$ of perturbations for $m=3$ and $a_T=1$ are shown in Figure 2-5. For values of ϕ in region I ($\phi < \phi_{c1}$), perturbations will not grow and the adherend will snap off the interlayer when the debonding criterion is satisfied. In region II ($\phi_{c1} < \phi < \phi_{c2}$), perturbations will grow with growth rate depending upon the wavenumber k . For a given value of ϕ the undulation will consist of infinitely many wavenumbers with positive growth rates, and the resulting displacement will not be a pure sine curve. In order to delineate this, we need to find amplitudes of perturbations which is beyond the scope of the linear analysis. The numerical solution of the problem by the FEM reported in Section 2.3 provides details of the debond nucleation and evolution. It is possible that the wavelength with the maximum growth rate will determine the minimum spacing between adjacent undulations as stipulated by Wright and Ockendon [34] in their study of adiabatic shear bands.

It can be noted from Figure 2-4a that the range of wavenumbers with positive growth rate increases as a function of ϕ , with the wavenumber $2.12/h$ having the fastest growth rate that is independent of ϕ . The growth rate as a function of the wavenumber plotted in Figure 2-4b illustrates an example of the behavior when $\phi > \phi_{c2}$, i.e., region labeled III in Figure 2-5. While the wavelength $\lambda_c = 2.96h$ is no longer expected in this region, two wavelengths with infinite growth rate will be close to $\lambda_c = \frac{2\pi}{\eta_1}h$, and $\frac{2\pi}{\eta_2}h$ where η_1 and η_2 are roots of

$$f(\eta) = \frac{\phi}{m+1}.$$

For an elastic interlayer, $\mu_1 \rightarrow 0$ or $m \rightarrow 0$, we get $\bar{\mu} \rightarrow \mu_\infty$ which implies that $\phi \rightarrow f$. Thus the right hand side of Eq. (14) approaches 0/0. Using L'Hôpital's rule, we obtain $\tilde{\omega} \rightarrow 0$. As depicted in Figure 2-6, the region (II) with positive growth rates collapses

gradually with decreasing m to that for a linear elastic interlayer. In region *III*, it is possible that the resulting debond nucleation wavelength will depend on ϕ .

The growth term $e^{\omega t}$ at the onset of softening in the CZM TS relation (i.e., point A in Figure 2-2) can be written as $e^{\tilde{\omega} \frac{T_c}{K\Delta\tau_T}}$. At a given value of ϕ , a higher value of the pulling rate $\dot{\Delta}$ implies a smaller amplitude of the sinusoidal oscillation that follows the onset of softening. Thus wavy debonding may not be experimentally discernible for very high pulling speeds. Since lowering the temperature implies increasing the effective relaxation time ($\bar{\tau}a_T$), lowering temperature for fixed $\dot{\Delta}$ will have similar effect as increasing $\dot{\Delta}$. This suggests the time-temperature equivalence of wavy debonding behavior and agrees with the experimental findings of Lakrout et al. [35]. Since the normalized growth rate $\tilde{\omega}$ increases from zero to infinity as ϕ is varied from f to $(m+1)f$ for fixed hk , therefore, at a given $\dot{\Delta}$ and operating temperature, ϕ can be increased to achieve physically discernible wavy debonding.

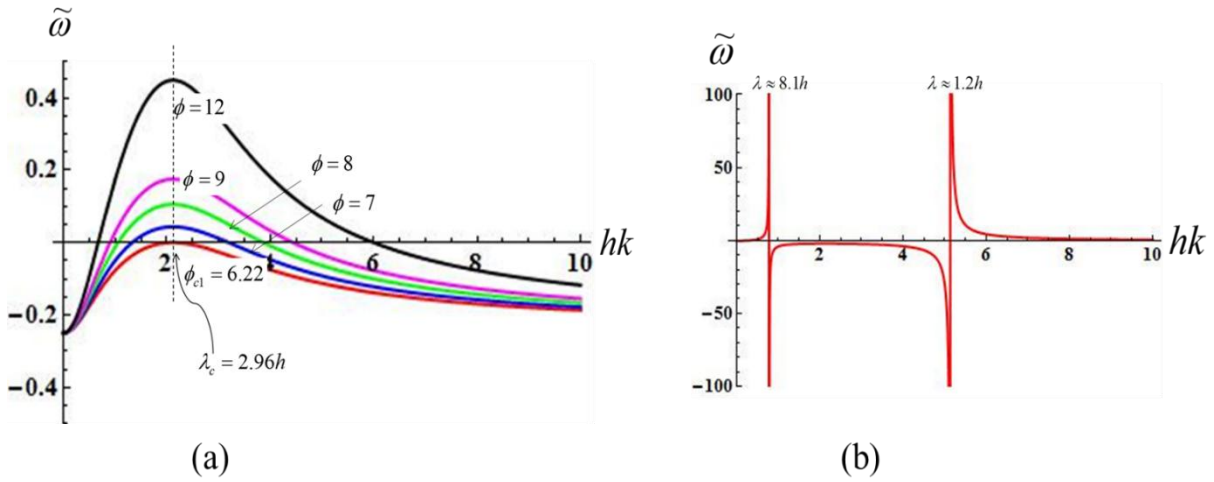


Figure 2-4: For $m = 3$, the dimensionless growth rate versus the dimensionless wave number (a) for different values, labelled in the figure, of ϕ in $[\phi_{c1}, \phi_{c2})$ and (b) for $\phi(=41.25) > \phi_{c2}$. Results in Fig. (a) imply that larger the value of ϕ , faster is the growth rate and wider is the range of the growing wavenumbers. However, the fastest growth rate always corresponds to the wavenumber of wavelength $2.96h$. Results in Fig. (b) show that for two indicated wavenumbers perturbations grow infinitely fast while for wavenumbers lying between them they decay due to their negative growth rates.

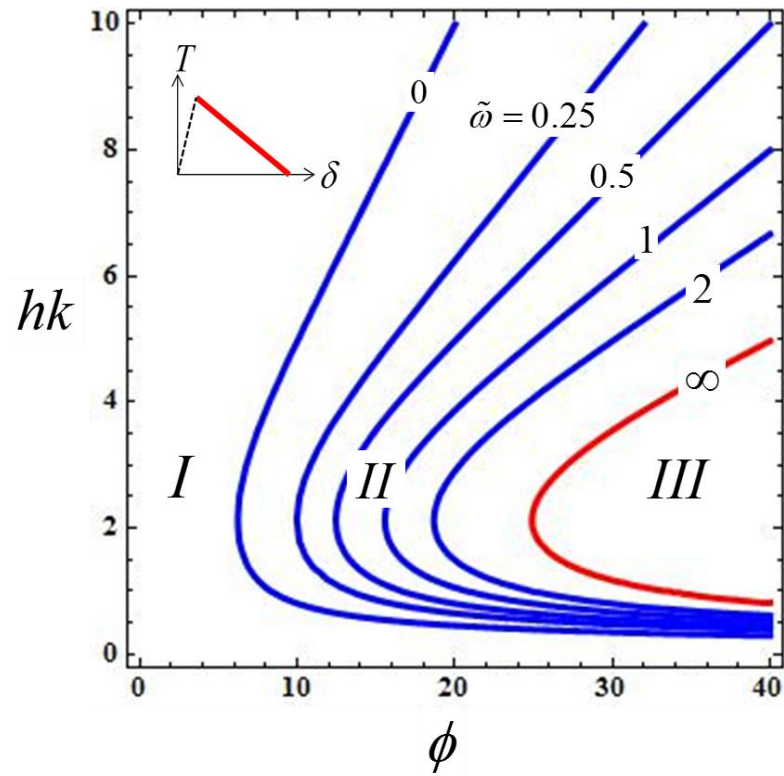


Figure 2-5: Contours in the wavenumber- ϕ plane of the normalized growth rate $\tilde{\omega}$ of perturbations for $m=3$. Values of $\tilde{\omega}$ are indicated on the contours. These plots imply that a sinusoidal perturbation of wavenumber hk will decay in regions *I* and *III* and grow in region *II*.

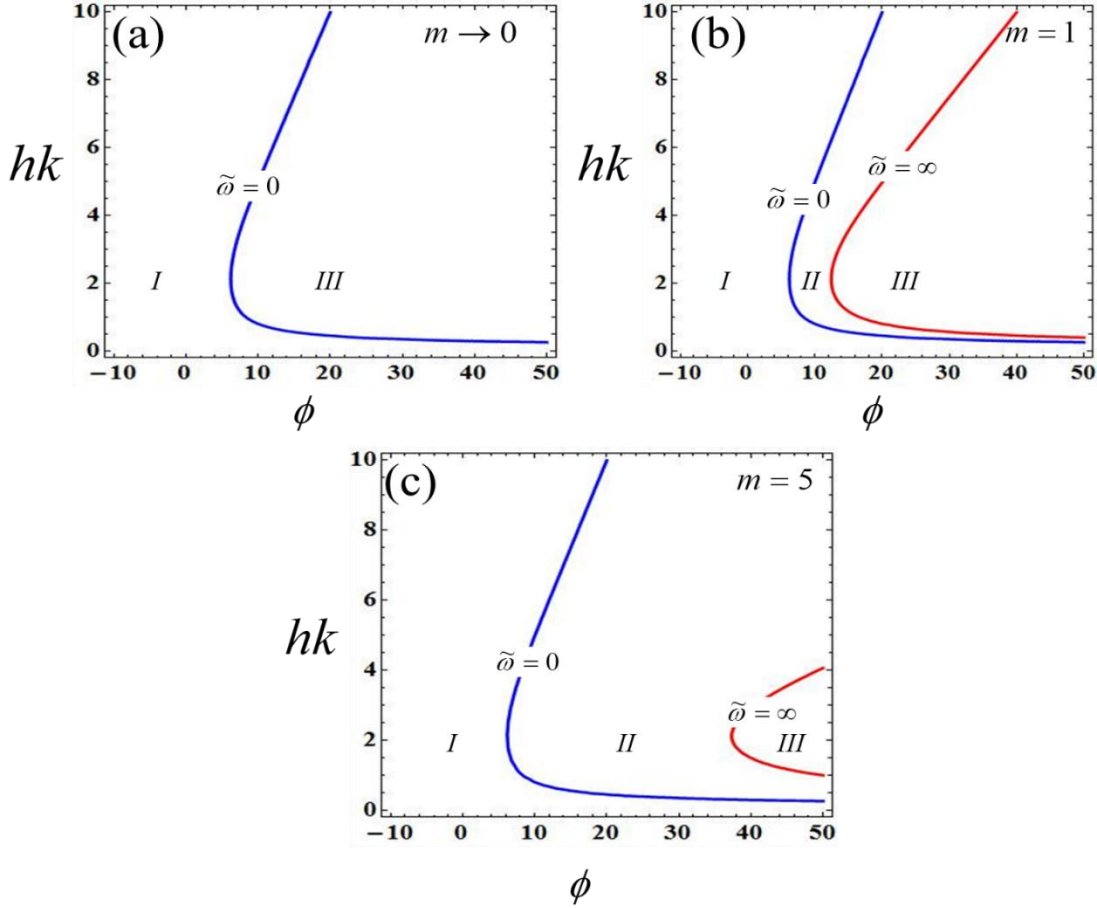


Figure 2-6: Effect of m : (a) elastic limit with two possible wavenumbers, (b) three regions for $m=1$, and (c) three regions with a wider region II for $m=5$.

Recalling that $\phi = \frac{\alpha h}{\mu_\infty}$, $\alpha = \frac{T_c}{\delta_f - \delta_c}$ (when $\delta_c \leq \delta \leq \delta_f$) and $K \gg 1$, the condition

$\phi > \phi_{cl} = 6.22$ gives the following requirement for the wavy debonding to ensue.

$$K_{softening} > 4.15K_{elastic} \quad (2-16)$$

Here $K_{softening} = \frac{T_c^2}{G_c}$ is a measure of the slope of the softening portion of the bilinear TS

relation and $K_{elastic} = \frac{E_\infty}{h}$, where $E_\infty = 3\mu_\infty$ is the long-term Young's modulus of the interlayer

material. The quantity $K_{elastic}$ can be thought of as the long-term stiffness of the interlayer.

On the other hand, $\phi > \phi_{c2}$ leads to $K_{softening} > 4.15K_{elastic}^{ins}$, where $K_{elastic}^{ins} = \frac{E_0}{h}$ and $E_0 = 3(\mu_\infty + \mu_1)$ is the instantaneous Young's modulus of the interlayer material. Eq. (2-16) suggests that for a wavy debonding to ensue, the stiffness (units: N/mm^3) of the interface during the softening regime must exceed the effective long-term stiffness of the interlayer by at least a factor of 4.15. Thus the TS parameters must satisfy this constraint for a wavy debonding. If the softening stiffness (divided by 4.15) lies between the long-term and the instantaneous stiffness of the elastomeric layer, the dominant wavelength is expected to be independent of the CZM parameters.

Equation (2-16) provides an interpretation of the debonding instability in terms of the CZM parameters. It stems from the interfacial traction decreasing with an increase in the interfacial separation, similar to what previous researchers [10, 14] stated in terms of the distance-dependent van der Waals forces acting at the interface that trigger instability when a rigid adherend approaches an elastic film. Our results imply that the elastomeric layer thickness and the interfacial adhesion can be selected to either avoid or produce wavy debonding. Similarly, given the TS relation and values of parameters of the interlayer material, one can discern if the necessary condition for undulations to occur is satisfied.

One needs to analyze the nonlinear problem to study the evolution of debonding. In the following section, we use the FEM to analyze plane strain deformations of the interlayer material with the bilinear TS relation and furthermore ascertain (i) the validity of Eq. (2-16), and (ii) the effect of ϕ on the spacing between the adjacent debonding undulations. Advantages of the FE work over the analytical work include no specific form of perturbations, using the finite size specimen, considering boundary conditions at specimen edges, not assuming a-priori the deformation field, and the capability to simulate material and geometric nonlinearities.

2.3 Debonding of elastomeric layer from a rigid adherend by the FEM

2.3.1 Approach

The problem studied in Section 2 is now analyzed by the FEM using the commercial software ABAQUS/Standard. To be consistent with the assumption made in Section 2 that

the system is infinitely wide in the x direction, we use a large L/h ratio³. The FE mesh and the prescribed boundary conditions are shown in [Figure 2-7](#). Five 4-node plane strain elements with hybrid formulation (CPE4H) are placed through the thickness of the interlayer. In order to characterize well the spacing between adjacent undulations, 20 elements are placed over the expected characteristic length of the undulation spacing, i.e., $3h$. Results for three different FE meshes are included in Appendix C. A uniform vertical displacement, $w = \Delta$, is applied at the rate of 1 mm/s on the top surface of the rigid adherend while its lower smooth (frictionless) surface is bonded to the top surface of the interlayer via the CZM interaction and the bilinear TS relation [36] with mode-independent values of TS parameters⁴. The bottom surface of the interlayer is held stationary. The remaining bounding surfaces of the interlayer are assumed to be traction free. To alleviate numerical instabilities, the “Damage Stabilization” option in ABAQUS is used. The value of the stabilization parameter was gradually reduced to 10^{-8} and further decrease in this value was found not to affect the computed results. The interlayer material is modeled either as linear elastic or linear viscoelastic with one term in the Prony series. For the linear viscoelastic material, unless otherwise mentioned, values assigned to the material parameters are: $\tau a_T = 10^{-5}$ s and $m = 3$. Numerical experiments are conducted by varying the parameter $\frac{K_{softening}}{K_{elastic}}$ using several combinations of values of the interlayer modulus, μ_∞ or μ , thickness, h , and cohesive zone parameters, K , T_c and G_c ⁵.

³ Dimensions of the elastomeric layer used in most of our FE simulations are $L = 23\text{ mm}$, $h = 0.25\text{ mm}$. The size of the rigid adherend is taken to be $25\text{ mm} \times 10\text{ mm}$.

⁴ We assume that $K_I = K_{II} = K$, $T_{cl} = T_{cII} = T_c$, and $G_{cl} = G_{cII} = G_c$, where subscripts signify modes of separation; see [36] for details on a mixed mode bilinear TS relation.

⁵ As an example, values of the parameters for the simulation with $K_{softening} / K_{elastic} = 4.15$ are: $h = 0.25\text{ mm}$, $\mu_\infty = 0.2\text{ MPa}$, $m = 3$, $\tau a_T = 10\text{ }\mu\text{s}$, $K = 10^6\text{ N/mm}^3$, $T_c = 0.04\text{ MPa}$, and $G_c = 0.1606\text{ N/m}$.

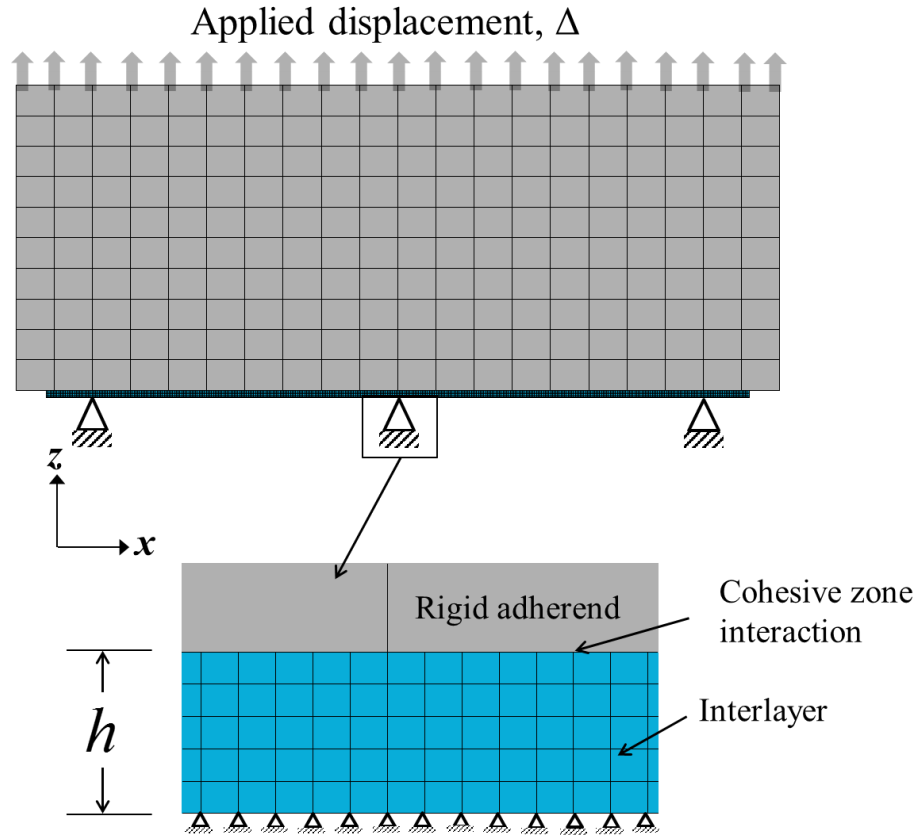


Figure 2-7: Details of the FE mesh and boundary conditions. Applied zero tractions in directions of the unconstrained displacement components are not shown.

2.3.2 Results and discussion

Wavy debonding is predicted, as shown in Figure 2-8, at sufficiently large values of $K_{softening}$. The critical $K_{softening}$ values plotted in Figure 2-9 versus the elastic stiffness of the interlayer agree with those given by Eq. (2-16). The predicted debonding nucleates periodically⁶ along the x -direction implying long debonding channels along the y -direction because of the plane strain assumption. However, in probe tack tests [7] and contact experiments [2], debond is found to nucleate periodically along both the x - and the y -directions. Motivated by the work of Huang et al. [14] we speculate that the condition for the onset of wavy debonding remains unchanged for 3D deformations of the interlayer. The simulated debonding evolution, in general, consists of the nucleation of interfacial cavities at a characteristic spacing, expansion of cavities and lateral propagation of each cavity until the

⁶ The inhomogeneity in the distribution of interfacial tractions, singular at the corners [37-40] triggered by the free-edges of the elastomer layer and the adjoining traction-free portion of the adherend likely acts as the perturbation to the homogeneous solution over the central region. If horizontal displacements at the free edges of the interlayer are constrained, then the undulatory debonding is not predicted. We have not attempted to capture the correct order of singularity at the corners. However, our key results are insensitive to further refinement of the FE mesh.

adherend separates from the elastomeric layer as cavities coalesce. Such debonding behavior in probe tack tests has been reported by Lakrouf et al. [7]. Two examples of the evolution of wavy contact opening are shown in Figure 2-10 for $\phi = 8.25$ and $\phi = 41.25$. The discrete Fourier transform method (available in the software MATHEMATICA [41]) is used to extract the dominant wavelength of the debond nucleation. Results are plotted in Figure 2-11 for a range of ϕ values for an elastic interlayer ($m \rightarrow 0$), and two viscoelastic interlayers with $m = 3$ and 25 . The dominant wavelength is close to $3h$ and independent of ϕ when ϕ lies in region II. This agrees with the value derived from the above analytical work and experimental findings of Mönch and Herminghaus [2]. For both the elastic and the viscoelastic layers, the wavelength to thickness ratio for ϕ near region III is found to be larger and dependent on ϕ than that when ϕ is near region II. It is noteworthy that at the larger ϕ value, shapes of the nucleated cavities change before they coalesce as was computed by Sarkar et al. [24]. Our numerical experiments suggest that the response becomes more mesh-dependent as ϕ is increased (see Appendix C).

Previous studies [2, 9] suggesting that the characteristic wavelength is independent of the adhesion seem to contradict at first sight our results for large values of ϕ . For typical experimental [5, 29] values of $m = 10^3$, $G_c = 0.04 - 0.2 J/m^2$, $\mu_\infty = 0.2 - 2 MPa$, and $h = 40 - 400 \mu m$, we get $T_c > 2.5\mu_\infty$ in the proximity of $\phi = \phi_{c2}$. Such large values of the critical traction imply probable onset of cohesive debonding mechanisms such as bulk cavitation [42] that occurs when $(-p) \geq 2.5\mu_\infty$. This suggests that the ϕ values for test conditions [2, 9] that exhibited pure interfacial separation were well below ϕ_{c2} and, therefore, the dominant wavelength was indeed independent of the adhesion.

Results depicted in Figure 2-9 for the interlayer material modeled as neo-Hookean do not exhibit any significant difference in the threshold softening stiffness because strains induced in the elastomer layer when softening ensues are negligible for the large value of K used.

Results summarized in Table 2-1 indicate that wavy debonding was not predicted when either $\dot{\Delta} = 100$ mm/s or a higher value of the relaxation time τa_T was used for a given value of ϕ . However, a lower value of τa_T or a higher value of ϕ at $\dot{\Delta} = 100$ mm/s resulted

in wavy debonding. These results qualitatively confirm the time-temperature equivalence discussed at the end of Section 2.2.

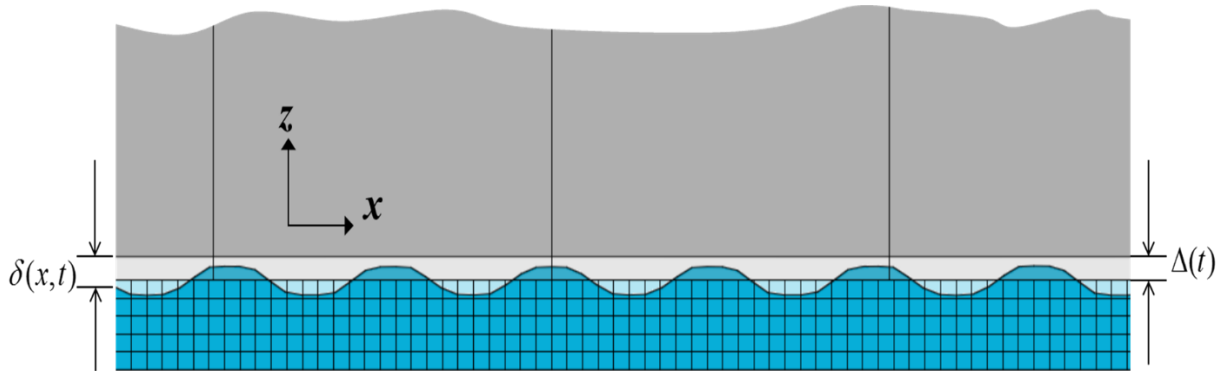


Figure 2-8: Deformed and undeformed configurations when a wavy debonding is predicted by the model. The FE mesh is shown only on the undeformed configuration. The gap between the adherend and the interlayer is due to the displacement jump at the interface. Debond occurs only when this jump exceeds its prescribed limiting value.

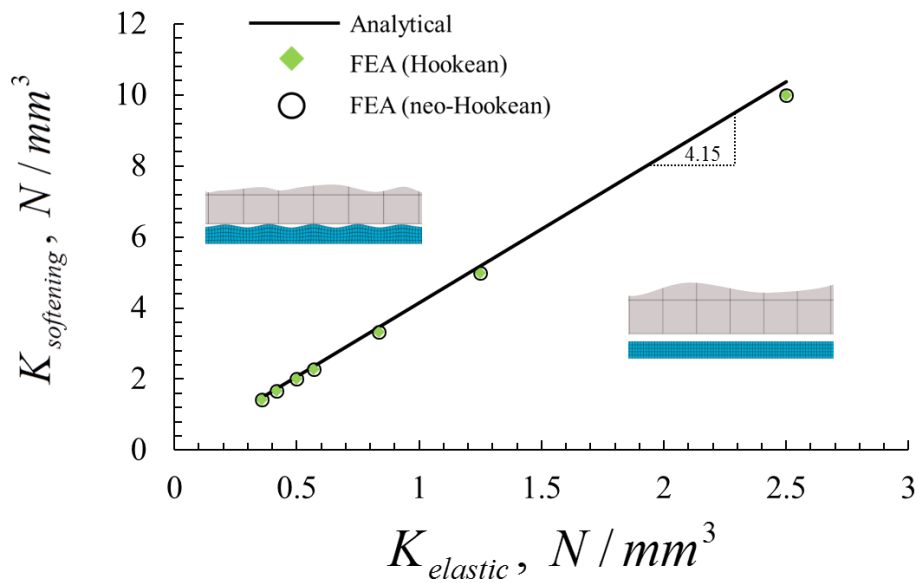


Figure 2-9: The map illustrating that the quantity T_c^2 / G_c must exceed approximately $4.15E_\infty / h$ for a wavy debond to ensue. This plot was generated for $m = 3$, $\tau = 10^{-5} s$, and $\dot{\Delta} = 1 mm/s$.

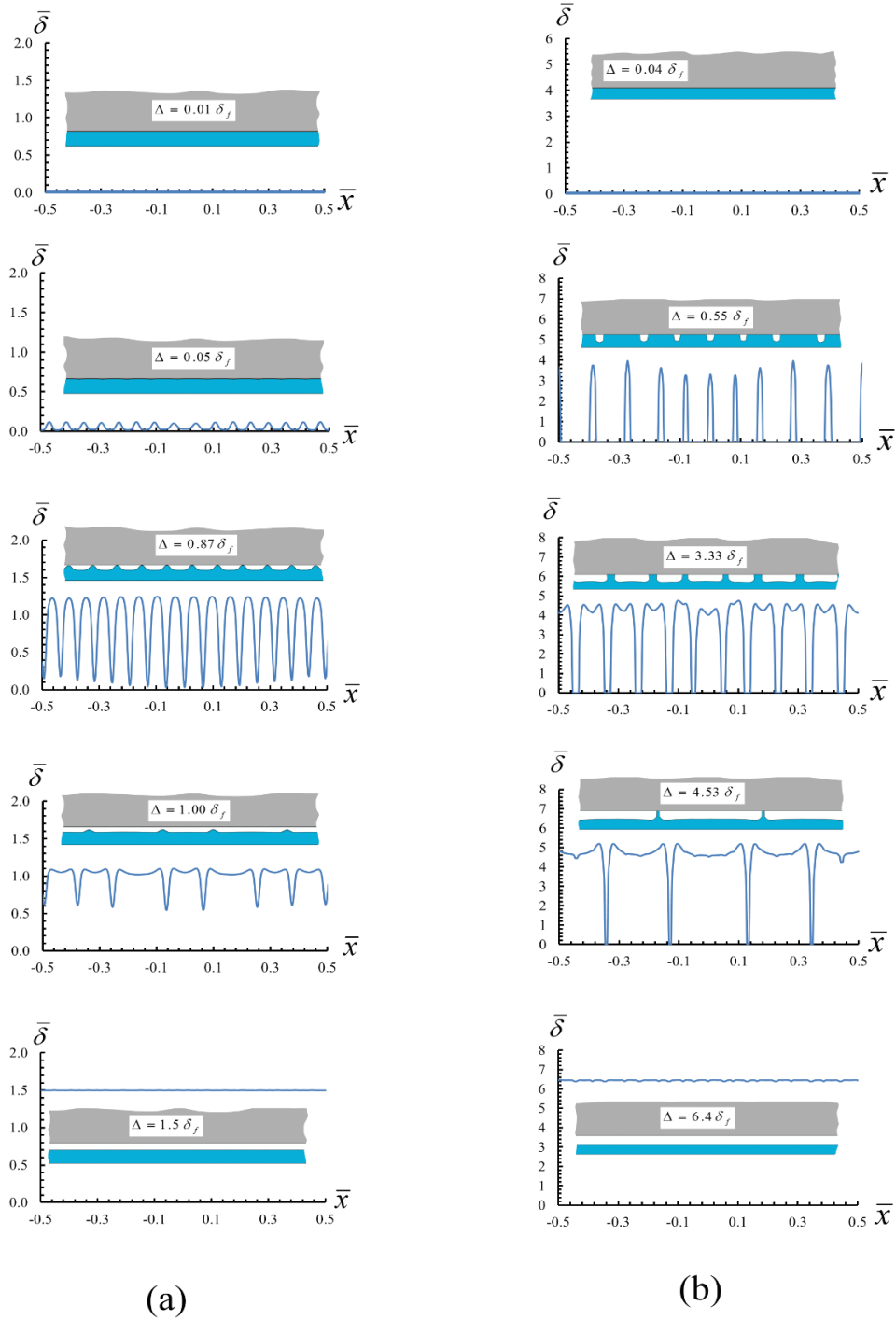


Figure 2-10: Evolution of the contact opening for $m=3$ and (a) $\phi = 8.25 (\phi_{c1} < \phi < \phi_{c2})$ and (b) $\phi = 41.25 (\phi > \phi_{c2})$. Variables in the plot are: $\bar{\delta} = \delta / \delta_f$ and $\bar{x} = 2x / L$. The deformation shown is multiplied by 5 for ease in visualization. Plots correspond to the central portion of the interface of non-dimensional length 1. Deformed configurations are for the interface portion of non-dimensional length 0.66.

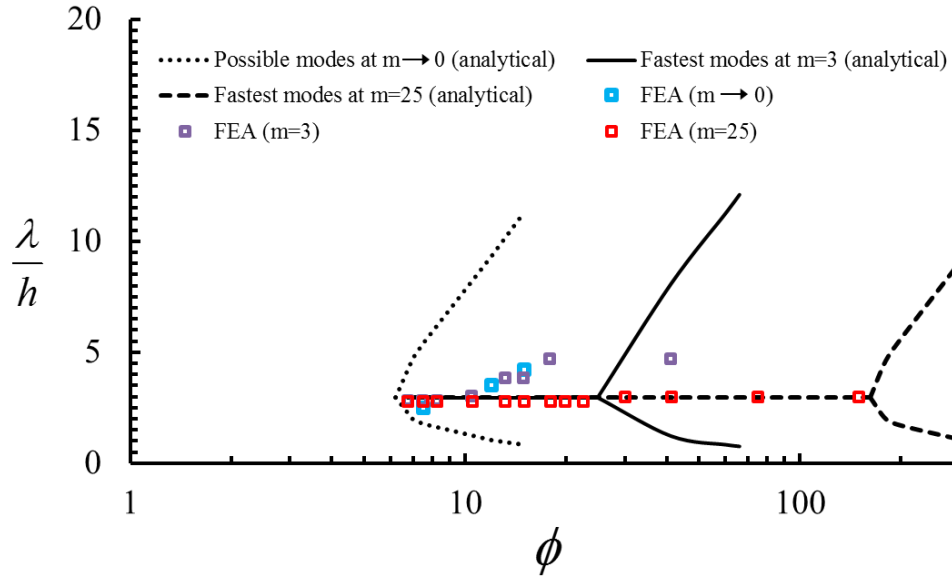


Figure 2-11: Effect of ϕ on the dominant wavelength (normalized by thickness) of the debonding undulation

Table 2-1: Qualitative evidence of the time-temperature equivalence in predictions from the model
 $\Delta = 14 \mu m$

ϕ	$\dot{\Delta}$ (mm/s)	τa_T (μs)	Debonding
7	1	10	
7	100	10	
7	1	1000	
7	100	0.1	
28	100	10	

2.4 Analysis of 3D deformations for peeling of a flexible plate off a soft elastomeric layer by the FEM

2.4.1 Approach

Results presented in the preceding two sections imply that values of parameters in the TS relation for the interface between an elastomeric layer and the rigid substrate, the applied pulling rate and the characteristic relaxation time determine whether or not a wavy debond will occur. In order to delineate fingering instability [4, 5, 9] for a deformable upper adherend, we study progressive crack propagation in the configuration of

Figure 2-12 that resembles the test set up often used to characterize interfacial adhesion and/or study mechanics of interfacial separation [5, 29, 43]. Major differences between this problem and those studied above include bending and stretching deformations of the upper adherend that may induce interfacial failure in all three modes whereas only mode I failure was dominant in the problems analyzed in Sections 2 and 3.

We model the plate/adherend and the interlayer of dimensions, respectively, $20\text{ mm} \times 30\text{ mm} \times 1\text{ mm}$ and $20\text{ mm} \times 25\text{ mm} \times h\text{ mm}$. Deformations of the interlayer may be large but those of the adherend plate are assumed to be infinitesimal. Furthermore, inertial effects are neglected. We use values of the material parameters given by Murray [43] who experimentally observed fingerlike debonding during the peeling of a glassy polymer plate from a hydrogel interlayer in a wedge test. The plate material is modeled as homogeneous and isotropic Hookean with Young's modulus, $E_{plate} = 2.1\text{ GPa}$ and Poisson's ratio = 0.4. However, we also compute results for different values of E_{plate} . The material for hydrogel interlayer is modeled as isotropic, homogeneous and incompressible with the constitutive relation (2-17) (e.g., see Simo [44]) implemented in ABAQUS [36].

$$\boldsymbol{\sigma}(t) = -p\mathbf{I} + a_1\mathbf{B} + a_2\mathbf{B}^2 + dev \left[\int_0^t \dot{g}_R \left(\frac{s}{a_T} \right) \mathbf{F}_t^{-1}(t-s) \boldsymbol{\sigma}_0^D(t-s) \mathbf{F}_t^{-T}(t-s) ds \right] \quad (2-17)$$

Here a_1 and a_2 are material constants, \mathbf{B} the left Cauchy-Green tensor, g_R the normalized relaxation modulus expressed as Prony series $\left(g_R(t) = \frac{\mu_R(t)}{\mu_R(0)} \right)$, $dev(A) = A - \frac{1}{3}tr(A)\mathbf{I}$, $tr(A)$ = sum of the diagonal elements of the matrix A when its components are written with respect

to an orthonormal basis, I = the identity matrix, σ_0^D the instantaneous deviatoric Cauchy stress, and $F_t(t-s)$ the deformation gradient at time $(t-s)$ with respect to the configuration at time (t) , defined as $F_t(t-s) = \frac{\partial x(t-s)}{\partial x(t)}$ with x giving the current position of a material point. Based on experimental results [45], the instantaneous elastic response is assumed to be neo-Hookean, i.e., $a_2 = 0$, and $a_1 =$ twice the constant shear modulus of the interlayer material. The Prony series parameters determined experimentally [45] at the reference temperature of 45°C are listed in Table B 1. The WLF constants at the reference temperature $\tilde{T}_{REF} = 45^\circ\text{C}$ are $C_1=4.57^\circ\text{C}$ and $C_2=142.2^\circ\text{C}$.

We assume a mixed-mode bilinear TS relation [36] with mode-independent values of the initial slope ($K = 10^6 \text{ MPa/mm}$), the peak traction ($T_c = 0.04 \text{ MPa}$), and the fracture energy ($G_c = 0.2 \text{ J/m}^2$). The value of the damage stabilization parameter for alleviating numerical instabilities was gradually reduced to 10^{-10} until a further decrease in this value did not affect computed results.

The boundary conditions and the FE mesh are shown in

Figure 2-12. The three displacement components of points on the lower face of the interlayer are set equal to zero to simulate its perfect bonding to the stationary rigid adherend. The same vertical displacement Δ is applied at 1 mm/s to all nodes on the plate right edge. Traction on the other bounding surfaces and tangential tractions on the right edge are null.

The eight-node brick elements (C3D8R) with reduced integration and the default hourglass control option have been used for the cover plate. Hybrid elements (C3D8RH)⁷ have been employed for the incompressible interlayer. The interlayer region is discretized into 5 (thickness) x 150 (width) x 100 (length) uniform FE mesh. This FE mesh is reasonably fine as the characteristic spacing between adjacent undulations is expected [5] to be $\lambda \approx 3h - 4h \approx 1 \text{ mm}$ for the smallest interlayer thickness used in the study. In order to

⁷For the 3D simulations, the overall energy balance applied to the ABAQUS output gave a discrepancy of about 20%. Additional numerical experiments revealed that this was due to our using the default value of the hourglass control. The use of selective reduced integration or other hourglass control options satisfied the energy balance within 1% error but triggered unphysical oscillations at the contact surface. The physically meaningful results computed with the default hour glass control and their agreement with the literature results obtained by other methods provide credence to results reported here.

demonstrate the effect of the CZM parameters on the debonding characteristics, we have not obtained a fully converged solution by successively refining the FE mesh since qualitative features of progressive debonding remained independent of the FE mesh.

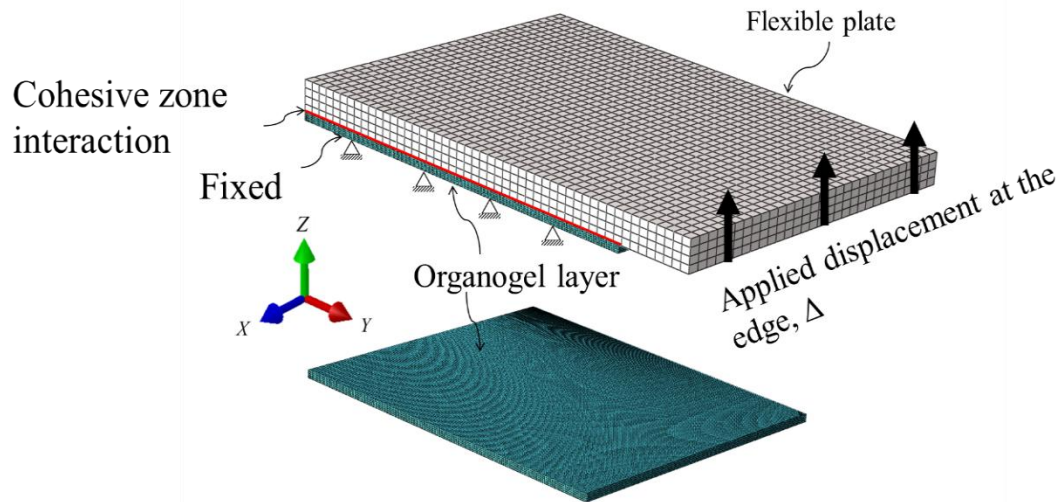


Figure 2-12: The FE mesh and boundary conditions with zero tractions along unconstrained displacement components not exhibited

2.4.2 Results and discussion

In general, the debond front is either fingerlike or straight as illustrated in Figure 2-13. An example of the evolution of the fingerlike debonding process is shown in Figure 2-14 in which we have plotted contours of the contact opening δ at three different times for a plate

of bending rigidity, $D = \frac{E_{plate} h_{plate}^3}{12(1-\nu^2)} = 21 \text{ Nm}$ (ν = Poisson's ratio, h_{plate} = the plate

thickness) and an interlayer of thickness $250 \mu\text{m}$. Computed values of $\delta > \delta_f$ are represented in red color. As experimentally observed [5, 9], the development of fingers is preceded by the nucleation of debonds spaced at approximately the same distance as that between the fingers that will ensue. Decaying plate displacement, undulatory debonding, and lateral propagation of debonds give rise to what resembles fingers at the debond front.

Progressive debonding was also simulated for a plate with $D = 2.1 \text{ Nm}$ and interlayers thicknesses $250 \mu\text{m}$, $500 \mu\text{m}$, $600 \mu\text{m}$ and $750 \mu\text{m}$. The spacing between the adjacent fingers, computed using the discrete Fourier transform method (using MATHEMATICA

[41]), versus the interlayer thickness is plotted in Figure 2-15a. We note that the computed spacing increases with an increase in the interlayer thickness and reasonably agrees with experimental findings of Ghatak and Chaudhury [9] who reported the approximate relation: $\lambda \approx 4h$. We note that for the highest thickness (750 μm) simulated, fingerlike debonding was not predicted. However, debonding exhibited a fingerlike front when a plate of higher flexural rigidity (7.5 Nm), consistent with the requirement of a threshold lateral confinement $(D/\mu h^3)^{1/3}$, expressed as the ratio of the two length scales, $(D/\mu)^{1/3}$ and h [9, 12]. Simulations conducted for different values of D and a constant interlayer thickness (250 μm) revealed that the length of the fingers increased monotonically with the quantity $(D/\mu)^{1/3}$ ⁸ which represents the characteristic stress decay distance for a flexible plate bonded to an elastomeric foundation [46]. The linear fit to the computed values depicted in Figure 2-15b is close to that obtained by Ghatak and Chaudhury [9] for a different materials system. We believe that this quantitative agreement in the finger amplitudes is coincidental because the softening zone length (in the y-direction) should also depend on the interfacial adhesion as discussed later. We found that the dominant frequency of undulation is relatively insensitive to the plate rigidity, consistent with findings of [9].

In order to demonstrate qualitatively the concept that the CZM parameters for confined interlayers determine whether or not contact separation resulting from tension is wavy, additional simulations were conducted by varying the TS parameters and the operating temperature by keeping the thickness of the interlayer, the plate rigidity and the pulling rate constant. The key parameters used in these simulations and the results are summarized in Table 2-2. For $T_c = 0.04$ MPa, setting the temperature equal to -30°C results in larger relaxation times following the WLF equation, and a fingerlike debond front was not predicted. Similarly, a fingerlike front was not predicted when $T_c = 0.004$ MPa was used for the operating temperature of 55°C .

Our computed results suggest that the debonding behavior during peeling a flexible plate off an elastomeric layer constrained to a rigid base is dictated by both the lateral

⁸ The shear modulus of the interlayer at time t and temperature \tilde{T} was estimated as

$$\mu(t, \tilde{T}) \approx \mu_R \left(\frac{t}{a_T} \right) = \mu_\infty + \sum_{i=1}^N \mu_i e^{-\frac{t}{a_T \tau_i}}.$$

confinement $(D/\mu h^3)^{1/3}$ and the adhesion parameter, $T_c^2 h/E_\infty G_c$. A detailed analysis probing their collective role in the debonding evolution will be undertaken in a future work.

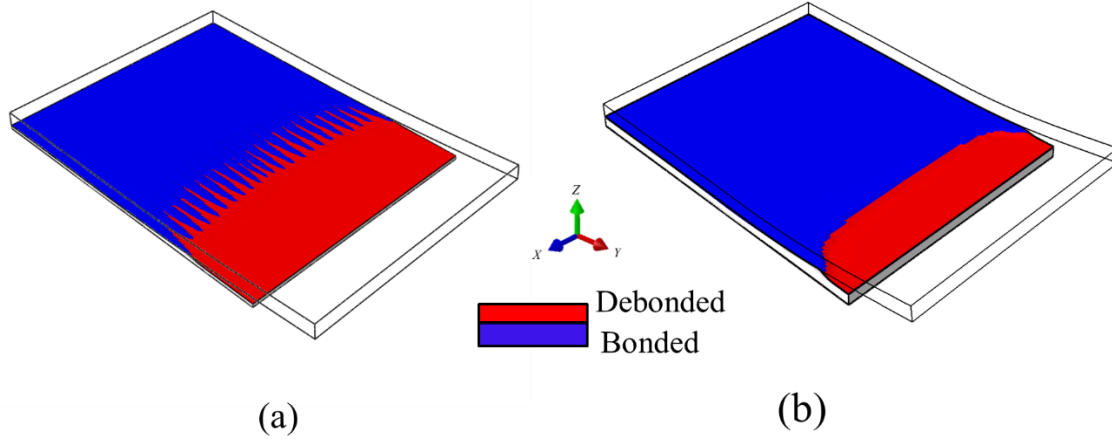


Figure 2-13: Two main types of debond front predicted by the simulations: debond front (a) with or (b) without fingerlike undulations. In these images, the bonded and the debanded regions are shown by plotting the damage variable, $\bar{d} = \frac{\delta_f (\delta - \delta_c)}{\delta (\delta_f - \delta_c)}$ defined for the region corresponding to segment

AB of the TS relation (for segment OA, $\bar{d} = 0$). The value of \bar{d} equals 1 over the debanded region (represented by red color) and varies from 0 to 1 over the region which is yet to deband (represented by blue color). Whether or not undulation is exhibited at the debond front depends on the plate bending rigidity, the viscoelastic properties and the thickness of the interlayer, temperature, pulling rate and values of the TS parameters.

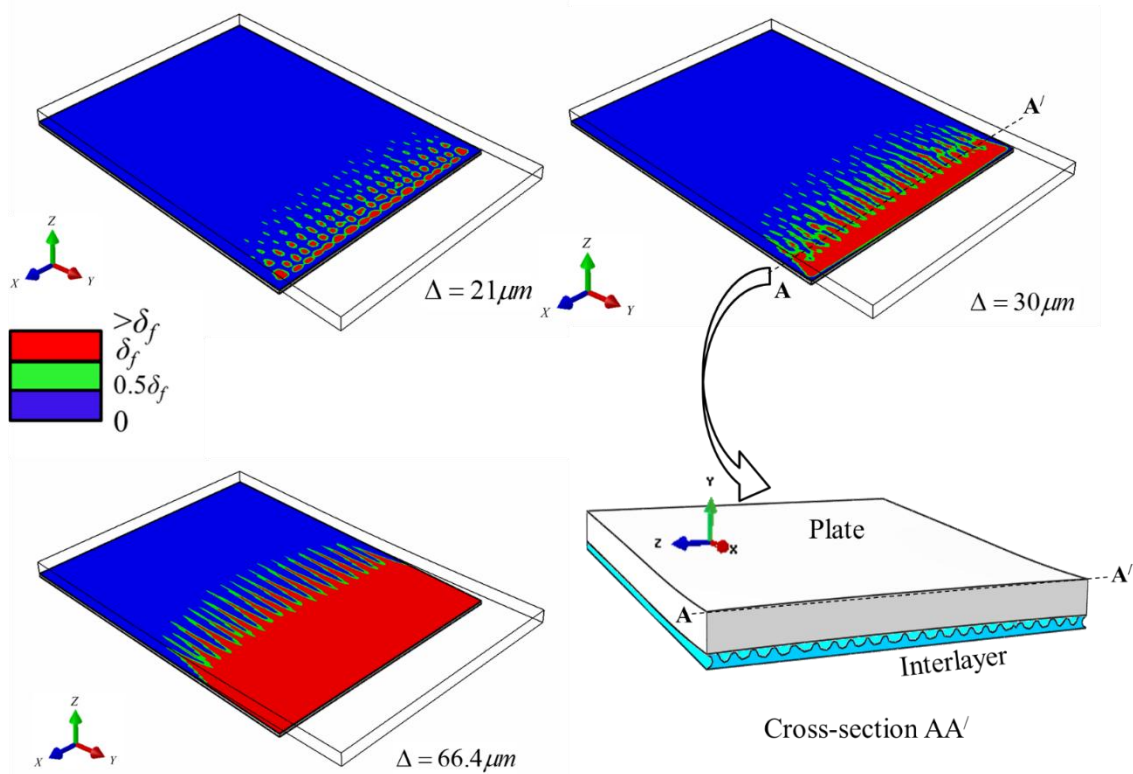


Figure 2-14: Contour plots of contact opening at three values of the applied displacement when the plate rigidity $D = 21Nm$ and the interlayer thickness $h = 250 \mu m$. For easy visualization, deformations are exaggerated by a factor of 10 and by a factor of 12 for the cross-section AA' illustrating wavy debonding.

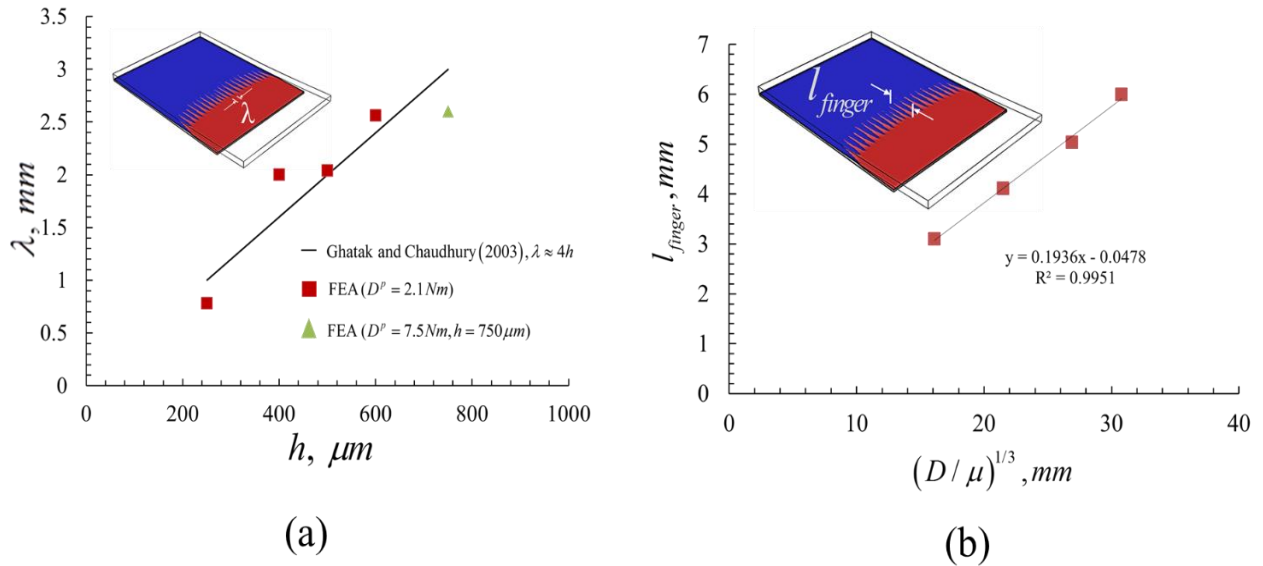


Figure 2-15: Dependence of the (a) dominant wavelength, λ , of the fingerlike pattern on the interlayer thickness, h , and (b) the fingers length, l_{finger} , on the length scale $(D/\mu)^{1/3}$ when $h = 250 \mu m$. As shown in (a) fingerlike debonding is not predicted when $D = 2.1Nm$ and $h = 750 \mu m$. However, a larger value of D causes fingerlike debonding. The linear fit of the data points shown in (b) agrees with the linear fit of experimental results of Ghatak and Chaudhury [9], $l_{finger} = 0.2(D/\mu)^{1/3} - 0.16$. The intercepts are not important since undulatory debond fronts do not occur for small values of $(D/\mu)^{1/3}$.

Table 2-2: Effect of the TS parameters (for plate rigidity = 2.1 Nm, interlayer thickness = 250 μm , and pulling rate = 1 mm/s), which evince that wavy undulations vanish when the interfacial softening is increased relative to the interlayer stiffness (lower effective stiffness at a higher temperature due to viscoelasticity).

\tilde{T} ($^{\circ}\text{C}$)	T_c (MPa)	\mathcal{G}_c (J/m^2)	Type of debonding front
55	0.04	0.2	Fingerlike undulations
55	0.004	0.2	No fingerlike undulations
-30	0.04	0.2	No fingerlike undulations

2.5 Conclusions

We have studied debonding of a confined elastomer layer from an adherend using the cohesive zone model (CZM) and the bilinear traction-separation (TS) relation for the interaction between the elastomer layer and the adjoining adherend. The stability analysis of the homogeneous solution (null displacements and constant hydrostatic pressure) of plane strain deformations of the elastomer and the analysis of deformations by the finite element method (FEM) have enabled us to conclude that a necessary condition for a wavy/undulatory debonding to ensue is $T_c^2 h / \mathcal{G}_c E_{\infty} > 4.15$, where T_c is the peak traction and \mathcal{G}_c the fracture energy in the TS relation, h the thickness and E_{∞} the long-term Young's modulus of the elastomeric layer modeled as linear viscoelastic. This result can help design a materials system for avoiding wavy debonding by choosing thickness of the soft adhesive and/or altering the interfacial softening by suitable surface treatment. It also serves to tailor the TS relation parameters for simulating spatially undulatory debonding evolution. The linear stability analysis also predicts that if undulations occur, their dominant wavelength is close to $3h$, when $T_c^2 / 4.15 \mathcal{G}_c$ lies between E_{∞} / h and E_0 / h where E_0 is the instantaneous modulus of the elastomeric layer. Analysis of the problem using the finite element method (FEM) provides details of the interfacial debonding evolution and sheds light on the effects of pulling rate and temperature.

We have also analyzed using the FEM three-dimensional deformations of a thin elastomeric interlayer (perfectly bonded to a rigid base) when a flexible plate is peeled from it by applying vertical displacements to points on one edge. This analysis predicts the progressive debonding with a fingerlike front is dictated by both the lateral confinement $(D/\mu h^3)^{1/3}$ and the adhesion parameter, ϕ where D equals the plate bending rigidity and μ the interlayer shear modulus at the operating temperature.

Acknowledgements

The authors thank the department of Biomedical Engineering and Mechanics and Institute of Critical Technology and Applied Sciences (ICTAS), Virginia Tech for the use of its facilities and Macromolecules and Interfaces Institute (MII), Virginia Tech for fostering interdisciplinary research in the adhesion area. The valuable feedback provided by the reviewers on an earlier version of the manuscript is deeply appreciated.

Appendix A

Using the non-dimensionalization $X = x/h, Z = z/h, U = u/h, W = w/h, P = p/\bar{\mu}$ and $T = t/t_{\text{int}}$ where $t_{\text{int}} = \delta_f / \dot{\Delta}$ is the time of interest, equations of motion become

$$\frac{\partial^2 U}{\partial T^2} + \left(\frac{t_{\text{int}}}{t_{\text{wave}}} \right)^2 \left(-\frac{\partial P}{\partial X} + \left(\frac{\partial^2 U}{\partial X^2} + \frac{\partial^2 U}{\partial Z^2} \right) \right) = 0,$$

$$\frac{\partial^2 W}{\partial T^2} + \left(\frac{t_{\text{int}}}{t_{\text{wave}}} \right)^2 \left(-\frac{\partial P}{\partial Z} + \left(\frac{\partial^2 W}{\partial X^2} + \frac{\partial^2 W}{\partial Z^2} \right) \right) = 0$$

where $t_{\text{wave}} = h\sqrt{\frac{\rho}{\bar{\mu}}}$ equals the time for an elastic wave to travel through the thickness, h , of the interlayer material of density ρ . For typical representative values

$$(m \approx 10^3, \tilde{\omega} \sim 0 - \infty, \phi \approx 4 - 4000, \dot{\Delta} \approx 1 \text{ mm/s}, G_c \approx 0.04 - 0.2 \text{ J/m}^2, h \approx 40 - 400 \mu\text{m} \text{ and } \rho \approx 1 \text{ kg/m}^3), \left(\frac{t_{\text{int}}}{t_{\text{wave}}} \right)^2 = \frac{4}{3\phi\dot{\Delta}^2} \frac{G_c}{\rho h} \left(1 + \frac{m}{1 + \tilde{\omega}^{-1}} \right) \gg 1. \text{ Thus inertia terms are negligible.}$$

However, the inertia term will potentially play a significant role for faster pulling speeds for

which $\left(\frac{t_{\text{int}}}{t_{\text{wave}}} \right)^2$ is not much greater than 1.

Appendix B

Table B 1: Values of material parameters in the Prony series at the reference temperature of 45°C [45]

i	1	2	3	4	5	6	7	8	9	10	11	12	13	14	15	16
μ_i (MPa)	4.11	4.11	4.11	4.082	3.194	0.420	0.186	0.052	0.016	0.003	0.001	0.001	0.017	0.014	0.017	0.009
τ_i (s)	10^{10}	10^9	10^8	10^7	10^6	10^5	10^4	10^3	10^2	10^1	1	10	10^3	10^4	10^5	∞

Appendix C

As suggested by a reviewer we include here the effect of the FE mesh on results of the plane strain problem studied in Section 2.3. Sensitivities of the load-displacement histories and the spatial variations of the contact opening for three FE mesh in the interlayer are examined. The FE meshes 1, 2, and 3 had, respectively, 5, 5, and 8 elements through the thickness with element widths of 0.05, 0.04 and 0.03 mm. Results plotted in Figure C 1 and Figure C 2 for $\phi = 8.25$ and $\phi = 41.25$, respectively, are sensitive to the FE mesh at the larger value of ϕ . A coarse mesh causes spurious oscillations as can be seen from Figure C 2b. However, discrete Fourier transforms of the computed contact openings for mesh 2 and mesh 3 (Figure C 2-a) yield the same dominant frequency ($\approx 4.1h$).

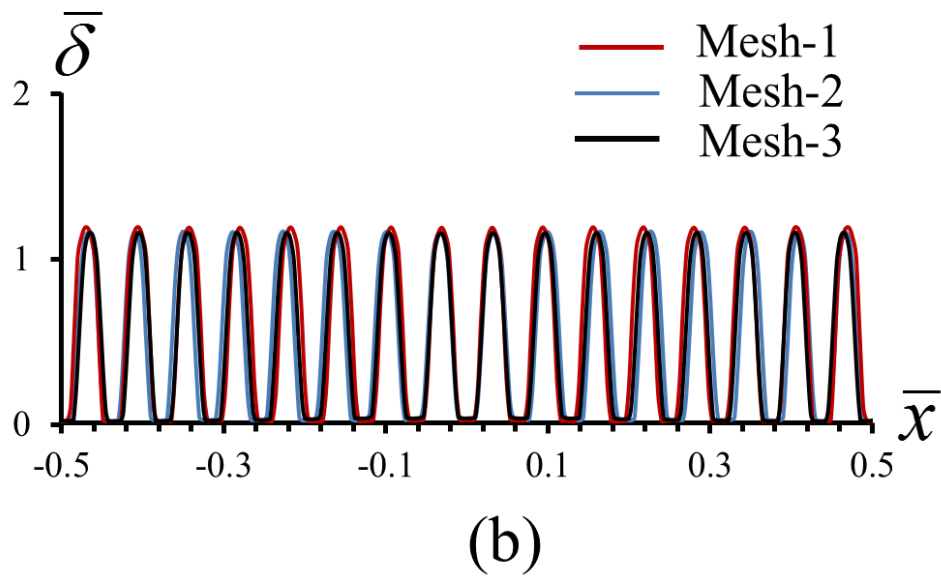
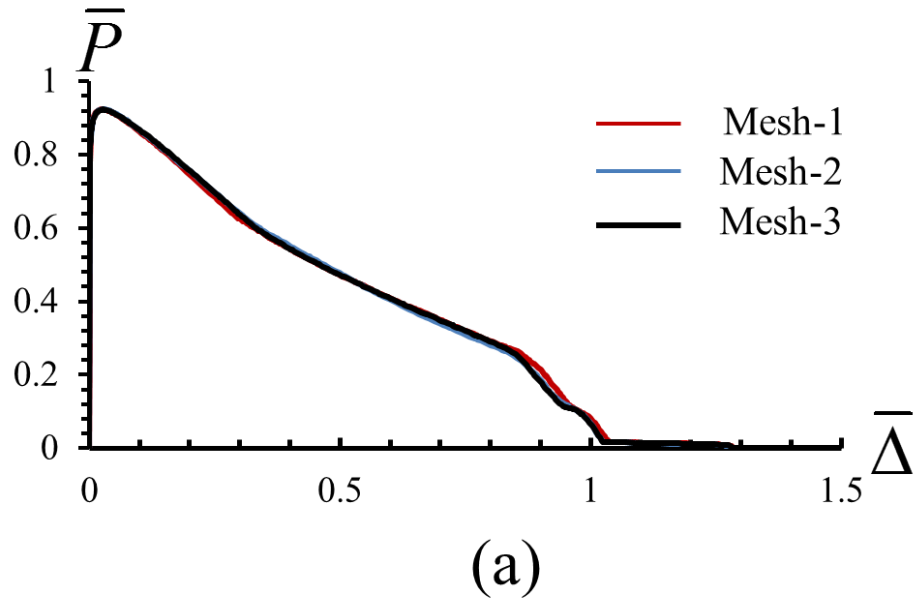
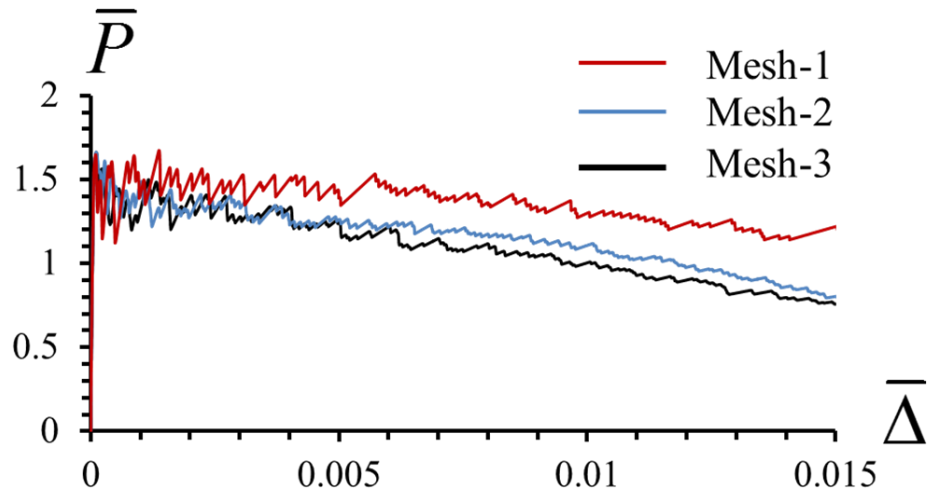
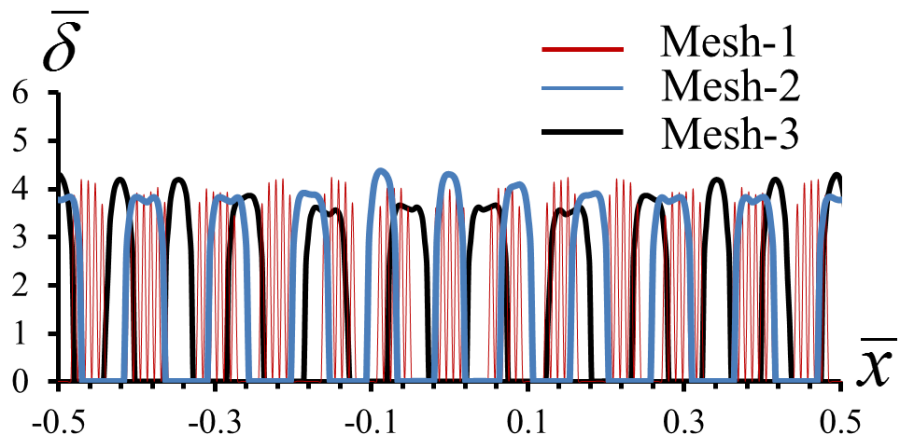


Figure C 1: For $\phi = 8.25$, sensitivity to the FE mesh of (a) the dimensionless reaction force ($\bar{P} = R/T_c \tilde{A}$) vs. the dimensionless displacement, $\bar{\Delta}$, applied at a rate of 1 mm/s when $m = 3$, and (b) the dimensionless interfacial contact opening when $\Delta = 0.54$.



(a)



(b)

Figure C 2: For $\phi = 41.25$, sensitivity to the FE mesh of (a) the dimensionless reaction force vs. dimensionless displacement applied at a rate of 1 mm/s when $m = 3$, and (b) the dimensionless interfacial contact opening when $\Delta = 1.67$.

References

- [1] Martin, W.A., T. Kindt-Larsen, and C.W. Walker, *Method and apparatus for demolding ophthalmic contact lenses*. 1999.
- [2] Mönch, W. and S. Herminghaus, *Elastic instability of rubber films between solid bodies*. EPL (Europhysics Letters), 2001. **53**(4): p. 525.
- [3] Chou, S.Y. and L. Zhuang, *Lithographically induced self-assembly of periodic polymer micropillar arrays*. Journal of Vacuum Science & Technology B, 1999. **17**(6): p. 3197-3202.
- [4] Ghatak, A., M.K. Chaudhury, V. Shenoy, and A. Sharma, *Meniscus instability in a thin elastic film*. Physical Review Letters, 2000. **85**(20): p. 4329.
- [5] Ghatak, A., L. Mahadevan, J.Y. Chung, M.K. Chaudhury, and V. Shenoy, *Peeling from a biomimetically patterned thin elastic film*. Proceedings of the Royal Society of London. Series A: Mathematical, Physical and Engineering Sciences, 2004. **460**(2049): p. 2725-2735.
- [6] Nase, J., A. Lindner, and C. Creton, *Pattern formation during deformation of a confined viscoelastic layer: From a viscous liquid to a soft elastic solid*. Physical review letters, 2008. **101**(7): p. 074503.
- [7] Lakrout, H., P. Sergot, and C. Creton, *Direct observation of cavitation and fibrillation in a probe tack experiment on model acrylic pressure-sensitive-adhesives*. The Journal of Adhesion, 1999. **69**(3-4): p. 307-359.
- [8] Creton, C. and H. Lakrout, *Micromechanics of flat-probe adhesion tests of soft viscoelastic polymer films*. Journal of Polymer Science Part B: Polymer Physics, 2000. **38**(7): p. 965-979.
- [9] Ghatak, A. and M.K. Chaudhury, *Adhesion-induced instability patterns in thin confined elastic film*. Langmuir, 2003. **19**(7): p. 2621-2631.
- [10] Shenoy, V. and A. Sharma, *Pattern formation in a thin solid film with interactions*. Physical review letters, 2001. **86**(1): p. 119.
- [11] Ghatak, A., *Confinement-induced instability of thin elastic film*. Physical Review E, 2006. **73**(4): p. 041601.
- [12] Adda-Bedia, M. and L. Mahadevan, *Crack-front instability in a confined elastic film*. Proceedings of the Royal Society A: Mathematical, Physical and Engineering Science, 2006. **462**(2075): p. 3233-3251.
- [13] Vilmin, T., F. Ziebert, and E. Raphaël, *Simple View on Fingering Instability of Debonding Soft Elastic Adhesives*. Langmuir, 2009. **26**(5): p. 3257-3260.
- [14] Huang, S.-Q., Q.-Y. Li, X.-Q. Feng, and S.-W. Yu, *Pattern instability of a soft elastic thin film under van der Waals forces*. Mechanics of materials, 2006. **38**(1): p. 88-99.
- [15] Arun, N., A. Sharma, V.B. Shenoy, and K. Narayan, *Electric-Field-Controlled Surface Instabilities in Soft Elastic Films*. Advanced Materials, 2006. **18**(5): p. 660-663.
- [16] Dugdale, D., *Yielding of steel sheets containing slits*. Journal of the Mechanics and Physics of Solids, 1960. **8**(2): p. 100-104.
- [17] Barenblatt, G.I., *The mathematical theory of equilibrium cracks in brittle fracture*. Advances in applied mechanics, 1962. **7**(1): p. 55-129.
- [18] Hui, C., A. Ruina, R. Long, and A. Jagota, *Cohesive zone models and fracture*. The Journal of Adhesion, 2011. **87**(1): p. 1-52.
- [19] Hillerborg, A., M. Modéer, and P.-E. Petersson, *Analysis of crack formation and crack growth in concrete by means of fracture mechanics and finite elements*. Cement and concrete research, 1976. **6**(6): p. 773-781.

- [20] Song, S.H., G.H. Paulino, and W.G. Buttlar, *A bilinear cohesive zone model tailored for fracture of asphalt concrete considering viscoelastic bulk material*. Engineering Fracture Mechanics, 2006. **73**(18): p. 2829-2848.
- [21] Rahul-Kumar, P., A. Jagota, S. Bennison, S. Saigal, and S. Muralidhar, *Polymer interfacial fracture simulations using cohesive elements*. Acta materialia, 1999. **47**(15): p. 4161-4169.
- [22] Li, S., M. Thouless, A. Waas, J. Schroeder, and P. Zavattieri, *Use of mode-I cohesive-zone models to describe the fracture of an adhesively-bonded polymer-matrix composite*. Composites Science and Technology, 2005. **65**(2): p. 281-293.
- [23] Xu, X.-P. and A. Needleman, *Numerical simulations of dynamic crack growth along an interface*. International Journal of Fracture, 1995. **74**(4): p. 289-324.
- [24] Sarkar, J., A. Sharma, and V. Shenoy, *Adhesion and debonding of soft elastic films: Crack patterns, metastable pathways, and forces*. Langmuir, 2005. **21**(4): p. 1457-1469.
- [25] Yamaguchi, T. and M. Doi, *Debonding dynamics of pressure-sensitive adhesives: 3D block model*. The European Physical Journal E: Soft Matter and Biological Physics, 2006. **21**(4): p. 331-339.
- [26] Lindsey, G., R. Schapery, M. Williams, and A. Zak, *The triaxial tension failure of viscoelastic materials*. 1963, DTIC Document.
- [27] Geubelle, P.H. and J.S. Baylor, *Impact-induced delamination of composites: a 2D simulation*. Composites Part B: Engineering, 1998. **29**(5): p. 589-602.
- [28] Kaelble, D., *Peel Adhesion: Micro-Fracture Mechanics of Interfacial Unbonding of Polymers*. Transactions of The Society of Rheology (1957-1977), 1965. **9**(2): p. 135-163.
- [29] Ghatak, A., L. Mahadevan, and M.K. Chaudhury, *Measuring the work of adhesion between a soft confined film and a flexible plate*. Langmuir, 2005. **21**(4): p. 1277-1281.
- [30] Turon, A., C.G. Davila, P.P. Camanho, and J. Costa, *An engineering solution for mesh size effects in the simulation of delamination using cohesive zone models*. Engineering Fracture Mechanics, 2007. **74**(10): p. 1665-1682.
- [31] Shen, B. and G. Paulino, *Direct extraction of cohesive fracture properties from digital image correlation: a hybrid inverse technique*. Experimental Mechanics, 2011. **51**(2): p. 143-163.
- [32] Gowrishankar, S., H. Mei, K.M. Liechti, and R. Huang, *A comparison of direct and iterative methods for determining traction-separation relations*. International journal of fracture, 2012. **177**(2): p. 109-128.
- [33] Brinson, H.F. and L.C. Brinson, *Polymer engineering science and viscoelasticity: an introduction*. 2007: Springer.
- [34] Wright, T. and H. Ockendon, *A scaling law for the effect of inertia on the formation of adiabatic shear bands*. International journal of plasticity, 1996. **12**(7): p. 927-934.
- [35] Lakrout, H., C. Creton, D. Ahn, and K.R. Shull, *Influence of molecular features on the tackiness of acrylic polymer melts*. Macromolecules, 2001. **34**(21): p. 7448-7458.
- [36] Hibbitt, K. and Sorensen, *ABAQUS/CAE User's Manual*. 2012: Hibbitt, Karlsson & Sorensen, Incorporated.
- [37] Dundurs, J., *Discussion: "Edge-bonded dissimilar orthogonal elastic wedges under normal and shear loading"* (Bogy, DB, 1968, ASME J. Appl. Mech., 35, pp. 460-466). Journal of applied mechanics, 1969. **36**(3): p. 650-652.
- [38] Bogy, D.B., *Edge-bonded dissimilar orthogonal elastic wedges under normal and shear loading*. Journal of Applied Mechanics, 1968. **35**(3): p. 460-466.

- [39] Qian, Z. and A. Akisanya, *Wedge corner stress behaviour of bonded dissimilar materials*. Theoretical and applied fracture mechanics, 1999. **32**(3): p. 209-222.
- [40] Chadegani, A. and R.C. Batra, *Analysis of adhesive-bonded single-lap joint with an interfacial crack and a void*. International Journal of Adhesion and Adhesives, 2011. **31**(6): p. 455-465.
- [41] Wolfram Research, I., *Mathematica*. 2014, Wolfram Research, Inc.: Champaign, Illinois.
- [42] Gent, A., *Cavitation in rubber: a cautionary tale*. Rubber Chemistry and Technology, 1990. **63**(3): p. 49-53.
- [43] Murray, K.V., *Characterization of the Interfacial Fracture of Solvated Semi-Interpenetrating Polymer Network (S-IPN) Silicone Hydrogels with a Cyclo-Olefin Polymer (COP)*. 2011, Virginia Polytechnic Institute and State University.
- [44] Simo, J., *On a fully three-dimensional finite-strain viscoelastic damage model: formulation and computational aspects*. Computer methods in applied mechanics and engineering, 1987. **60**(2): p. 153-173.
- [45] Tizard III, G.A., *Characterization of the Viscoelastic Fracture of Solvated Semi-Interpenetrating Polymer Network (S-IPN) Silicone Hydrogels*. 2010, Virginia Polytechnic Institute and State University.
- [46] Dillard, D., *Bending of plates on thin elastomeric foundations*. Journal of applied mechanics, 1989. **56**(2): p. 382-386.

3 Effect of confinement and interfacial adhesion on peeling of a flexible plate from an elastomeric layer

Bikramjit Mukherjee^a, Romesh C. Batra^a and David A. Dillard^{a*},
Department of Biomedical Engineering and Mechanics, M/C 0219
Virginia Polytechnic Institute and State University
Blacksburg, Virginia 24061, USA

(The material of this chapter has been submitted for possible publication in a peer-reviewed journal)

Abstract

The finite element method and a cohesive zone model are used to analyze debonding at an interface between an elastomeric layer and a deformable plate overhanging on one side when a normal displacement at the edge of the overhang is applied and deformations are approximated as plane strain. The collective role of the material and the geometric parameters, and those in a bilinear traction-separation (TS) relation on the interfacial debonding is studied by using a cohesive zone model. The following two non-dimensional parameters are found to play critical roles: (i) the confinement parameter, α , defined in terms of the flexural rigidity of the plate, and the modulus and the thickness of the interlayer, and (ii) the adhesion parameter, ϕ , defined in terms of the TS variables, and the modulus to thickness ratio of the interlayer. When α is greater than α_c , damage is found to initiate at an interior point on the interface and at the interface corner irrespective of the value of ϕ . However, when ϕ is greater than ϕ_c , the debonding may become wavy/undulatory. The critical value, ϕ_c , of the adhesion parameter agrees with the necessary condition found in our previous work on debonding of an elastomeric layer from a rigid block when it is uniformly pulled outward. For $\alpha < \alpha_c$, damage/debonding initiates only from the interface corner, and no wavy debonding ensues. The peak peeling force is found to be a monotonically increasing function of ϕ/α suggesting its potential use as a design variable and as a guide for determining the TS parameters. Results of several additional numerical experiments in which the elastomer can debond from both adherends provide insights into designing a demolding process for a sandwiched elastomer layer.

Keywords: Elastomeric interlayer, debonding, cohesive zone model (CZM), instability

* Corresponding author, Email: dillard@vt.edu, Tel.: +1- 540-231-4714, Fax: +1- 540-231-9187

3.1 Introduction

A soft elastomeric interlayer sandwiched between two adherends is encountered in a wide variety of engineering applications such as manufacturing of bio-implants, micro-printing processes, and modern bio-inspired adhesive systems. The requirement of controlling interfacial separation of the confined interlayer in such applications necessitates understanding collective roles of the geometric, the material, and the interfacial adhesion parameters on the processes of initiation and propagation of interfacial debonding of the interlayer from the adherend(s).

It is well known that the lateral constraint imposed by the geometric confinement plays a crucial role in the adhesion/debonding characteristics of a sandwiched interlayer. An often studied problem in this context is the debonding of a rigid cylindrical adherend from a deformable interlayer attached to a fixed base, shown schematically in [Figure 3-1a](#). It has been shown [1, 2] that the ratio, a/h , of the adherend radius (a) to the interlayer thickness (h) and the compressibility [3, 4] of the interlayer material quantify confinement and determine the traction distribution at the interface. For small values of a/h ($< \sim 1$), the singularity at the corner (edge) dominates the distribution of the normal traction (peel stress) at the interface. Therefore, for axisymmetric deformations an annular crack initiates at the edge and propagates towards the center. However, for larger values of a/h ($> \sim 1$) and an incompressible interlayer, the peel stress has a peak value at the center with a small singularity-dominant region at the edge, and the debonding initiates from an interior point. Systematic experimental investigations by [Webber et al. \[5\]](#) and [Anderson et al. \[6\]](#) support these statements (or observations). Peeling of a flexible plate from an elastomeric interlayer ([Figure 3-1b](#)) is another problem of practical interest in which the confinement has been shown to play a major role in the debonding process [7-9]. Even when stresses in the external edge region become high because of the peeling action, the interlayer confinement and the internal debonding control the failure process. Several investigations have suggested that the ratio of the lengths, $(D_p / \mu)^{1/3}$ and h , describes the geometric confinement. Here D_p is the flexural rigidity of the deformable plate, and μ the shear modulus of the interlayer. Large confinement is found to be relieved by the nucleation of debonding at a location away from the edge [10].

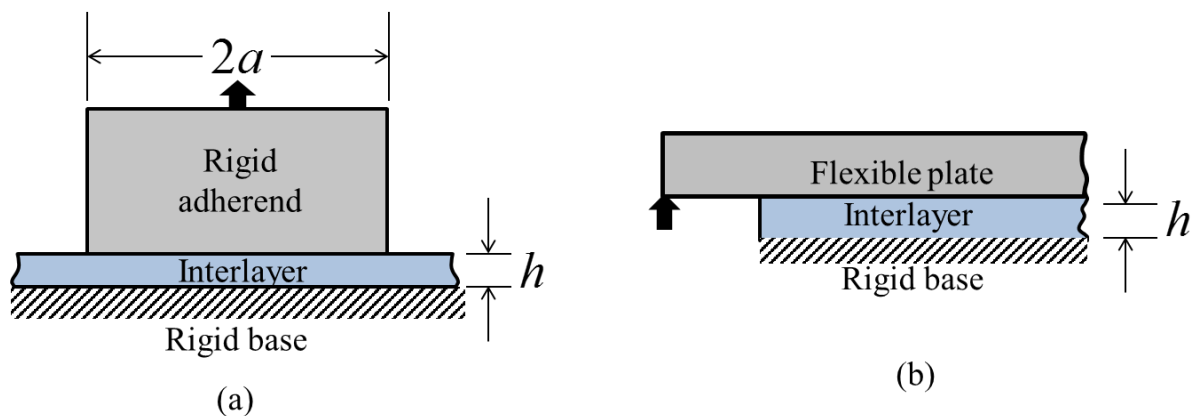


Figure 3-1: Schematic sketches of (a) a probe-tack configuration, and (b) a flexible plate peeled from a thin elastomeric layer bonded to a fixed rigid base

While the geometric confinement has a significant bearing on the adhesive debonding mechanisms of a sandwiched layer, its intricate coupling with the interfacial adhesion must be understood to delineate the debonding process. For example, in the debonding phase of a probe tact test (Figure 3-1a), the geometric confinement, a/h , and the dimensionless descriptor of adhesion, $G_c/\mu a$ where G_c is the critical strain energy release rate of the interface, collectively govern the debonding behavior. For a large value of $G_c/\mu a$ dictated by the degree of confinement [2, 11, 12] cavities have been observed to initiate within the bulk interlayer. For highly confined films and relatively weak interfaces, the internal adhesive debonding often involved nucleation of multiple cavities at the interface and their eventual coalescence into a crack [11, 13]. Even though these internal debonds were initially thought to have initiated from local defects, the theoretical analysis by Mönch and Herminghaus [14] suggested that they are adhesion-induced instabilities that occur when the interfacial effects dominate over elastic deformations of the interlayer. This determines spacing between the cavities that scales with the thickness of the interlayer. An approximate analysis showed that the coalescence behavior of the adjacent cavities is governed by $G_c/\mu a$ and its large value impedes lateral propagation of the interfacial cracks and results in fibrillation (Creton et al. [12]). When a flexible plate is peeled from an elastomer layer (Figure 1b), the adhesion-induced instability initiating and growing over the stressed zone results in fingerlike debonding [10, 15]. The spacing between these fingers scales with the interlayer thickness and their length in the peeling direction with $(D_p/\mu)^{1/3}$. Adda-Bedia and Mahadevan [8] and Ghatak [9] have proposed that the spacing between the fingers does not depend on the interfacial adhesion. However, the coupling between the geometric confinement and the

adhesion on debonding for this problem has not been thoroughly studied. Here we attempt to address this coupling by numerical simulations of the peeling problem.

A frequently used technique for studying debonding employs a cohesive zone model (CZM) [16-18]. In a CZM the interaction of adjoining points at the interface is phenomenologically represented by a spring of zero-length that softens after it has been extended by a prescribed value (reached a peak traction) and breaks at a pre-specified value of the extension (when the fracture energy criterion is met). It involves prescribing *a-priori* a relation between the traction and the corresponding separation/displacement-jump (relative displacement of two adjoining points) at the interface. For a given mode of debonding, two parameters, namely the fracture energy (G_c) and the peak traction (T_c) characterize commonly used traction-separation (TS) relations [16, 18, 19]. With a CZM both the nucleation of debonding and its propagation can be simulated. The CZM bridges the gap between the classical linear elastic fracture mechanics (LEFM) and the stress-based approach [20] of predicting failure. Whereas G_c can be deduced from the test data [21, 22], it is not easy to estimate values of parameters in the TS relation for a given interface. An indirect (brute-force) approach [23-25] is often used to find the TS relation which, when used in numerical simulations, predicts well the experimental load-displacement curve. Digital image correlation [26], interferometry [27], and molecular dynamics simulations [28, 29] have been used to extract values of parameters in the TS relation.

Here we use the finite element method (FEM), the CZM and a bilinear TS relation, to study debonding of a flexible plate from an elastomeric layer that is assumed not to debond from a rigid base, e.g., see the configuration shown in Figure 3-1b. Mukherjee et al. [30] have recently analyzed with the CZM and a bilinear TS relation wavy debonding during plane strain deformations of an infinitely wide confined elastomer layer from a rigid adherend pulled upwards using a configuration similar to that shown in Figure 3-1a. They found that the large peeling traction over the central region induced a damage zone (cohesive zone) over which wavy/undulatory debonding ensues due to competition between the interfacial softening and the elastic deformations of the interlayer. A necessary condition for homogeneous deformations of the interlayer to become unstable (undulatory debonding/adhesion-induced instability) is that the parameter $\phi = T_c^2 h / E G_c$ exceed approximately 4.15, where $E = 3 \mu$ is the Young's modulus of the interlayer material. This condition implies that for a given adhesion and interlayer material, its thickness must exceed a critical value for an interfacial instability to occur.

During peeling of an overhanging flexible plate from an elastomeric layer with the displacement applied at the edge of the overhang, the bending of the plate results in a stressed zone of characteristic length $(D_p / \mu)^{1/3}$ near the edge of the interlayer. Results of Ghatak and Chaudhury [10] and Adda-Bedia and Mahadevan [8] for peeling of a flexible plate suggest that the interlayer thickness must be smaller than a critical value dictated by the length $(D_p / \mu)^{1/3}$ for an undulatory debonding to ensue. This and the aforementioned condition, $h > 4.15EG_c / T_c^2$, determine whether or not debonding will be undulatory. This reiterates the importance of coupling between confinement and adhesion when studying debonding in this problem. The analysis of the peeling of an overhanging beam from an elastomer layer by using a TS relation for the interface enables us to probe this coupling.

Results of numerical experiments for studying the collective effect of confinement and adhesion reported here advance our current understanding of the peeling phenomenon, help in developing predictive models for complex manufacturing processes involving separation of confined elastomeric layers, shed light on the global behavior such as the pull-off force as a function of geometric confinement and interfacial adhesion and its transition from a strength-dominated regime to a fracture-energy dominated regime, and may help in determining the TS parameters for the interface between an elastomer layer and a stiff adherend.

The rest of the paper is organized as follows. We describe in Section 2 the problem studied, outline in Section 3 the numerical approach used to solve the problem, and present and discuss in Section 3.4 results obtained by the FEM that relate the damage growth and debonding to the confinement and the interfacial adhesion. The findings are summarized in Section 3.5. The appendices include mesh refinement studies, computed energy balance for one example problem, and results of some three-dimensional (3-D) problems that support conclusions drawn from the analysis of 2-D problems.

3.2 Formulation of the problem

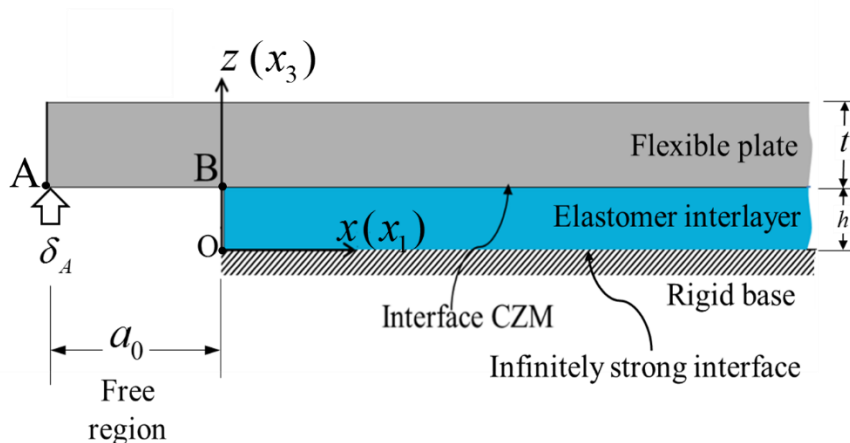


Figure 3-2: Schematic sketch of the problem studied.

A schematic sketch of the problem studied is shown in Figure 3-2. The domain of interest consists of an elastomeric layer sandwiched between a deformable plate and a fixed rigid base. It is assumed that debonding occurs only at the interface between the plate and the interlayer. Neglecting body and inertia forces⁹, equations of motion in the rectangular Cartesian coordinate axes $(x, y, z$ or $x_1, x_2, x_3)$ are

$$\frac{\partial \sigma_{ij}}{\partial x_j} = 0, \quad (3-1)$$

where σ_{ij} is the stress tensor and a repeated index implies summation over the range of values of the index. The plate and the interlayer materials are assumed to be homogeneous, isotropic and Hookean¹⁰, and the elastomer layer is also assumed to be incompressible. Constitutive equations are

Flexible plate:
$$\sigma_{ij} = \frac{2\mu_p \nu_p}{(1-2\nu_p)} \varepsilon_{kk} \delta_{ij} + 2\mu_p \varepsilon_{ij}, \quad (3-2)$$

⁹ Since the time of interest is much larger than the time taken for an elastic wave to traverse the elastomer thickness several times, inertia terms are neglected in the equations of motion.

¹⁰ The maximum computed strain, except possibly at points near the edges where singularities may occur, in our simulations is 6%. Thus it is reasonable to assume the interlayer material to be linear elastic.

Interlayer:
$$\sigma_{ij} = -p\delta_{ij} + 2\mu\varepsilon_{ij} \quad (3-3)$$

Here μ_p and ν_p are, respectively, the shear modulus and Poisson's ratio of the flexible plate, μ the shear modulus of the elastomer interlayer, p the unknown hydrostatic pressure in the elastomer layer arising due to the incompressibility constraint, δ_{ij} the Kronecker delta, and ε_{ij} the strain tensor for infinitesimal deformations defined as

$$\varepsilon_{ij} = \frac{1}{2} \left(\frac{\partial u_i}{\partial x_j} + \frac{\partial u_j}{\partial x_i} \right), \text{ where } u_i \text{ is the displacement component along the } x_i \text{-axis.}$$

The system is assumed to be very wide in the y-direction so that a plane strain state of deformation prevails¹¹ in the xz - (or x_1x_3 -) plane, i.e., $u_y = 0$ and the deformation is uniform along the y-direction. All displacement components at points on the lower surface of the interlayer are assumed to be zero to simulate no debonding at its interface with the rigid base. A monotonically increasing vertical peeling displacement, δ_A , is applied at the tip point, A, of the flexible plate. These displacement boundary conditions are written as

Lower surface
$$u_x = u_z = 0 \quad (3-4)$$

($z = 0$) of the interlayer:

Point A:
$$u_z = \delta_A \quad (3-5)$$

The remaining bounding regions that include the overhang AB (of length a_0) of the plate are assumed to be traction-free, i.e.,

$$T_i = \sigma_{ij}n_j = 0 \quad (3-6)$$

where $n_j (= \delta_{3j})$ denotes the j^{th} component of the unit outward normal at a point on the bounding surface.

¹¹ As will be shown later, a plane strain deformation cannot accurately predict details of debonding after interfacial instability has set in. A three-dimensional analysis is needed for finding these details.

In linear elasticity one should apply displacements on a surface of finite area. Thus our applying vertical displacement δ_A at points on the edge of the lower surface of the flexible plate is an approximation. In the numerical solution of the problem, one can easily satisfy this boundary condition.

The interaction at the interface between the plate and the interlayer is modelled by a TS relation that relates interfacial tractions to the displacement jumps. Following [Maugis \[31\]](#) we assume that the interface fails in mode-I¹². The bilinear TS relation, used herein, is given by Eq. (2-3) and plotted in [Figure 3-3](#).

$$T_n(\delta) = \begin{cases} K\delta & (0 \leq \delta \leq \delta_c) \\ \frac{T_c}{\delta_f - \delta_c}(\delta_f - \delta) & (\delta_c \leq \delta \leq \delta_f) \\ 0 & (\delta_f \leq \delta) \end{cases} \quad (3-7)$$

That is, the normal traction, T_n , first increases linearly with the displacement jump, δ , commonly termed the contact opening/separation, over the region OE. Point E with $T_n = T_c$ and $\delta = \delta_c$ denotes the initiation of damage/softening beyond which the traction decreases affinely with an increase in the contact opening (line EF). Should unloading occur at point R, the traction follows the path RO. Subsequent reloading occurs along the path ORF. Point F signifies complete separation at a point on the interface. The energy release rate at debonding (i.e., the fracture energy) equals the area of the triangle OEF. That is,

$$G_c = \frac{1}{2} T_c \delta_f \quad (3-8)$$

In general, the value of the initial slope K_e must be sufficiently large [\[33\]](#) to minimize the artificial compliance introduced into the system and to avoid inter-penetration under compression. A very large value of K_e can make the system matrices ill-conditioned when the problem is analyzed by the FEM.

A damage variable, $D = \frac{\delta_f}{\delta_f - \delta_c} \left(1 - \frac{\delta_c}{\delta}\right)$, $\delta \geq \delta_c$, is used to quantify the extent of damage at an interfacial point; The variation of D with δ is illustrated in [Figure 3-3](#). The damage first rapidly increases in δ and then very slowly approaches the ultimate value of 1.

¹² This assumption implies that in the TS relation for mixed-mode damage (see [Hibbitt and Sorensen \[32\]](#)) the peak traction and the fracture energy for mode-II damage are much larger than those for mode-I damage. This is a reasonable assumption since the global loading is mode-I dominant.

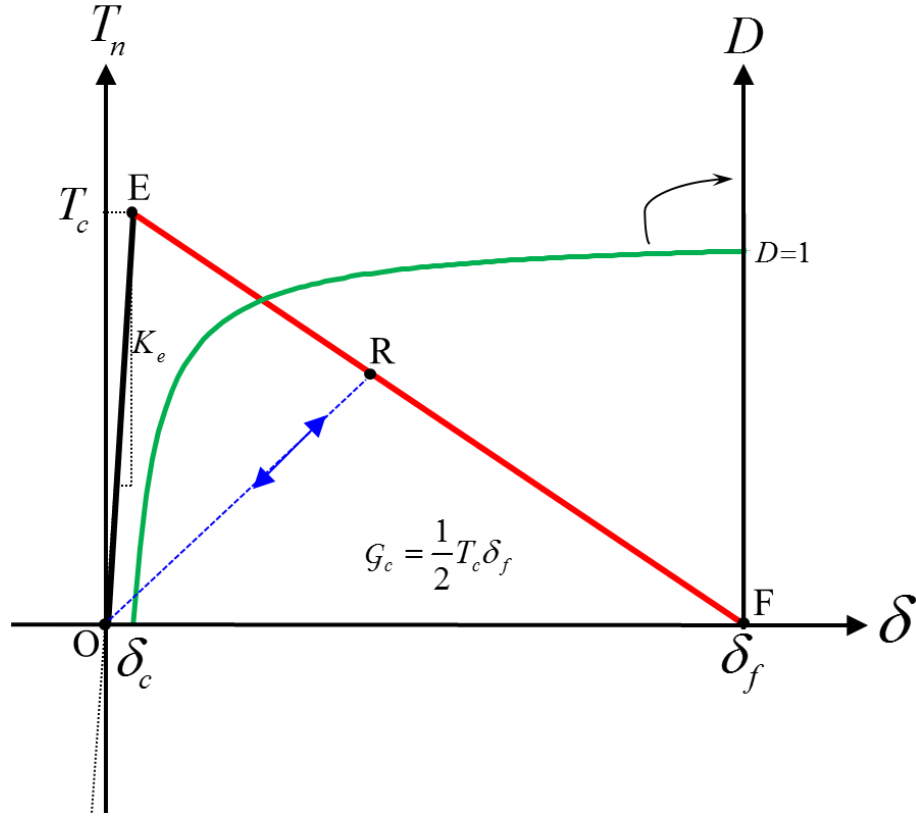


Figure 3-3: Bilinear traction-separation relation between the interfacial normal traction and the jump (contact-opening) in the interface normal displacement. Also included is a plot of the variation of the damage variable as a function of the contact-opening.

Equations (3-1)-(2-4) define the boundary value problem (BVP) analyzed in this work. The possibility of debonding at *a priori* unknown points on the interface makes the BVP challenging.

3.3 Numerical Solution of the Problem

3.3.1 Approach

The commercial FE software ABAQUS/Standard¹³ [32] is used to numerically analyze the BVP by employing 4-node square/rectangular elements in the FE mesh shown in Figure 3-4. In the ABAQUS terminology we use CPE4 (plane strain, 4-point integration) elements for the plate and the CPE4H (H stands for hybrid formulation appropriate for incompressible materials in which both displacements and the pressure are taken as unknowns) elements for the interlayer. Sensitivities of the computed peel stress distributions and the load-displacement variations to the FE mesh are reported in Appendix A. The vertical

¹³ The computed results satisfied energy balance within 8% discrepancy between the external work and the sum of the strain energy, the dissipation due to interfacial damage, and the dissipation due to viscous regularization (Appendix B).

displacement δ_A of point A in Figure 3-4 is gradually increased. A surface-based cohesive contact interaction [32] is used for the interface between the flexible plate and the interlayer¹⁴. We have not captured a converged value of the order of singularity [34-36] at the initial debond tip ($x = 0$). However, key findings reported herein are found to be insensitive to refining further the FE mesh (see Appendix A). In order to alleviate numerical instabilities and associated convergence difficulties, the “Damage Stabilization” option (viscous regularization) in ABAQUS is used. The value of the stabilization parameter was chosen to be 10^{-7} ; using a lower value was found not to affect the computed results but significantly increase the computation time.

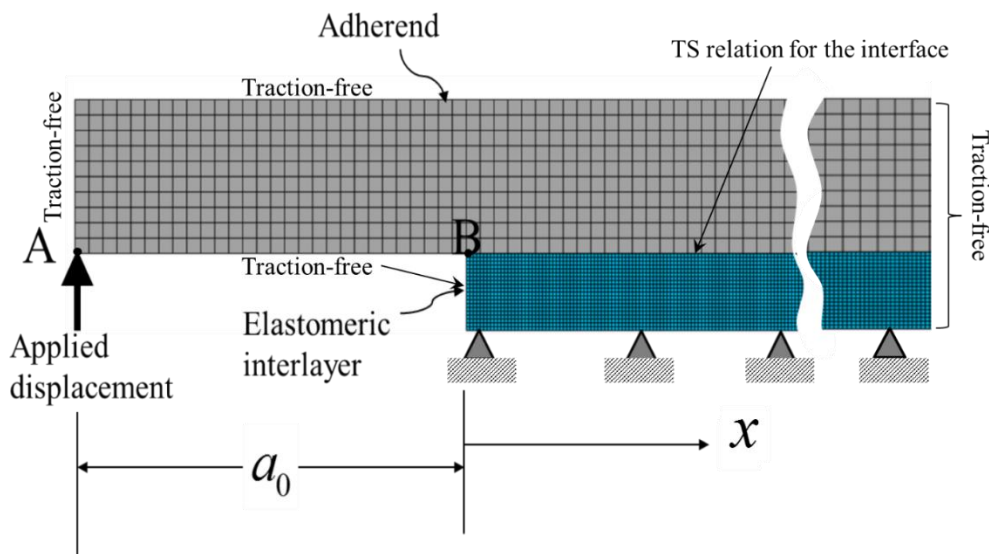


Figure 3-4: The FE mesh and the boundary conditions on the region whose plane-strain deformations are analyzed.

3.4 Results and discussion

3.4.1 Choice of Parameters

The problem being studied has the following five independent length scales¹⁵:

$$\underbrace{h, (D_p / \mu)^{1/3}, a_0}_{\text{Material and geometry}}, \underbrace{\delta_f, G_c \mu / T_c^2}_{\text{CZM}}$$

¹⁴ In ABAQUS terminology a node-to-surface discretization is used with the plate surface defined as the ‘master’ surface and the interlayer surface as the ‘slave’ surface (see Hibbitt and Sorensen [32] for details). While computing the displacement jump at a slave node, the displacement of the closest point on the master surface is computed by using the displacements of neighbouring nodes.

¹⁵ In order to understand the corner B singularity (cf. Figure 3-4) oscillations in the interfacial tractions, we recall that the Williams [37] solution is of the form $\sin(1/2\pi \ln(\frac{1-\beta_D}{1+\beta_D}) \ln r)$ where r is the radial distance from point B, and $\beta_D = \frac{1}{2} \frac{\mu_p(1-2\nu) - \mu(1-2\nu_p)}{\mu_p(1-\nu) + \mu(1-\nu_p)}$ where μ_p is the shear modulus of the flexible plate and ν Poisson’s ratio of the interlayer. For materials of interest here $\nu \approx 0.5, \nu_p \approx 0.3 - 0.4, \mu/\mu_p \approx 10^{-5}$, we get $\beta_D \approx 0$

The flexural rigidity of the plate, D_p , is given by $D_p = E_p t^3 / 12(1 - \nu_p^2)$ where E_p is Young's modulus of the plate material, ν_p Poisson's ratio and t the plate thickness. The geometric mean of the first two lengths, $\sqrt{h(D_p / \mu)^{1/3}}$, quantifies the characteristic stress decay distance [22, 38] from the edge, and their ratio, $\alpha = (D_p / \mu h^3)^{1/3}$, signifies confinement [9] of the interlayer. The ratio of h and the CZM length scale $G_c \mu / T_c^2$ yields the parameter $\phi = T_c^2 h / G_c E$ (note that $E = 3\mu$ for the incompressible elastomer layer) that determines the onset of contact instability [30] during plane strain deformations of the elastomer layer sandwiched between two rigid blocks and one rigid block pulled away from it and the other kept stationary. Following Adda-Bedia and Mahadevan [8], Ghatak [9], Vilmin et al. [15], we call α the confinement parameter, and following Mukherjee et al. [30] ϕ the CZM/adhesion parameter.

In terms of non-dimensional variables the interfacial traction is written as

$$T_i = T_c \bar{T}_i(\alpha, \phi, \Delta_A, X, A) \quad (3-9)$$

where T_i stands for either the normal (T_n) or the tangential traction (T_s) at the interface, T_c is the peak normal traction when damage initiates, $\Delta_A = \delta_A / \delta_f$, $X = x\beta$, $A = a_0\beta$ and $\beta = (12\mu / D_p h^3)^{1/6}$.

3.4.2 Analysis of interfacial tractions with no damage allowed at the interface

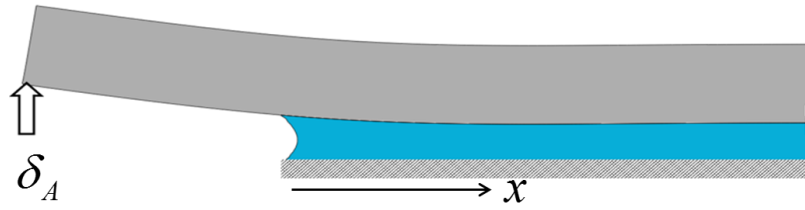
In this sub-section, we report interfacial tractions as a function of the confinement when the flexible plate is peeled away from the interlayer but no separation is allowed to occur at the interface. Results are computed for constant vertical displacement, $\delta_A = 1 \mu m$, at different values of the confinement parameter, α , varied by choosing lengths $(D_p / \mu)^{1/3}$ and h such that $\beta^{-1} = 1 mm$. A very large value is assigned to T_c so that damage does not initiate

for $\delta_A = 1 \mu m$ and the FE mesh used¹⁶. Unless otherwise specified, we set $a_0 = 2.83 mm$ and the length of the plate = 50 mm.

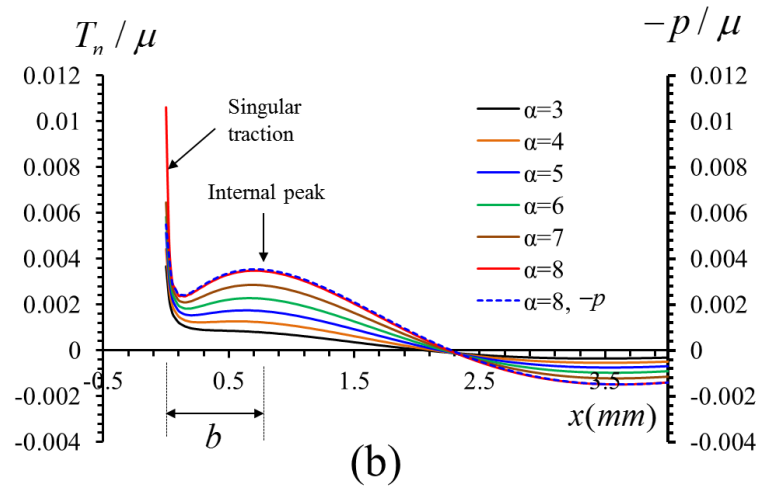
The distributions (nodal values) of T_n (peel stress) and T_s are plotted in Figure 3-5 as functions of the distance x measured from the corner point B. With an increase in α , the peel stress, in addition to the large value exhibited at corner B, has a local maximum (secondary/internal peak) where the tangential stress is nearly zero. However, for low confinement (e.g., $\alpha = 3$), this local maximum is not exhibited, though evidence of a shoulder remains. The computed distribution of the interfacial peel stress is compared in Figure 3-6 with that from approximate ‘mechanics of materials’ solutions of other investigators. The approximate solution of Ghatak et al. [22] captures qualitatively the interfacial normal traction distribution for low values of α . The solution of Ghatak et al. [39], who enforced a boundary condition of zero peel stress at point B, captures the location of the secondary peak for confined interlayers. Ghatak et al. [22] assumed that the peel stress had a local maximum at point B. As shown by Adda-Bedia and Mahadevan [8], the edge singularity must be considered to capture details of the interfacial tractions.

The non-dimensional distance, $b\beta$, from point B where the local maximum in T_n occurs for sufficiently confined interlayers, is computed for a range of values of α and β , and plotted in Figure 3-7 as a function of α . It can be seen that $b\beta$ becomes relatively insensitive to the confinement level for large values of α . For the experimental set-up of Ghatak et al. [39], $\alpha > 15$, our prediction of this distance lies between the experimentally measured, $b\beta \approx 1.1$, and the approximate theoretical prediction, $b\beta \approx 0.74$ [39]. The assumption $b\beta \approx \text{constant}$ leads to the relation, $b \propto (E_p / E)^{1/6} (t)^{1/2} (h)^{1/2}$, which is similar to the characteristic lag distance $l_{shear-lag} \propto (E_p / E)^{1/2} (t)^{1/2} (h)^{1/2}$ found from Volkersen’s shear lag analysis [40]. This correlation is understandable in that the internal peak in the peel stress occurs because shear stresses at the interface transfer load into the elastomer interlayer through shear lag but in a decreasing traction field; e.g., see the analysis of a beam on an elastic foundation (6th order equation [38]).

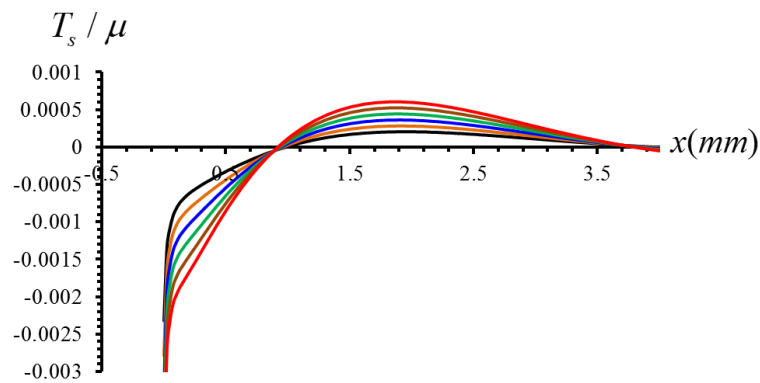
¹⁶ One example is $\mu = 5 MPa$, $h = 0.67 mm$, $t = 1 mm$, $E_p = 2.115 GPa$, $\nu_p = 0.3$, $T_c = 10 MPa$ and $K_c = 10^6 N/mm^3$. For these values of parameters, the damage does not initiate when elements of dimensions $0.0125 mm \times 0.0125 mm$ and $0.1 mm \times 0.1 mm$ are used to discretize the interlayer and the flexible plate, respectively.



(a)



(b)



(c)

Figure 3-5: (a) A schematic sketch of the deformed shape of the specimen; the computed (b) interfacial normal traction (T_n) and (c) the interfacial tangential traction (T_s) as functions of the distance x from the corner point B for different levels of confinement, α ($\mu = 5MPa$). Note that these results correspond to a very high value of the interfacial strength to prevent debonding at the interface

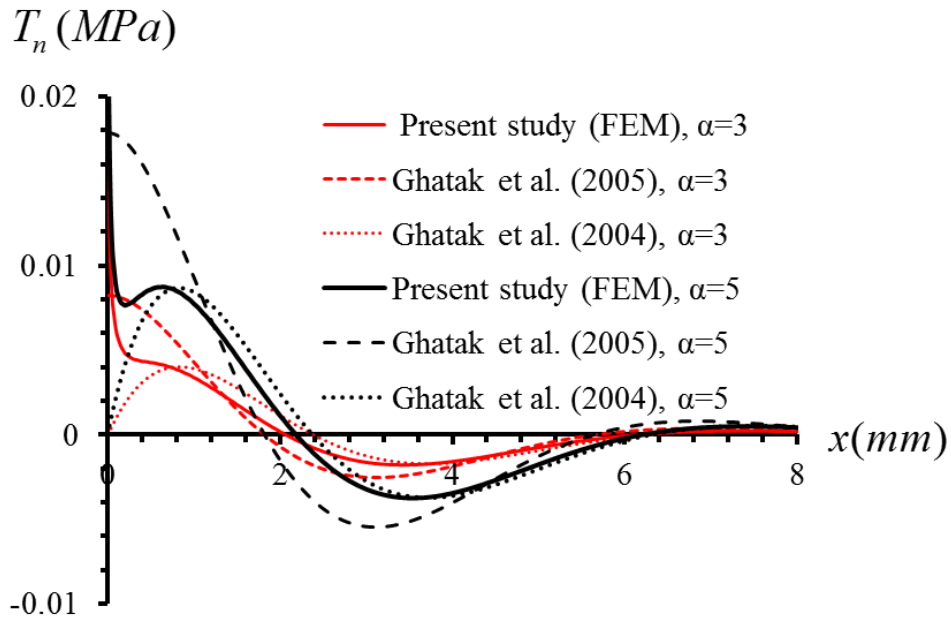


Figure 3-6: Comparison of present results with those from the literature for $\alpha=3$ and $\alpha=5$ (for $\mu=5\text{ MPa}$). Note that these results correspond to a very high value of the interfacial strength to prevent debonding at the interface.

For $\alpha=8$, the variation with x of the computed hydrostatic pressure, p , plotted in Figure 3-5a reveals that the normal traction on the interface essentially equals the hydrostatic pressure. Thus the shear stress, σ_{xz} , in the elastomer layer is much smaller than the normal stresses, σ_{xx} and σ_{zz} , as also evinced by results plotted in Figure 3-5a.

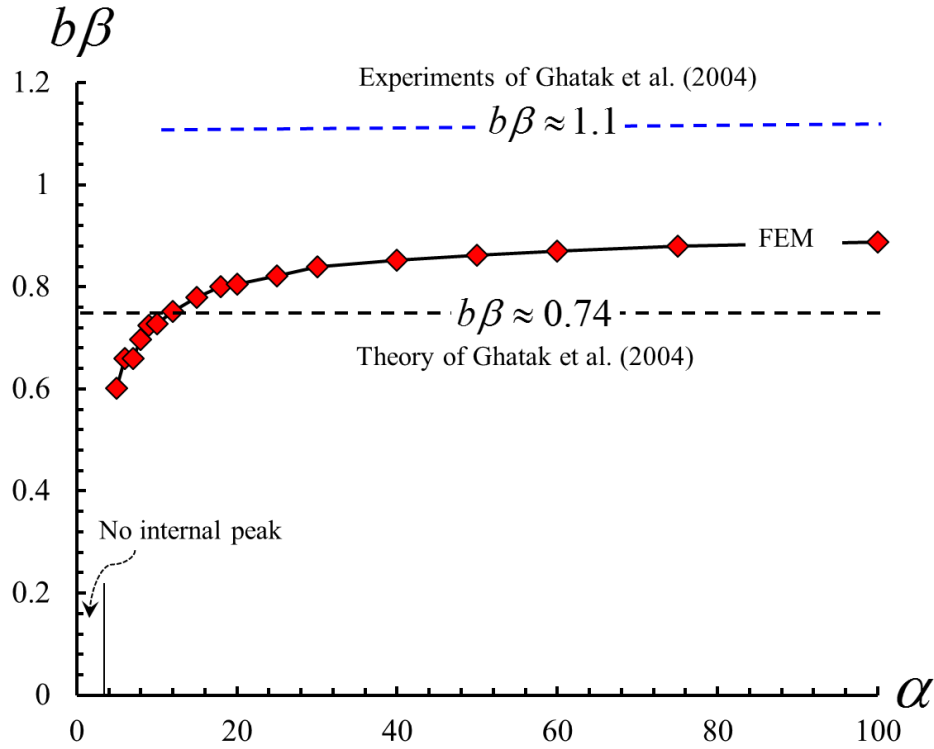


Figure 3-7: Non-dimensional location of the internal peak as a function of the confinement level. Note that these results correspond to a very high value of the interfacial strength to prevent debonding at the interface.

3.4.3 Analysis of damage growth and debonding

In the CZM, damage initiates at an interfacial point when the peel stress there just exceeds the prescribed peak traction, T_c . Further increase in the applied displacement δ_A causes the peel stress at that point to follow the softening segment EF of the TS relation in Figure 3-3. The region where softening (sometimes called damage) has occurred in the TS relation is henceforth referred to as the cohesive zone (CZ). It is conjectured that for large values of α the damage/softening initiation at the corner point B is accompanied by the initiation of damage at an interior point situated at a distance b (analogous to the shear-lag distance) from point B due to the local peak peel stress there increasing with α . The literature results [30, 41, 42] suggest that the post-damage response will be influenced by the value of the parameter ϕ . In order to delineate the collective role of α and ϕ on the damage/debonding behavior, we simulate progressive debonding with a gradual increase of

δ_A . Unless specified otherwise, we use $\beta^{-1} = 1 \text{ mm}$, $a_0 = 2.83 \text{ mm}$, $K_e = 10^6 \text{ N/mm}^3$, and vary α and ϕ .¹⁷

3.4.3.1 Analysis of damage growth and debonding

Figure 3-8 exhibits the evolution of the peel stress and the damage variable¹⁸ with a monotonic increase in the applied displacement δ_A when $\alpha = 3$ and $\phi = 0.1$ ¹⁹. With increasing δ_A applied at the plate edge²⁰, damage initiates at the corner and forms a CZ accompanied by a redistribution of the stress. Note that the peel stress at point B is now limited by the peak traction T_c in the TS bilinear relation. With continued loading, the contact opening at point B reaches the ultimate value δ_f the peel stress vanishes and the plate is debonded there from the elastomer. The further increase in δ_A results in the propagation of this debond with a CZ at its front. This edge debonding, named type-1 for later reference, has been studied by a semi-analytical method using a CZM by Mukherjee et al. [43] who extended techniques of Dillard [38] and Ghatak et al. [22]. Their results reveal that the CZ size increases with an increase in the quantity α/ϕ . For small values of α/ϕ , the CZ size becomes vanishingly small and the edge debonding process can be analyzed by the LEFM approach, e.g., see Ghatak et al. [22].

In Figure 3-9, 10 and 11 we have plotted for $\phi = 4, 5$, and 50, respectively, computed evolutions of the interfacial peel stress and the damage variable for a very high level of confinement, $\alpha = 100$. Results shown in Figure 3-9 reveal that the damage initiation and the

¹⁷ The FE height had to be adjusted as the interlayer thickness was modified to vary confinement and adhesion parameters; however, at least 10 elements were placed through the thickness of the interlayer. Rectangular elements had aspect ratio less than 4:1.

¹⁸ The distribution of D (CSDMG in ABAQUS terminology) is plotted in Figs. 8-11 in order to exhibit the damaged/debonded region. Recalling that $D = (1 - \delta_c / \delta_f)^{-1} (1 - \delta_c / \delta)$, $\delta \geq \delta_c$, we obtain $D=0$ over the bonded region, $D=1$ over the debonded region and $0 < D < 1$ over the CZ. However, $D \sim 1$ over the CZ on the scale used in these plots because of the following reason. Consider the example problem, $\alpha = 100$, $\phi = 4$, $\beta^{-1} = 1 \text{ mm}$, $\mu = 5 \text{ MPa}$, $T_c = 1.265 \text{ MPa}$, $K_e = 10^6 \text{ N/mm}^3$, for which we get $\delta_c = 1.6 \times 10^{-6} \text{ mm}$ and $\delta_f = 6.38 \times 10^{-3} \text{ mm}$. This yields $D > 0.95$ for $\delta > 20\delta_c$. This explains why D appears to be ~ 1 over almost the entire CZ(s). For clarity, we have inserted in Figs. 8-11 insets showing variations of D on magnified scales. Using smaller values of K_e while keeping other TS parameters constant gives better distributions of D over the CZ but may introduce artificial compliance into the system as stipulated by Song et al. [33].

¹⁹ It has been checked that the computed results are stable with respect to variations in the TS parameters. For example, for $\alpha = 100$, $\phi = 4$, $\beta^{-1} = 1 \text{ mm}$, $\mu = 5 \text{ MPa}$, $T_c = 1.265 \text{ MPa}$, $K_e = 10^6 \text{ N/mm}^3$, and $\Delta_A = 0.7$, the maximum % changes in nodal values of the peel stress over the internal CZ were found to be 0.02% and 4.58% when $T_c = 1.266265 \text{ MPa}$ and $K_e = 10^8 \text{ N/mm}^3$ was used, respectively.

²⁰ Note that an infinitesimal displacement should cause a CZ to initiate at point B since linear elasticity theory implies a singular traction at point B. However, in an FE simulation using a CZM, the value of the applied displacement required to initiate a CZ at point B depends upon the FE mesh used.

concomitant CZ formation over a negligibly small region at the edge are accompanied by the damage initiating internally at a distance 0.85 (consistent with the result shown in Figure 3-7) from point B and spreading of a CZ due to the local peak peel stress there. As δ_A is increased further, the internal CZ coalesces with the edge CZ, and the resulting debond propagates with one CZ at its front. This qualitatively agrees with the experimental finding that debonds initiate internally and eventually coalesce with the edge debond and the resulting debond front propagates on continued loading [39]. However, our plane strain analysis implies long tunnel-like debond with no undulations in the out-of-plane direction. An FE analysis of 3D deformations by Mukherjee et al. [30] indicated that the internal debonding process became undulatory (wavy) when the softening stiffness of the TS relation (slope of line EF in Figure 3-3) was large enough in comparison with the modulus to thickness ratio of the elastomer layer. Recalling that the spacing (λ) between undulation peaks [9, 14, 44] is expected to be $\approx 3h$, the size of the CZ in a plane strain analysis must be $\gg 3h$ to capture the undulatory debonding phenomenon. Our numerical experiments reveal that the size of this CZ decreases with an increase in ϕ and a decrease in α . However, as ϕ is increased, if the CZ size is several times the interlayer thickness determined by the combined values of both α and ϕ , the peel stress begins to oscillate with amplitudes large enough to cause wavy debonding. An example of such wavy debonding is illustrated in Figure 3-10 for $\phi = 5$. Multiple debonds initiate over the CZ resulting in traction-free regions separated by portions of the damaged interface. The average spacing between these debonds is approximately $3h$, which agrees with the results of the interfacial instability [9, 14, 44]. A comparison of our computed results for $\phi = 4$ and $\phi = 5$ suggests that the threshold $\phi(\phi_c)$ likely occurs in the range (4, 5). This agrees with $\phi_c \approx 4.15$ found [30] for debonding of an infinitely confined elastomer interlayer from a rigid block pulled outwards; however, we have not conducted sufficient number of simulations to extract the precise value of ϕ_c . The internal debonding process without wavy debonding is named type-2 and that with the softening-induced undulations is named type-3. Note that if ϕ is very large, the CZ formed at the internal peak location does not spread; instead debonding occurs and the local peel stress vanishes as illustrated in Figure 3-11. The redistributed peel stress exhibits a peak at a shear-lag distance from this debond. Continued loading causes nucleation of a second internal debond which, in turn, leads to a third internal debond. This debonding mechanism is named type-4. The average spacing between the type-4 debonds is greater than $3h$. However, the

spacing converges to $4.6h$ as ϕ is increased, as evident from the plots of Figure 3-12. It is worth mentioning here that the sensitivity of the debonding evolution to the FE mesh increases with an increase in the value of ϕ [30]. However, findings regarding the mechanisms of damage/debonding remain unaffected.

Presently computed predictions of the afore-mentioned four types of damage growth/debonding mechanisms are plotted in the $\alpha\phi$ – plane in Figure 3-13. These results suggest that there is a threshold confinement, α_c , above which the peak peel stress at an interior point begins to initiate and spread damage internally. This can be explained as follows. The reduction in the load carrying capacity due to damage at the location of the internal peak begins to outweigh that due to the edge peel stress when the confinement is sufficiently large. We note that even though the peel stress has a local peak at an interior point for confinements greater than 4, the threshold confinement level, α_c , beyond which a CZ forms internally lies between 8 and 9. For the edge initiated debonding mechanism that occurs for $\alpha < \alpha_c$, the interfacial instability is not found to occur. Results from a semi-analytical model for such debonding [43] show that the CZ size, d , normalized by the characteristic wavelength of undulation ($\lambda \sim 3h$), scales as $(d/\lambda) \sim (\alpha/\sqrt{\phi})$, and at $\alpha = \alpha_c$ and $\phi = \phi_c$, $d/\lambda < 1$. An increase in the confinement changes the debonding initiation mechanism and an increase in ϕ reduces the size of the CZ that is too small to accommodate undulations that may ensue due to the softening induced instability. This qualitatively agrees with the experimental finding of Ghatak and Chaudhury [10] in that the confinement must exceed approximately 18 for the appearance of a fingerlike convoluted crack front. The underestimation by our analysis may be due to errors introduced by the assumption of plane strain deformations, and the lack of knowledge of contact conditions between the glass cover plates and the PDMS layer used in the experiments.

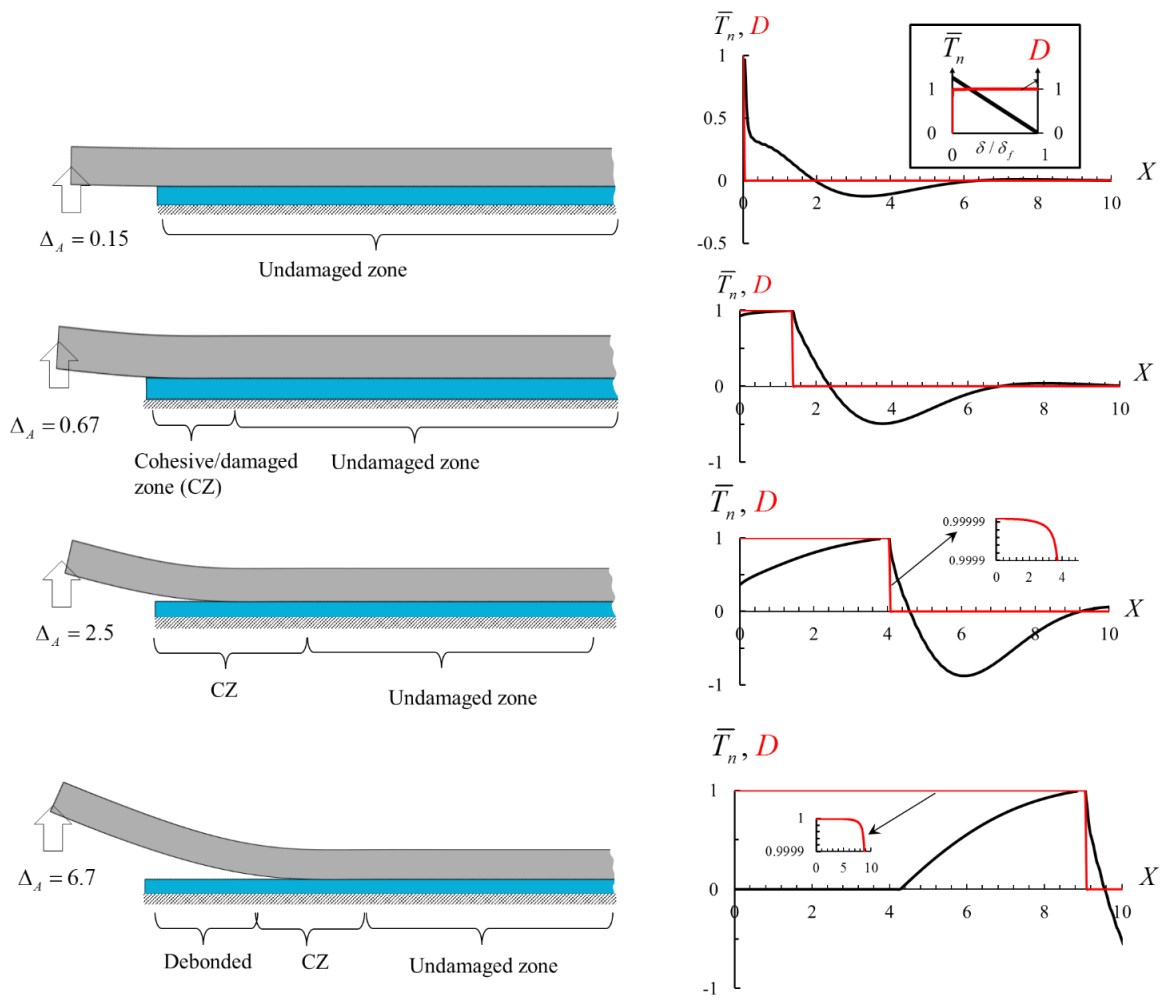


Figure 3-8: For $\alpha = 3, \phi = 0.1$, distributions of the non-dimensional normal traction ($\bar{T}_n = T_n / T_c$) and the damage variable (D) at the interface as a function of the non-dimensional distance (X) measured from point B at increasing values of the non-dimensional applied displacement (Δ_A). The deformed configurations, shown on the left, have been exaggerated by a factor of 5. This is an example of the type-1 debonding mechanism shown in Figure 3-13. The inset included in the top figure illustrates the TS relation used and the variation of D as a function of $\delta(>\delta_c)$ normalized by δ_f . The insets included in the third and the fourth figures illustrate the variation of D on magnified scales.

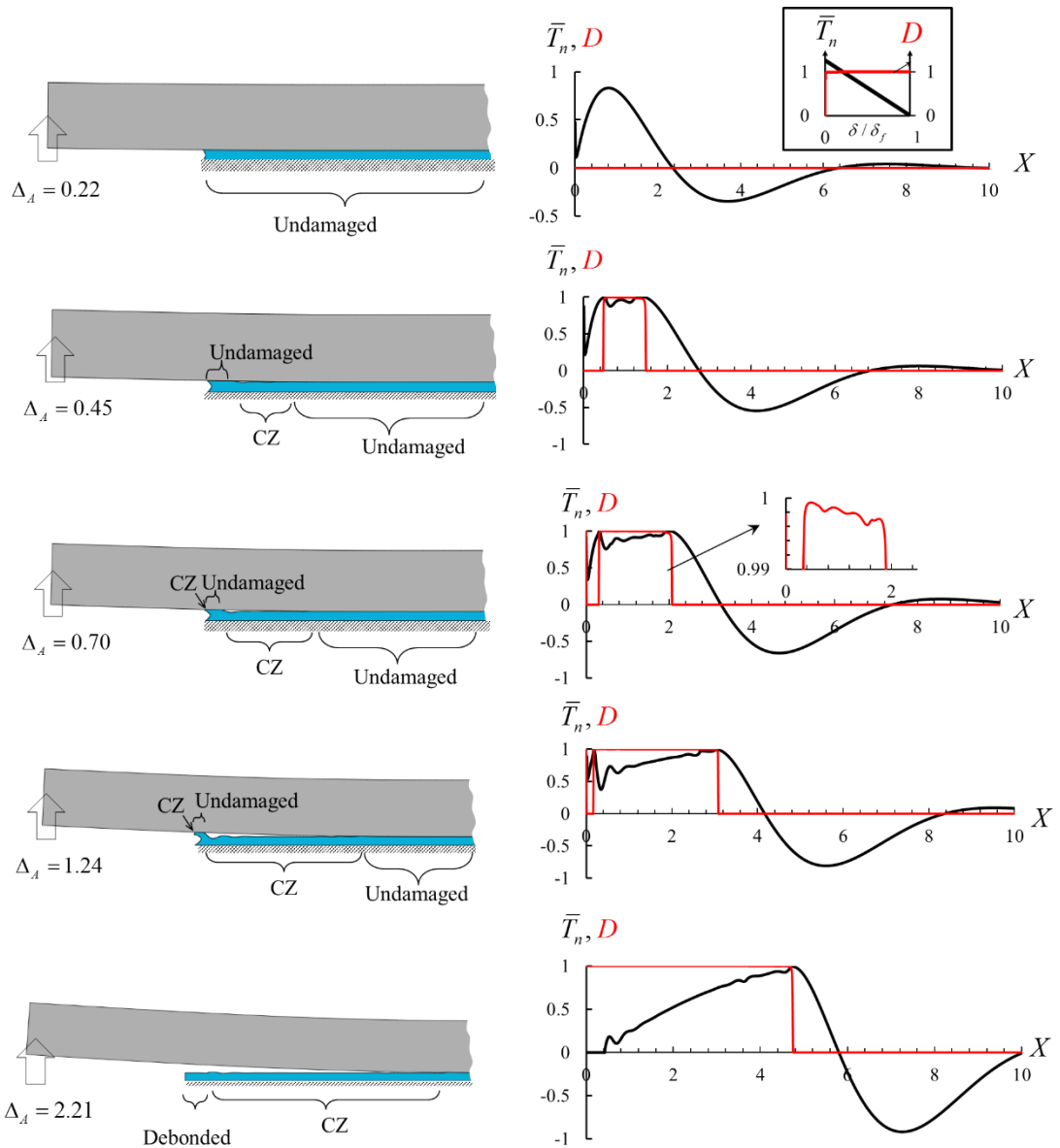


Figure 3-9: For $\alpha = 100, \phi = 4$, distributions of the non-dimensional normal traction (\bar{T}_n) and the damage variable (D) at the interface as a function of the non-dimensional distance (X) measured from point B at increasing values of the non-dimensional applied displacement (Δ_A). The deformed configurations, shown on the left, have been exaggerated by a factor of 25. This is an example of the type-2 debonding mechanism exhibited in Figure 3-13. The inset included in the top figure illustrates the TS relation used and the variation of D as a function of $\delta (> \delta_c)$ normalized by δ_f . The inset included in the third figure illustrates the variation of D on a scale from 0.99 to 1.

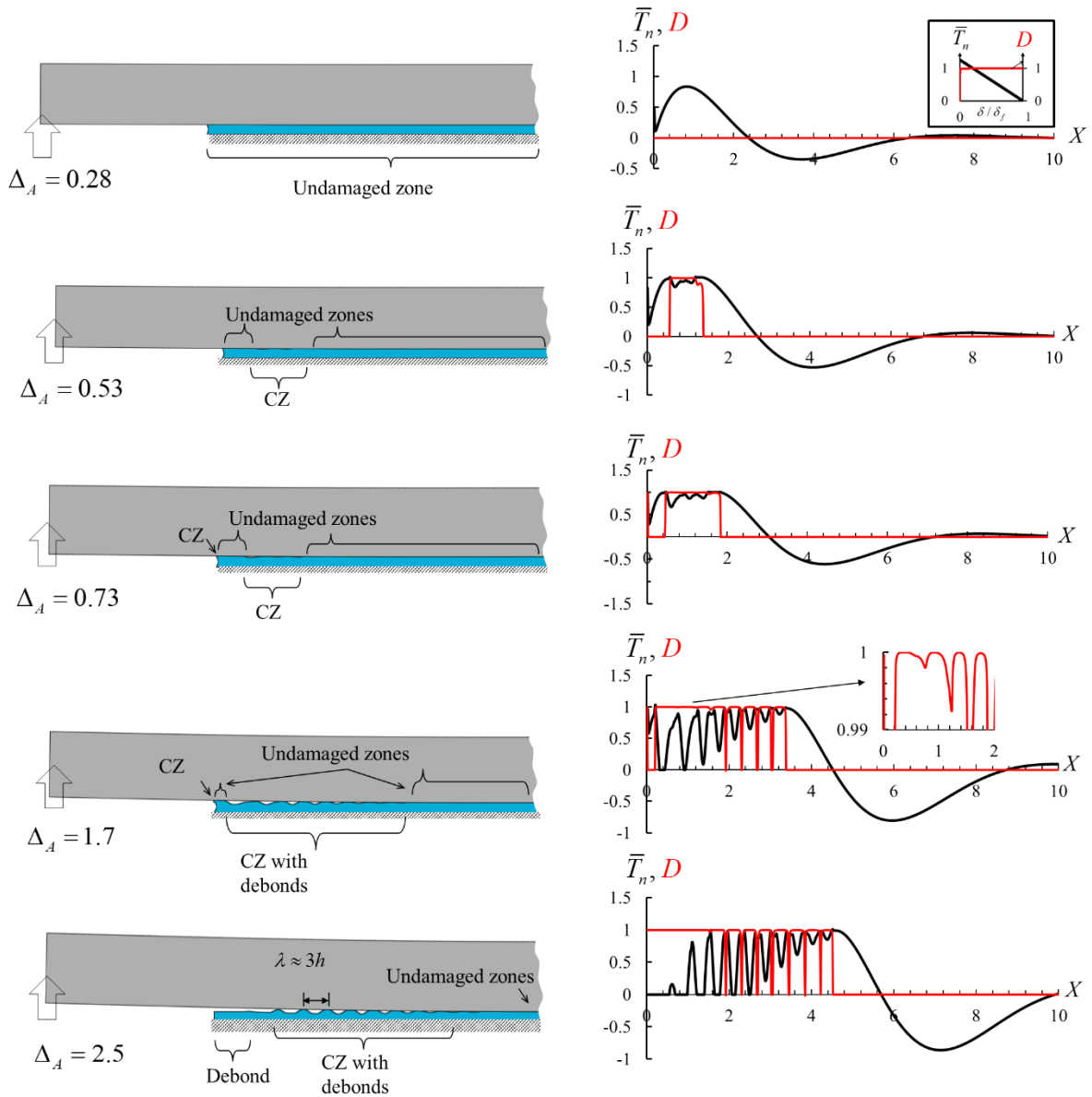


Figure 3-10: For $\alpha = 100, \phi = 5$, distributions of the non-dimensional normal traction (\bar{T}_n) and the damage variable (D) at the interface as a function of the non-dimensional distance (X) measured from point B at increasing values of the non-dimensional applied displacement (Δ_A). The deformed configurations, shown on the left, have been exaggerated by a factor of 25. This is an example of the type-3 debonding mechanism displayed in Figure 3-13. The inset included in the top figure illustrates the TS relation used and the variation of D as a function of δ / δ_c normalized by δ_f . The inset included in the third figure illustrates the variation of D on a scale from 0.99 to 1.

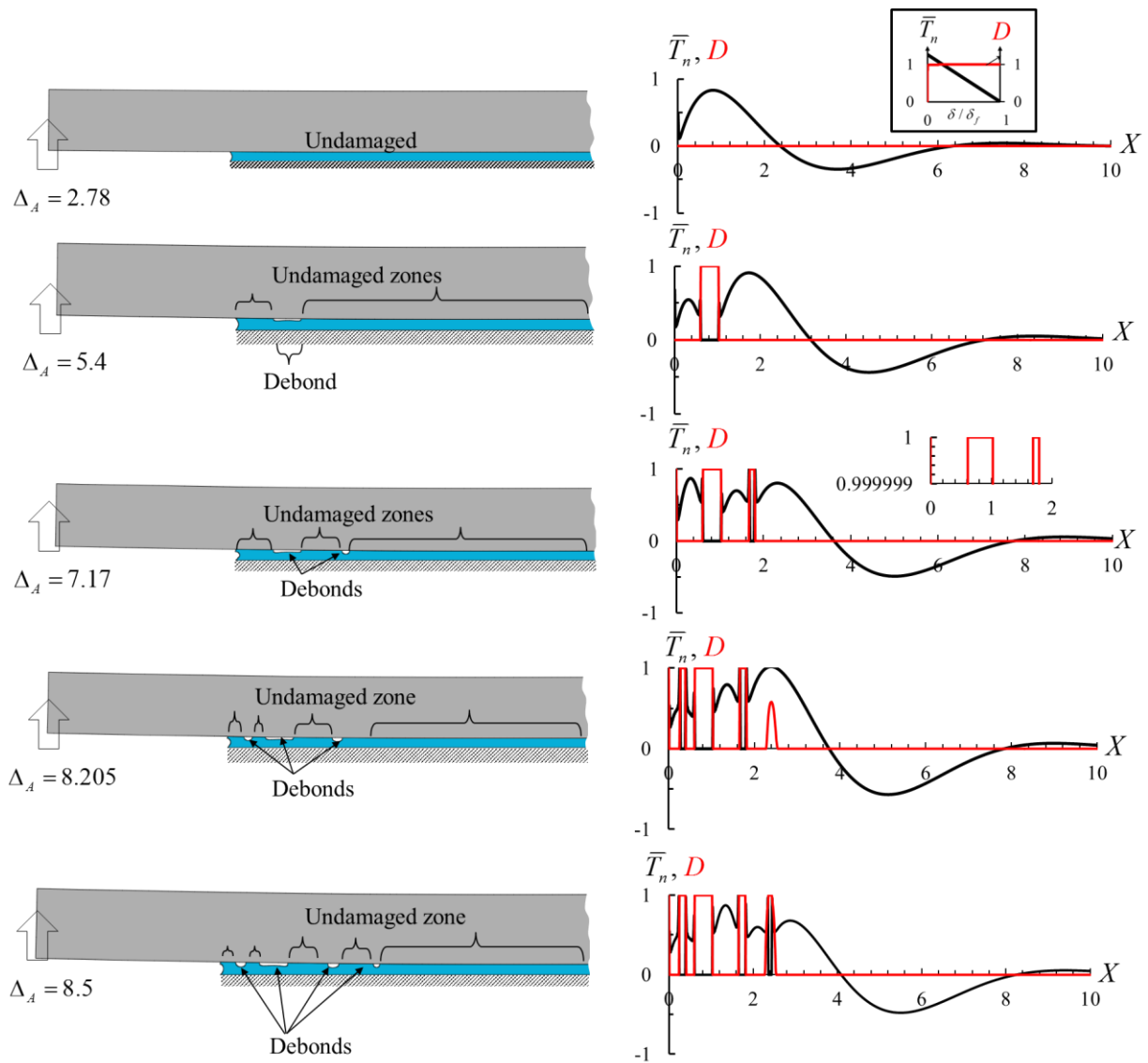


Figure 3-11: For $\alpha = 100, \phi = 50$, distributions of the non-dimensional normal traction (\bar{T}_n) and the damage variable (D) at the interface as a function of the non-dimensional distance (X) measured from point B at increasing values of the non-dimensional applied displacement (Δ_A). The deformed configurations, shown on the left, have been exaggerated by a factor of 25. This is an example of the type-4 debonding mechanism evinced in Figure 3-13. The inset included in the top figure illustrates the TS relation used and the variation of D as a function of $\delta (> \delta_c)$. The inset included in the third figure illustrates the variation of D on a scale from 0.999999 to 1.

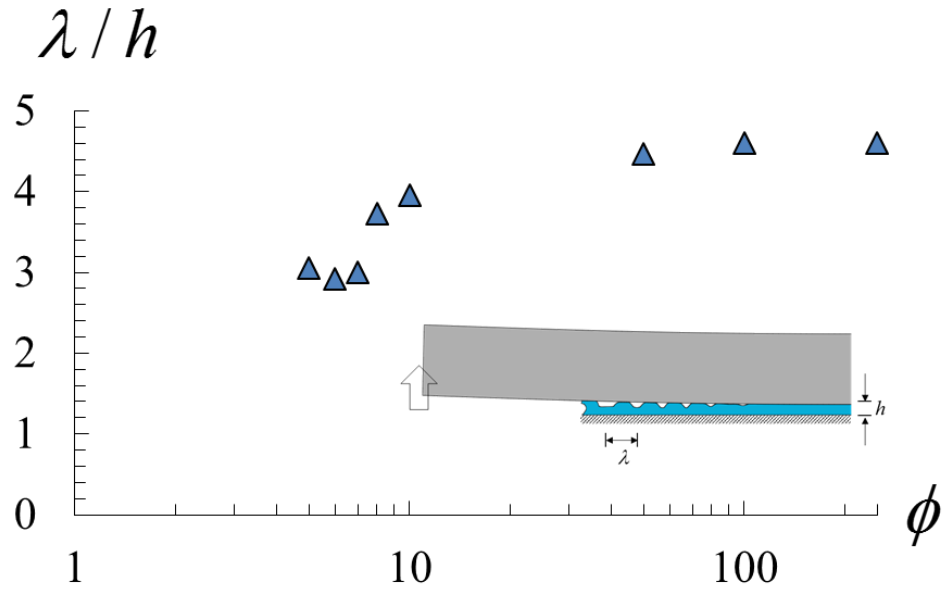


Figure 3-12: On a semi-log plot, computed average spacing between the internal debonds normalized by the interlayer thickness as a function of ϕ when $\alpha = 100$, $\beta^{-1} = 1 \text{ mm}$ and $a_0 = 2.83 \text{ mm}$.

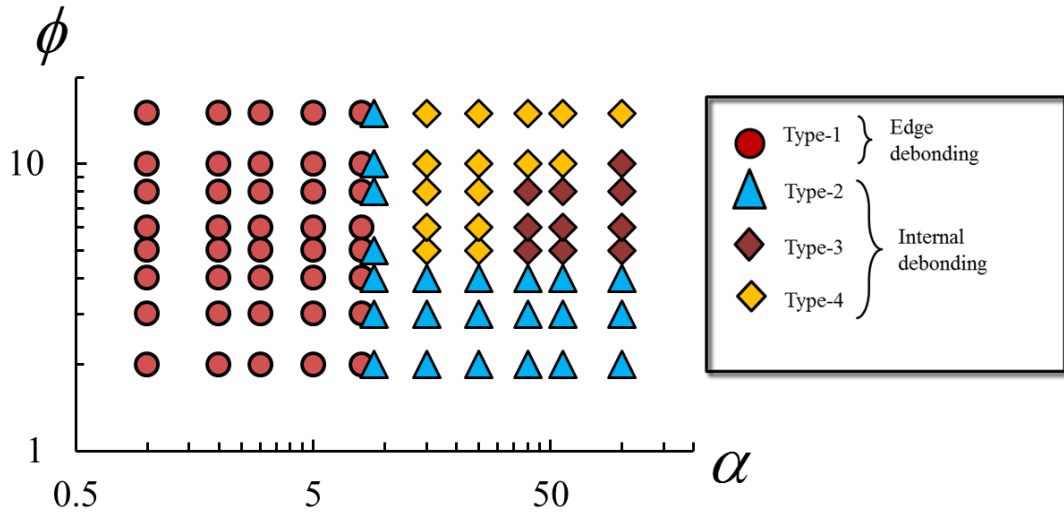


Figure 3-13: Computed mechanisms of damage growth/debonding in the $\alpha\phi$ - plane. Values of other parameters are: $a_0 = 2.83 \text{ mm}$, and $\beta^{-1} = 1 \text{ mm}$.

3.4.3.2 Load-displacement curves

In terms of our normalization, the load-displacement (LD) relation found using an LEFM approach by Ghatak et al. [22] is

$$\bar{P}_A = \frac{P_A}{D^p \beta^3 \delta_f} = \frac{6\Delta_A}{(6 + 2A + 9A^2 + 2A^3)}$$

where the non-dimensional length, A , of a propagating crack is found from the relation

$$\frac{(6+12A+9A^2+2A^3)^3}{(12+46A+72A^2+56A^3+21A^4+3A^5)} = 6.853\Delta_A^2 \frac{\phi}{\alpha}, \text{ and } P_A \text{ is the reaction force at A. In}$$

Figure 3-14 we have plotted the computed \bar{P}_A vs. Δ_A from this relation as well as from our FE analysis of the debonding problem for $\phi=1,3,25,$ and 60 , $\phi/\alpha=1$, and $A_0=2.83$. With increasing values of applied Δ_A , \bar{P}_A increases up to a peak value and then decreases. The nonlinearities, if any, in the initial ascending portions of these curves are attributed to the formation of the CZ near point B. For type-I (edge initiation) debonding ($\phi=1,$ and 3), the descending portions of the LD curves are smooth. Computed \bar{P}_A at a given Δ_A for an edge-initiated debonding is significantly greater (peak load is greater by 45%) than that predicted the LEFM approach because of the consideration of the damage at the interface but the presently computed peak loads for $\phi=1$ and 3 differ, respectively, by less than 3.9% and 0.1% from those found using a semi-analytical method coupled with a CZM and the FEM (Mukherjee et al. [43]). The other two computed LD curves plotted in Figure 3-14 correspond to type-4 internal debonding (curves with similar features are obtained for type-2 and type-3 internal debonding). These LD histories exhibit a saw-tooth behavior which becomes more pronounced with an increase in ϕ . The LD plots for $\alpha=100$ and $\phi=250, 500,$ and 1000 , and the corresponding deformed shapes are exhibited in Figure 3-15a. These results reveal that values of δ_A corresponding to local drops in the saw-tooth behavior correlate well with those for the nucleation of internal debonds. The subsequent increase of the load with the increase in δ_A until the nucleation of the next debond is due to the retardation of the internal debond(s) in the presence of the adjacent debond. This is reminiscent of the experimental observations of [39, 45] during the peeling of a flexible plate from an elastomer layer containing incisions. They observed trapping of nucleated debonds near the incisions. Our results suggest that higher values of ϕ at a given level of confinement correspond to slower propagation of debonding as evidenced by plots in Figure 3-15b of the non-dimensional X coordinate of the debond tip(s) as a function of Δ_A for $\phi=250$ and 1000 . The approximate growth rate of the 1st internal debond between its nucleation (p) and coalescence (q) with the 2nd internal debond is estimated as $(X_q - X_p)/((\Delta_A)_q - (\Delta_A)_p) = 0.0016$ for $\phi=1000$. For $\phi=250$, the corresponding growth rate from p' to q' equals approximately 0.0045. The

increase in resistance to debond growth with increasing ϕ agrees with the saw-tooth behavior becoming more pronounced with an increase in ϕ . The growth of one debond in the presence of another adjacent internal debond controlled by the parameter ϕ has also been reported by Hill et al. [41] in their investigation of the growth of a wedge-driven external crack in the presence of an internal void behind the crack tip.

In order to probe the scaling of the maximum reaction force (pull off force), numerous numerical simulations have been conducted by varying α and ϕ . The non-dimensional maximum pull-off force, \bar{P}_A^{\max} , is plotted in Figure 3-16 as a function of ϕ/α . For small values of ϕ/α all data collapse on the same line for types 1 through 3 debonding and agree well with predictions of a semi-analytical model of [43] for type-1 debonding. The least squares fit to the data for $\phi/\alpha < \sim 2$ reveals that for types 1, 2 and 3 debonding, $\bar{P}_A^{\max} \propto (\phi/\alpha)^{0.8}$ and the constant of proportionality depends on the non-dimensional initial overhang length, A_0 . For larger values of ϕ/α ($> \sim 2$), it is found that data for the edge-initiated debonding (type 1) satisfy the following relation derived by Ghatak et al. [22] using the LEFM approach.

$$\bar{P}_A^{\max} \approx \left(0.66 \sqrt{\frac{6 + 12A_0 + 9A_0^2 + 2A_0^3}{12 + 46A_0 + 72A_0^2 + 56A_0^3 + 21A_0^4 + 3A_0^5}} \right) \sqrt{\frac{\phi}{\alpha}}$$

Our computed results suggest that for type - 4 debonding the maximum pull-off force begins to increase linearly for $\phi/\alpha > \sim 2$, i.e., $\bar{P}_A^{\max} \propto \phi/\alpha$, although the computed data points at different confinement levels suggest additional weak dependence on α . We have summarized in Table 1 the collective role of the confinement and the interfacial adhesion on the non-dimensional pull-off force. For ease of interpretation, the dependence of the dimensional force on the plate flexural rigidity, the interlayer thickness, the interlayer modulus, the peak traction (T_c) and the fracture energy (G_c) is also included. These results suggest that the pull-off force depends on T_c more strongly than on other parameters for small values of the adhesion parameter. For small values of the confinement and large values of the adhesion parameter, the results can be described by the LEFM - based analysis; the pull-off force then strongly depends on the geometric and material parameters, and on G_c but does not depend on the peak traction. For large value of the confinement and large values of the adhesion parameter, the pull off force scales with the T_c , shows weak dependence on the

plate rigidity, and depends on the thickness and the modulus of the interlayer in a way opposite to that for less confined interlayers and exhibits no dependence on the fracture energy. These dependencies can potentially be used to find values of the TS parameters from the pull-off force data obtained in suitably designed experiments.

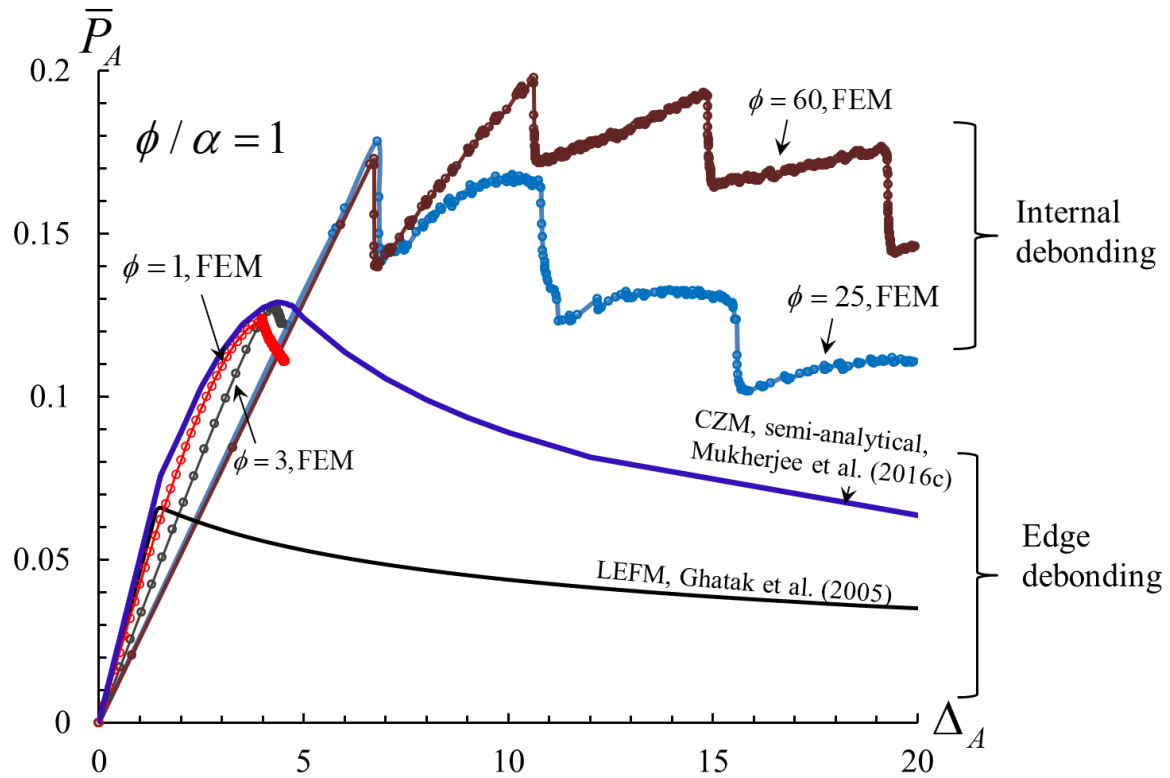


Figure 3-14: Non-dimensional load vs. non-dimensional displacement for $\phi / \alpha = 1$. Values of other parameters are: $a_0 = 2.83 \text{ mm}$, and $\beta^{-1} = 1 \text{ mm}$.

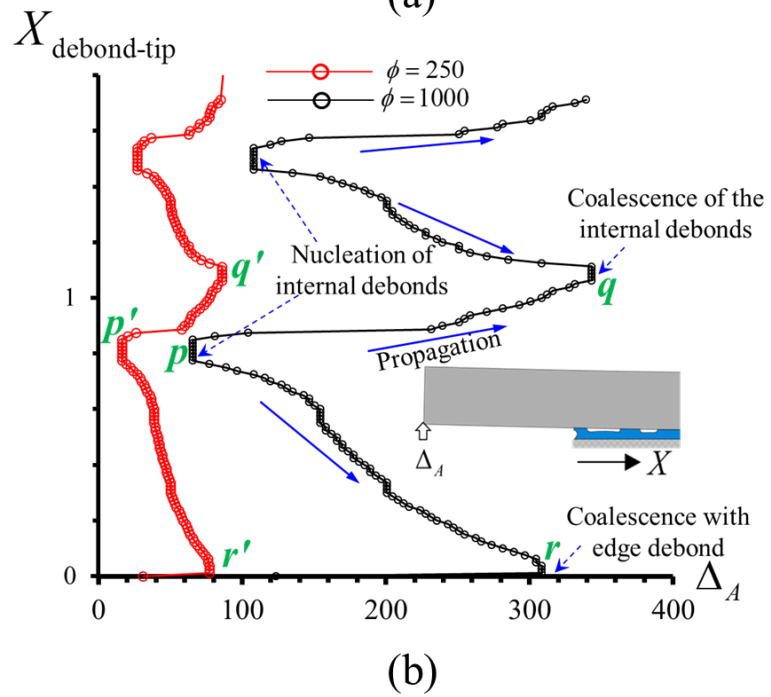
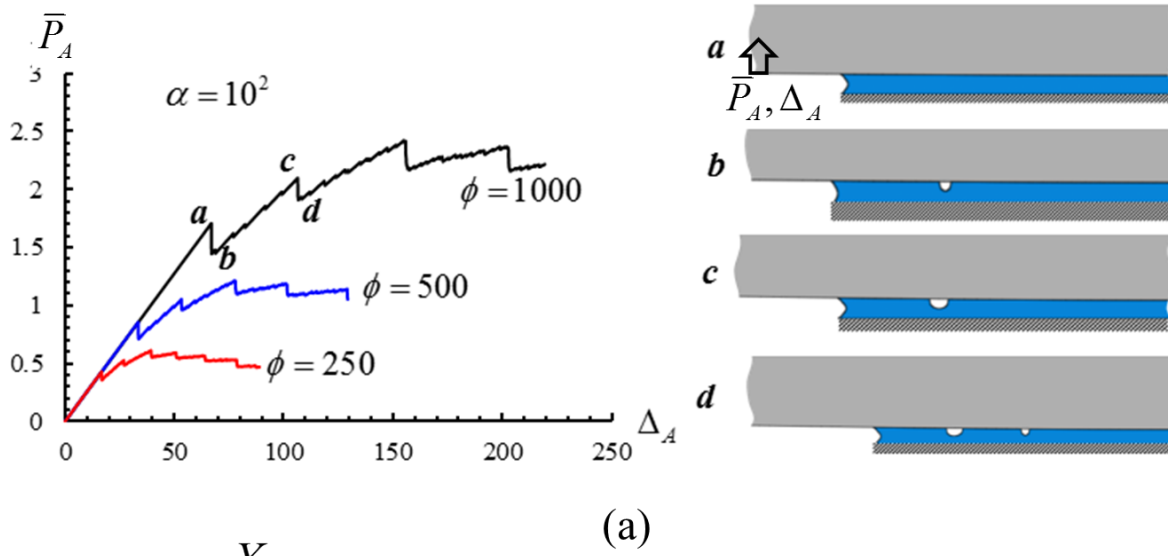


Figure 3-15: (a) Non-dimensional load versus non-dimensional tip-displacement plots for $\alpha = 100$ and three values of ϕ . Deformed shapes (exaggerated by a factor of 20) corresponding to points **a, b, c** and **d** are included in the right figure. Values of other parameters are: $a_0 = 2.83 \text{ mm}$, and $\beta^{-1} = 1 \text{ mm}$; (b) Plots of X-coordinate of the debond tip as a function of the applied non-dimensional tip-displacement for $\phi = 250$, and 1000.

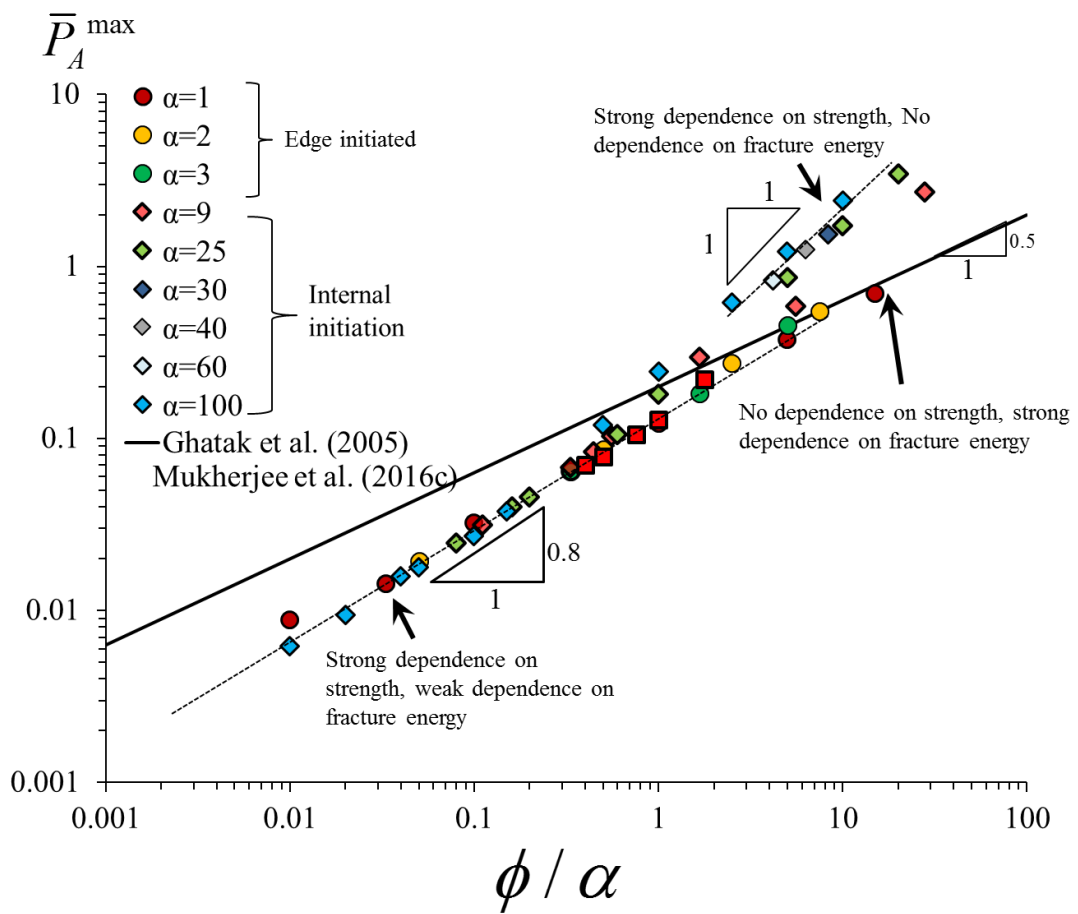


Figure 3-16: Dependence of the non-dimensional pull-off force on the non-dimensional number ϕ / α

Table 3-1: Effect of confinement and adhesion on the pull-off force

Confinement, α	Adhesion, ϕ	Classification of damage/debonding initiation	The non-dimensional pull off force, \bar{P} , is proportional to	The dimensional pull off force, P , is proportional to
Small [†]	Small	Type-1	$(\phi/\alpha)^{0.8}$	$D_p^{7/30} \mu^{-1/30} h^{1/10} G_c^{1/5} T_c^{3/5}$
Large	Small	Type-2,3		
Small	Large	Type-1	$(\phi/\alpha)^{0.5}$	$D_p^{1/3} \mu^{1/6} h^{1/2} G_c^{1/2}$
Large	Large	Type-4	ϕ/α	$D_p^{1/6} \mu^{-1/6} h^{1/2} T_c$

[†] Small confinement is defined as one for which $\alpha < 9$; edge debonding. Small adhesion is defined as one for which $\phi/\alpha < \sim 2$ approximately.

3.4.3.3 Limitations

Experimental findings [10, 39] and results of simulations of 3-D deformations [30, 46] suggest that the adhesion-induced instability triggers oscillations in the out-of-plane (the y –) direction resulting in a fingerlike debonding front. However, the assumption of plane strain deformations, and hence no variation in the out-of-plane direction, forces the instability to develop in the x -direction. Instabilities in both the x - and the y -directions have been experimentally observed for very large values of the confinement ($\alpha = 67$) by Ghatak et al. [47]. A plane-strain assumption, in general, fails to predict details of pattern formation during the debonding process because the inhomogeneity in the out-of-plane traction distribution due to the presence of traction-free surfaces and anticlastic bending of the plate lead to (i) undulatory debonding in the y -direction and (ii) multiple debonds rather than a tunnel-like debond computed for plane-strain deformations. This is confirmed by comparing results of analyzing 3-D deformations with and without restraining the y -displacement of points on the lateral surfaces. Nevertheless, results presented here are useful for predicting the onset of different types of debonding in a semi-infinite geometry as a function of the confinement and the CZM parameters. Results for a few 3-D problems included in Appendix C support conclusions drawn from the analysis of plane strain deformations.

3.4.4 Debonding at both interfaces of the interlayer

Industrial fabrication of soft bio-implants such as ophthalmic lenses often involves the release of an elastomer interlayer sandwiched between two molds from a desired mold interface by mechanically prying open one of the molds [48]. A potential problem, when the interfaces have identical adhesion, is the occurrence of debonding at the undesirable interface and/or at both interfaces, resulting possibly in a bridge of the interlayer suspended between the two molds. This renders the interlayer susceptible to tearing failure. Computed results of some additional numerical experiments are presented that may help design potential strategies for engineering a desired release mechanism.

The configuration analyzed is similar to that depicted in Figure 3-4 except that the lower adherend is also made of an isotropic and homogeneous linear elastic material and the two adherends have the same overhang length of 2.83 mm^{21} . The edge of the upper flexible plate is monotonically displaced upwards and the three displacement components of points on the bottom surface of the lower plate are set equal to zero to simulate the fixed base as schematically shown in Figure 3-17a. As the upper plate is loaded, the asymmetry of materials, loading and boundary conditions on the two adherends causes a shearing bias at point B in Figure 17a that results in opening at the upper interface near point B due to peeling-shearing coupling. We recall that when the lower interface has infinite strength, the confinement has to exceed a threshold value for debonding to initiate at an interior point due to the peak stress there. Before damage initiation the computed distributions of the peel stress at the two interfaces reveal that the peel stresses are nearly identical at the two interfaces except at points close to the corners. Due to the opening bias at point B, it is speculated that a lower threshold confinement level is needed for the internal debonding to ensue at the lower interface than that at the upper interface. When the two interfaces have the same strength, the simulation results shown in Figure 17b-d indicate that there is a range of confinement values for which internal debonding initiates at the lower interface with the edge crack initiated at the upper interface. For $\alpha = 8$ the internal debond does not nucleate at the upper interface but nucleates and grows at the lower interface thereby causing an undesirable bridge of the interlayer suspended between the two adherends as shown in Figure 3-17b. One way to mitigate this is to reduce the level of confinement so that the peak peel stress at interior points is small. The simulation results for $\alpha = 2$ plotted in Figure 3-17c support this.

²¹ 4-node square elements of dimensions $0.1 \text{ mm} \times 0.1 \text{ mm}$ and $0.025 \text{ mm} \times 0.025 \text{ mm}$ have been used to discretize the molds (CPE4 elements) and the interlayer (CPE4H elements), respectively.

However, for sufficiently confined interlayers, such as that shown in Figure 3-17d for $\alpha = 10$, damage may occur at interior points on both interfaces at locations of peak stresses. Continued loading causes the lower interface CZ to become shielded [49] by the growth of the CZ on the upper interface. These observations suggest that an improper level of confinement may result in an erratic debonding process. In practical situations, however, the choice of tailoring the confinement by tuning the mold flexibilities may be limited. As was suggested by [50], thermal pre-conditioning can be used to bias debonding to a desired interface. For example, pre-cooling the assembly before mechanically pulling the upper mold for $\alpha = 8$ causes the internal debond to initiate and grow at the upper interface as can be seen from the results exhibited in Figure 3-18. Due to the mismatch in the coefficients of thermal expansion of the molds and the interlayer and the associated bending of the flexible upper mold, the peel stress is compressive near the upper interface corner point B and tensile at the lower interface corner point M. As a result of the opening bias at the lower interface corner, the edge debond initiates at M and the internal debonding nucleates and grows at the upper interface. These debonding characteristics remain unchanged upon refining the FE mesh. A detailed investigation of tailoring the confinement, the ratio of the elastic moduli of the two adherends, and the thermal pre-conditioning to cause preferential debonding will be reported elsewhere [51].

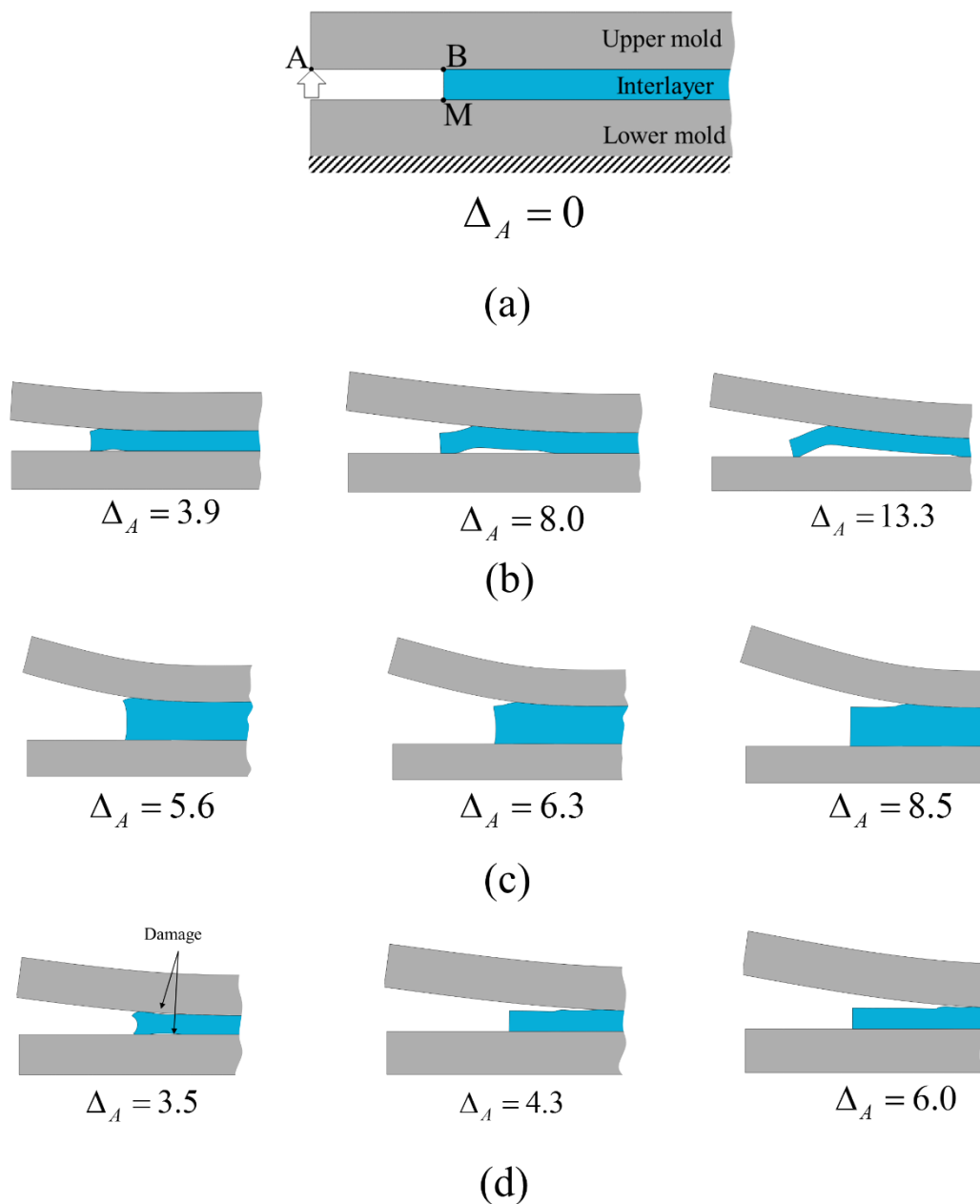


Figure 3-17: (a) The configuration analyzed ; snapshots (exaggerated by a factor of 100) of the interfacial debonding for (b) $\alpha = 8$, (c) $\alpha = 2$ and (d) $\alpha = 10$, and the same values of the TS parameters at both interfaces corresponding to $\phi = 4$ when vertical displacement is monotonically increased at point A. The total length of each plate in the numerical simulations is taken to be 50 mm. Values of other parameters are: $a_0 = 2.83 \text{ mm}$, and $\beta^{-1} = 1 \text{ mm}$.

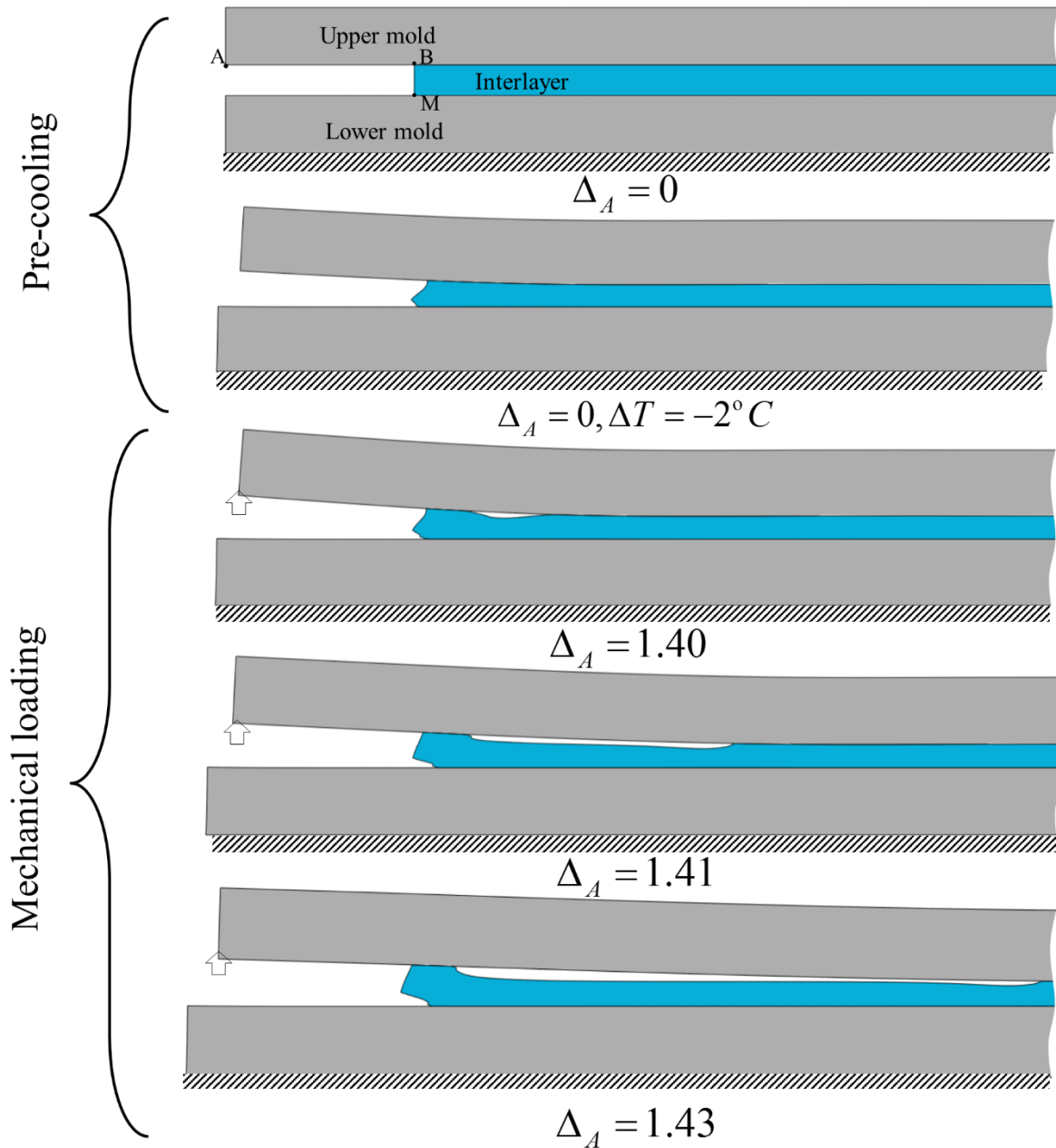


Figure 3-18: Snapshots of debond growth (exaggerated by a factor of 100) when the assembly is pre-cooled homothermally by $-2^{\circ}C$ followed by a vertical displacement applied at point A while the displacement components at the bottom surface of the lower mold equal zero. The coefficients of thermal expansion are assumed to be $7 \times 10^{-5} / ^{\circ}C$ and $6 \times 10^{-4} / ^{\circ}C$ for the two molds and the interlayer materials, respectively. The pre-cooling stage is simulated by inputting $\Delta T = -2^{\circ}C$ and no thermal effects are simulated for the mechanical loading stage. These results are for a confinement level of $\alpha = 8$ and equal values of TS parameters at both interfaces corresponding to $\phi = 4$. Values of other parameters are: $a_0 = 2.83 \text{ mm}$, $\mu = 5 \text{ MPa}$, and $\beta^{-1} = 1 \text{ mm}$. Both molds have identical values of material parameters.

3.5 Conclusions

We have studied interfacial debonding of a flexible plate from an elastomeric layer strongly bonded to a rigid substrate by using a cohesive zone model (CZM) and analyzing plane strain infinitesimal deformations of the linear elastic flexible plate and the elastomer layer by using the finite element commercial software, ABAQUS/Standard. The following two parameters have been found to govern the interfacial damage growth and debonding at the interface between the soft elastomer layer and the flexible plate.

- (i) Confinement parameter, $\alpha = (D_p / \mu h^3)^{1/3}$, relating the plate flexural rigidity, D_p , the shear modulus of the interlayer material, μ (= Young's modulus $E/3$), and its thickness, h . This parameter was also shown to be important by [8, 10, 15]
- (ii) CZM/adhesion parameter, $\phi = T_c^2 h / G_c E$, relating the peak traction T_c for damage initiation at an interface point and the fracture energy G_c in the CZM traction-separation (TS) relation. Mukherjee et al. [30] have elucidated the importance of this parameter for wavy interfacial debonding of a rigid adherend from an elastomer interlayer when the adherend is pulled outward.

Results of numerical simulations have been plotted on the $\alpha\phi$ - plane to identify values of α and ϕ for four different interfacial debonding types. For confinement levels less than a threshold value (~ 9), damage at the interface between the interlayer and the deformable plate initiates at the edge, forms a cohesive zone (CZ), and leads to debonding which propagates with a CZ at its front. When confinement exceeds the threshold value, the damage in addition to occurring at the edge initiates at an internal interface point located at dimensionless distance $\beta^{-1} \sim (\mu / D_p h^3)^{-1/6}$ from the edge, which is proportional to the characteristic stress decay distance (one can also think of this as a shear-lag distance). For such interlayers a wavy debonding occurs when the adhesion parameter exceeds a critical value. However, for large values of ϕ dictated by the confinement two adjacent nucleated debonds are separated by a perfectly bonded region rather than by a portion of the damaged interface. The spacing, λ , between the internal debonds scales with the interlayer thickness.

The non-dimensional pull-off force is found to increase with the quantity ϕ / α and depend on the debonding type.

For an elastomeric layer sandwiched between a flexible adherend and a rigid substrate with the two interfaces having identical TS relations, it was found that for confinement not in the appropriate range separation can occur at both interfaces resulting in an erratic release process and leading to bridging which can result in undesirable tearing of the interlayer.

Acknowledgments

The authors thank the department of Biomedical Engineering and Mechanics at Virginia Tech for the use of its facilities and the Macromolecules and Interfaces Institute, Virginia Tech, for fostering interdisciplinary research in the adhesion area.

Appendix D

Included here are the sensitivities of the interfacial normal traction and the load-displacement plots to four FE meshes listed in Table D 1. In Figure D 1a, we have plotted the distribution of the peel stress at the interface which is yet to damage. It is clear that the peel stress distribution is insensitive to the FE mesh used except for the discretization close to point B. However, the interfacial damage type is unaltered as evinced by the plot of the contact opening shown in Figure D 1b. Figure D 1-Figure D 4 show distributions of the non-dimensional peel stress upon damage initiation at the interface (a) and the non-dimensional load-displacement variations (b) for the debonding types 2, 3 and 4, respectively. As was reported in Mukherjee et al. [30], one can observe that the results are more sensitive to the changes in the FE mesh for a large ϕ value as compared to that for small ϕ . Nonetheless, our conclusions about the type of debonding and the scaling of the pull-off force remain unaffected on refining further the FE mesh 2.

Table D 1: The FE meshes used [†]

FE meshes	Dimensions in <i>mm</i> of an element of the interlayer	Dimensions in <i>mm</i> of an element of the plate
Mesh-1	0.025×0.025	0.1×0.1
Mesh-2	0.0125×0.0125	0.1×0.1
Mesh-3	Height: 0.0125, width: graded from 0.05 at the farthest end to 0.005 near point B.	0.1×0.1

[†] Results reported in this paper were obtained with FE mesh-2

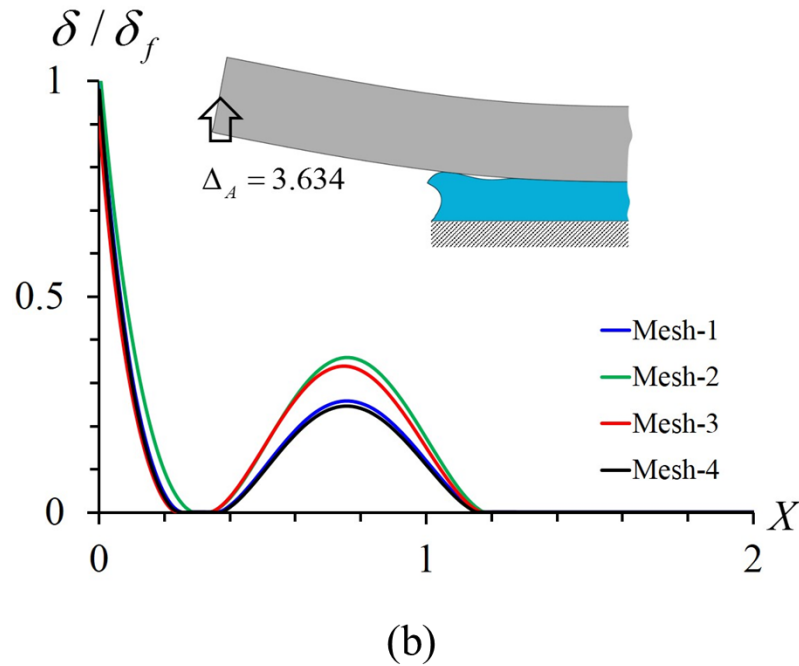
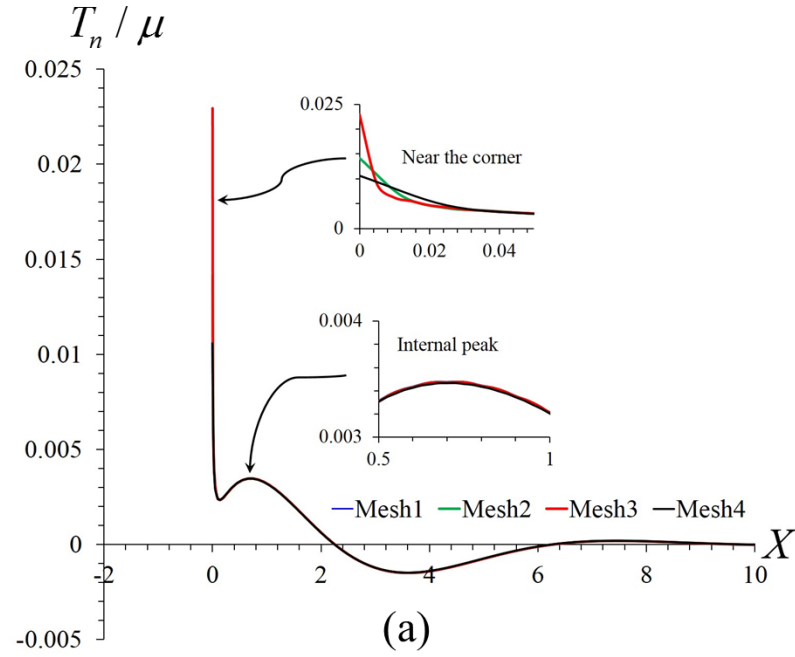


Figure D 1: For $\alpha = 8, \beta^{-1} = 1mm, a_0 = 2.83mm$, sensitivity to the FE mesh of (a) distribution of the peel stress at the interface (yet to damage) when $\delta_A = 1\mu m$, and (b) distribution of the contact opening when $\phi = 4, \Delta_A = 3.634$.

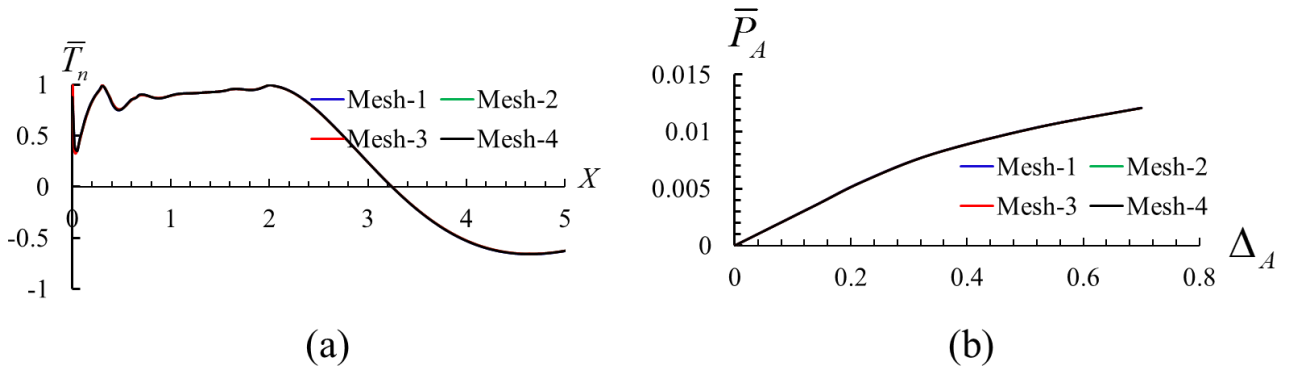


Figure D 2: For $\alpha = 100, \phi = 4, \beta^{-1} = 1mm$, sensitivity to the FE mesh of (a) the non-dimensional peel stress distribution for $\Delta_A = 0.7$, and (b) the non-dimensional load-displacement variation until $\Delta_A = 0.7$. This represents a type-2 debonding as illustrated in Figure 3-9.

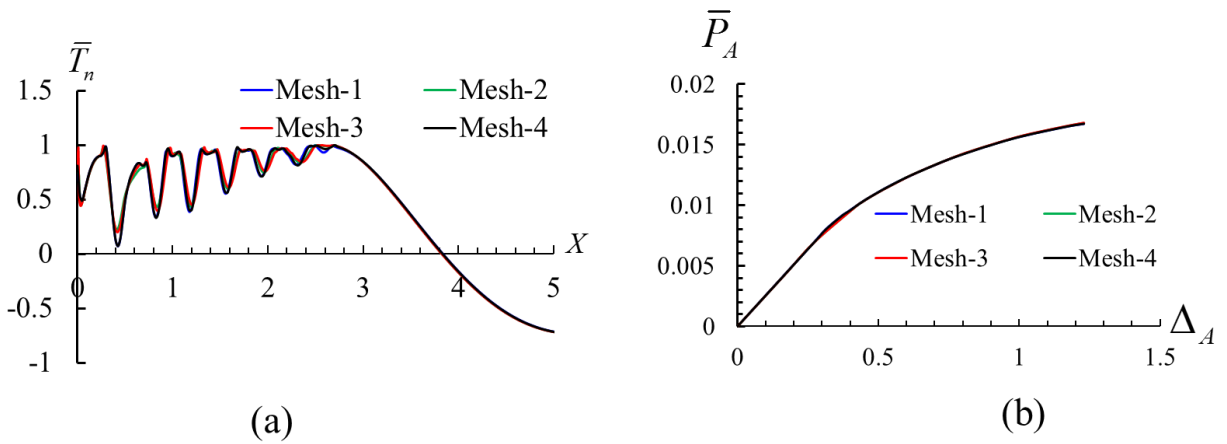


Figure D 3: For $\alpha = 100, \phi = 5, \beta^{-1} = 1mm$, sensitivity to the FE mesh of (a) the non-dimensional peel stress distribution for $\Delta_A = 1.2$, and (b) the non-dimensional load-displacement variation until $\Delta_A = 1.2$. This represents type-3 debonding as illustrated in Figure 3-10.

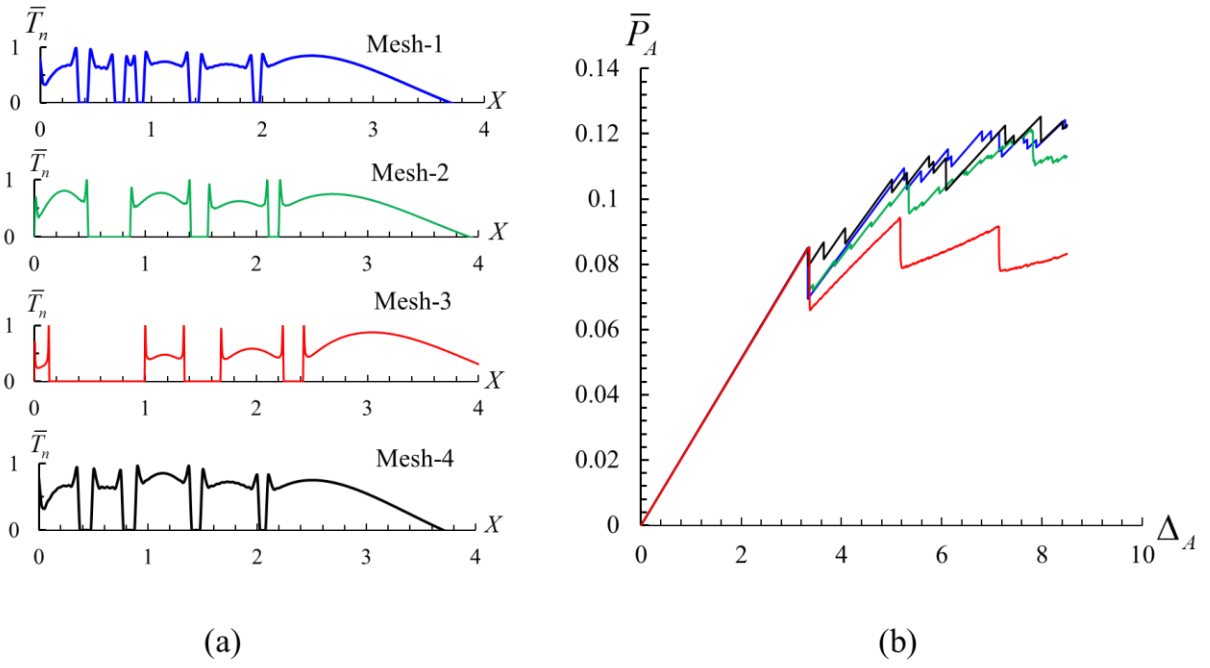


Figure D 4: For $\alpha = 100, \phi = 50, \beta^{-1} = 1mm$, sensitivity to the FE mesh of (a) the non-dimensional peel stress distribution for $\Delta_A = 0.85$, and (b) the non-dimensional load-displacement variation until $\Delta_A = 0.85$. This represents a type-4 debonding as illustrated in Figure 3-11.

Appendix E

The work done by the external force should equal the sum of the increase in the strain energy of the system, the energy lost due to interfacial damage/debonding, and the energy loss due to the damage stabilization (viscous regularization) option used in ABAQUS. For one of the problems studied, the evolutions of these energies are plotted in Figure E 1. It is clear that the energy balance is satisfied with the maximum error of 7.3%.

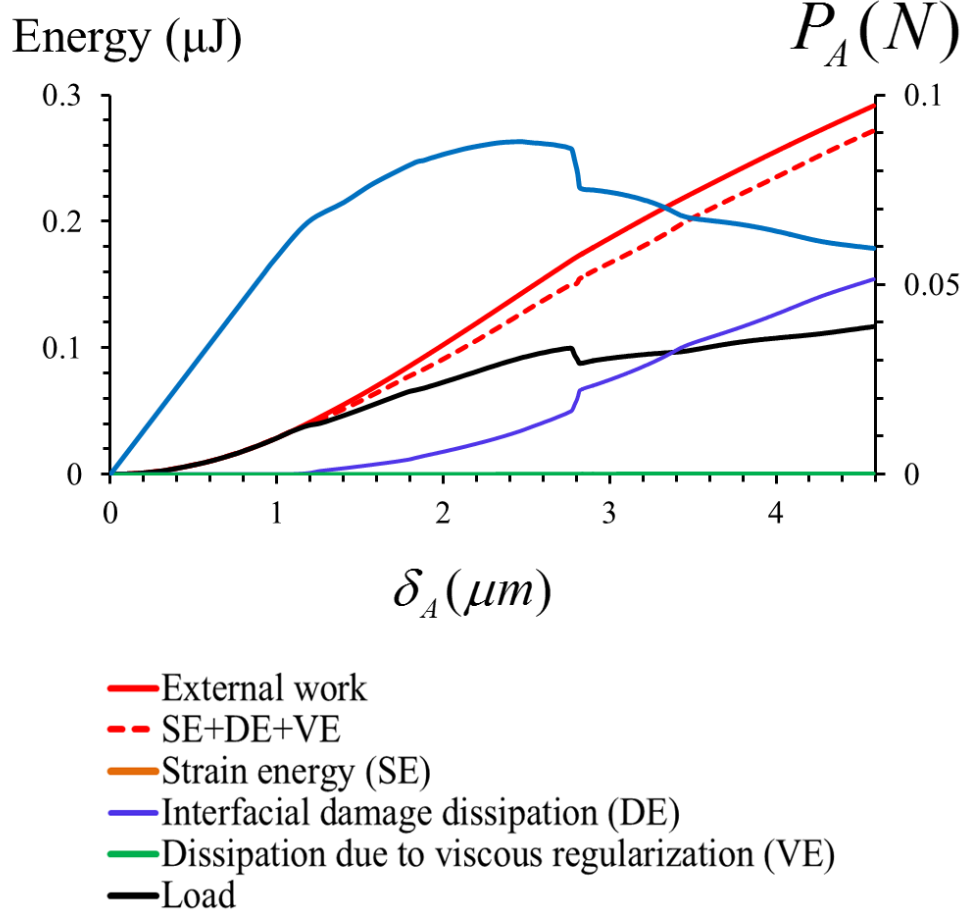


Figure E 1: Computed energy histories for mesh-1, and $\alpha = 25, \phi = 4, \beta^{-1} = 1mm, \mu = 5MPa, T_c = 0.04MPa$, and $a_0 = 2.83mm$. The out-of-plane dimension (width) is taken to be $1mm$ when computing the total energy. As discussed in Section 3.4, the dip in the load-displacement plot corresponds to the initiation of internal debonding.

The energy dissipated due to damage dissipation for $\delta_A = 4.59\mu m$ agreed well (8% difference) with that found from the equation, $DE = G_c a + \int_{l_{CZ}} \left(G_c - \frac{T_c^2}{4G_c} \left(\frac{2G_c}{T_c} - \delta(x) \right)^2 \right) dx$.

Here the integrand represents, for $K_e \gg 1$, the area under the portion of the TS curve traced by a point in the CZ up to the contact opening of $\delta(>\delta_c \text{ and } <\delta_f)$ and the integral is

computed using the Trapezoidal rule, a is the total length of the interfacial debond, l_{CZ} the total length of the CZ, and $\delta(x)$ the contact opening at a point in the CZ.

Appendix F

Three-dimensional (3-D) deformations have been studied for four cases to check if predictions of the debonding types on the $\alpha\phi$ - plane from analysis of plane strain deformations agree with those from the analysis of 3-D deformations. The out-of-plane width (y-direction) and the length (x-direction) of the assembly are assumed to be 5 mm and 12.83 mm, respectively, and the thickness is chosen to get the desired degree of confinement. In ABAQUS terminology, the plate and the interlayer are discretized using C3D8R and C3D8H elements, respectively. Brick elements of dimensions $0.025\text{mm} \times 0.025\text{mm} \times 0.025\text{mm}$, and $(h/5)(\text{thickness}) \times l(\text{length}) \times 0.025\text{mm}(\text{width})$ are used to discretize the plate and the interlayer, respectively, where l is the element length reducing from 0.075 mm at the farthest end of the interlayer to 0.03 mm near the free edge. Results of the 3-D simulations are depicted in Figure F 1. For $\alpha = 25$, multiple internal openings appear (type-3) along the y-direction for $\phi = 5$ whereas only a tunnel-like opening (type-2) occurs for $\phi = 4$. For $\alpha = 2$, debonding initiates from the edge and undulations are not found to occur for both values of ϕ (type-1). These simulations support the conclusions drawn from the analysis of plane strain deformations in the xz -plane. The above simulations of 3D deformations were conducted by setting to zero the y-displacements of nodes on the lateral surfaces of the elastomer layer but not those of the plate. The bottom right figure exhibits a snapshot of the computed contact opening for $\alpha = 25$ and $\phi = 5$ when the lateral surfaces of the plate were also restrained in the y-direction. The deformation becomes equivalent to a plane-strain deformation on the xz -plane and accordingly, a tunnel-like debonding was predicted.

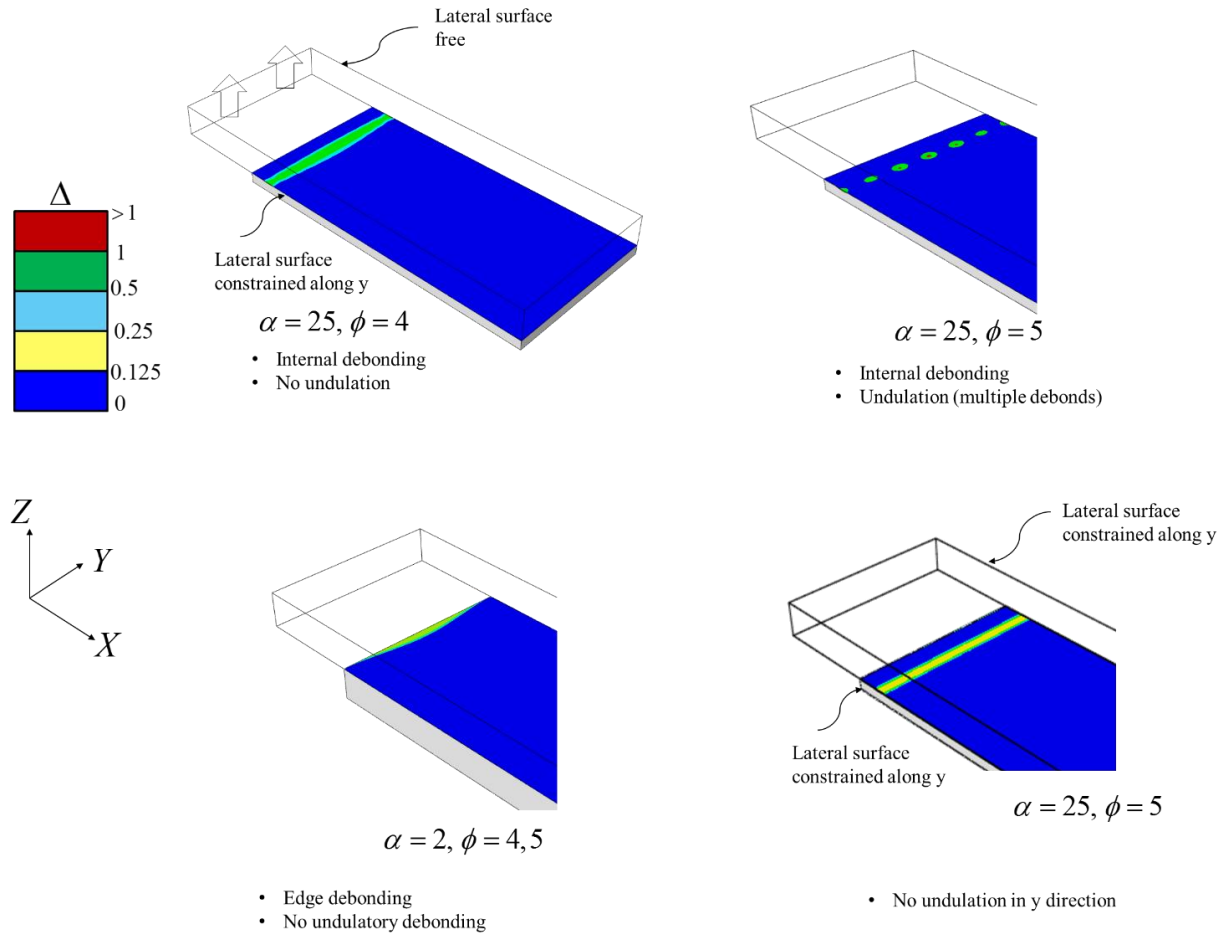


Figure F 1: Snapshots of interfacial dimensionless contact opening for $\phi = 4$, and 5 and confinement levels of $\alpha = 25$, and 2, when the lateral surfaces of the interlayer are prevented to deform in the y-direction but those of the plate are free. The bottom right figure corresponds to $\alpha = 25$ and $\phi = 5$ when the lateral surfaces of both the plate and the interlayer are restrained in the y-direction.

References

- [1] Messner, A., *Stress Distributions in Poker Chip Tensile Specimens*. Aerojet-General Technical Paper, 1963.
- [2] Crosby, A.J., K.R. Shull, H. Lakrout, and C. Creton, *Deformation and failure modes of adhesively bonded elastic layers*. Journal of Applied Physics, 2000. **88**(5): p. 2956-2966.
- [3] Lai, Y.-H., D. Dillard, and J. Thornton, *The effect of compressibility on the stress distributions in thin elastomeric blocks and annular bushings*. Journal of applied mechanics, 1992. **59**(4): p. 902-908.
- [4] Gent, A., *Compression of rubber blocks*. Rubber chemistry and technology, 1994. **67**(3): p. 549-558.
- [5] Webber, R.E., K.R. Shull, A. Roos, and C. Creton, *Effects of geometric confinement on the adhesive debonding of soft elastic solids*. Physical Review E, 2003. **68**(2): p. 021805.

- [6] Anderson, G., K. DeVries, and M. Williams, *Mixed mode stress field effect in adhesive fracture*. International Journal of Fracture, 1974. **10**(4): p. 565-583.
- [7] Lefebvre, D.R., D.A. Dillard, and H. Brinson, *The development of a modified double-cantilever-beam specimen for measuring the fracture energy of rubber to metal bonds*. Experimental mechanics, 1988. **28**(1): p. 38-44.
- [8] Adda-Bedia, M. and L. Mahadevan, *Crack-front instability in a confined elastic film*. Proceedings of the Royal Society A: Mathematical, Physical and Engineering Science, 2006. **462**(2075): p. 3233-3251.
- [9] Ghatak, A., *Confinement-induced instability of thin elastic film*. Physical Review E, 2006. **73**(4): p. 041601.
- [10] Ghatak, A. and M.K. Chaudhury, *Adhesion-induced instability patterns in thin confined elastic film*. Langmuir, 2003. **19**(7): p. 2621-2631.
- [11] Creton, C. and H. Lakrout, *Micromechanics of flat-probe adhesion tests of soft viscoelastic polymer films*. Journal of Polymer Science Part B: Polymer Physics, 2000. **38**(7): p. 965-979.
- [12] Creton, C., J. Hooker, and K.R. Shull, *Bulk and interfacial contributions to the debonding mechanisms of soft adhesives: extension to large strains*. Langmuir, 2001. **17**(16): p. 4948-4954.
- [13] Yamaguchi, T., K. Koike, and M. Doi, *In situ observation of stereoscopic shapes of cavities in soft adhesives*. EPL (Europhysics Letters), 2007. **77**(6): p. 64002.
- [14] Mönch, W. and S. Herminghaus, *Elastic instability of rubber films between solid bodies*. EPL (Europhysics Letters), 2001. **53**(4): p. 525.
- [15] Vilmin, T., F. Ziebert, and E. Raphaël, *Simple View on Fingering Instability of Debonding Soft Elastic Adhesives*. Langmuir, 2009. **26**(5): p. 3257-3260.
- [16] Dugdale, D., *Yielding of steel sheets containing slits*. Journal of the Mechanics and Physics of Solids, 1960. **8**(2): p. 100-104.
- [17] Barenblatt, G.I., *The mathematical theory of equilibrium cracks in brittle fracture*. Advances in applied mechanics, 1962. **7**(1): p. 55-129.
- [18] Xu, X.-P. and A. Needleman, *Numerical simulations of dynamic crack growth along an interface*. International Journal of Fracture, 1995. **74**(4): p. 289-324.
- [19] Geubelle, P.H. and J.S. Baylor, *Impact-induced delamination of composites: a 2D simulation*. Composites Part B: Engineering, 1998. **29**(5): p. 589-602.
- [20] Anderson, T.L., *Fracture mechanics: fundamentals and applications*. 2005: CRC press.
- [21] Kaelble, D., *Peel Adhesion: Micro-Fracture Mechanics of Interfacial Unbonding of Polymers*. Transactions of The Society of Rheology (1957-1977), 1965. **9**(2): p. 135-163.
- [22] Ghatak, A., L. Mahadevan, and M.K. Chaudhury, *Measuring the work of adhesion between a soft confined film and a flexible plate*. Langmuir, 2005. **21**(4): p. 1277-1281.
- [23] Li, S., M. Thouless, A. Waas, J. Schroeder, and P. Zavattieri, *Use of mode-I cohesive-zone models to describe the fracture of an adhesively-bonded polymer-matrix composite*. Composites Science and Technology, 2005. **65**(2): p. 281-293.
- [24] Turon, A., C.G. Davila, P.P. Camanho, and J. Costa, *An engineering solution for mesh size effects in the simulation of delamination using cohesive zone models*. Engineering Fracture Mechanics, 2007. **74**(10): p. 1665-1682.
- [25] Tsai, C., et al., *Analysis of cohesive failure in adhesively bonded joints with the SSPH meshless method*. International Journal of Adhesion and Adhesives, 2014. **51**: p. 67-80.

- [26] Shen, B. and G. Paulino, *Direct extraction of cohesive fracture properties from digital image correlation: a hybrid inverse technique*. *Experimental Mechanics*, 2011. **51**(2): p. 143-163.
- [27] Gowrishankar, S., H. Mei, K.M. Liechti, and R. Huang, *A comparison of direct and iterative methods for determining traction-separation relations*. *International journal of fracture*, 2012. **177**(2): p. 109-128.
- [28] Zhou, X., J. Zimmerman, E. Reedy, and N. Moody, *Molecular dynamics simulation based cohesive surface representation of mixed mode fracture*. *Mechanics of Materials*, 2008. **40**(10): p. 832-845.
- [29] Sinko, R. and S. Keten, *Traction–separation laws and stick–slip shear phenomenon of interfaces between cellulose nanocrystals*. *Journal of the Mechanics and Physics of Solids*, 2015. **78**: p. 526-539.
- [30] Mukherjee, B., D.A. Dillard, R.B. Moore, and R.C. Batra, *Debonding of Confined Elastomeric Layer using Cohesive Zone Model*. *International Journal of Adhesion and Adhesives*, 2016a. **66**: p. 114-127.
- [31] Maugis, D., *Adhesion of spheres: the JKR-DMT transition using a Dugdale model*. *Journal of colloid and interface science*, 1992. **150**(1): p. 243-269.
- [32] Hibbitt, K. and Sorensen, *ABAQUS/CAE User's Manual*. 2012: Hibbitt, Karlsson & Sorensen, Incorporated.
- [33] Song, S.H., G.H. Paulino, and W.G. Buttlar, *A bilinear cohesive zone model tailored for fracture of asphalt concrete considering viscoelastic bulk material*. *Engineering Fracture Mechanics*, 2006. **73**(18): p. 2829-2848.
- [34] Dundurs, J., *Discussion: "Edge-bonded dissimilar orthogonal elastic wedges under normal and shear loading" (Bogy, DB, 1968, ASME J. Appl. Mech., 35, pp. 460–466)*. *Journal of applied mechanics*, 1969. **36**(3): p. 650-652.
- [35] Bogy, D.B., *Edge-bonded dissimilar orthogonal elastic wedges under normal and shear loading*. *Journal of Applied Mechanics*, 1968. **35**(3): p. 460-466.
- [36] Chadegani, A. and R.C. Batra, *Analysis of adhesive-bonded single-lap joint with an interfacial crack and a void*. *International Journal of Adhesion and Adhesives*, 2011. **31**(6): p. 455-465.
- [37] Williams, M., *The stresses around a fault or crack in dissimilar media*. *Bulletin of the seismological society of America*, 1959. **49**(2): p. 199-204.
- [38] Dillard, D., *Bending of plates on thin elastomeric foundations*. *Journal of applied mechanics*, 1989. **56**(2): p. 382-386.
- [39] Ghatak, A., L. Mahadevan, J.Y. Chung, M.K. Chaudhury, and V. Shenoy, *Peeling from a biomimetically patterned thin elastic film*. *Proceedings of the Royal Society of London. Series A: Mathematical, Physical and Engineering Sciences*, 2004. **460**(2049): p. 2725-2735.
- [40] Anderson, G.P., S.J. Bennett, and K.L. DeVries, *Analysis and testing of adhesive bonds*. 1977.
- [41] Hill, J., et al., *Co-planar crack interaction in cleaved mica*. *International journal of fracture*, 2003. **119**(4): p. 365-386.
- [42] Bao, G. and Z. Suo, *Remarks on crack-bridging concepts*. *Applied Mechanics Reviews*, 1992. **45**(8): p. 355-366.
- [43] Mukherjee, B., D.A. Dillard, R.B. Moore, and R.C. Batra, *CZM analysis of edge debonding during peeling of a flexible plate from an elastomeric layer*. In preparation, 2016c.
- [44] Sarkar, J., A. Sharma, and V. Shenoy, *Adhesion and debonding of soft elastic films: Crack patterns, metastable pathways, and forces*. *Langmuir*, 2005. **21**(4): p. 1457-1469.

- [45] Chung, J.Y. and M.K. Chaudhury, *Roles of discontinuities in bio-inspired adhesive pads*. Journal of The Royal Society Interface, 2005. **2**(2): p. 55-61.
- [46] Biggins, J.S., B. Saintyves, Z. Wei, E. Bouchaud, and L. Mahadevan, *Digital instability of a confined elastic meniscus*. Proceedings of the National Academy of Sciences, 2013. **110**(31): p. 12545-12548.
- [47] Ghatak, A., M.K. Chaudhury, V. Shenoy, and A. Sharma, *Meniscus instability in a thin elastic film*. Physical Review Letters, 2000. **85**(20): p. 4329.
- [48] Larsen, H.-O., *Mold for making contact lenses, either the male or female mold sections being relatively more flexible*. U.S. Patent 4,640,489. 1987
- [49] Hutchinson, J.W., *Crack tip shielding by micro-cracking in brittle solids*. Acta metallurgica, 1987. **35**(7): p. 1605-1619.
- [50] Feurer, B., *Method for molding contact lenses using microwave energy*. U.S. Patent 4390482. 1983
- [51] Mukherjee, B., D.A. Dillard, R.B. Moore, and R.C. Batra, *Numerical investigation of demolding of a sandwiched elastomeric layer*. In preperation, 2016d.

4 Analysis of edge debonding in peeling of a thin flexible plate from an elastomer layer

Bikramjit Mukherjee, Romesh C. Batra, and David A. Dillard*,
Department of Biomedical Engineering and Mechanics, M/C 0219
Virginia Polytechnic Institute and State University
Blacksburg, Virginia 24061, USA

(This manuscript is ready to be submitted for possible publication in a peer-reviewed journal)

Abstract

A cohesive zone modeling (CZM) approach is used to study the peeling of a thin overhanging plate from the edge of an incompressible elastomer layer bonded firmly to a stationary rigid base. The deformations are approximated as plane strain and the materials are assumed to be linear elastic. Furthermore, the governing equations for the elastomer deformations are simplified using lubrication theory approximations. A bilinear traction-separation relation is considered in the CZM. Our analysis reveals that the peeling is governed by one non-dimensional number defined in terms of the interfacial strength, the interface fracture energy, the plate rigidity, the elastomer shear modulus, and the elastomer layer thickness. Furthermore, increases in this non-dimensional number lead to monotonic increases in the size of the CZ ahead of the debond tip, and the pull-off force transitions from a fracture energy dominated to a strength dominated regime. These findings could guide elastomeric adhesive design for load capacity and may help find experimental configurations for extracting the strength and the fracture energy of an interface from test data.

Keywords: Elastomer interlayer; debonding; cohesive zone model (CZM); peeling

* Corresponding author, Email: dillard@vt.edu, Tel.: +1- 540-231-4714, Fax: +1- 540-231-9187

4.1 Introduction

Understanding and controlling factors that affect adhesive/interfacial debonding of sandwiched elastomer layers are critical in numerous applications such as fabrication of soft ophthalmic lenses, optimizing transfer printing processes, ensuring durability of sealants, designing laminated safety glasses and biomimetic adhesives as well as restricting fouling of barnacles on ship hulls. The mechanics of interfacial debonding of elastomer interlayers, especially the collective role played by the geometric and the material parameters, and the interfacial adhesion has been a subject of considerable interest.

Here we analyze a prototype problem, namely, the peeling off of an overhanging flexible plate from an elastomer layer bonded firmly to a stationary rigid base. Previous studies on similar problems [1-4] that focused not necessarily on elastomer interlayers recognized the importance of the collective role of the flexural rigidity (D_p) of the plate, and Young's modulus (E) and the thickness (h) of the interlayer on the elastomer deformations and on the pull-off force required for peeling. For example, Bikerman [3] treated the interlayer as a Winkler elastic foundation, used a critical peel stress (T_c) as the debonding criterion, and found that the pull-off force per unit plate width was given by $P_c \sim T_c (D_p h / E)^{1/4}$ where $(D_p h / E)^{1/4}$ quantifies the length scale of the peel stress oscillations decaying along the peeling direction. The coupling of a linear elastic fracture mechanics (LEFM) approach with the Winkler foundation analysis [5, 6] predicts that $P_c \sim (D_p h / E)^{1/4} \sqrt{G_c E / h}$ where G_c is the fracture energy of the interface. These studies approximated deformations of the interlayer as uniaxial stretching of independent strands (effective Poisson's ratio of zero). This assumption becomes erroneous for nearly incompressible elastomers. The state of hydrostatic stress in the interlayer causes the displacement of an elastomer point to scale with the Laplacian of the hydrostatic stress.

As illustrated by Dillard [7] for a general loading of a plate supported on an elastomeric foundation and extended by Ghatak et al. [8] for the variation of the peel stress in the peeling direction, stresses in the elastomeric foundation significantly deviate from that predicted by the Winkler solution due to the constraint of incompressibility. For incompressible elastomers, the governing differential equation becomes 6th order (rather than the conventional uncoupled 4th order for Winkler foundations) resulting in exaggerated oscillations in displacements and peel stresses.

Ghatak et al. [8] employed an LEFM approach to correlate the reaction force and the debond length to the fracture energy of the interface and the geometric and material parameters. Their analysis yielded a much slower decay of oscillatory peel stress characterized by the length scale $(D_p h^3 / E)^{1/6}$ as opposed to $(D^p h / E)^{1/4}$ predicted by the Winkler solution and resulted in a different scaling of the pull off force, $P_c \sim (D_p / E)^{1/3} \sqrt{G_c E / h}$. The LEFM approach uses fracture energy, G_c , as a single measure of the adhesion integrity. This represents the energy required for an existing debond to grow by a unit area and tacitly treats the debond tip as a mathematical point. This approach usually breaks down in large-scale bridging problems [9] in which there is a finite-size zone holding tractions in the wake of the debond, as seen, for example, during fibrillation of pressure-sensitive adhesives (PSA) or in fiber-bridging in composites.

An approach better suitable for such problems [9] is the cohesive zone model (CZM). It employs a traction-separation (TS) relation to phenomenologically model debonding when two adjoining planes are separated. This allows debonding to nucleate and propagate when the interface is stressed. The often used TS relations [10-12] involve two significant parameters: the fracture energy, G_c , and the interfacial peel stress or strength, T_c , to characterize the interfacial interaction, though other metrics are sometimes explicitly given. By using these two parameters, the CZM approach bridges the gap between a strength based criterion and the fracture energy based LEFM approach to model failure/debonding. For cohesive cracking in a medium of Young's modulus E^* and characteristic length l Bao and Suo [9] pointed out that in the CZM approach the non-dimensional group $T_c^2(l) / G_c E^*$ governs the transition from large-scale bridging (large process zone, strength driven, LEFM not valid) to small-scale bridging conditions (small process zone, fracture energy driven, LEFM applicable).

Tang and Hui [13] analyzed the debonding of a rigid cylindrical punch (of radius a) from an elastic interlayer using a Dugdale-type TS relation, and showed that the single non-dimensional number $\chi = (T_c^2 a / E G_c) g(a/h)$ governs the global response under suitable normalization of variables. With the process zone (CZ) size monotonically decreasing with this quantity, the global response transitions from a strength (T_c) - dominated regime to an energy (G_c) - dominated regime. The pull-off force scales as $\sqrt{G_c E / a} \sqrt{1 / g(a/h)}$ in the energy dominated region ($\chi \gg 1$), and equals $\pi a^2 T_c$ in the strength dominated region.

The CZM has been widely used to analyze peeling problems [14-20]. These studies modeled adherends as bonded to a Winkler spring foundation with the interface failure characterized by either a force-elongation or a TS relation. However, a Winkler foundation approach, as mentioned earlier, is unsuitable when analyzing peeling from an elastomeric layer. Mukherjee et al. [21] used the finite element method (FEM) coupled with a CZM to analyze the peeling of a flexible plate from an elastomeric layer and delineated the collective role of the geometric and the material parameters as well as the interfacial adhesion on the interfacial damage/debonding and the global response such as the pull-off force. In agreement with the earlier findings [22, 23] they showed that for the system studied here with the interlayer thickness $h \gg (D_p / \mu)^{1/3} / 9$, damage initiates at the edge, forms a CZ and propagates with a CZ at its front with continued loading at the plate edge. Here we use a CZM and a bilinear TS relation to analyze this debonding mechanism by a semi-analytical method built on earlier approaches of Dillard [7] and Ghatak et al. [8] for modeling elastomeric foundations.

4.2 Problem description and analysis

The problem exhibited in Figure 4-1a consists of a flexible plate adhered to an elastomer layer (interlayer) that is firmly bonded to a stationary rigid base so that debonding can occur only at the plate/elastomer interface when a monotonically increasing vertical displacement δ_A is applied at point A of the plate edge. Plane strain deformations of the system are described and analyzed by using a rectangular Cartesian coordinate system, xyz , with origin at the moving debond tip shown in Figure 4-1a. The origin of the fixed rectangular Cartesian coordinate system $\tilde{x}yz$ is at the corner point G. It is thus tacitly assumed that the system extends to infinity in the y -direction and deformations of the plate and the elastomer layer in the xz - plane are analyzed.

Following previous works [13, 24] we assume that damage/debonding is triggered only by the peel stress at the interface and study only mode-I failure at the interface. The debonding between the interlayer and the flexible plate is simulated by a CZM with a bilinear TS relation depicted in Figure 4-2 and described by Eq.(4-1).

$$T = \begin{cases} K_e \delta & (0 \leq \delta \leq \delta_c) \\ K_s (\delta_f - \delta) & (\delta_c \leq \delta \leq \delta_f) \\ 0 & (\delta_f \leq \delta) \end{cases} \quad (4-1)$$

Here K_e is the slope of the portion OM of the TS curve and $K_s = T_c / (\delta_f - \delta_c)$ where T_c is the maximum normal traction supported by the interface when the relative normal displacement between the two adjoining surfaces equals δ_c . The point M (δ_c, T_c) signifies the initiation of damage (softening) and the point N $(\delta_f, 0)$ the onset of debonding. The energy release rate at the initiation of debonding equals area of the triangle OMN, i.e.,

$$\mathcal{G}_c = T_c \delta_f / 2 \quad (4-2)$$

The initial slope K_e in Eq. (4-1) is assigned a large enough value to not influence the debond initiation and propagation at the plate/elastomer layer interface. Because of monotonically increasing displacement δ_A applied at point A, no unloading at any point of the interface is expected.

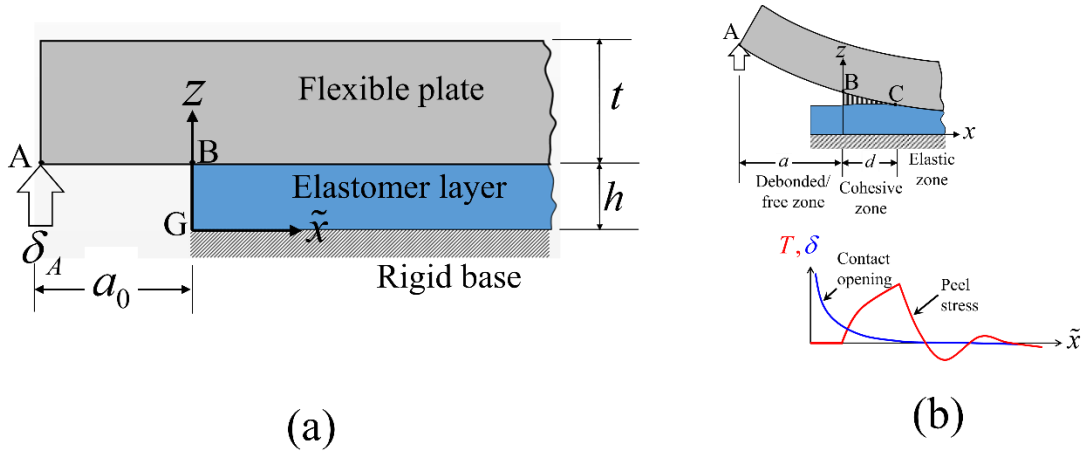


Figure 4-1: Sketch of (a) the problem studied, and (b) various zones near the debond tip B after it has moved in the \tilde{x} direction by the distance $a - a_0$. Also schematically plotted are variations of the peel stress (normal traction) and the corresponding contact opening (displacement jump) along the \tilde{x} -axis.

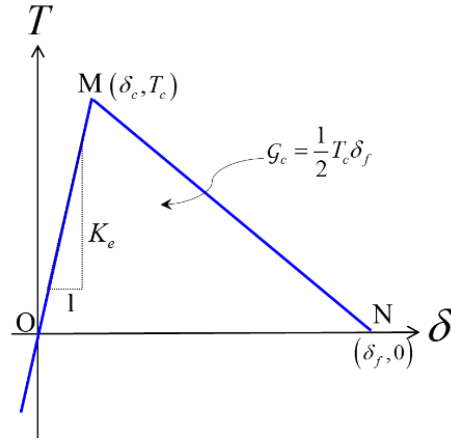


Figure 4-2: A bilinear TS relation

It is anticipated that a CZ will develop near the corner B followed by debonding there. The subsequent propagation of the debond with a CZ at its front and the associated distribution of the interfacial peel stress and the separation at the interface are schematically illustrated in Figure 4-1b.

4.2.1 Governing Equations

Plane strain deformations of the thin flexible plate are assumed to be governed by the following Kirchhoff-Love (KL) equation [25] for infinitesimal bending deformations with the y-displacements set equal to zero.

$$\Lambda^4 w_p = -T / D_p \quad (4-3)$$

Here $\Lambda^n = d^n / dx^n$, and w_p is the vertical displacement of a point in the plate, T the normal traction acting on the plate, and $D_p = E_p t^3 / 12(1-\nu^2)$ is the plate flexural rigidity in terms of its thickness t , Young's modulus E_p and Poisson's ratio ν .

Plane strain deformations of the homogenous, incompressible, isotropic, and linear elastic elastomer layer with the body and the inertia forces neglected are governed by

$$p_x = \mu(u_{xx} + u_{zz}), p_z = \mu(w_{xx} + w_{zz}) \quad (4-4)$$

$$u_x + w_z = 0 \quad (4-5)$$

where p is the hydrostatic pressure not determined by the deformations, μ ($= E/3$, where E is Young's modulus) is the shear modulus, u and w the displacement components in the x - and

the z - directions, respectively, $p_x = \frac{\partial p}{\partial x}$, and Eq. (4-5) expresses the incompressibility constraint. The following boundary conditions for the elastomer layer are presumed.

$$u(x, 0) = w(x, 0) = 0, \quad u(x, h) = 0 \quad (4-6)$$

That is, the elastomer particles are firmly bonded to the rigid base, there is no slip at the elastomer/plate interface, and horizontal displacements of the plate particles are negligible.

4.2.2 Approximate solution of the governing equations

Using assumptions analogous to those made in the classical lubrication theory [26] for thin films, i.e., $|u_{zz}| \gg |u_{xx}|$, and $p_z = 0$, Eq. (4-4) simplifies to

$$p_x = \mu(u_{zz}), \quad p_z = 0 \quad (4-7)$$

When employing the lubrication theory, deformations cannot be accurately predicted over a length-scale of order h from the edge [26]. Nevertheless, we use these assumptions for simplicity. In the approximate solution sought here, no attempt is made to satisfy the boundary condition of null traction on the free surface $\tilde{x}=0$. Similar assumptions were used by Ghatak et al. [8] in their LEFM analysis of this problem.

Integrating Eqs. (4-5) and (4-7) and using boundary conditions (4-6) gives

$$u(x, z) = \frac{1}{2\mu} \frac{dp}{dx} (z^2 - hz), \quad w(x, z) = -\frac{1}{2\mu} \frac{d^2 p}{dx^2} \left(\frac{z^3}{3} - h \frac{z^2}{2} \right) \quad (4-8)$$

Vertical displacement, w_f , of points on the elastomer top surface is given by²²

$$w(x, h) = w_f(x) = \frac{h^3}{12\mu} \frac{d^2 p}{dx^2} \quad (4-9)$$

The normal stress, $\sigma_{zz}(x, z) = -p(x, z) + \mu \partial w / \partial z$, at the elastomer top surface becomes $\sigma_{zz}(x, h) = -p(x)$. The continuity of normal traction across the elastomer/plate interface implies that $p = -T(\delta)$ where

²² Zero-friction condition at the upper interface leads to $w_f(x) = h^3 / 3\mu (d^2 p / dx^2)$, the rest of the analysis remains the same.

$$\delta = w_p - w_f \quad (4-10)$$

is the separation/opening at an interfacial point. Substitution for w_p from Eq. (4-10) and for w_f from Eq. (4-9) into Eq. (4-3) results in the following 6th order ordinary differential equation (ODE) for T .

$$-\Lambda^6 T + \frac{12\mu}{h^3} \left(\Lambda^4 \delta + \frac{1}{D_p} T \right) = 0 \quad (4-11)$$

Substitution for T in terms of δ from Eq. (4-1) into Eq. (4-11) gives a 6th order ODE in δ which is solved under the pertinent boundary conditions. In principle, any TS relation can be used and the resulting non-linear ODE can be solved numerically using, for example, a shooting method.

Corresponding to the three relations in Eq. (4-1) that hold, respectively, in the free/debonded zone ($-a \leq x \leq 0, \delta \geq \delta_f$), the CZ ($0 \leq x \leq d, \delta_c \leq \delta < \delta_f$) and the bonded zone ($d \leq x < \infty, \delta \leq \delta_c$), three ODEs from Eq. (11) are deduced. The variables are non-dimensionalized (normalized) as $X = x\beta$, and $\Lambda = \delta / \delta_f$ where $\beta = (12\mu / D_p h^3)^{1/6}$. The normalized debond length, a ($A = a\beta$), and the CZ size, d ($D = d\beta$), are denoted by A and D , respectively. The three ODEs and their solutions are listed below.

Debonded region ($-A \leq X \leq 0$): Since $T = 0$, Eq. (4-11) becomes

$$\Lambda^4 \Delta = 0 \quad (4-12)$$

where $\Lambda^n = d^n / dX^n$. However, $()'$ is also sometimes used to denote a derivative with respect to X . The solution of Eq. (4-12) is

$$\Delta(X) = D_1 X^3 + D_2 X^2 + D_3 X + D_4 \quad (4-13)$$

where D_1, \dots, D_4 are integration constants. The same notation with different numeric subscripts will be used below for other integration constants.

Cohesive zone ($0 \leq X \leq D$): Now Eq. (4-1)₂ holds, and Eq. (4-11) reduces to

$$(\Lambda^6 + \eta_s^2 \Lambda^4 - 1) \Delta + 1 = 0 \quad (4-14)$$

where $\eta_s = (12\mu / K_s h^3)^{1/2} \beta^{-1}$. The solution of Eq. (4-14) depends on roots of the characteristic cubic equation, $(\Lambda^2)^3 + \eta_s^2 (\Lambda^2)^2 - 1 = 0$. The three roots for Λ^2 are real and distinct if $\eta_s > \eta_s^c (= (27/4)^{1/6})$, they are real and at least two are equal if $\eta_s = \eta_s^c$, and one root is real and the other two are complex conjugates otherwise. Listed below are the general solutions of Eq. (4-14) for these three cases:

$$\begin{aligned} \text{Case-I:} \quad & \Delta(X) = D_5 e^{-pX} + D_6 e^{pX} + e^{-qX} (D_7 \cos(qX) + D_8 \sin(qX)) + \\ \eta_s < \eta_s^c \quad & e^{qX} (D_9 \cos(rX) + D_{10} \sin(rX)) + 1 \end{aligned} \quad (4-15)$$

$$\begin{aligned} \text{Case-II:} \quad & \Delta(X) = D_5 e^{-pX} + D_6 e^{pX} + (D_7 \cos(qX) + D_8 \sin(qX)) + \\ \eta_s = \eta_s^c \quad & X (D_9 \cos(rX) + D_{10} \sin(rX)) + 1 \end{aligned} \quad (4-16)$$

$$\begin{aligned} \text{Case-III:} \quad & \Delta(X) = D_5 e^{-pX} + D_6 e^{pX} + (D_7 \cos(qX) + D_8 \sin(qX)) + \\ \eta_s > \eta_s^c \quad & (D_9 \cos(rX) + D_{10} \sin(rX)) + 1 \end{aligned} \quad (4-17)$$

Here p , q and r are found from roots of the characteristic cubic equation.

Bonded zone ($D \leq X \leq \infty$): Using Eq. (4-1)₁, Eq. (4-9) becomes

$$(\Lambda^6 - \eta_e^2 \Lambda^4 - 1)\Delta = 0 \quad (4-18)$$

where $\eta_e = (12\mu / K_e h^3)^{1/2} \beta^{-1}$. For $K_e \gg 1$, and assuming that $\Lambda^4 \Delta$ is finite, Eq. (4-18) reduces to the ODE, $(\Lambda^6 - 1)\Delta = 0$, which was analyzed in [7, 8] that considered perfect bonding at the interface. The general solution of Eq. (4-18) for $K_e \gg 1$ is

$$\begin{aligned} \Delta(X) = & D_{11} e^{-X} + D_{12} e^X \\ & + e^{\frac{X}{2}} \left(D_{13} \cos\left(\frac{\sqrt{3}}{2} X\right) + D_{14} \sin\left(\frac{\sqrt{3}}{2} X\right) \right) + e^{\frac{X}{2}} \left(D_{15} \cos\left(\frac{\sqrt{3}}{2} X\right) + D_{16} \sin\left(\frac{\sqrt{3}}{2} X\right) \right) \end{aligned} \quad (4-19)$$

Boundary conditions on Δ :

The 16 integration constants appearing in Eqs. (4-13)-(4-19), the size D of the CZ, and either the separation Δ_B at point B prior to the initiation of debonding or the crack length A during propagation of the debonded region are determined from the following 18 conditions.

The bending moment at the left end where the vertical displacement is prescribed is assumed to be zero. Thus

$$\Delta(-A) = \Delta_A, \quad \Delta''(-A) = 0 \quad (4-20)$$

The continuity of the plate deflection (w_p), the slope (w_p'), the bending moment ($\sim w_p''$), the shear force ($\sim w_p'''$) and the normal traction ($\sim w_p''''$) at points B and C shown in Figure 4-1 gives the following 10 conditions at these points where superscripts + and - denote, respectively, the location just on the right and on the left side of a point.

At point B:

$$\begin{aligned} \Delta(0^-) &= \Delta(0^+) + \eta_s^{-2} \Delta''(0^+), \quad \Delta'(0^-) = \Delta'(0^+) + \eta_s^{-2} \Delta'''(0^+), \quad \Delta''(0^-) = \Delta''(0^+) + \eta_s^{-2} \Delta''''(0^+), \\ \Delta'''(0^-) &= \Delta'''(0^+) + \eta_s^{-2} \Delta''''(0^+), \quad \Delta''''(0^-) = \Delta''''(0^+) + \eta_s^{-2} \Delta''''''(0^+) \end{aligned} \quad (4-21)$$

At point C:

$$\begin{aligned} \Delta(D^-) + \eta_s^{-2} \Delta''(D^-) &= \Delta(D^+) - \eta_e^{-2} \Delta''(D^+), \quad \Delta'(D^-) + \eta_s^{-2} \Delta'''(D^-) = \Delta'(D^+) - \eta_e^{-2} \Delta'''(D^+), \\ \Delta''(D^-) + \eta_s^{-2} \Delta''''(D^-) &= \Delta''(D^+) - \eta_e^{-2} \Delta''''(D^+), \quad \Delta'''(D^-) + \eta_s^{-2} \Delta''''''(D^-) = \Delta'''(D^+) - \eta_e^{-2} \Delta''''''(D^+) \\ \Delta''''(D^-) + \eta_s^{-2} \Delta''''''(D^-) &= \Delta''''(D^+) - \eta_e^{-2} \Delta''''''(D^+) \end{aligned} \quad (4-22)$$

The relative vertical displacements at these points can be written as

$$\Delta(0^-) = \Delta_B \quad \text{and} \quad \Delta(D^+) - \eta_e^{-2} \Delta''(D^+) = \Delta_c \quad (4-23)$$

with $\Delta_B = 1$ when debonding initiates at point B. Until then, Δ_B is treated as a variable with length $A = A_0$ of the debond known. The non-dimensional contact opening Δ_c at point C equals $T_c^2 / 2G_c K_e$.

The assumption of zero displacement at points far away from point C can be stated as

$$\lim_{X \rightarrow \infty} \Delta = 0 \quad (4-24)$$

Finally the overall equilibrium requires that the reaction (or the shear) force, p_A , at point A, equal the total restoring force exerted by the elastomer interlayer. From the KL plate theory, one gets $p_A = D w_p'''(-a) = D \beta^3 \delta_f \Delta'''(-A)$. It equals the peel stress integrated over the interface, i.e., $\beta^{-1} \int_0^\infty T(\delta) dX$. Thus

$$\frac{1}{D_p \beta^4 \delta_f} \int_0^{\infty} T(\delta) dX = \Delta'''(-A) \quad (4-25)$$

The decay condition (4-24) implies that constants D_{12}, D_{15}, D_{16} must be zero. Eq. (4-20) gives Eq. (4-26) upon eliminating D_2 , and Eq. (4-1) is used to reduce Eq. (4-25) to Eq. (4-27).

$$2D_1 A^3 - D_3 A + \Delta_B - \Delta_A = 0 \quad (4-26)$$

$$\eta_s^{-2} D - \eta_s^{-2} \int_0^D \Delta dX + \eta_e^{-2} \int_D^{\infty} \Delta dX - 6D_1 = 0 \quad (4-27)$$

Constants D_1, \dots, D_{14} are found in terms of A and D by simultaneously solving algebraic equations resulting from conditions (4-21)-(4-23) using the software MATHEMATICA [27]. Eq. (4-27) is simplified by substituting for Δ from Eqs. (4-15) - (4-17) and (4-19). The transcendental equations (4-26) and (4-27) are then numerically solved using the function FINDROOT.

4.3 Results and discussion

Recall that $\eta_s = (12\mu / K_s h^3)^{1/2} \beta^{-1}$ where $K_s \approx T_c^2 / 2G_c$ and $\beta^{-1} = (12\mu / D_p h^3)^{-1/6}$. Thus $\eta_s \approx 3.238 \sqrt{(G_c \mu / T_c^2) (D_p / \mu h^6)^{1/3}}$. The length scale β^{-1} is related to the deformability of the interlayer [7, 8] relative to that of the flexible plate. Values of Δ , A , D and P_A are numerically evaluated by solving Eqs. (4-26) and (4-27). The effects of η_e and Δ_c are assumed to be negligible since $\eta_e \ll \eta_s$ and $\Delta_c \ll \Delta_B$ when $K_e \gg 1$.

Unless stated otherwise results given below are for the initial debond length $A_0 = 2$, and $\eta_s = 2$. One combination of values of the material, the geometric and the TS parameters that give $A_0 = 2$, and $\eta_s = 2$ are:

$$\text{Plate : } a_0 = 2 \text{ mm}, t = 1 \text{ mm}, E_p = 1201.5 \text{ MPa}, \nu_p = 0.3$$

$$\text{Elastomer : } h = 817 \mu\text{m}, \mu = 5 \text{ MPa},$$

$$\text{Interface : } T_c = 0.04 \text{ MPa}, G_c = 0.029 \text{ J / m}^2, K_e = 10^6 \text{ N / mm}^3$$

Evolutions of the plate deflection, $W_p = w_p / \delta_f$, and the non-dimensional peel stress, T / T_c , are plotted in Figure 4-3 as functions of the global horizontal distance measured from point G shown in Figure 4-1. As expected for the bending of a plate on an elastomer

foundation, the plate deflection exhibits decaying oscillatory distribution. The computed deflection profile agrees well with that reported by Ghatak et al. [8] and with that computed using the FEM [21]. Plots exhibited in Figure 4-3b reveal that with continued loading, a CZ develops and the peel stress reduces to zero at the initial debond tip, i.e., $\tilde{X} = 0$, at a critical value, $\Delta_{A0} = 3.1$, of the applied non-dimensional displacement. The comparison of the present results with the LEFM solution of Ghatak et al. [8] is also exhibited in Figure 4-3b for the propagating debond at $\Delta_A = 4.0$. Whereas the debond tip in their work is the point with the maximum peel stress, it is the point of zero peel stress in our analysis. The point with the maximum peel stress, T_c , in the present work is the tip of the CZ. The presently predicted peel stress distribution at $\Delta_A = 4.0$ agrees reasonably well with that computed using the FEM [21] with the FEM predicting 0.6% smaller debond length A and 24% smaller CZ length D than that given by the current approximate analysis. These differences are possibly due to using the lubrication theory and neglecting shearing deformations of the plate in the present work. For example, deformations computed with the FEM reveal that at $\Delta_A = 4.0$, the values of u_{xx} and u_{zz} at the point ($x =$ location of predicted damage tip, $z = h/2$) are -0.00069 and -0.00096, respectively. Thus lubrication theory approximation, $|u_{xx}| \ll |u_{zz}|$, is not appropriate. However, as shown later in the paper, the presently computed pull-off force agrees well with that found from the solution of the plane strain deformation equations using the FEM.

The computed dimensionless debond length A as a function of the displacement Δ_A and predictions of the LEFM analysis with [8] and without [28] considering the interlayer deformability are exhibited in Figure 4-4. For a deformable interlayer the crack length A can be found from

$$\Delta_A^2 = \eta_s^{-2} A^4 / 9\Omega(A) \text{ where } \Omega(A) = \frac{8A^4 (12 + 46A + 72A^2 + 56A^3 + 21A^4 + 3A^5)}{3(6 + 12A + 9A^2 + 2A^3)^3}. \quad (4-28)$$

In the limit of a rigid interlayer ($A \rightarrow \infty$, $\Omega(A) \rightarrow 1$), Eq. ((4-28) reduces to Obreimoff's [28] result $\Delta_A^2 = \eta_s^{-2} A^4 / 9$ in terms of the current non-dimensional variables. As can be observed from Figure 4-4, the debond length at a given displacement is over-predicted if the deformability of the interlayer is neglected. Our results predict even smaller debond length at a given displacement due to the consideration of the CZ at the debond tip.

Evolutions of the CZ size, the opening at the debond tip, and the slope of the plate at the debond tip as functions of the applied displacement are exhibited in Figure 4-5. The dashed lines in these plots correspond to the damage growth at point B until debonding occurs there and the solid lines with the subsequent propagation phase. Each dashed line intersects with the corresponding solid one at $\Delta_B = 1$ when $\delta = \delta_f$. One can observe that the CZ size increases with the applied displacement until debonding ensues at point B. During the propagation phase, the CZ size slowly decreases. This trend was also noted [19, 20] when the interlayer was modeled as a Winkler foundation and in the context of cohesive cracking [29]. The slow decrease in the CZ size during propagation agrees with the observation that the slope at debond tip (B) increases while the plate deflection stays constant. The maximum CZ size (D_0) at the onset of debonding is plotted in Figure 4-6a as a function of η_s for three values of the initial overhang length, A_0 , and as a function of A_0 for two values of η_s . One can see that the CZ size increases with η_s and decreases with A_0 , although the latter dependence is much weaker. Recalling $\eta_s \sim \sqrt{(G_c \mu / T_c^2) (D_p / \mu h^6)^{1/3}}$, the former is attributed to an increase in the cohesive length $G_c \mu / T_c^2$ relative to the length $(D_p / \mu h^6)^{1/3}$ arising from the material and the system geometry. The slow decrease of the CZ size with the debond length is similar to the dependence of the near-tip tensile zone size (\tilde{D}) on the debond length (A) predicted by Ghatak et al.'s [8] LEFM analysis and exhibited in Figure 4-6b. The decrease in the CZ size observed with increasing debond length could be attributed to deformations moving from being force-dominated to moment-dominated [30] as the lever arm (of length a) increases.

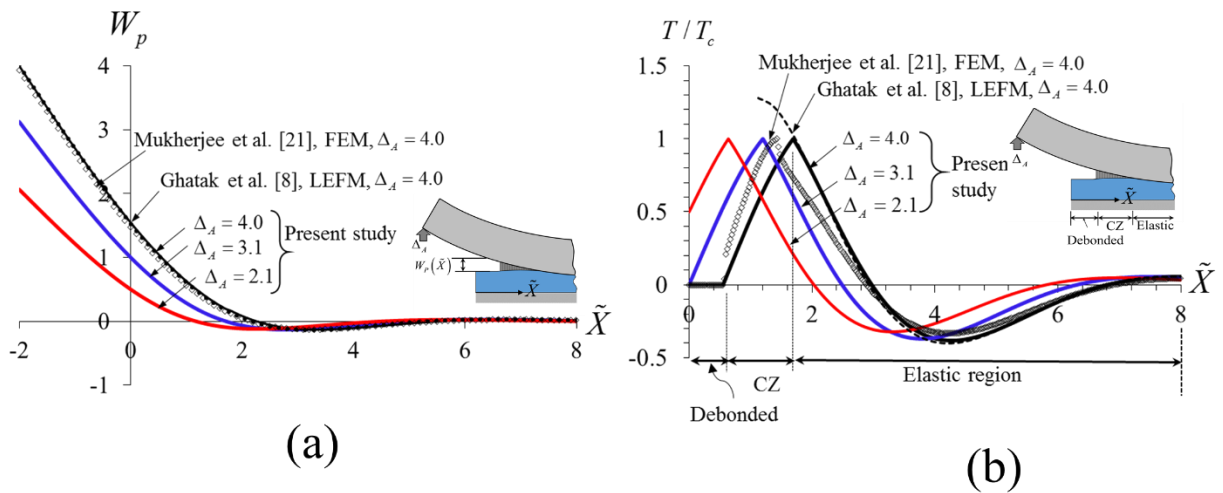


Figure 4-3: For three values of the non-dimensional applied displacement, Δ_A , distributions of the non-dimensional (a) plate deflection and (b) peel stress (T/T_c) on the global horizontal axis $\tilde{X} = \beta\tilde{x}$. For $\Delta_A = 4.0$, the three regions around a debond are marked in (b)

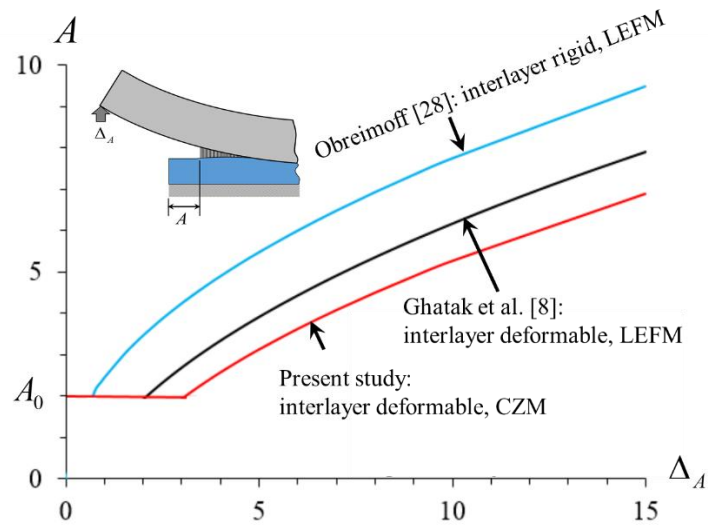


Figure 4-4: Non-dimensional debond length as a function of the applied non-dimensional displacement.

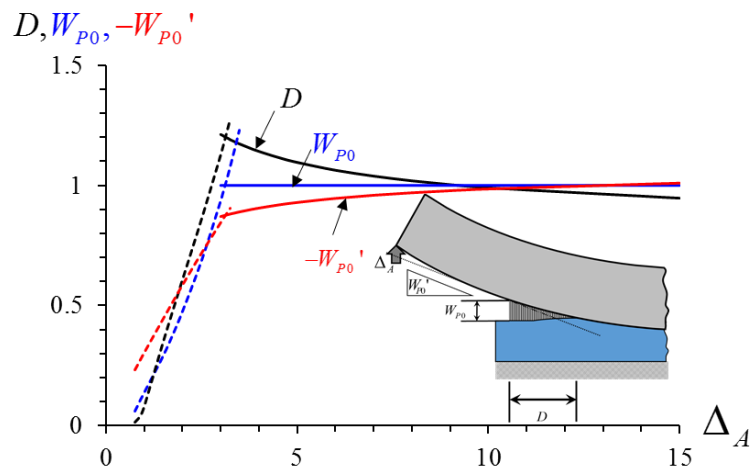


Figure 4-5: Non-dimensional CZ size, the plate deflection at the debond tip and the plate slope at the debond tip versus the non-dimensional applied displacement. The dashed lines represent results prior to the initiation of debonding.

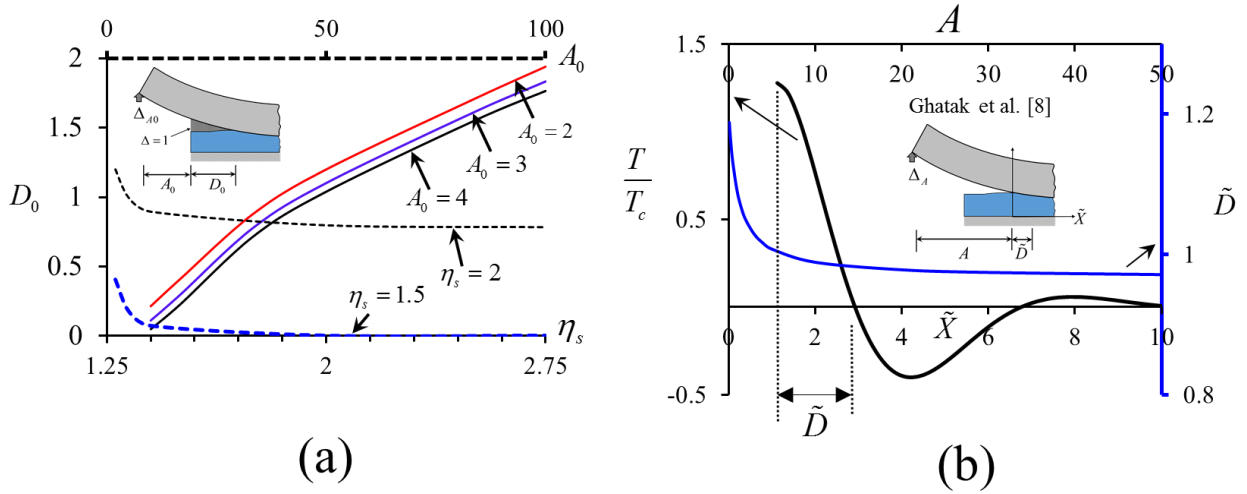


Figure 4-6: (a) The CZ size at debond initiation versus η_s for three values of the initial overhang length A_0 (solid lines) and versus A_0 for two values of η_s (dashed lines). (b) Peel stress distribution at $\Delta_A = 4.0$ and the size of the tensile region near the debond tip as a function of the debond length given by Ghatak et al.'s [8] solution.

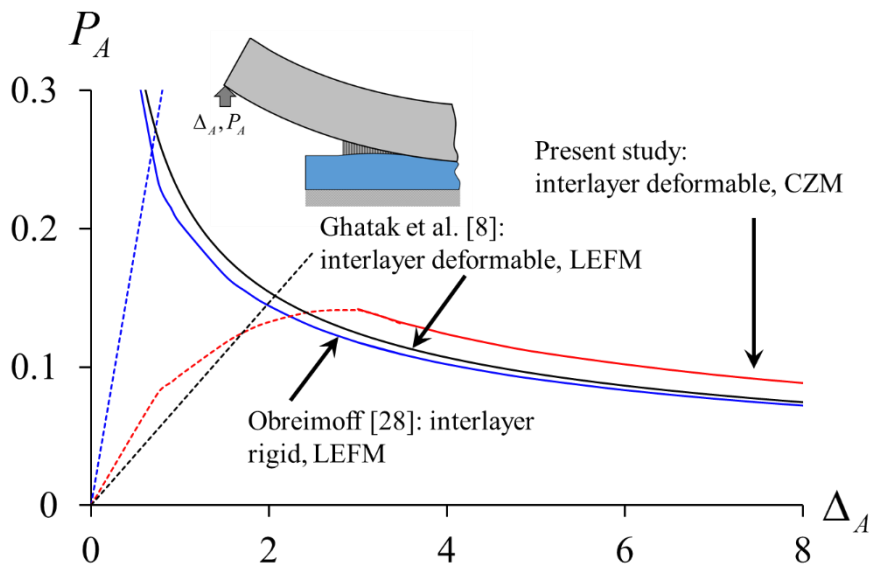


Figure 4-7: Non-dimensional load versus the applied non-dimensional displacement. The dashed lines represent results prior to the initiation of debonding.

The dimensionless load-displacement relation from Ghatak et al.'s analysis is given by $P_A = 6\Delta_A / (6 + 2A + 9A^2 + 2A^3)$ which for a rigid interlayer reduces to $P_A = 3\Delta_A / A^3$. The load-displacement results are plotted in Figure 4-7 in which dashed lines correspond to results

prior to debonding initiation and solid lines are for the propagation phase. The nonlinearity in the ascending portion of the load-displacement curve can be attributed to the softening associated with the damage/growth of the CZ at the tip of the initial debond. The maximum value of P_A (pull-off force) is plotted on a log-log scale in [Figure 4-8](#) as a function of the quantity $\psi = (G_c \mu / T_c^2) (D_p / \mu h^6)^{1/3} = \eta_s^2 / 3.497$. One can observe that the pull-off force deviates significantly from that predicted by the LEFM analyses of [Ghatak et al. \[8\]](#) for small values of ψ but the two sets of results are close to each other for large values of ψ . This is consistent with the variation of the CZ size suggesting a transition from small-scale bridging to large-scale bridging conditions [9]. A power-law fit of the data points ($R^2 = 0.9904$) reveals the approximate scaling of the dimensionless pull-off force, $P_A^{\max} \propto \psi^{0.8}$ or in dimensional units, $p_A^{\max} \sim D_p^{7/30} \mu^{-1/30} h^{1/10} G_c^{1/5} T_c^{3/5}$ (exponents are approximate). Thus the pull-off force is dominated by the cohesive strength, T_c , and weakly depends on the fracture energy G_c and other parameters. On the contrary, the LEFM results [8] give $p_A^{\max} \sim D_p^{1/3} \mu^{1/6} h^{-1/2} G_c^{1/2}$ (exponents are exact). That is, the pull-off force at very large values of ψ does not depend on the cohesive strength and is dominated by the fracture energy. This knowledge can potentially be utilized to extract fracture energy values from the pull-off force data for a very thick ($\psi \propto h^2$) elastomer layer, and interface strength for a thin elastomer layer. The close agreement of the present pull-off force values with those from the solution of the plane strain deformations using the FEM provide credence to the approximate model.

Our analysis assumed initiation of debonding at the corner B. However, as reported in [\[21, 22\]](#) debonding may initiate at interior points of the interface for elastomer interlayers that are sufficiently confined laterally. The confinement is quantified by $\alpha = (D_p / \mu)^{1/3} / h$. For $\alpha > \sim 9$, a CZ may begin to form over the interior of the interface at a distance $\sim \beta^{-1}$ from the edge; this is not captured by the present approach which considers the formation of only one CZ at the edge. Moreover, the internal opening begins to exhibit waviness when the parameter $\phi = T_c^2 h / G_c E$ exceeds a critical value ≈ 5 . The numerical solution of plane strain deformations using the FEM [\[21\]](#) gave values of α and ϕ when interfacial debonding will initiate from the edge and at interior points, and also of the pull-off force. Noting that $\psi = \alpha \phi^{-1} / 3$, computed values of the pull-off force for the strength-dominated region in

Figure 4-8 corresponded to internal rather than edge debonding for $\alpha > 9$. However, it is encouraging to see that the present data-points are on the same power-law fit as those from the FEM solution of the problem but not on the fit derived from the LEFM based approach. Additional discussion is available in Mukherjee et al. [21].

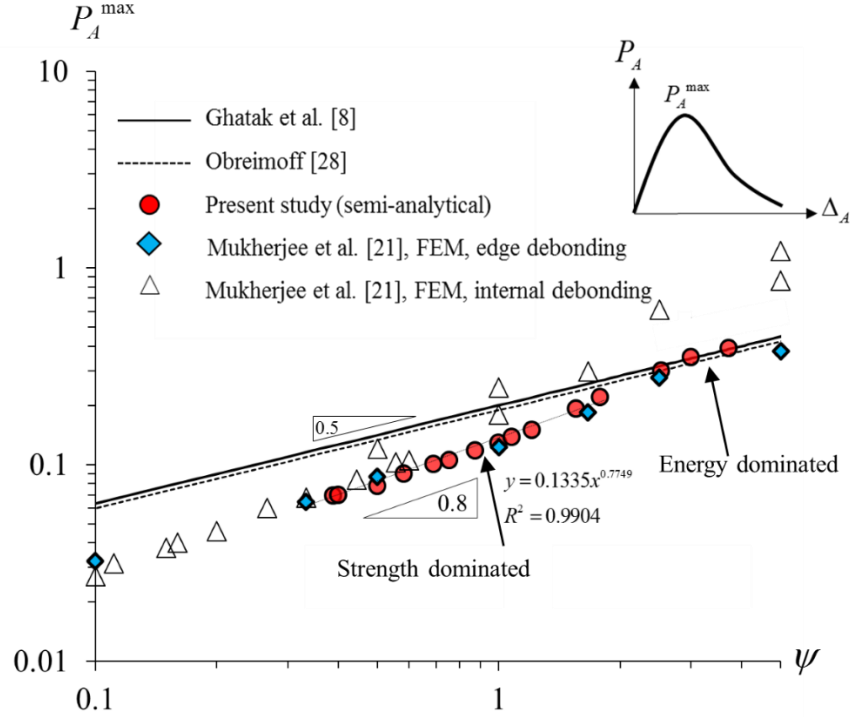


Figure 4-8: For $A_0 = 2.83$, the peak load (pull-off force) as a function of the non-dimensional number ψ on a log-log scale.

4.4 Conclusions

We have studied the initiation of damage and debonding at the corner of a flexible plate overhanging on and peeled from an elastomer layer firmly bonded to a rigid base. The analysis employs a bilinear traction-separation relation in a cohesive zone model (CZM) for the plate/elastomer interface and builds on the works of Dillard [7] and Ghatak et al. [8].

The key finding is that the single non-dimensional number $\psi = (\mathcal{G}_c \mu / T_c^2) (D_p / \mu h^6)^{1/3}$ governs the interfacial opening normalized by δ_f , the debond length and the CZ size normalized by $\beta^{-1} = (12\mu / D_p h^3)^{-1/6}$, and the load normalized by $D_p \beta^3 \delta_f$. Here T_c is the interfacial strength, \mathcal{G}_c the fracture energy of the interface, μ the shear modulus of the elastomer, h its thickness, D_p the flexural rigidity of the plate, β^{-1} the length scale of oscillations of the interfacial peel stress for bending of a Kirchhoff-Love plate on an

elastomer foundation, and $\delta_f = 2G_c / T_c$ the debond tip opening. The CZ size decreases as ψ increases. Consequently, the response transitions from a strength dominated regime to an energy dominated regime. For small CZ sizes, the predicted pull-off force agrees well with that found by Ghatak et al. [8] from the linear elastic fracture mechanics analysis.

Besides its potential use as guiding design for load capacity, the scaling of the pull-off force could be utilized to extract values of T_c and G_c for the interface by suitably designing interlayer thickness and/or the flexural rigidity of the plate.

4.5 Acknowledgments

The authors thank the department of Biomedical Engineering and Mechanics at Virginia Tech for support of BM and the use of its facilities, and Macromolecules and Interfaces Institute at Virginia Tech for fostering interdisciplinary research in adhesion science.

References

- [1] Kaelble, D., *Theory and analysis of peel adhesion: mechanisms and mechanics*. Transactions of The Society of Rheology (1957-1977), 1959. **3**(1): p. 161-180.
- [2] Kaelble, D., *Theory and analysis of peel adhesion: bond stresses and distributions*. Transactions of The Society of Rheology (1957-1977), 1960. **4**(1): p. 45-73.
- [3] Bikerman, J., *Theory of peeling through a Hookean solid*. Journal of applied physics, 1957. **28**(12): p. 1484-1485.
- [4] Spies, G., *The peeling test on redux-bonded joints: A theoretical analysis of the test devised by aero research limited*. Aircraft Engineering and Aerospace Technology, 1953. **25**(3): p. 64-70.
- [5] Kaelble, D., *Peel Adhesion: Micro-Fracture Mechanics of Interfacial Unbonding of Polymers*. Transactions of The Society of Rheology (1957-1977), 1965. **9**(2): p. 135-163.
- [6] Budzik, M., J. Jumel, K.I. ´nska, and M. Shanahan, *Effect of adhesive compliance in the assessment of soft adhesives with the wedge test*. Journal of Adhesion Science and Technology, 2011. **25**(1-3): p. 131-149.
- [7] Dillard, D., *Bending of plates on thin elastomeric foundations*. Journal of applied mechanics, 1989. **56**(2): p. 382-386.
- [8] Ghatak, A., L. Mahadevan, and M.K. Chaudhury, *Measuring the work of adhesion between a soft confined film and a flexible plate*. Langmuir, 2005. **21**(4): p. 1277-1281.
- [9] Bao, G. and Z. Suo, *Remarks on crack-bridging concepts*. Applied Mechanics Reviews, 1992. **45**(8): p. 355-366.
- [10] Xu, X.-P. and A. Needleman, *Numerical simulations of dynamic crack growth along an interface*. International Journal of Fracture, 1995. **74**(4): p. 289-324.
- [11] Geubelle, P.H. and J.S. Baylor, *Impact-induced delamination of composites: a 2D simulation*. Composites Part B: Engineering, 1998. **29**(5): p. 589-602.
- [12] Dugdale, D., *Yielding of steel sheets containing slits*. Journal of the Mechanics and Physics of Solids, 1960. **8**(2): p. 100-104.

- [13] Tang, T. and C.Y. Hui, *Decohesion of a rigid punch from an elastic layer: Transition from “flaw sensitive” to “flaw insensitive” regime*. Journal of Polymer Science Part B: Polymer Physics, 2005. **43**(24): p. 3628-3637.
- [14] Williams, J. and H. Hadavinia, *Analytical solutions for cohesive zone models*. Journal of the Mechanics and Physics of Solids, 2002. **50**(4): p. 809-825.
- [15] Georgiou, I., et al., *Cohesive zone models and the plastically deforming peel test*. The Journal of Adhesion, 2003. **79**(3): p. 239-265.
- [16] Blackman, B., H. Hadavinia, A. Kinloch, and J. Williams, *The use of a cohesive zone model to study the fracture of fibre composites and adhesively-bonded joints*. International Journal of Fracture, 2003. **119**(1): p. 25-46.
- [17] Ouyang, Z. and G. Li, *Local damage evolution of double cantilever beam specimens during crack initiation process: a natural boundary condition based method*. Journal of Applied Mechanics, 2009. **76**(5): p. 051003.
- [18] Plaut, R.H. and J.L. Ritchie, *Analytical solutions for peeling using beam-on-foundation model and cohesive zone*. Journal of Adhesion, 2004. **80**(4): p. 313-331.
- [19] Stigh, U., *Damage and crack growth analysis of the double cantilever beam specimen*. International Journal of Fracture, 1988. **37**(1): p. R13-R18.
- [20] Biel, A. and U. Stigh, *An analysis of the evaluation of the fracture energy using the DCB-specimen*. Archives of Mechanics, 2007. **59**(4-5): p. 311-327.
- [21] Mukherjee, B., D.A. Dillard, R.B. Moore, and R.C. Batra, *Effect of confinement and interfacial adhesion on peeling of a flexible plate from an elastomeric layer*. In preperation, 2016b.
- [22] Ghatak, A., L. Mahadevan, J.Y. Chung, M.K. Chaudhury, and V. Shenoy, *Peeling from a biomimetically patterned thin elastic film*. Proceedings of the Royal Society of London. Series A: Mathematical, Physical and Engineering Sciences, 2004. **460**(2049): p. 2725-2735.
- [23] Adda-Bedia, M. and L. Mahadevan, *Crack-front instability in a confined elastic film*. Proceedings of the Royal Society A: Mathematical, Physical and Engineering Science, 2006. **462**(2075): p. 3233-3251.
- [24] Maugis, D., *Adhesion of spheres: the JKR-DMT transition using a Dugdale model*. Journal of colloid and interface science, 1992. **150**(1): p. 243-269.
- [25] Timoshenko, S., *Theory of Plates and Shells*. 1940: McGraw-hill Book Company.
- [26] Reynolds, O., *On the Theory of Lubrication and Its Application to Mr. Beauchamp Tower's Experiments, Including an Experimental Determination of the Viscosity of Olive Oil*. Proceedings of the Royal Society of London, 1886. **40**(242-245): p. 191-203.
- [27] Wolfram Research, I., *Mathematica*. 2014, Wolfram Research, Inc.: Champaign, Illinois.
- [28] Obreimoff, J., *The splitting strength of mica*. Proceedings of the Royal Society of London. Series A, Containing Papers of a Mathematical and Physical Character, 1930: p. 290-297.
- [29] Ha, K., H. Baek, and K. Park, *Convergence of fracture process zone size in cohesive zone modeling*. Applied Mathematical Modelling, 2015. **39**(19): p. 5828-5836.
- [30] Li, S., J. Wang, and M. Thouless, *The effects of shear on delamination in layered materials*. Journal of the Mechanics and Physics of Solids, 2004. **52**(1): p. 193-214.

5 On preferential debonding during demolding of a sandwiched elastomeric layer

Bikramjit Mukherjee ^a, David A. Dillard ^a, Robert B. Moore ^b, Romesh C. Batra ^a,
^aDepartment of Biomedical Engineering and Mechanics, M/C 0219, Virginia Polytechnic Institute and State University, Blacksburg, Virginia 24061, USA
^bDepartment of Chemistry, M/C 0212, Virginia Polytechnic Institute and State University, Blacksburg, Virginia 24061, USA

Abstract

Separation of an elastomeric layer sandwiched between two flexible molds is a processing step in the fabrication of soft bio-implants such as ophthalmic lenses. The demolding process typically involves prying open the flexible mold assembly by a displacement controlled loading and is engineered so that interfacial separation occurs preferentially from a desired interface. When molds made of the same material are used in a practical manufacturing line, the demolding process runs the risk of causing debonding from the wrong interface and/or both interfaces. These may result in an erratic separation process potentially causing tearing of the interlayer. Of primary interest here is to study roles of (i) the relative flexural rigidities of the two molds, (ii) the curvature when the interlayer is in the shape of a portion of a hemisphere, and (iii) preheating the two molds and the interlayer differentially prior to mechanical loading to steer debonding to the desired interface. These objectives are accomplished by numerically analyzing axisymmetric deformations of a sandwiched elastomeric layer of uniform thickness with its two surfaces bonded to flexible molds with flanges where prying displacements are applied. The interaction at the interfaces between the molds and the interlayer are modeled using a bilinear traction-separation (TS) relation. Results of numerical experiments suggest that (i) debonding occurs preferentially from the edge of the interface between the elastomer and the more flexible mold; however, internal debonding ensues and may grow on the other interface when the molds have high flexural rigidity that depends on the modulus and the thickness of the elastomeric layer, (ii) edge debonding is inherently biased to the interface with the smaller radius mold interface when the interlayer is in the shape of a portion of a hemisphere, and (iii) preferential debonding can be engineered by preheating the assembly differentially; however, a differential large enough dictated by the absolute level of heating may cause internal debonding. Sensitivities of the predicted debonding mechanisms to prescribed biases in the

TS parameters are assessed. The outcomes of this work may be useful in designing demolding processes to achieve desired separation characteristics.

Keywords: Elastomeric interlayer; debonding; cohesive zone model (CZM); peeling; preferential debonding; crack path selection; demolding

5.1 Introduction

The separation of the middle layer in a tri-layer structure from a desired interface is required in a wide variety of manufacturing processes[1-4]. One example is fabrication of soft ophthalmic lenses [5, 6] that involves the release of a sandwiched elastomeric interlayer from a chosen interface. A typical process, shown schematically in Figure 5-1, consists in casting a polymerizable material into a desired shape dictated by two molds, and a subsequent demolding/release process engineered to separate the interlayer from the assembly. The demolding step involves peeling one mold from the interlayer using a displacement-controlled loading. The interlayer retained on the lower mold is subsequently separated by a non-mechanical release process such as hydration. The defect-free separation of the interlayer from the desired interface is pivotal to the success of a demolding process.

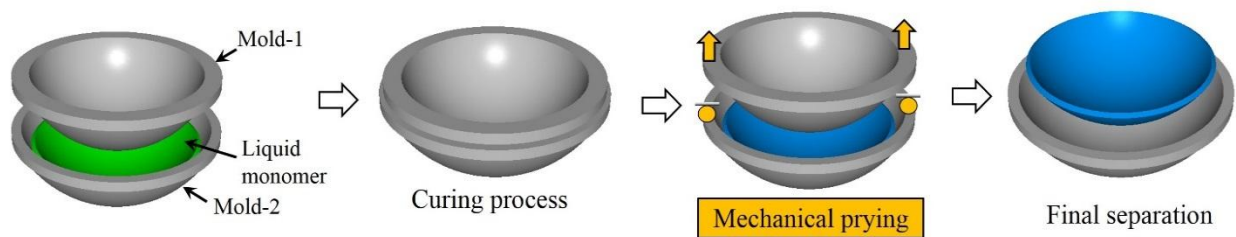


Figure 5-1: Schematics of a demolding process for fabrication of an ophthalmic lens made of an organogel.

The adhesion at the two interfaces must be weak relative to the cohesive strength of the interlayer for the bulk failure not to occur within the confined interlayer under stresses[7] generated during the demolding process. However, the presence of two equally weak interfaces may render the interlayer susceptible to undesirable failure modes (see Figure 5-2), such as debonding from the wrong interface (Figure 5-2b) and/or both interfaces, with the latter leading to stretching of a portion of the pliable interlayer material suspended between the two molds, as illustrated in Figure 5-2c. One possible strategy for biasing debond to the desired interface is to employ sufficient adhesion differential, e.g., via suitable surface treatment [8, 9]. However, in practice molds of the same material are used due to a number of

desirable attributes[10]. Engineering of the demolding process, therefore, involves challenges of identifying the geometric, the material, and the loading parameters that could be tuned to bias and restrict debonding to the desired interface even when both interfaces are equally weak.

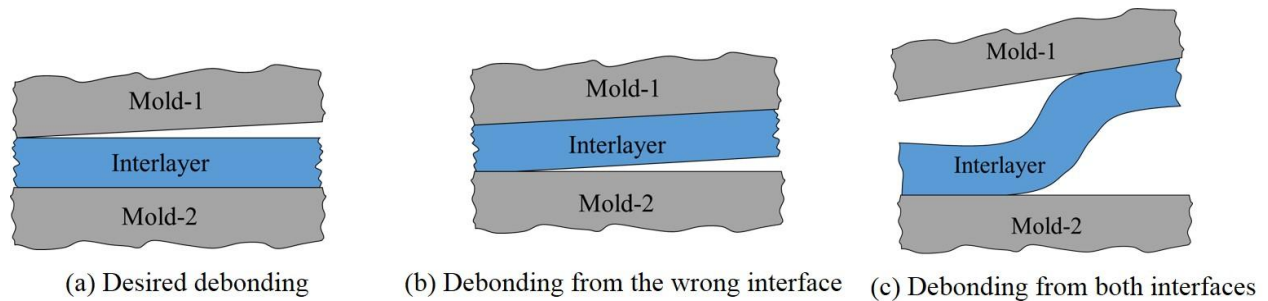


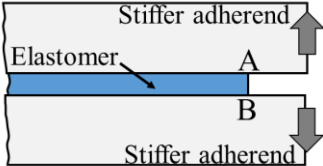
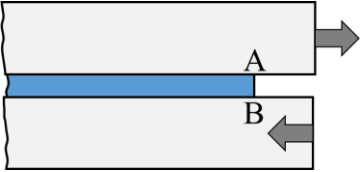
Figure 5-2: Schematic sketches of (a) the desired failure mode of separation from one interface and the undesired modes of separation (b) from the wrong interface and (c) from both interfaces resulting in ‘bridging’.

Debonding from a desired surface has been studied in the context of transfer printing techniques[1] which rely on interfacial separation of substrates from two different sides of an ink layer at different stages during the fabrication process. These studies¹⁰⁻¹⁴ suggest that the preferential debonding can be achieved by adjusting the loading and the geometric parameters. However, there are no similar results available for the above-mentioned demolding problem. Here an attempt has been made to understand preferential debonding of an elastomer layer sandwiched between two flexible but stiffer molds (or adherends) which are mechanically pulled apart by applying axisymmetric displacements at their flat flanges. For two interfaces with identical adhesion, the debonding force should be relatively larger on the desired interface by an amount sufficient to account for stochastic spatial variations in the adhesion expected for real interfaces. There must be at least one source of asymmetry arising possibly from the geometry, the material and the loading to result in different traction distributions on the two interfaces.

As illustrated by sketches in Table 1, the sign of the interfacial shear stresses induced at the edge and the coupling between them and the peeling stress determine if they will tend to open the interface or close it. These examples are for an elastomeric layer sandwiched between two stiff adherends and two loading situations: symmetric normal remote loading and remote shear loading. The effect of interfacial shear induced near the edge on opening/closing is evinced by experimental observations of [Liechti and Wu \[11\]](#) for debonding of a rubber layer sandwiched between metallic adherends, and by [Rahul-Kumar et](#)

al. [12] for a glass/polymer interface in a compressive shear strength test. Asymmetry between stresses at the two interfaces can be induced so that one interface edge has a greater opening shear stress that biases peeling towards it. As potential sources of asymmetric deformation and a concomitant debonding bias, we explore effects of relative flexural rigidities of the two molds, the characteristic curvature of the assembly (flat vs. curved), and differentially preheating the two molds prior to mechanical demolding.

Table 5-1: Illustration of opening and closing at the edge due to the sign of the shear stress

Loading	Corner A		Corner B	
	Shear stress	Peel stress	Shear stress	Peel stress
	Positive	Tensile (opening)	Negative	Tensile (opening)
	Positive	Tensile (opening)	Positive	Compressive (closing)

Analyses[13-15] of the peeling of a flexible plate from an elastomeric layer (firmly bonded to a rigid base) reveal that debonding ensues at interior points on the interface due to a peak in the peel stress there when the confinement, quantified by $(D/\mu h^3)^{1/3}$, is very large. Here D is the bending rigidity of the plate, μ the shear modulus of the interlayer and h its thickness. The confinement also depends on the system geometry. For example, the confinement is given by the ratio a/h for a rigid circular punch of radius a adhered to an elastomeric layer firmly bonded to a rigid base. Interfacial debonding initiates when this ratio exceeds a threshold[16]. However, whether or not internal debonding will occur for a confined interlayer is dictated also by the loading conditions. For example, in the ‘cone tests’ conducted by Anderson et al. [17], as the normal component of the applied load on the interfaces increased, large peel stresses occurred over the interior of the interface for some values of the cone angle. Accordingly, the debonding mechanism began to include internal

initiation. This phenomenon of internal debonding for confined interlayers has potential implications in the demolding of a sandwiched interlayer. With one debond initiated at the edge singularity dominant region at the interface dictated by engineered opening bias, internal debonding on the other interface may cause the undesirable failure mode of bridging as displayed in [Figure 5-2b](#).

As a model problem we analyze by the finite element method (FEM) axisymmetric deformations of an elastomeric layer of constant thickness sandwiched between two curved molds that are parts of spheres and have flat edge overhangs where normal displacements are applied to pull apart the assembly. The interaction at the interfaces are simulated using a cohesive zone model (CZM)[18, 19] and a bilinear traction-separation (TS) relation[20]. In a CZM, two adjoining points at an interface are conceived to be connected by a spring of zero length characterized by the TS relation. The spring begins to soften after the traction reaches a prescribed peak value (strength) and the separation occurs at that interfacial location when the spring breaks at a critical value of the spring extension. The energy dissipated in the spring at failure equals the fracture energy of the interface. Unlike linear elastic fracture mechanics (LEFM) based methods, the CZM offers the advantage of modeling nucleation as well as propagation of interfacial debonding.

As mentioned above, the objectives are to explore avenues for biasing debonding to one of the two interfaces by (i) using one mold relatively stiffer than the other, (ii) the radius of curvature, and (iii) differential pre-heating of the two molds.

5.2 Problem description and computational approach

A schematic of the problem studied is displayed in [Figure 5-3](#). The domain of interest consists of an elastomeric layer of constant thickness h that is in the shape of a portion of a hemisphere with the radius and the semi arc-length of the upper surface equal to r_1 and s , respectively. The layer is sandwiched between two molds of the same geometry as the interlayer. Each mold has a small flat flange where pry displacements[10] are applied to pull apart the assembly. The two molds may be made of different materials.

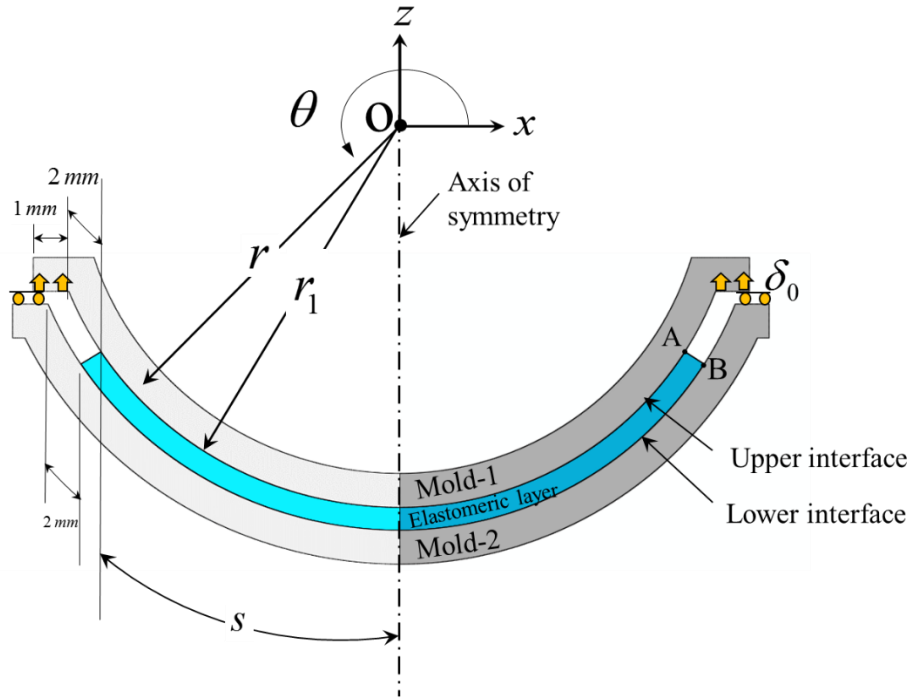


Figure 5-3: Schematic of the problem studied

The infinitesimal deformations of the two molds and the elastomeric layer are described by using a spherical coordinate system (r, θ, φ) where r is the radial direction from the origin O , θ the in-plane angular direction, and φ the out-of-plane angular direction (not shown), and are assumed to be symmetric about the axis $\theta = \pi/2$. Neglecting body and inertia forces the deformations are governed by

$$\begin{aligned} \frac{\partial \sigma_{rr}}{\partial r} + \frac{1}{r} \frac{\partial \sigma_{r\theta}}{\partial \theta} + \frac{1}{r} (2\sigma_{rr} - \sigma_{\theta\theta} - \sigma_{\varphi\varphi} + \sigma_{r\theta} \cot \theta) &= 0, \\ \frac{\partial \sigma_{r\theta}}{\partial r} + \frac{1}{r} \frac{\partial \sigma_{\theta\theta}}{\partial \theta} + \frac{1}{r} ((\sigma_{\theta\theta} - \sigma_{\varphi\varphi}) \cot \theta + 3\sigma_{r\theta}) &= 0 \end{aligned} \quad (5-1)$$

where σ_{rr} , $\sigma_{\theta\theta}$ and $\sigma_{\varphi\varphi}$ are normal stresses in the r , θ and φ directions, respectively, and $\sigma_{r\theta}$ the in-plane shear stress.

For infinitesimal deformations the strain-displacement relations are

$$\begin{aligned}\varepsilon_{rr} &= \frac{\partial u_r}{\partial r}, \varepsilon_{\theta\theta} = \frac{1}{r} \frac{\partial u_\theta}{\partial \theta} + \frac{u_r}{r}, \varepsilon_{\phi\phi} = \frac{u_\theta \cot \theta}{r} + \frac{u_r}{r}, \\ 2\varepsilon_{r\theta} &= 2\varepsilon_{\theta r} = \frac{\partial u_\theta}{\partial r} - \frac{u_\theta}{r} + \frac{1}{r} \frac{\partial u_r}{\partial \theta}, \\ \varepsilon_{r\varphi} &= \varepsilon_{\varphi r} = \varepsilon_{\theta\varphi} = \varepsilon_{\varphi\theta} = 0,\end{aligned}\tag{5}$$

where ε_{rr} , $\varepsilon_{\theta\theta}$ and $\varepsilon_{\phi\phi}$ are normal strains and $\varepsilon_{r\theta}$ is the in-plane shear strain. The radial and the circumferential components of the displacement vector are denoted by u_r and u_θ , respectively.

We assume that the temperature change, if any, is known. In linear thermoelasticity the normal strains can be split as

$$\varepsilon_{rr} = \varepsilon_{rr}^e + \varepsilon_{rr}^T, \varepsilon_{\theta\theta} = \varepsilon_{\theta\theta}^e + \varepsilon_{\theta\theta}^T, \varepsilon_{\phi\phi} = \varepsilon_{\phi\phi}^e + \varepsilon_{\phi\phi}^T,\tag{5}$$

where superscripts ‘ e ’ and ‘ T ’ denote the elastic and the thermal components, respectively. The thermal strains are given by

$$\varepsilon_{rr}^T = \varepsilon_{\theta\theta}^T = \varepsilon_{\phi\phi}^T = \tilde{\alpha} \Delta T\tag{5}$$

where $\tilde{\alpha}$ and ΔT are, respectively, the coefficient of thermal expansion and the change in temperature.

Subscripts ‘1’, ‘2’, and ‘*elas*’ are used to denote quantities for mold-1, mold-2, and the elastomeric interlayer, respectively, unless indicated otherwise.

The molds and the interlayer materials are assumed to be homogeneous, isotropic and Hookean. Thus their constitutive equations are

$$\sigma_{ij} = \frac{2\mu\nu}{(1-2\nu)} \varepsilon_{kk}^e \delta_{ij} + 2\mu \varepsilon_{ij}^e,\tag{5-5}$$

Indices i and j take values r, θ and φ with a repeated index implying summation over the range of the index. Furthermore, μ and ν are, respectively, the shear modulus and Poisson’s ratio of a material, and δ_{ij} is the Kronecker delta. With the shear modulus of the interlayer appearing frequently in the paper, we drop the subscript ‘*elas*’ from μ_{elas} . In order to model the nearly-incompressible deformations of the elastomer its Poisson’s ratio is set equal to 0.4999999.

The smooth (frictionless) flange of the upper mold is vertically displaced by applying to it a monotonically increasing displacement δ_0 while the smooth flange of the lower mold is restrained from moving vertically. The assumed axisymmetry of deformations implies that the horizontal displacement of points on the axis of symmetry must equal zero. These boundary conditions can be written as

$$\text{Upper flange} \quad u_i n_i = \delta_0 \quad (5-6)$$

$$\text{Lower flange, and axis of symmetry} \quad u_i n_i = 0 \quad (5-7)$$

The remainder of the bounding region is assumed to be traction-free. That is,

$$\sigma_{ij} n_j = 0 \quad (5-8)$$

In eqs. (5-6)-(5-8), n_j is the j^{th} component of the outward unit normal at a point on the bounding surface.

The interactions between the molds and the interlayer at their interfaces are modeled by the bilinear traction-separation (TS) relation (2-3) that is plotted in Figure 5-4. For simplicity, it is assumed that the interfaces are much weaker in the normal (or the radial) direction than in the tangential traction and, therefore, fail in mode-I when subjected to combined tangential and normal tractions[21].

$$T_n(\delta) = \begin{cases} K\delta & (0 \leq \delta \leq \delta_c) \\ \frac{T_c}{\delta_f - \delta_c}(\delta_f - \delta) & (\delta_c \leq \delta \leq \delta_f) \\ 0 & (\delta_f \leq \delta) \end{cases} \quad (5-9)$$

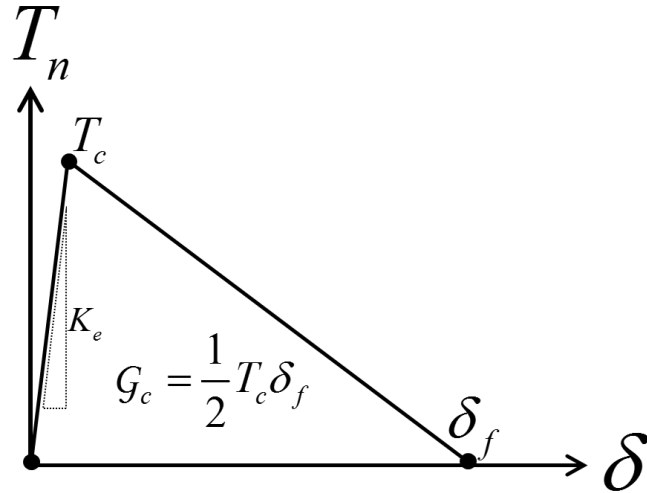


Figure 5-4: The bilinear TS relation

That is, the peel stress (T_n) increases linearly (with slope K_e) with an increase in the jump in the normal component δ of the interfacial displacement until $\delta = \delta_c$ and $T_n = T_c$ when damage initiates at that point. The peel stress then decreases affinely with further increase of δ until $\delta = \delta_f$ when the two surfaces separate from each other. The area under the TS curve equals the fracture energy, G_c , of the interface. That is,

$$G_c = \frac{1}{2} T_c \delta_f \quad (5-10)$$

The value of the initial slope K_e must be large enough[22] to minimize the artificial compliance introduced into the system and avoid inter-penetration under compression. However, a very large value of K_e can make the system matrices ill-conditioned when the problem is numerically analyzed by the FEM. An appropriate value of K_e is usually found by trial and error even though a few guidelines are available in the literature.

The boundary value problem (BVP) defined by Eqs. (5-1) - (2-4) is challenging due to the possibility of debonding at *a priori* unknown points. The FEM is used to numerically solve the BVP with the commercial software ABAQUS/Standard[23]. In the ABAQUS terminology CAX4 (axisymmetric rectangular, 4-node, 4-point integration) elements are used to discretize the molds and the interlayer. A surface-based contact interaction[23] is used for the interfaces between the molds and the interlayer. Numerical instabilities and the associated convergence difficulties are alleviated by employing the “Damage Stabilization” option (viscous regularization) in ABAQUS. The value 10^{-7} of the

stabilization parameter was found as a compromise between the computation time required to solve the problem and the numerical dissipation introduced into the solution.

The solution of the present BVP depends upon the following non-dimensional parameters.

Geometry	$(D_1 / \mu h^3)^{1/3}, (D_2 / D_1)^{1/3}, s\beta_1, r_1\beta_1, \theta$
Thermal expansion effects	$\Delta T_1 \tilde{\alpha}_1, \Delta T_2 \tilde{\alpha}_2, \Delta T_{elas} \tilde{\alpha}_{elas}$
Adhesion (TS parameters)	$T_{c1}^2 h / G_{c1} E, T_{c1} / T_{c2}, G_{c1} / G_{c2}$
Loading	Δ_0

where $D = Et^3 / 12(1 - \nu^2)$ is the flexural rigidity of a mold of thickness t and Young's modulus E , $\beta_1^{-1} = (D_1 h^3 / 12\mu)^{1/6}$, $\Delta_0 = \delta_0 / \delta_{f1}$ is the critical contact opening for debonding initiation at the interlayer/mold-1 interface. A larger value of D implies a lower flexibility.

In problems involving peeling of a flexible flat plate from an elastomer layer whose other surface is firmly bonded to a fixed flat rigid base[13, 24], the parameter $\alpha_1 = (D_1 / \mu h^3)^{1/3}$ quantifies the geometric confinement of the interlayer and significantly affects the distribution of the peel stress on the interface being debonded. However, in the present problem, the effective confinement should also depend on $\alpha_2 = (D_2 / \mu h^3)^{1/3} = \alpha_1 (D_2 / D_1)^{1/3}$ since debonding is allowed at both interfaces. The symbol η is introduced for $(D_2 / D_1)^{1/3}$. The length β_1^{-1} represents the characteristic decay of oscillations[25] of the plate deflection along the direction of peeling of one flexible flat plate from an elastomeric layer bonded to a fixed base (although there may be additional dependence on the curvature for finite values of r_1). Numerical simulations have shown that the parameter[15] $\phi = T_{c1}^2 h / \mu G_{c1}$ governs the interfacial damage zone size (cohesive zone length) and the onset of adhesion-induced instability[15] in debonding of a confined elastomeric interlayer. Quantities T_{c1} / T_{c2} and G_{c1} / G_{c2} are, respectively, ratios of the strengths and the fracture energies of the interlayer interfaces with molds 1 and 2, and may be used to quantify bias in the adhesion

characteristics of the two interfaces. Unless otherwise specified identical adhesion at the two interfaces with $T_{c1}/T_{c2} = G_{c1}/G_{c2} = 1$ is assumed.

The investigation is started with a flat mold assembly as a special case of curved assemblies ($r_1 \rightarrow \infty$) with identical values of material and geometric parameters for both molds and $s = 10 \text{ mm}$. Whereas axisymmetric deformations with both molds deformable are studies here, in the previous work[15] the elastomeric layer was firmly bonded to the rigid flat mold 2. As expected, the debonding initiates symmetrically at both interfaces, although numerical perturbations introduced in an FE solution may subsequently cause asymmetry. With the objective of investigating systematically the possibility of preferential debonding at the upper/lower interface by utilizing asymmetric deformations, η is varied at different values of α_1 to explore the effect of using one mold relatively more flexible than the other at different values of the confinement. What emerges is a ‘map’ of interfacial debonding modes as a function of the relative and the absolute rigidities of the molds for elastomeric layers of given modulus and thickness. A similar investigation is then conducted for curved mold-assemblies to explore how the above results are affected by the curvature.

Finally, the effect of heating one mold more than the other on debonding bias is explored for the flat mold assembly. For simplicity, heating is simulated, instead of solving the energy balance equation, by specifying homothermal temperature increments, ΔT_1 and ΔT_2 , for the upper and the lower molds, respectively. The interlayer temperature increment is set as $(\Delta T_1 + \Delta T_2)/2$. The temperature increment of the lower mold, ΔT_2 , (a lower value means a larger temperature differential) is varied for different values of ΔT_1 to explore the effect of differential temperature increment. The outcome is again a ‘map’ of debonding modes as a function of the absolute level of heating and the temperature differential between the molds. An approximation made here is that there is no heat exchange across the interface between two materials at different temperatures.

The TS parameters are adjusted so that all numerical experiments correspond to a constant value $\phi = 3$. Unless otherwise specified, $K_e = 10^6 \text{ N/mm}^3$ is used. It has been checked that the key conclusions remain unaffected upon further increasing the value of K_e , although interfacial damage accumulation at a given displacement is relatively less for a larger K_e value. For example, the total damaged/debonded length at $\Delta_0 = 2.35$ is $\sim 13\%$ larger when a 50% larger value of K_e was used for the parameters

$\alpha_1 = 10, \eta = 0.7, \beta_1^{-1} = 1\text{mm}, \mu = 20\text{MPa}, \phi = 3, T_c = 0.08\text{MPa}, \Delta_o = 2.35$ and damage was suppressed at the lower interface.

In order to rationalize our findings about damage initiation at the two interfaces, the problem is first analyzed by assigning large sufficiently values to T_{c1} and T_{c2} (the value of 100MPa was large enough for all the cases investigated and the FE mesh-1) to prevent damage initiation at the interfaces. It is critical, therefore, to address the singular stress fields near the corners A or B. For our material pairs of interest, the Dundurs[26] parameters are $\alpha_D \sim 1$ and $\beta_D \sim 0$, which yield[27] $T_n \sim H_1 R^{-0.406}$ where H_1 is the intensity of the singular field near the corner and R the radial distance from the corner. The FE mesh 1 used to analyze the problem is sufficiently fine close to the corners to capture the correct order of singularity. However, for analyses of damage/debonding initiation, a coarser FE mesh 2 is used. It has been concluded by comparing the results for the two FE meshes that the damage/debonding behavior is essentially the same. The details of these FE meshes and the results of mesh refinement studies are included in the following section.

In order to judge whether the computational approach captures the physics of debonding in a confined geometry as a function of geometry/loading changes, the ‘cone test’ was simulated [28] in light of its relevance to the demolding problem. The predicted debonding mechanisms were found to qualitatively agree with the experimental results of Anderson et al. [17].

For the example problem $\alpha_1 = 10, \eta = 0.7, \beta_1^{-1} = 1\text{mm}, \mu = 20\text{MPa}, \phi = 3, T_c = 0.08\text{MPa}$, and $\Delta_o = 9.4$, the computed results gave the stored energy = $2.04\mu\text{J}$, the energy spent in damage/debonding = $5.2\mu\text{J}$, and the artificial viscous losses = $0.053\mu\text{J}$. These energies add up to $7.3\mu\text{J}$ which is found to differ by 1.55% from the work, $7.41\mu\text{J}$, done by external forces. For all problems studied the energy balance was satisfied within ~5% discrepancy. The computed strain energy is much smaller than the damage/debonding energy because most of the interfacial region is damaged/debonded for the indicated value of the applied displacement. Estimating the total dissipated energy as $\sim G_c A_{\text{debonded}}$ (where A_{debonded} is the total debonded area) shows agreement (~10% difference) with that computed by ABAQUS.

5.3 Results and discussion

5.3.1 Effect of the FE mesh

Axisymmetric deformations in the xz -plane of the elastomeric layer sandwiched between flat molds ($r_1 \rightarrow \infty$) are analyzed to establish the adequacy of the FE mesh for (i) resolving stress singularities near the corners with interfacial damage suppressed, and (ii) for computing the damage and debonding at interfaces between the interlayer and the molds.

Results are examined for three FE meshes. For each mesh the two mold regions are discretized with uniform square elements of side 0.05 mm. In FE mesh 1, except for a 0.125 mm wide region abutting the traction free edge, the interlayer region is divided into uniform square elements of side 0.0125 mm and the 0.125 mm \times h region with non-uniform quadrilateral elements of width and height (as defined on the interface and the free edge, respectively) varying from 0.0125 mm in the interior to 10^{-5} mm at the corner. The FE mesh 3 differs from the mesh 1 only in the 0.125 mm \times h region. In mesh 3 the element height varied from 0.0125 mm to 0.5×10^{-5} mm for elements at the corners. Sketches of FE meshes 1 and 2 are exhibited in Figure 5-5.

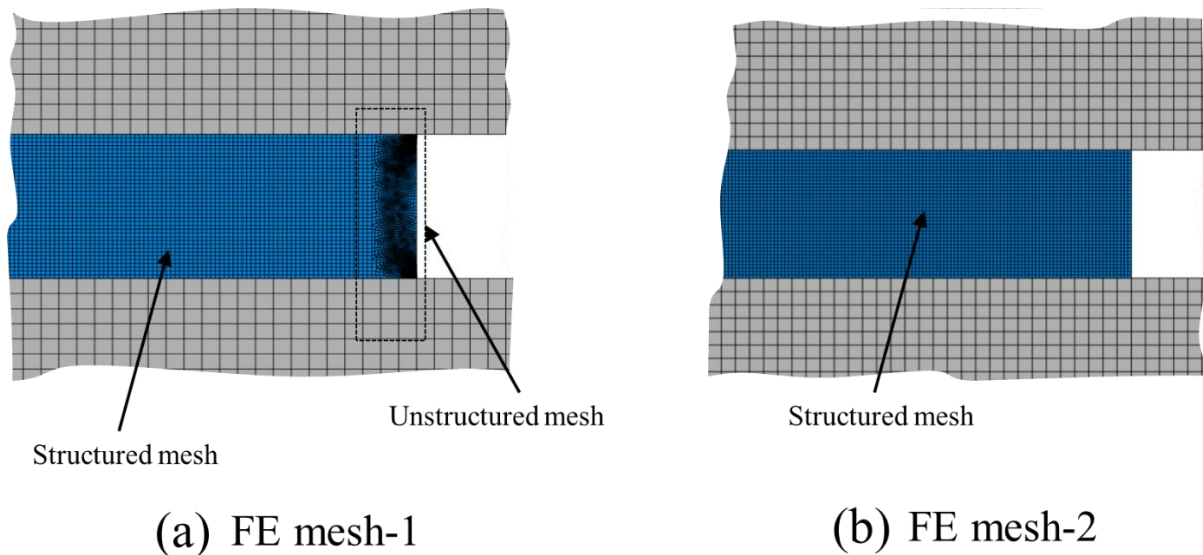


Figure 5-5: The FE meshes 1 and 2 used, respectively, for analyzing stresses over interfaces without (FE mesh 1) and with (FE mesh 2) the possibility of damage initiation and propagation.

It should be evident from distributions of the peel stress on the interface between the elastomeric layer and mold 1 computed with the FE meshes 1 and 2 and displayed in Figure

5-6a that the two distributions overlap each other except at points near the corner of the free edge. The distributions of the peel stress at interfacial points near the corner found using FE meshes 1 and 3 are exhibited in Figure 5-6b. The orders of singularity obtained by linear fit to the data points are -0.408 and -0.407, respectively. They agree well with the theoretically predicted order of -0.406. Thus FE meshes 1 and 3 in the region near the corner are fine enough to resolve the order of stress singularity at the interface.

The non-dimensional interfacial openings computed with FE meshes 1 and 2 and plotted in Figure 5-7 are close to each other over the entire interface. Thus the FE mesh 2 is reasonable for analyzing damage/debonding even though it is not suitable for finding stress singularities near the corner. The FE mesh 2 is used for most of the simulation results reported below.

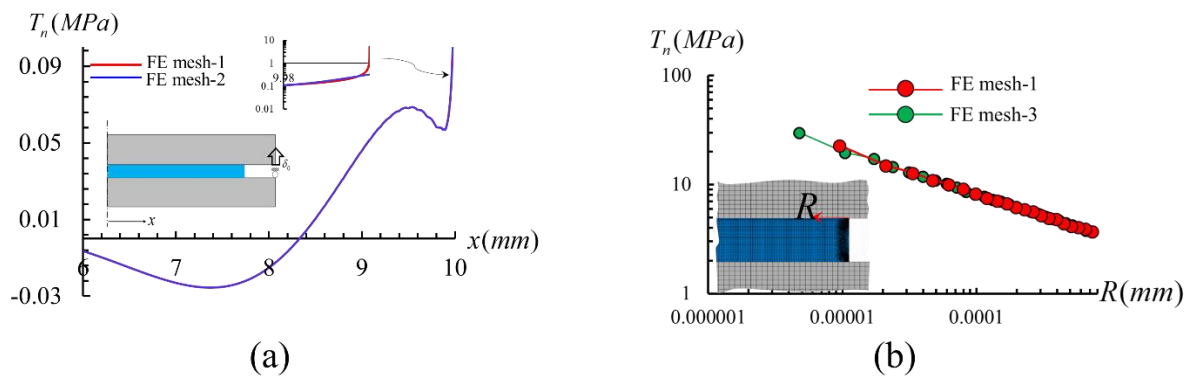


Figure 5-6: Distributions of the peel stress (a) over the upper interface for FE meshes 1 and 2, and (b) near the upper interface corner for FE meshes 1 and 3 plotted on a log-log scale. $\alpha_1 = 10, \eta = 0.2, \beta_1^{-1} = 1\text{mm}, \mu = 5\text{MPa}, \Delta T_1 = \Delta T_2 = \Delta T_{elas} = 0$, and $\delta_0 = 4\mu\text{m}$

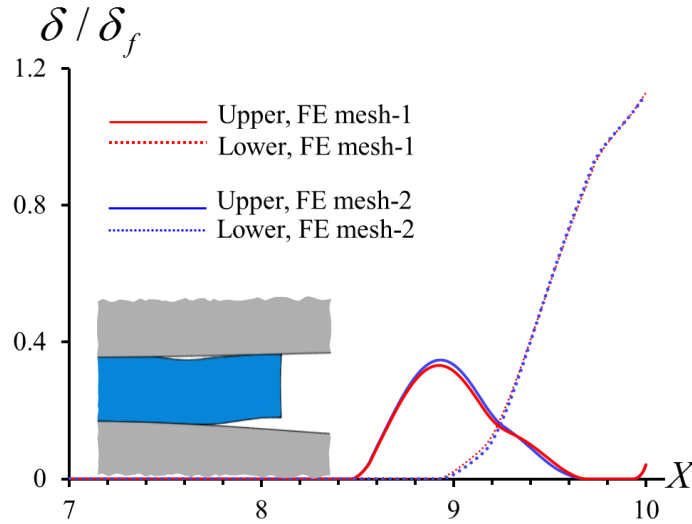


Figure 5-7: Comparison of the non-dimensional interfacial opening computed with FE meshes 1 and 2 for following values of parameters: $\alpha_1 = 10, \eta = 0.7, \phi = 3, \beta_1^{-1} = 1mm, \Delta T_1 = \Delta T_2 = \Delta T_{elas} = 0, \Delta_0 = 2.35$

5.3.2 Flat molds of different flexural rigidities

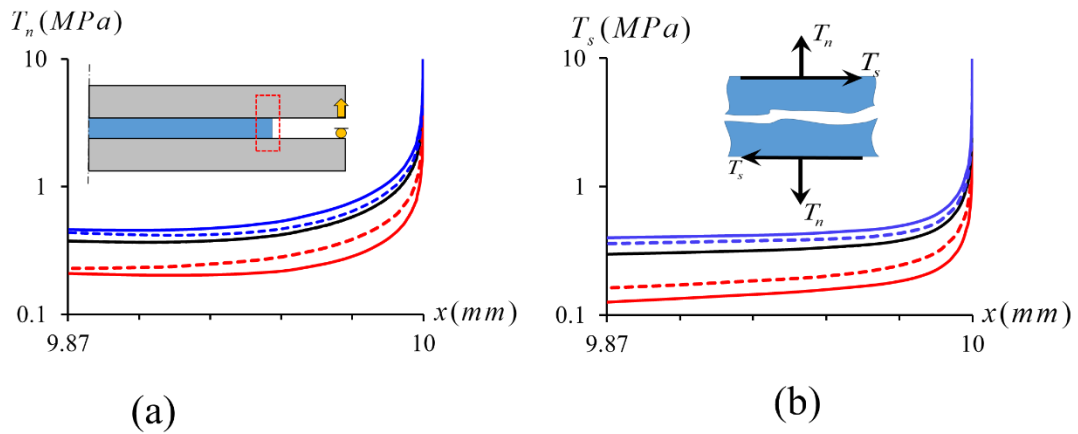
5.3.2.1 Interfacial damage suppressed

Figure 5-8 exhibits distributions of the computed interfacial traction components at points close to the interlayer edge for three values of η when $\alpha_1 = 10^{xxiii}$ and $\delta_0 = 4\mu m$. The distributions of the normal (Figure 5-8a) and the tangential tractions (Figure 5-8b) are the same for the two interfaces when $\eta = 1$, i.e., for identical molds (recall $\eta = (D_2 / D_1)^{1/3}$). It is evident that for $\eta = 0.5$, i.e., when the lower mold is twice as flexible (or half as rigid) than the upper one, the peel stress at the lower interface decays at a slower rate from corner B than that at the upper interface from corner A. This is consistent with a similar bias in the decay rate in the opening shear stress near the two corners (the lower interface shear traction is multiplied by -1 to facilitate comparison of the opening shear stresses). This asymmetry is qualitatively reversed when the upper mold is more flexible than the lower one ($\eta = 2$). However, this is not exactly opposite to that for $\eta = 0.5$ since for $\eta = 2$ the flexural rigidity of the lower mold is made twice while keeping that of the upper mold fixed. This results in an increase in the overall confinement of the system. The asymmetric deformation and the

^{xxiii} One set of values for $\eta = 1, \alpha_1 = 10, \beta_1^{-1} = 1mm$, and $\phi = 3$ is $E_1 = E_2 = 5981.13MPa, \nu_1 = \nu_2 = 0.3, t_1 = t_2 = 1mm, \mu = 20MPa, h = 478.48\mu m$, and $K_e = 10^6 N / mm^3, T_{c1} = T_{c2} = 0.08MPa, G_{c1} = G_{c2} = 1.701 \times 10^{-5} N / mm$

concomitant opening shear bias can be visualized from the exaggerated deformed shapes shown in Figure 5-8c.

Distributions of the peel and the shear stresses over the entire interfaces exhibited in Figure 5-9a-c evince a local peak in the peel stress at interior points of the interfaces away from the corners. The points of the internal peak peel stress are situated at a the minimum distance $b \sim \beta^{-1}$ from the corner, where the shear stress is close to zero as can be seen from Figure 5-9c. Here β^{-1} is the characteristic stress-decay distance from the edge, and $\beta_1^{-1} \sim (D_1 \mu / h)^{1/6}$ when the lower mold is almost rigid [13, 24]. The hydrostatic stress (multiplied by -1) on the upper interface for $\eta = 1$ is also plotted in Figure 5-9a. It reveals that the normal traction essentially equals the hydrostatic in the internal peak region as also evinced by much smaller values of shear tractions plotted in Figure 5-9c. The magnitude of the internal peak and the area over which large internal peel stresses occur increases with an increase in the value of η at a fixed value of $\alpha_1 (=10)$ and with an increase in the value of α_1 at a fixed value of $\eta (=1)$. Previous analyses [13, 14, 24] of plane strain deformations of peeling of a semi-infinite plate from an elastomeric layer bonded to a rigid base (i.e., $\eta \rightarrow \infty$) gave similar trends. While confinement was quantified in those studies by the single dimensionless number α_1 , the overall/effective confinement in the present problem depends on both α_1 and η as evinced by the plots in Figure 5-9a,b. Figure 5-9d exhibits magnitudes of the internal peak peel stress at the upper interface, denoted as $T_{n\max}^{\text{internal}}$, as a function of η for three values of α_1 . Also plotted is the % difference, $\Omega = 100 \left(1 - \left(T_{n\max}^{\text{internal}} \right)_{\text{lower}} / \left(T_{n\max}^{\text{internal}} \right)_{\text{upper}} \right)$, between magnitudes of the internal peak peel stresses at the two interfaces. One can observe that while magnitudes of the peak peel stress increase monotonically as the overall confinement increases with α_1 and/or η , the upper interface has a slightly larger magnitude of the internal peak when $\eta < 1$. This suggests that possible debonding initiation at the location of the local peak peel stress is slightly biased towards the interface with the less flexible mold. However, the absolute value of Ω decreases as the overall confinement increases, implying that internal damage may nucleate at both interfaces for large values of the confinement.



Dashed: lower interface, Solid: upper interface Black: $\eta=1$, Blue: $\eta=2$, Red: $\eta=0.5$

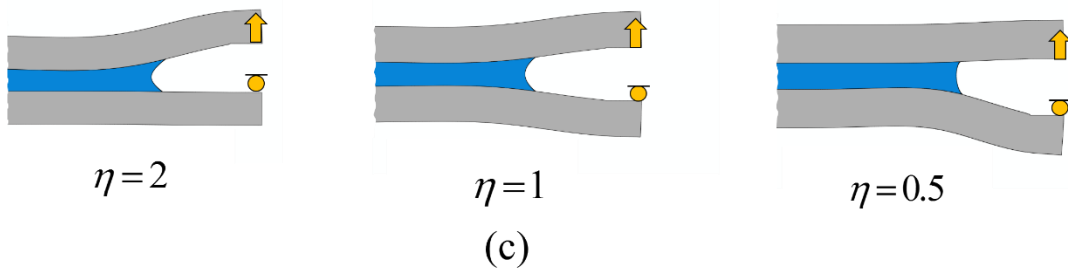


Figure 5-8: Distributions of the computed interfacial (a) peel and (b) shear stress at interface points close to the free edge of the interlayer for three values of η when $\alpha_1 = 10$, $\mu = 20 \text{ MPa}$, $\beta_1^{-1} = 1 \text{ mm}$, and $\delta_0 = 4 \mu\text{m}$. The inset in (b) illustrates directions of the positive interfacial traction components. To facilitate comparison in (b), the shear stress at the bottom interface is multiplied by -1. Deformed shapes (exaggerated by a factor of 100) are illustrated in (c) for the three values of η . These results are for interfaces that are yet to damage.

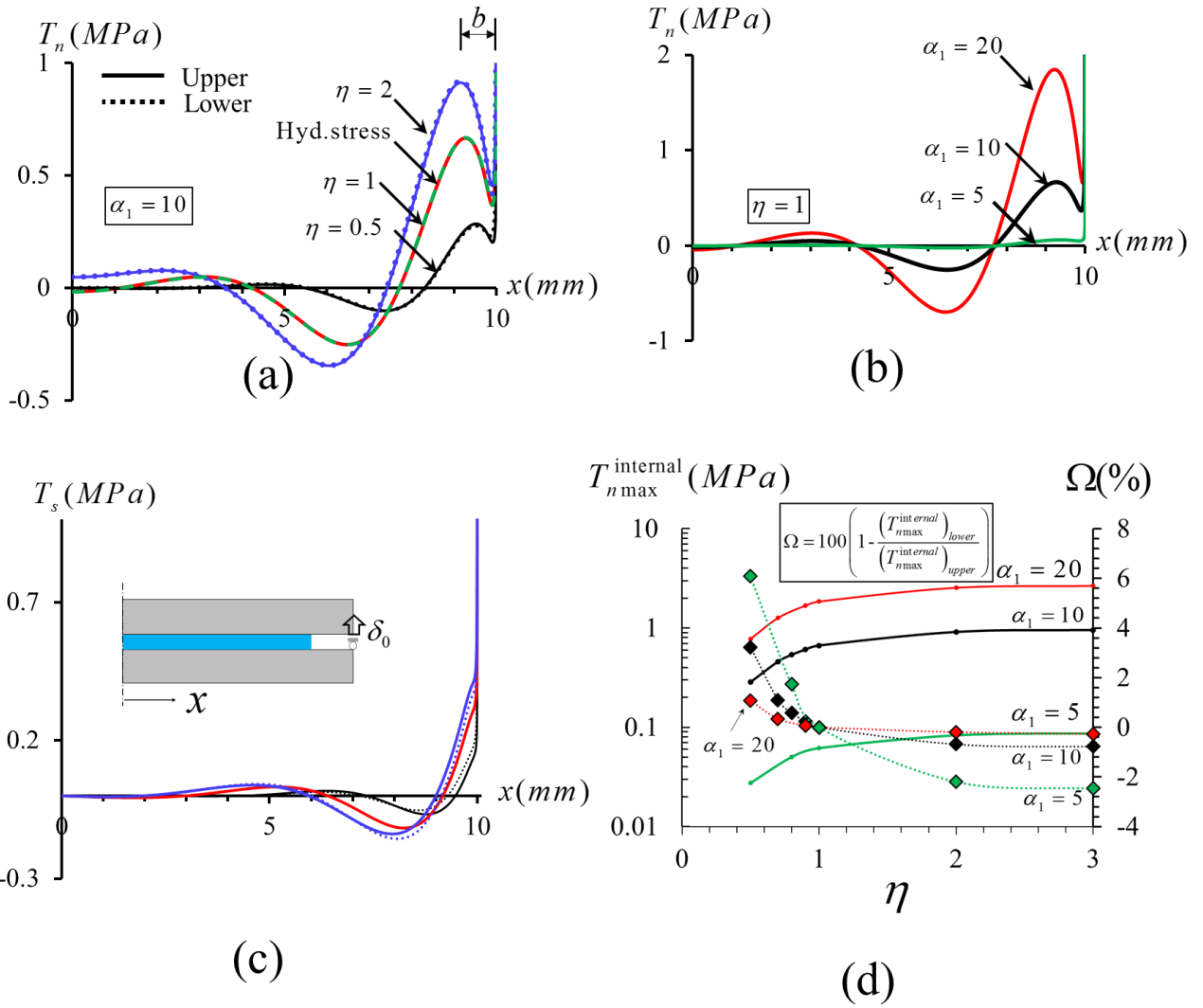


Figure 5-9: Distributions of the interfacial peel stress (a) for three values of η when $\alpha_1 = 10$, (b) for three values of α_1 when $\eta = 1$, (c) distributions of the interfacial shear stress for three values of η when $\alpha_1 = 10$; (d) variations of the magnitude of internal peak peel stress at the upper interface as a function of η for three values of α_1 and the % difference, Ω , between the magnitudes of internal peaks at the two interfaces (Ω is plotted on the vertical axis on the right hand side). For illustration in (c), the shear stress at the bottom interface is multiplied by -1. The plot of hydrostatic tension on the upper interface is included in (a).

5.3.2.2 Interfacial damage considered

Recall that after the peel stress at an interfacial point reaches the prescribed strength T_c , softening for $\delta > T_{cl} / K_e$ ensues at that point with the two surfaces separating from each other when the relative vertical displacement, δ , equals the critical value δ_f . Henceforth, the term cohesive zone (CZ) is used for the region over which the peel stress corresponds to the softening portion of the TS relation. Numerical experiments are conducted by varying η for

three values of α_1 . The exaggerated deformed shapes at three values of the applied non-dimensional displacement, Δ_0 , are exhibited in Figure 5-10 for $\eta = 1, 2, 0.7$ and 0.2 when $\alpha_1 = 10$. As can be seen from Figure 5-10a, the debonding behaviors are identical at the two interfaces for $\eta = 1$. Although it seems to contradict at first sight experimental observations, this is expected in a deterministic analysis. Nevertheless, as mentioned before, the debonding evolution may become asymmetric in FE simulations due to numerical perturbations. At each interface, when the peak peel stress exceeds T_c at an interior point (see Figure 5-9b), the damage begins to initiate there and at the corner. Upon continued loading the two CZs coalesce to form one single opening which propagates as an edge crack. However, for $\eta = 2$, with the upper mold bending more than the lower mold and the associated peeling bias at corner A, the damage near the edge of the interlayer occurs preferentially at A as shown in Figure 5-10b. Owing to a very small ($\sim 0.2\%$) difference (see Figure 5-9d) in magnitudes of the peak peel stresses at the two interfaces prior to damage initiation, a CZ forms at interior points on both interfaces. With continued loading an edge crack forms on the upper interface upon the coalescence of the internal CZ with the edge CZ. The internal CZ on the lower interface begins to propagate preferentially away from the edge CZ which is shielded by the growth of the edge crack on the upper interface. With internal debonding growing at the lower interface in addition to the edge crack on the upper interface, the debonding process becomes complex and is envisioned to be detrimental to a manufacturing operation as it may tear the interlayer due to the bridging phenomenon. The mechanism gets reversed when the lower mold is more flexible than the upper mold. An example, $\eta = 0.7$, is illustrated in Figure 5-10c. When the overall confinement of the interlayer becomes sufficiently small as the value of η is gradually decreased, the internal peak, if any, in the peel stress distribution is no longer large enough to cause initiation of damage internally. In such cases, debonding initiates and propagates only from the edge that has the opening bias dictated by the relative flexural rigidities of the two molds. For example, as exhibited in Figure 5-10d, when the lower mold is more flexible than the upper mold, e.g., $\eta = 0.4$, debonding initiates at corner point B and propagates on the lower interface. Our numerical experiments revealed that for some intermediate values of η , damage may initiate at interior points on both interfaces and one internal CZ may get shielded due to the dominant edge damage at the other interface.

The debonding mechanisms are summarized in Figure 5-11 on the $\alpha_1\alpha_2 - \eta$ plane. Unfilled circles denote symmetric debonding for $\eta = 1$. Green diamonds and blue triangles, respectively, are used to represent debonding from points B and A with no internal opening. All other mechanisms include internal opening in addition to that at the edge and are indicated in Figure 5-11 using red filled circles. It is clear that for each value of α_1 there is a threshold value of η beyond which internal opening ensues in addition to the edge debonding dominant at the interface with the more flexible mold. Similarly, for a given value of α_2 , internal debonding ensues in addition to the edge debonding at point A when η is small enough. It is noteworthy that the threshold value of η decreases (increases) with α_1 (α_2). This implies that interfaces become more susceptible to internal opening as the overall confinement increases. Although details of the debonding evolution following internal initiation may vary, different mechanisms within this category are not distinguished since this debonding mechanism is conjectured to be a pre-cursor to bridging or an erratic debonding process.

While our focus is on problems with identical adhesion at the two interfaces, one may argue that there may be stochastic variations of these quantities on the two interfaces owing to fabrication, roughness, improper curing, surface cleanliness, and other factors. Therefore, it is instructive to assess how sensitive the predictions of debonding mechanisms are to a prescribed variation (bias) in the TS parameters. For $\alpha_1 = 10$ numerical experiments have been conducted for $\eta = 0.4$ and 0.7 , and results are summarized in Table 5-2 and Table 5-3, respectively. One can see that the predicted mechanism of debonding from corner B remains unchanged even when the strength of the lower interface is 200% larger than that of the upper interface. This mechanism is relatively more sensitive to a prescribed bias in the fracture energy, although it remains insensitive to a bias as large as 100%. For the imposed G_c -bias of 200%, edge damage is still predominant near corner B, while the weaker upper interface begins to debond internally and coalesces with the edge CZ. The dominant edge CZ at the lower interface is subsequently shielded. The results summarized in Table 5-3 for the debonding mechanism predicted for $\eta = 0.7$ reveal that imposed biases as small as 5% and 1%, respectively, in the strength and the fracture energy change the debonding mechanism. This finding substantiates the conjecture that internal debonding should be avoided from an

engineering perspective as local weak regions, if any, are likely to debond internally near the region of internal large peel stresses and may lead to bridging.

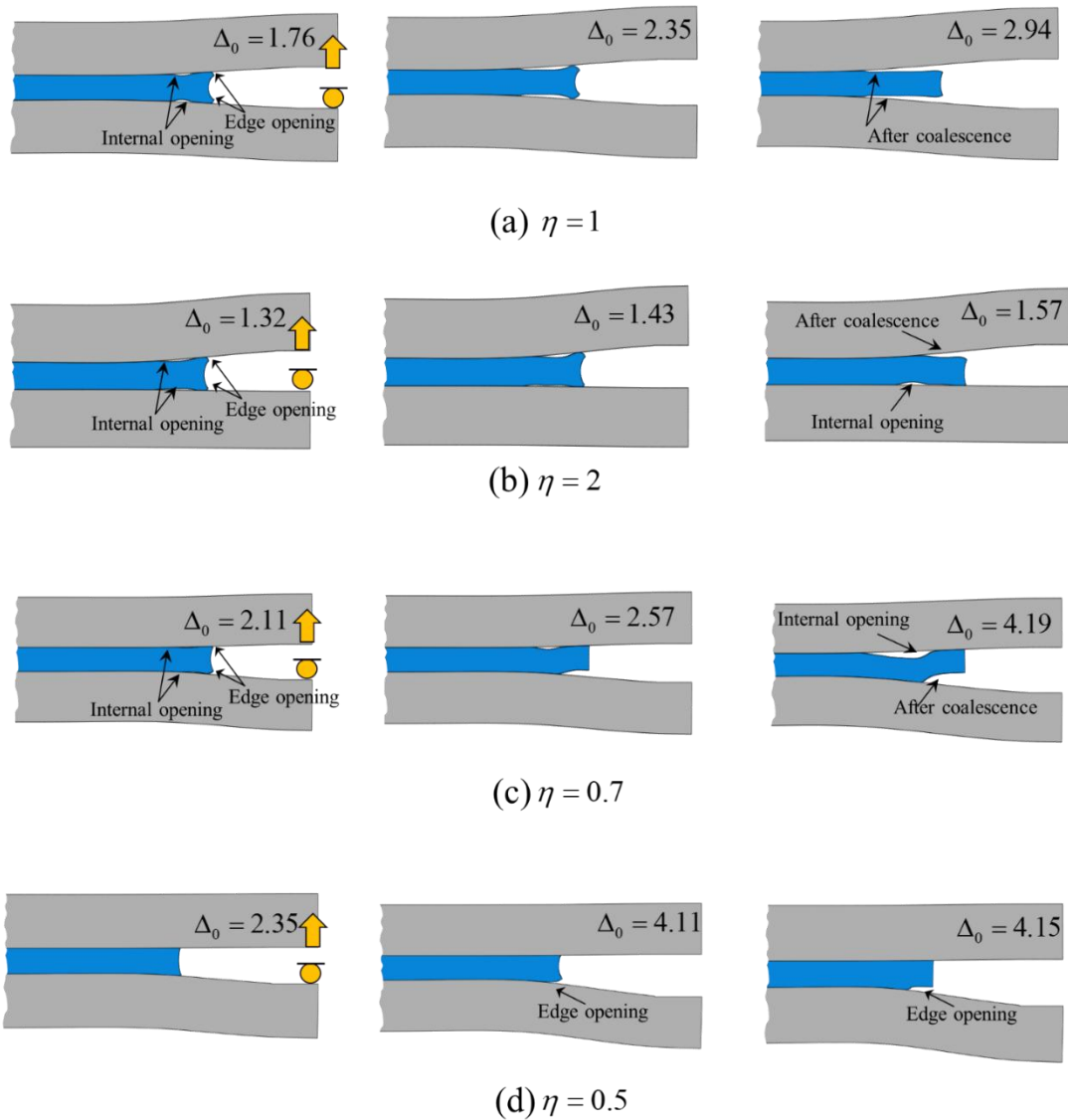


Figure 5-10: Snapshots of computed deformed shapes for the flat mold assembly at indicated values of the applied non-dimensional displacements for (a) $\eta = 1$, (b) $\eta = 2$, (c) $\eta = 0.7$, and (d) $\eta = 0.5$ when $\alpha_1 = 10$. The applied displacements at debonding initiation differ among these cases due to the change in the overall confinement when η is varied.

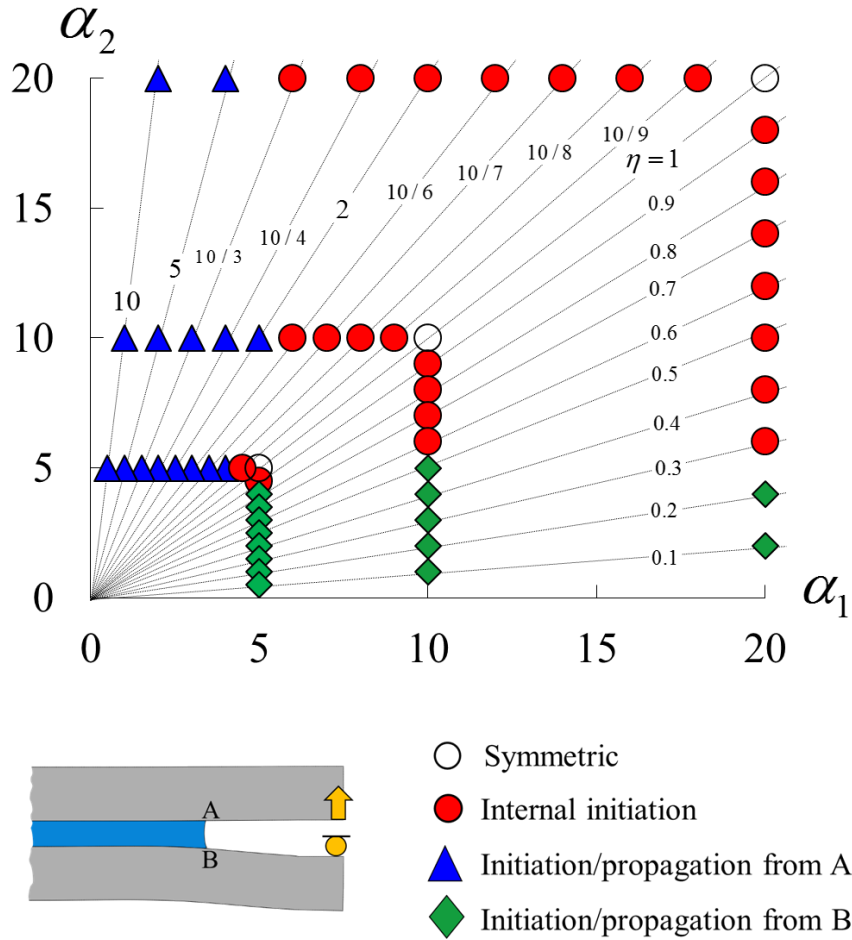


Figure 5-11: Debonding mechanisms on the $\alpha_1\alpha_2$ – plane for the flat mold assembly. Results correspond to the indicated values of $\eta = \alpha_2 / \alpha_1$ when $\alpha_1 = 5, 10$ and 20 , and $\alpha_2 = 5, 10$ and 20 .

Table 5-2: Sensitivity of computed predictions of debonding to a prescribed strength/fracture energy bias (lower interface stronger than the upper interface) when $\alpha_1 = 10$, and $\eta = 0.4$. The biases are expressed in terms of % difference.

Bias in interface strength, T_c		
$(T_{c2} / T_{c1} - 1) \times 100$	Edge debonding	Internal debonding
≤ 0	Lower	-
200	Lower	-
300	Upper	-
Bias in interface fracture energy, G_c		
$(G_{c2} / G_{c1} - 1) \times 100$	Edge debonding	Internal debonding

≤ 0	Lower	-
100	Lower	-
200	CZ formation predominant at the lower interface	Internal debonding occurs at the upper interface and coalesces with the edge CZ

Table 5-3: Sensitivity of computed predictions of debonding to a prescribed strength/fracture energy bias (lower interface stronger than the upper interface) $\alpha_1 = 10$, and $\eta = 0.7$. The biases are expressed in terms of % difference.

Bias in interface strength		
$(T_{c2} / T_{c1} - 1) \times 100$	Edge debonding	Internal debonding
0,0.1,1	Damage/debonding predominant at the lower interface	CZ initiates internally at both interfaces; internal damage at the upper interface dominates resulting in bridging
5		Internal debonding occurs at the upper interface and coalesces with the edge CZ.
Bias in interfacial fracture energy		
$(G_{c2} / G_{c1} - 1) \times 100$	Edge debonding	Internal debonding
0,0.1%	Damage/debonding predominant at the lower interface	CZ initiates internally at both interfaces; internal damage at the upper interface dominates resulting in bridging
1%		Internal debonding occurs at the upper interface and coalesces with the edge CZ

5.3.3 Molds as portions of a hemisphere

5.3.3.1 Interfacial damage suppressed

For curved mold assemblies, i.e., finite values of r_1 , deformations are expected to be inherently asymmetric due to curvature since additional shear components are inevitably introduced when the vertical displacement δ_0 is applied. This is confirmed by inspection of

the computed interfacial stresses close to the edge of the interlayer. Figure 5-12 shows the peel stress and the shear stress distributions at the two interfaces near the free edges for the flat mold assembly and the four curved assemblies when $\alpha_1 = \alpha_2 = 10$ and $\delta_0 = 4\mu m$. One can observe that the peel stress and the magnitude of the shear stress (positive at the upper and negative at the lower interface; to facilitate comparison of opening shear, the sign of the lower interface shear is reversed in the plots) have slower decay rates at the upper interface than that at the lower interface as the curvature increases. An examination of the through-the-thickness (at the angular location corresponding with the interlayer edge) variations of the circumferential strain, $\varepsilon_{\theta\theta}$, plotted for these five assemblies and the aforementioned values of parameters, shown in Figure 5-13, reveals increasing effect of the in-plane stretching of the molds with increasing curvature. This is evinced by the increasing horizontal shifts of the plots with decreasing value of r_1 . One can further observe that the asymmetry between results plotted on interfaces with the upper and the lower molds becomes more pronounced with increasing curvature. As exhibited for $r_1 = 10mm$ in Figure 5-14a and Figure 5-14c, distributions on the interfaces of surface tractions computed for $\eta = 0.5$ and 0.2 reveal that the biases are present even when the lower mold is more flexible ($\eta < 1$) than the upper mold. These observations suggest that the additional shearing introduced due to curvature causes an opening bias at corner A. This bias may outweigh that introduced due to the lower mold being more flexible than the upper one. The variation of the peel stress over the entire interface exhibited in Figure 5-14b reveals the occurrence of a peak in the peel stress at interior points of the interface as the value of η increases. While this is consistent with findings discussed above for the flat mold assembly in that the internal peel stresses begin to dominate as confinement increases, this also reminds us of the findings for cone test specimens of [Anderson et al. \[17\]](#), which exhibited large internal peel stresses with a slight increase in the normal component of the applied loading. Noteworthy is the occurrence of a second internal peak near the specimen center in addition to the first internal peak near the free edge. These peaks in the peel stress occur at points where the shear stress is nearly zero as can be seen from Figure 5-14d. As was observed for flat molds, the internal large peel stress equals the hydrostatic tension as also evinced by the plot of the hydrostatic pressure (multiplied by -1) for $\eta = 1$ included in Figure 5-14b.

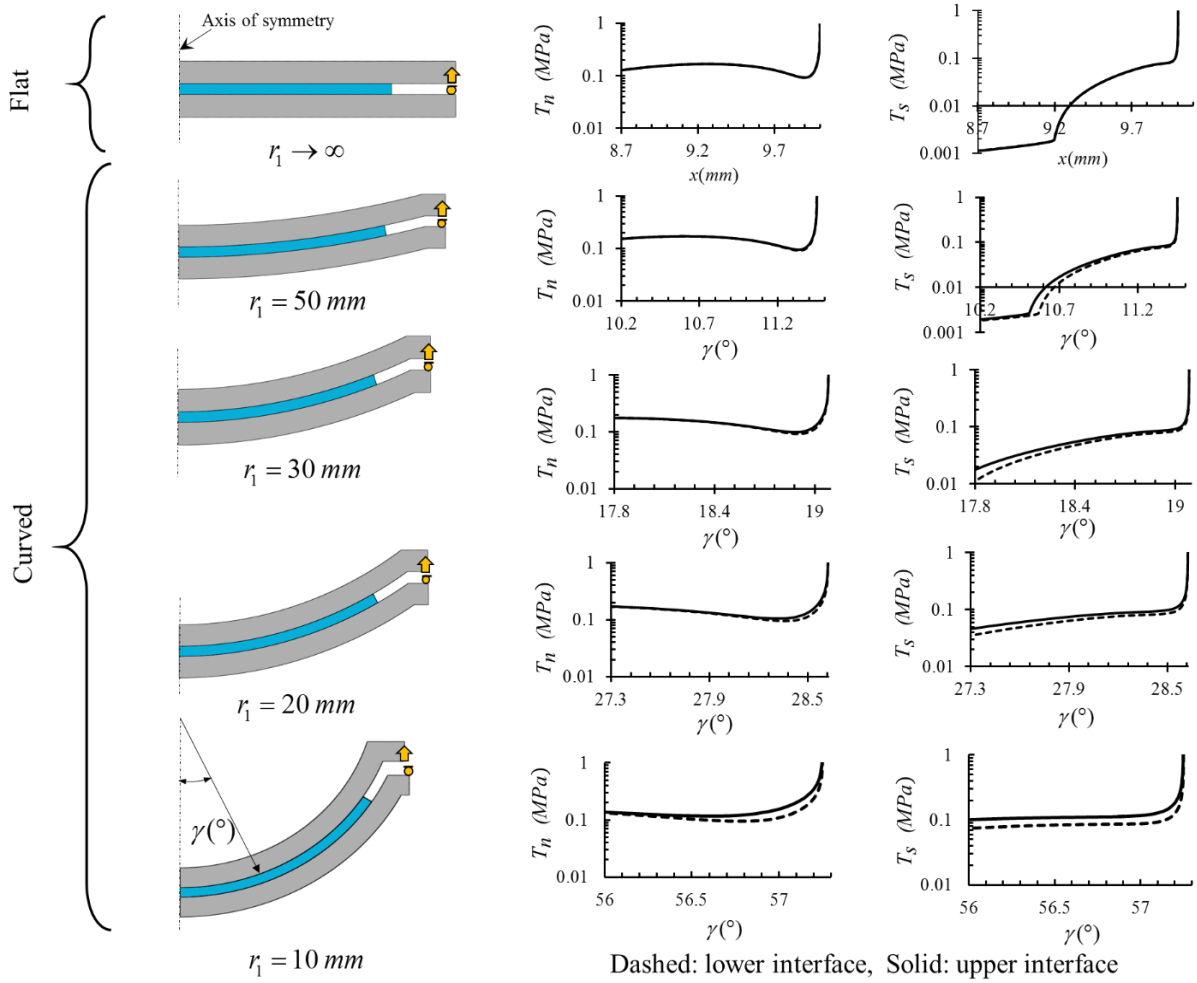


Figure 5-12: For $\alpha_1=10, \eta=1, \beta_1^{-1}=1\text{mm}$, $\mu=5\text{MPa}$ and $\delta_0=4\mu\text{m}$, and prior to the initiation of damage, distributions of the computed interfacial peel and shear stresses close to the free edge of the interlayer for one flat and for four curved mold assemblies. For the flat mold assembly the horizontal axis corresponds to the horizontal distance x measured from the axis of symmetry and for the curved cases it corresponds to the angular position, γ in degrees, measured from the axis of symmetry. A log scale is used on the vertical axis. The shear stress on the lower interface is multiplied with -1 to facilitate comparison of the opening shear.

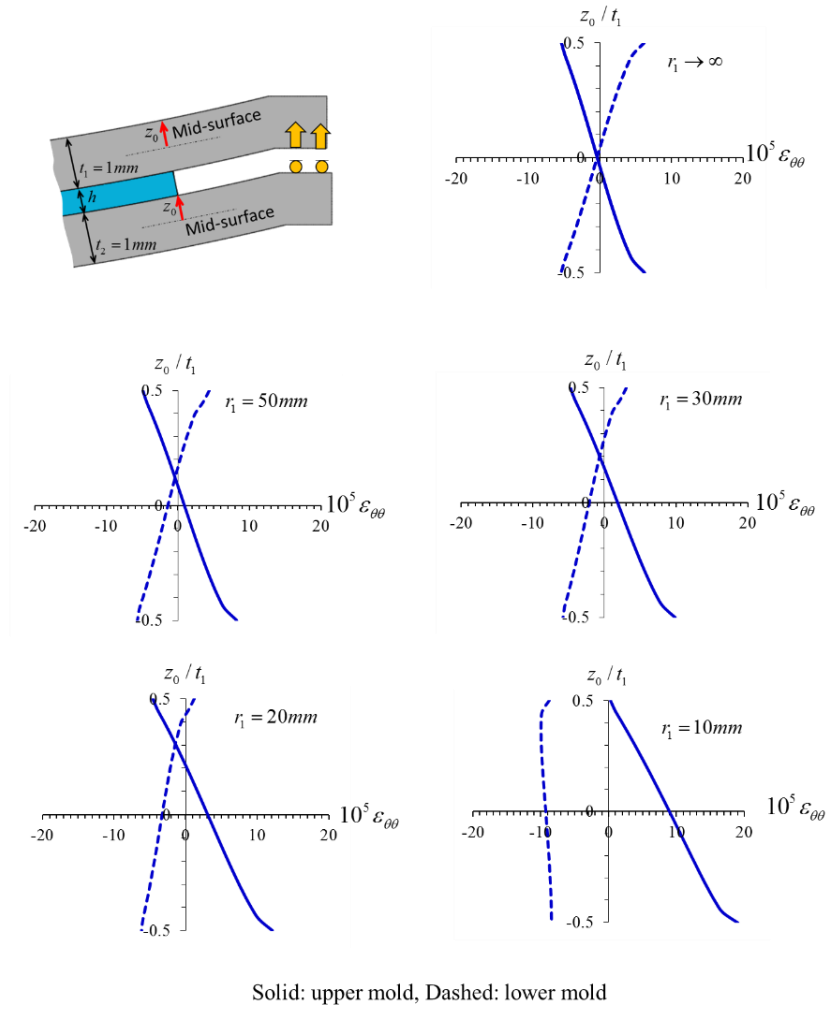
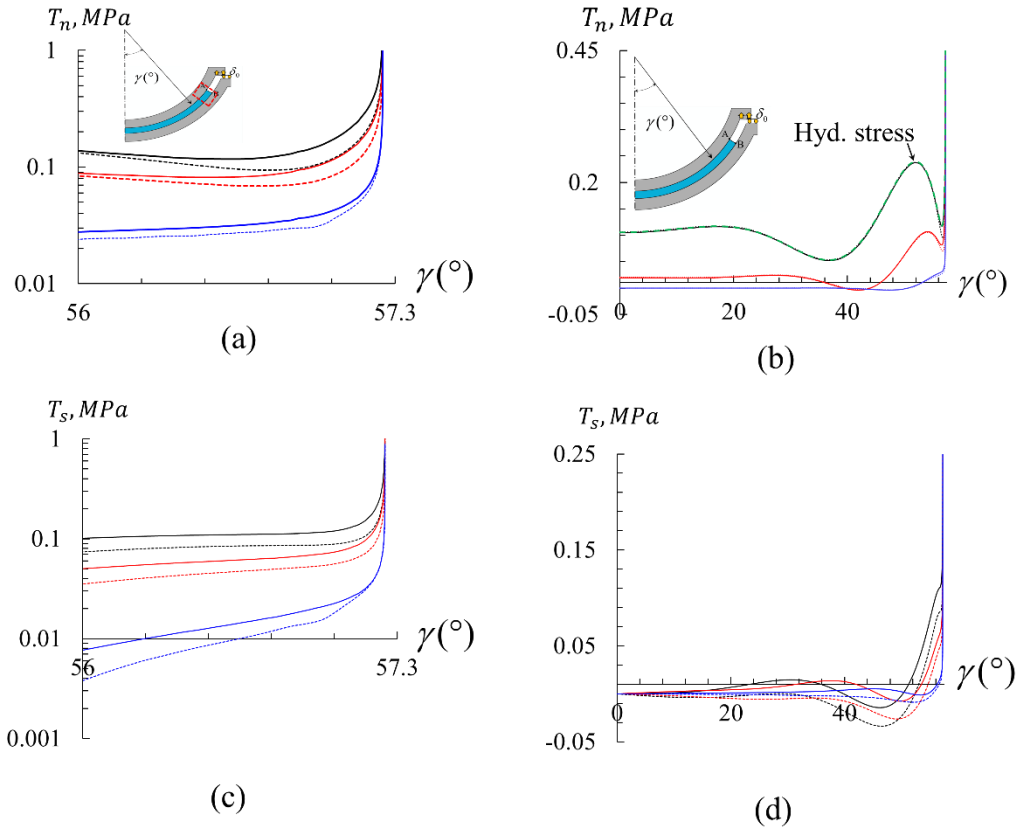


Figure 5-13: For $\alpha_1 = 10, \eta = 1, \beta_1^{-1} = 1\text{mm}, \mu = 5\text{MPa}$ and $\delta_0 = 4\mu\text{m}$, and prior to the initiation of damage through-the-thickness variation of $\epsilon_{\theta\theta}$ for one flat and four curved molds with their radii of curvatures, r_1 , indicated in the plots. The angular positions at which through-the-thickness variations are plotted correspond with those of the interlayer edge. The distance z_0 is measured from the mid-surface (upper mold: $r = r_1 - t_1 / 2$, and Lower mold $r = r_1 + h + t_2 / 2$) of each mold.



Dashed: lower interface
Solid: upper interface

Black : $\eta = 1$, Red: $\eta = 0.5$, Blue: $\eta = 0.2$

Figure 5-14: For $\alpha_1=10, \eta=1, \beta_1^{-1}=1mm, \mu=5MPa$ and $\delta_0=4\mu m$, and prior to the initiation of damage, distributions of the computed peel stress for $r_1=10mm$ (a) close to the free surface of the interlayer, and (b) over the entire interface for $\eta=0.2, 0.5$ and 1 . The corresponding plots of the interfacial shear stress are shown in (c) and (d). For illustration in (c) and (d), the shear stress at the bottom interface is multiplied by -1 . The plot of the hydrostatic pressure on the upper interface is included in (b) for $\eta=1$

5.3.3.2 Interfacial damage allowed

For the mold assembly with $r_1=10mm$, the predicted mechanisms of debonding are summarized on the $\alpha_1\alpha_2$ - plane in Figure 5-15. Due to the inherent asymmetric in-plane deformations due to curvature, symmetric debonding at the two interfaces is not predicted for all values of η . As suggested by the inspection of the peel stresses prior to damage initiation, edge debonding at corner A is predicted even when the flexural rigidity of the lower mold is significantly smaller than that of the upper mold. The damage begins to dominate at corner B only when η is small with the exact value determined by the value of α_1 . Similar to predictions for the flat mold assembly, internal debonding ensues when the value of η is

increased at a given α_1 and vice versa. Since the opening bias becomes more pronounced with an increase in the curvature, the value of η for edge debonding to occur from point B is predicted to be 0.2 for $r_1 = 20mm$ as opposed to 0.1 for $r_1 = 10mm$. For $r_1 = 30mm$, the result equals that for the flat assembly.

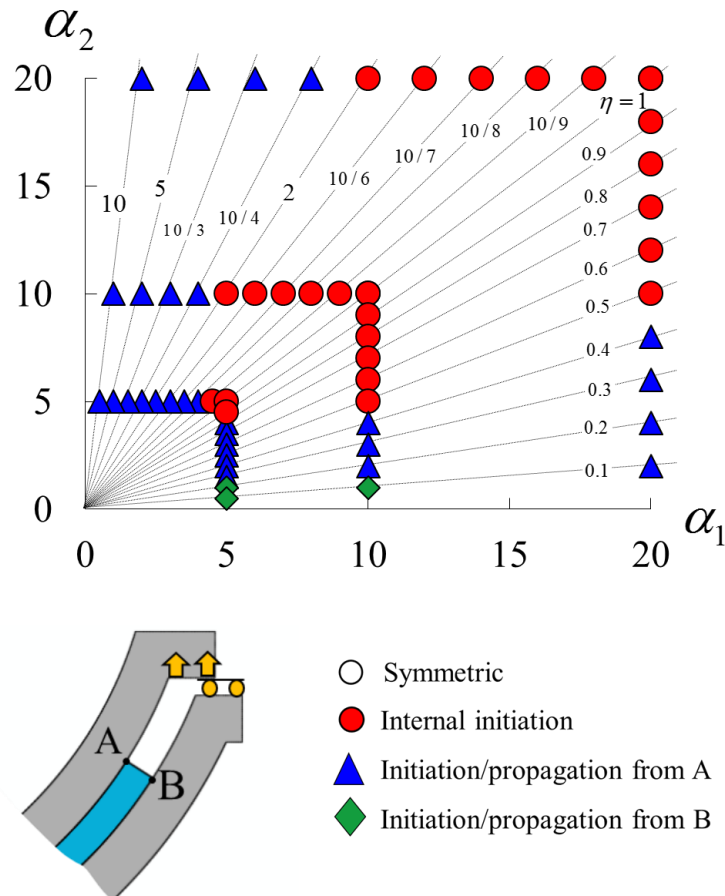


Figure 5-15: Debonding mechanisms on the $\alpha_1\alpha_2$ - plane for the curved mold assembly with $r_1 = 10mm$ and $\eta = \alpha_2 / \alpha_1$.

5.3.4 Increasing temperature of the flat molds differentially

The role of heating the components by different amounts (differential heating) in biasing debonding to one of the two interfaces is explored in this subsection. Other sources of asymmetry are suppressed by considering a flat mold assembly with identical molds ($\eta = 1$).

5.3.4.1 Interfacial damage suppressed

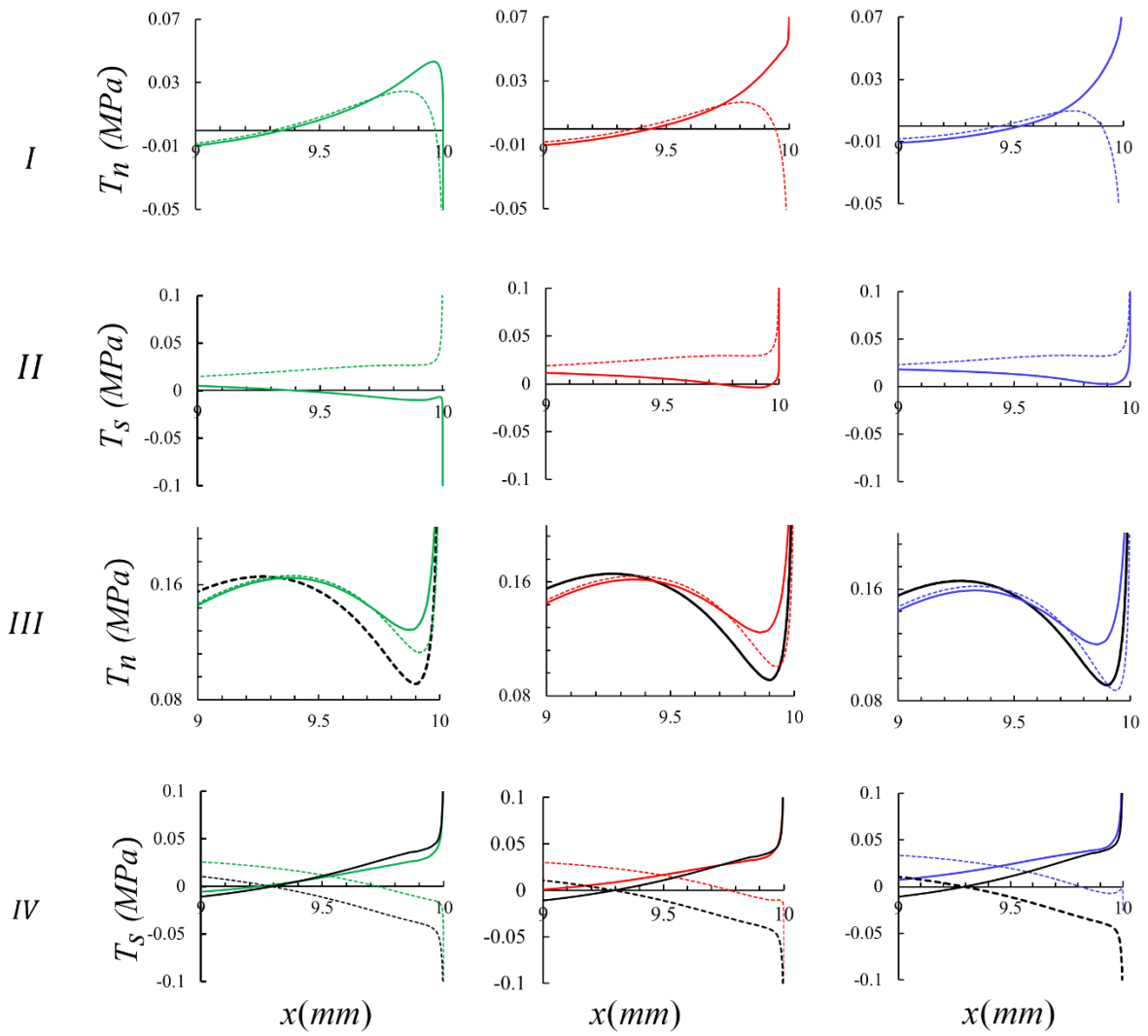
Due to mismatch in coefficients of thermal expansion of the interlayer and the two molds, the interfaces become stressed when the three components are at different temperatures. With one mold expanding more than the other one due to differential heating,

peeling is expected to be biased towards one interface due to the introduction of additional opening shear stress. This has been investigated by prescribing a uniform temperature change ΔT_2 of the lower mold and ΔT_1 of the upper one, and assuming that $\Delta T_{elas} = 1/2(\Delta T_1 + \Delta T_2)$. Unless otherwise specified, we assume $\tilde{\alpha}_1 = \tilde{\alpha}_2 = 7 \times 10^{-5} / ^\circ C$ and $\tilde{\alpha}_{elas} = 6 \times 10^{-4} / ^\circ C$.

As in the preceding sub-sections, distributions of tractions at the two interfaces prior to their getting damaged are examined. Exhibited in Figure 5-16 are the computed distributions of the interfacial peel and shear stresses after the change in temperature occurs (see rows *I* and *II*) and after a displacement of $\delta_0 = 4 \mu m$ is applied subsequently (rows *III* and *IV*). The columns correspond to three different values of ΔT_2 , as indicated. Also plotted in rows *III* and *IV* for comparison are distributions of the interfacial tractions for the case of no heating before applying the mechanical displacement. Inspection of results in row *I* reveals that the upper interface develops an opening bias near the edge, which becomes more pronounced as ΔT_2 decreases. The figures in row *II* reveal differentials in the shear stress at the two interfaces which are consistent with the bias observed in the peel stresses. These asymmetries occur due to different amounts of bending and stretching of the adherends under unequal temperature increments. Due to the bias provided by the thermal effect, one observes from results in row-*III* that the peel stresses occurring after the displacement is applied are elevated close to the edge at both interfaces but with a bias towards the upper interface. This bias becomes more pronounced as ΔT_2 is reduced. The figures in row *IV* exhibit plots of shear stresses at the two interfaces. The increase of the bias in magnitudes of the positive shear stress at the upper interface and the negative shear stress at the lower interface with decreasing values of ΔT_2 is consistent with the increasing opening bias towards the upper interface. Referring to figures in row *III*, the distribution of the peel stress is seen to become relatively more flat at the upper interface due a greater elevation of the peel stresses near the edge. On the other hand, the large compressive peel stress that occurs near corner B upon heating causes the internal large peel stress at the lower interface to become more localized. One can observe, furthermore, that the magnitude of the internal peak becomes slightly biased to the upper interface as the value of ΔT_2 decreases; the % difference increases from $\sim 0.025\%$ to $\sim 0.045\%$ as ΔT_2 is reduced from $2^\circ C$ to $1^\circ C$. Figure 5-17a and Figure 5-17b exhibit, respectively, the plots of the peel stresses close to the corners at the three indicated

values of ΔT_1 with the differential $\Delta T_1 - \Delta T_2$ fixed at $3^\circ C$. One can see that the distributions of peel stresses at both interfaces become more flat as ΔT_1 increases.

The afore-mentioned results suggest that increasing the temperature of the upper mold by a greater amount than that of the lower mold provides an opening bias at the upper interface edge. However, the susceptibility to internal debonding may increase with increasing temperature differential between the two molds and may decrease with an increase in the level of absolute temperature increment. To investigate the debonding mechanisms, we now allow damage to initiate and debonding to occur at both interfaces.



(a) $\Delta T_2 = 2^\circ C$

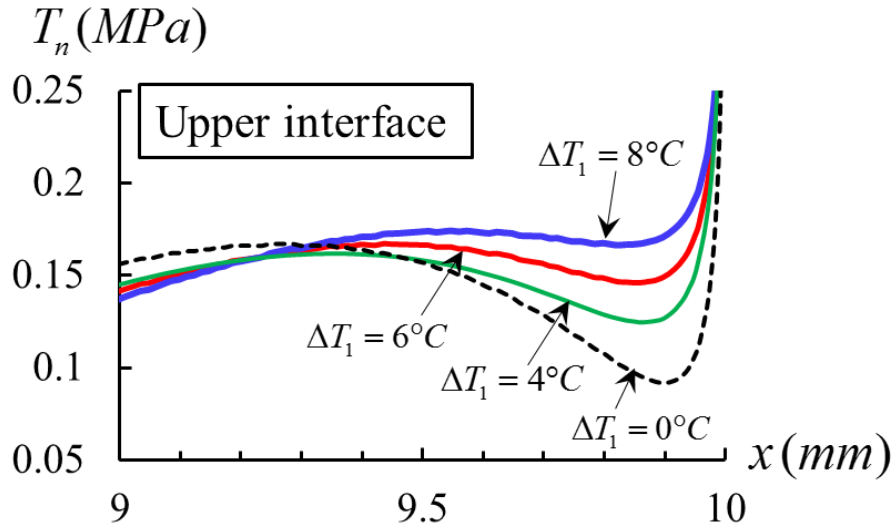
(b) $\Delta T_2 = 1^\circ C$

(c) $\Delta T_2 = 0^\circ C$

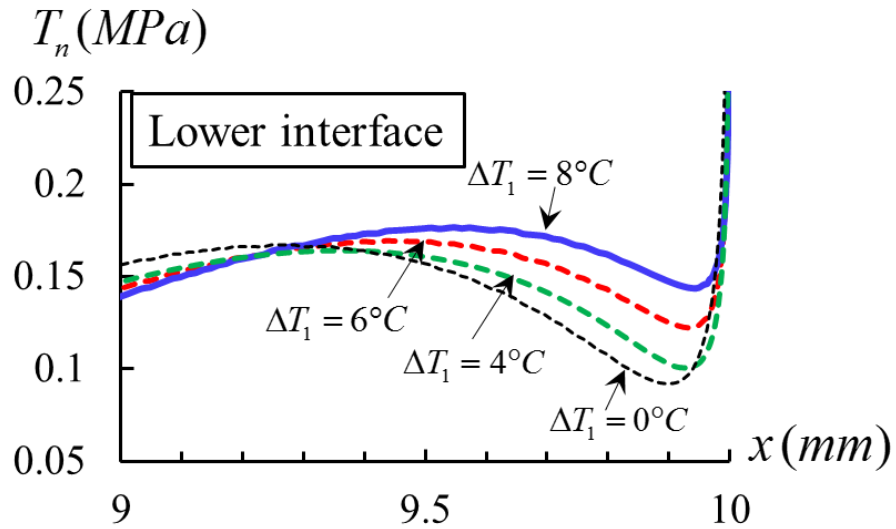
Dashed: lower interface
 Solid: upper interface

Black: Mechanical loading, no heating

Figure 5-16: For $\alpha_1 = 10$, $\beta_1^{-1} = 1mm$, $\mu = 5MPa$ and $\Delta T_1 = 4^\circ C$, and no damage allowed at the two interfaces, distributions of the interfacial peel and shear stresses after preheating (Figs. *I* and *II*), and of the interfacial peel and shear stresses upon applying $\delta_0 = 4\mu m$ with and without preheating (Figs. *III* and *IV*). The three columns correspond to results for (a) $\Delta T_2 = 2^\circ C$, (b) $\Delta T_2 = 1^\circ C$ and (c) $\Delta T_2 = 0^\circ C$.



(a)



(b)

Figure 5-17: Computed distributions of peel stresses after application of $\delta_0 = 4\mu m$ at the (a) upper and the (b) lower interfaces at different levels of heating of the upper mold while the difference of temperature between the upper and the lower mold stays constant at $3^\circ C$ except for the black lines which correspond to no pre-heating. The values of other input parameters are: $\alpha_1 = 10$, $\beta_1^{-1} = 1mm$, $\mu = 5MPa$. These results are obtained when damage is not allowed at the interfaces.

5.3.4.2 Interfacial damage considered

Results of simulations of damage growth/debonding indeed reveal that if the temperature increment of the upper mold is greater than that of the lower mold, debonding

occurs preferentially at the upper interface, as exhibited in [Figure 5-18a](#) for $\Delta T_1 = 4^\circ C$ and $\Delta T_2 = 3^\circ C$. If the temperature increment of the lower mold is reduced, e.g., $\Delta T_2 = 1^\circ C$, edge debonding at the upper interface is followed by nucleation of internal debond at the lower interface. The predictions of the debonding mechanisms are summarized in [Figure 5-19](#) on the $\Delta T_2 \Delta T_1$ -plane by using green filled diamonds for edge debonding from corner A, blue filled triangles for edge debonding from corner B, red filled circles for edge debonding from either interfaces followed by internal debonding, and unfilled circles for the symmetric case when there is no temperature differential. Corroborating further predictions from the stress analysis when damage was suppressed, it is noted that the threshold differential $\Delta T_1 - \Delta T_2$ beyond which internal debonding ensues increases with the absolute level of heating ΔT_1 . For the flat mold assembly studied, results are symmetric about the line $\Delta T_1 = \Delta T_2$.

Sensitivities of the predictions to prescribed biases in the interfacial strength and the fracture energy are summarized in [Table 5-4](#). The edge debonding mechanism predicted to occur at $\Delta T_1 = 4^\circ C$ and $\Delta T_2 = 3^\circ C$ is sensitive to an imposed bias of 8% in the strength. However, it is sensitive to a smaller bias of 1% when the temperature differential is larger, i.e., for $\Delta T_1 = 4^\circ C$ and $\Delta T_2 = 1^\circ C$. However, at the same temperature differential of $3^\circ C$, the sensitivity is less when the absolute heating is increased, i.e., $\Delta T_1 = 6^\circ C$. While the results show a similar trend in terms of the effects of temperature differential and the absolute heating in influencing the sensitivities, a much larger bias (~100%) is required in the fracture energy in order to alter the debonding mechanism.

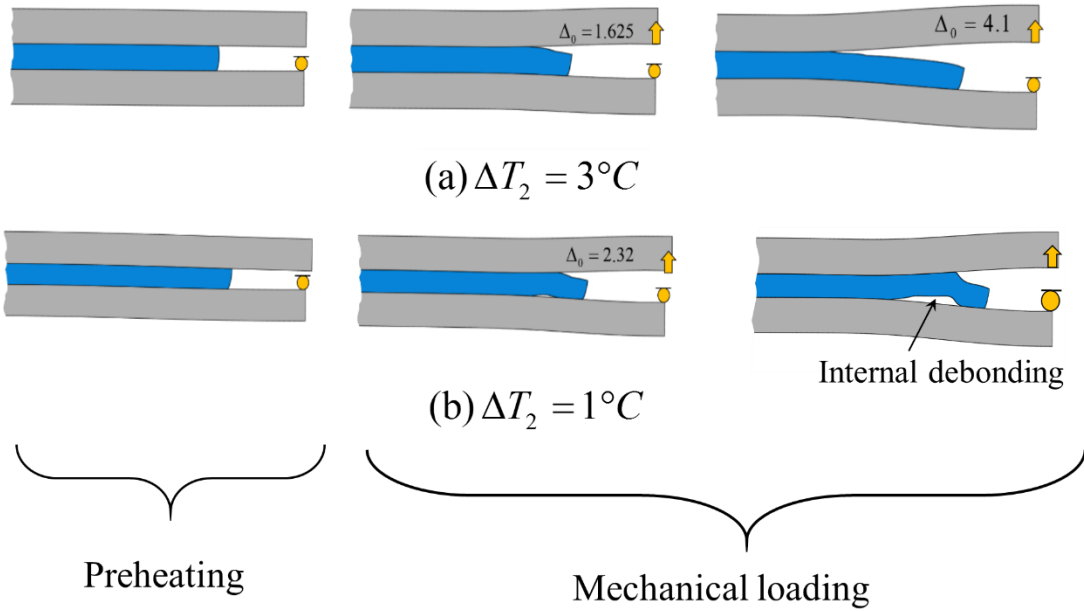


Figure 5-18: Snapshots illustrating evolution of debonding for $\Delta T_1 = 4^\circ\text{C}$, and (a) $\Delta T_2 = 3^\circ\text{C}$ and (b) $\Delta T_2 = 1^\circ\text{C}$

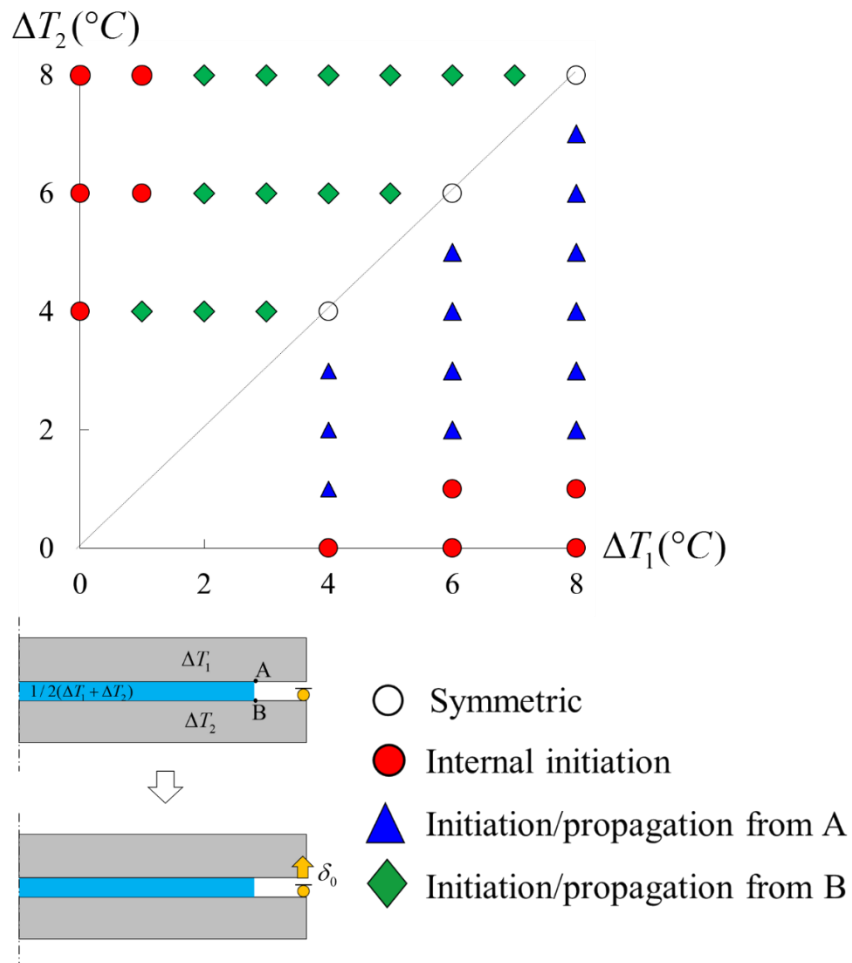


Figure 5-19: Debonding mechanisms 'map' on the $\Delta T_2 \Delta T_1$ -plane for the curved mold-assembly when $\alpha_1 = 10$ and $\eta = 1$.

Table 5-4: Sensitivity of debonding to a prescribed strength/fracture energy bias (lower interface stronger than the upper interface) when $\alpha_1 = 10$, and the level of heating is varied.

Bias in interface strength, T_c			
$(T_{c1}/T_{c2} - 1) \times 100$	$\Delta T_1 = 4^\circ C$		$\Delta T_1 = 6^\circ C$
	$\Delta T_2 = 3^\circ C$		$\Delta T_2 = 3^\circ C$
0,0.1	Edge debonding from A	Edge debonding from A	Edge debonding from A
1			
5		Edge debonding from A and internal initiation at lower interface	Edge debonding from A and internal initiation at lower interface
8	Edge debonding from A and internal initiation at the lower interface		
Bias in interface fracture energy, \mathcal{G}_c			
$(\mathcal{G}_{c1}/\mathcal{G}_{c2} - 1) \times 100$	$\Delta T_1 = 4^\circ C$		$\Delta T_1 = 6^\circ C$
	$\Delta T_2 = 3^\circ C$		$\Delta T_2 = 3^\circ C$
0	Edge debonding from A	Edge debonding from A	Edge debonding from A
200		CZ forms at A and B as well as internally at the lower interface. The internal CZ coalesces with the edge CZ and separation occurs from the lower interface.	
300	CZ forms at A and B as well as internally at the lower interface. The internal CZ coalesces with the edge CZ and finally a single debonding grows occurs on the lower interface.		CZ forms at A and B as well as internally at the lower interface. The internal CZ coalesces with the edge CZ and separation occurs from the lower interface.

5.3.5 Limitations of the present analysis

While the present analysis offers insights into how to achieve preferential debonding in a demolding process, there are many limitations of this work. Some key limitations are listed below.

(1) It is not clear whether initiations of internal and edge debonding at two interfaces will lead to eventual separation from the wrong interface and/or tearing of the interlayer. Detailed evolution of progressive debonding while considering failure of the interlayer should be studied in a future work to gain more in-depth understanding of the problem.

(2) Only two-dimensional deformations have been studied in the present work. In response to spatial perturbations caused by factors such as a pre-existing weak spot on the

interface or non-axisymmetric loading, the debonding may exhibit adhesion-induced instability [29] for highly confined elastomeric layers. While an internal debonding predicted under the assumption of axisymmetric deformations implies a circular tunnel-like opening, the adhesion-induced instability may trigger nucleation of multiple openings. This may eventually lead to a fingerlike debond propagation, adding further complication to the debonding evolution. As was also observed in our previous analysis of plane strain deformation during peeling of a flexible plate from a highly confined elastomer layer ($\alpha_1 \sim 100$) bonded to a fixed base[24], an adhesion-induced instability is exhibited when $\phi > \sim 5$.

(3) Viscoelastic effects, both in the bulk elastomer and at its interface with the molds, are ignored in the present work. However, they may play an important role in determining separation from a desired interface[30, 31].

5.4 Conclusions

Axisymmetric deformation of an elastomeric layer sandwiched between two molds that are separated by displacement controlled loading have been numerically analyzed using the finite element method (FEM). The interfaces are characterized by a bilinear traction-separation (TS) relation. Numerical experiments have been conducted to gain insights into the debonding bias caused by (i) molds of different bending rigidities, (ii) curvature of the molds, and (iii) heating the mold-assembly differentially prior to mechanical demolding. The key findings are listed below.

- The elastomeric layer begins to debond preferentially from the edge of its interface with the more flexible mold. However, if the overall confinement of the system is large enough as dictated by the mold rigidities for an elastomeric interlayer of given modulus and thickness, debonding initiates internally in addition to that at the edge due to large peel stresses occurring at interior points of the interface.
- For a mold assembly with the interlayer having the shape of a portion of a hemisphere and the imposed normal loading conditions, edge peeling is inherently biased toward the interface associated with the smaller radius mold.
- Differential heating can be used to steer debonding to the desired interface. Edge peeling becomes biased towards the interface with the mold heated more. A sufficiently large temperature differential between the two molds as

dictated by the absolute level of temperature increment can result in internal debonding to ensue. However, increasing the temperature change at a fixed temperature differential makes the system less susceptible to internal debonding.

- The debonding at interior points of an interface is highly sensitive to small variations in the interfacial strength and the fracture energy. In light of the unavoidable statistical variations of interfacial parameters for real interfaces, it is recommended that the molds for an elastomer of given modulus and thickness be so designed that debonding at interior points is avoided.

Although the present analysis is based on many restrictive assumptions, the outcomes are envisioned to be useful in understanding interfacial debonding in a demolding process involving a sandwiched elastomeric layer.

Acknowledgements

The authors thank the department of Biomedical Engineering and Mechanics at Virginia Tech for the use of its facilities and the Macromolecules and Interfaces Institute, Virginia Tech, for fostering interdisciplinary research in the adhesion area.

Appendix H

Included here are the schematic sketch of the configuration (see Figure H 1) of the cone test simulated to examine the fidelity of our computational approach, and a tabulated summary (see Table H 1) of the predicted debonding mechanisms and the experimentally found ones by [Anderson et al. \[17\]](#). As Figure H 1 shows a cross-sectional view of the configuration considered in which an elastomeric adhesive layer in shape of a hollow thin cone is sandwiched between two rigid adherends. The inner adherend is subjected to normal displacement as shown while the bottom surface of the outer adherend is fixed. The values of material parameters are taken from [Anderson et al. \[17\]](#) and the TS parameters are chosen assuming, as in our computational approach for problems studied in the paper, that the interface fails in tension. Additionally, damage is only allowed at the inner interface for simplicity as well as due to the lack of information about which interface failed in the experiments[17]. CAX4 elements of dimensions $0.025\text{ mm} \times 0.025\text{ mm}$ and $0.05\text{ mm} \times 0.05\text{ mm}$ are used to discretize the adhesive interlayer and the adherends, respectively.

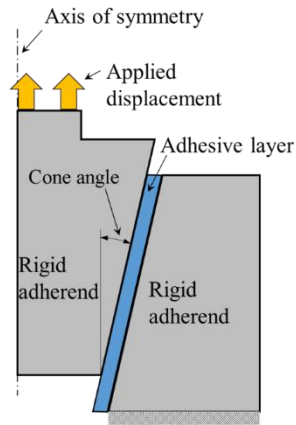


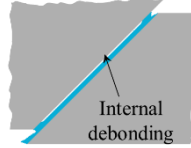


Figure H 1: Schematic sketch of the configuration of Anderson et al.'s cone test[17]

Table H 1: Summary of computed predictions of debonding in a cone test

Cone angle (°)	Debonding mechanism	
	Experimental (Anderson et al. [17])	Present study (FEM)
0	Initiation and propagation from corners	
5	Debonding nucleation over the bondline central region	
45	Debonding nucleation over the bondline central region	

Appendix I

Understanding bridging of a soft organogel layer by numerical simulations

Bikramjit Mukherjee¹, Orkun Kaymakci², Romesh C. Batra¹, David A. Dillard¹, Robert B. Moore³,

¹Department of Engineering Science & Mechanics

²Macromolecular Science and Engineering,

³Department of Chemistry,

Virginia Polytechnic Institute and State University

Blacksburg, Virginia 24061, USA

(Portion of this work appeared as a proceeding [31] of the Annual Adhesion Society Meeting held in Daytona Beach, Florida in February, 2013)

Introduction

Separation of a soft organogel layer, sandwiched between two relatively stiff molds[32], from one desired interface is a common process in manufacturing of hydrogel products. The organogel interlayer begins to debond from an interface when stretched beyond capacity. For a thin interlayer and similar adhesion at the two interfaces, the debonding can switch to the other interface, leaving in the wake region a bridge suspended between the two substrates. The bridge, thus formed, may grow in size and render the interlayer susceptible to tearing failure caused by the high stresses exceeding the cohesive strength of the bulk material. This necessitates the process variables be carefully chosen in order that the separation is completed across the desired interface without damaging the interlayer. For rate and temperature dependent constitutive behavior of the interlayer, the applied separation rate and the operating temperature are two process variables that are believed to influence the demolding behavior. In this study, a cohesive zone model is used in a finite element framework to numerically simulate axisymmetric demolding of an organogel layer enclosed between two plastic molds. The organogel is in the shape of a portion of a spherical surface (shown in Figure I 1), as might be appropriate for a variety of hydrogel applications. Sensitivities of the separation behavior to the applied separation speed and the operating temperature have been probed. We show that for a given set of interfacial properties, one can use a combination of applied separation speed and operating temperature so that the demolding is from a desired interface, and the deformation of the bridge is not severe enough to cause tears. The rate and temperature dependence of the demolding behavior can be used to bias the separation to the desired interface when other variables such as the adhesion, mold thickness and interlayer thickness are less accessible.

Method

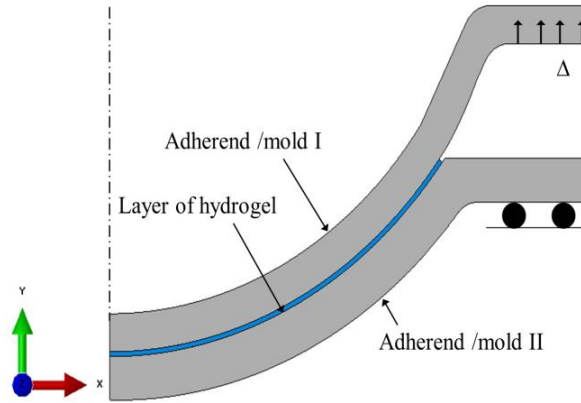


Figure I 1: The computational domain

The plastic molds are assumed to be linear elastic with a Young's modulus $E = 2.1$ GPa and Poisson's ratio $\nu = 0.41$. The organogel is modeled as incompressible and viscoelastic with neo-Hookean instantaneous response. The Prony series and the WLF shift factors determined from experimental data [33] are, respectively, listed in Table I 1 and are $C_1 = 4.57$ and $C_2 = 142.2$ °C at a reference temperature of $T_{REF} = 45$ °C. The interfaces are modeled by a bilinear traction separation law (Figure I 2) in which we specify the peak traction $T_c = 30.49$ kPa and the cohesive energy $G_0 = 0.2$ J/m², consistent with the previous work on this material [32]. The entire assembly is specified to be at a uniform operating temperature T_0 . The displacement boundary conditions simulating a pry-opening operation are shown in Figure I 1. The remaining regions of the boundary (except the axis of symmetry) are assumed traction-free. A 2D axisymmetric large deformation analysis is carried out.

Table I 1: The Prony series parameters

Terms	Relaxation time , τ_i , sec	Shear modulus, G_i , MPa
1	1E-06	3.194
2	1E-05	0.420
3	1E-04	0.186
4	1E-03	0.052
5	1E-02	0.016
6	1E-01	0.003
7	1E+00	0.001
8	1E+01	0.001
9	1E+03	0.017
10	1E+04	0.014
11	1E+05	0.017
12	Infinite	0.009

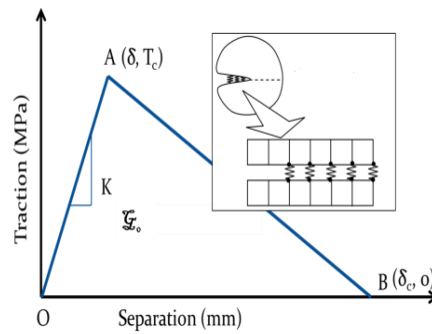


Figure I 2: The bi-linear traction separation law

Even though inertia effects are ignored, effects of different values of the rate of applied displacement Δ and the temperature T_0 are simulated to account for the viscoelastic behavior of the adhesive and to probe the sensitivity of the separation behavior to the rate of loading and temperature.

Results and discussion

Figure I 3 shows the separation status at 1 mm of applied displacement (Δ) when the applied rates are 0.1, 1, 10 and 100 mm/s and the operating temperature is $-20\text{ }^\circ\text{C}$. At 0.1 and 1 mm/s, separation is completed across the lower interface, whereas at 100 mm/s, it occurs across the upper interface. At the intermediate speed 10 mm/s, debonding initiates at the upper interface but switches to the lower, thereby forming a bridge suspended between the substrates. A slow debond propagation at the lower interface results in growth of the suspended portion until it begins to separate from the upper interface at a vertical displacement (Δ) of approximately 3 mm, as shown in Figure I 5. The Contour plots of the maximum principal stresses are shown on the deformed interlayer profiles at increasing values of separation in Figure I 6. High stresses in the interlayer caused by bridging may lead to initiation and propagation of cohesive cracks, especially when the organogel layer is fragile. However, one can choose a lower temperature such as $-30\text{ }^\circ\text{C}$, for which results are shown in Figure I 4, to achieve complete separation from the upper interface with little bridging. Results plotted in Figure I 4 suggest that a lower temperature biases the debonding towards the upper interface.

Further investigation revealed that internal debonding initiation led to bridging in all of the above case studies but the interaction of the internal debonding with the external one at the edge dictated the final separation interface. From preliminary computed data, significant

bridging occurring at intermediate pulling speeds and temperatures was attributed to large viscoelastic dissipation occurring in the organogel.

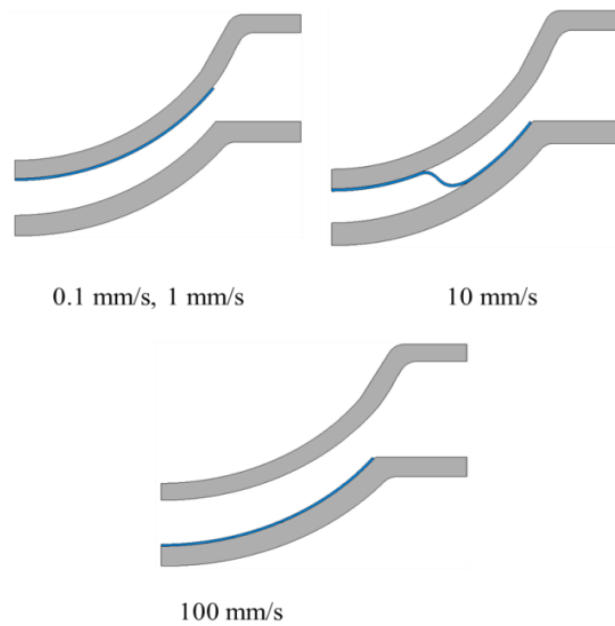


Figure I 3: Separation behavior at different separation speeds and -20°C , shown at 1 mm separation

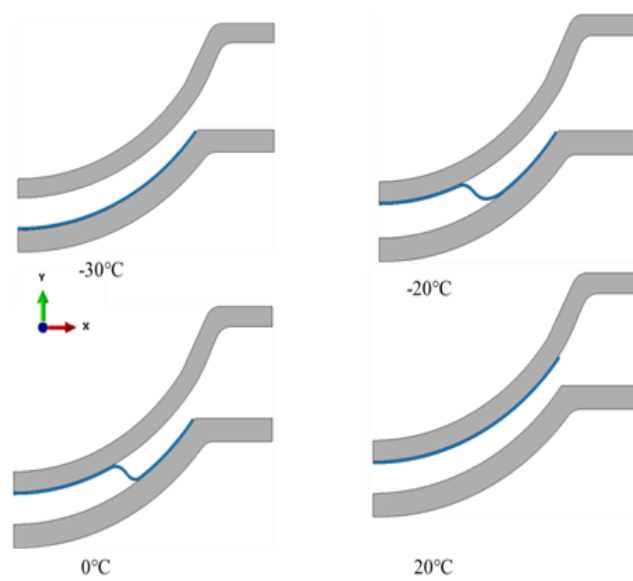


Figure I 4: Separation behavior at different temperatures at 10 mm/s separation speed, shown at 1 mm separation

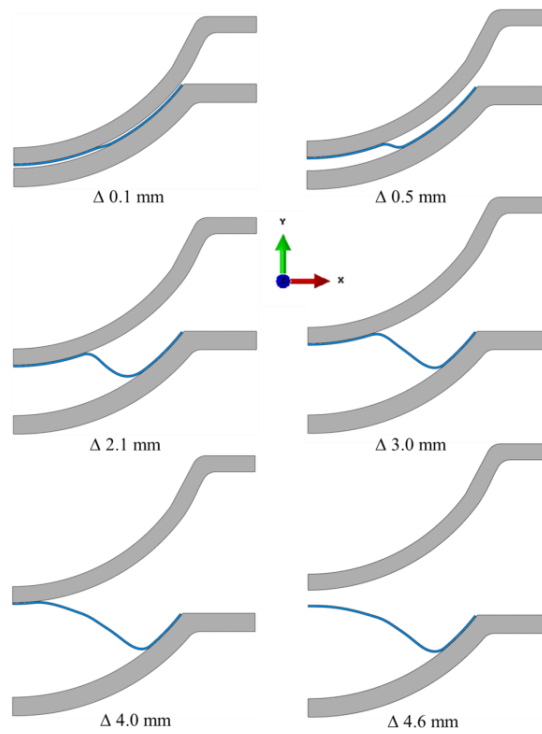


Figure I 5: Frames showing the growth and propagation of bridge at -20°C and 10 mm/s separation speed

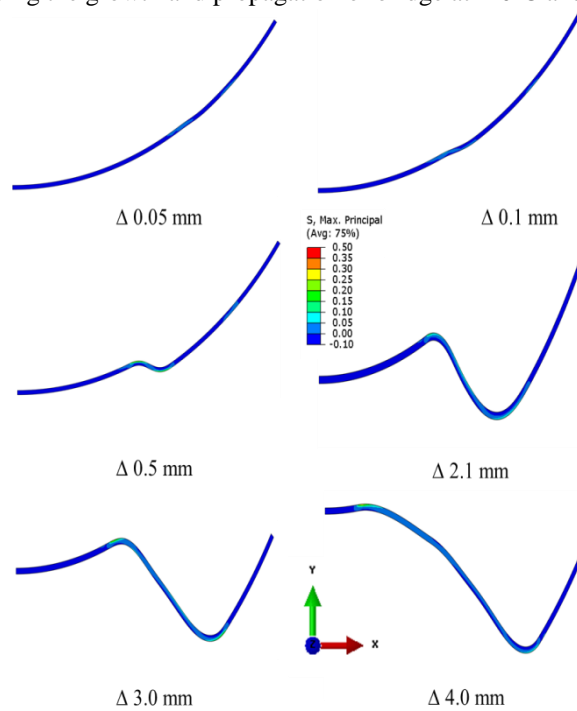


Figure I 6: Contours of maximum principal stresses on the deformed shapes of the interlayer at -20°C and 10 mm/s separation speed

Conclusions

In summary, simulations of pry-opening of an organogel layer sandwiched between two plastic molds reveal that a combination of the separation speed and operating temperature can be chosen in order that the separation is from a desired interface with little

bridging. At a given operating temperature, an increase in the separation speed biases the separation toward the upper interface. At a given separation speed, a decrease in the temperature biases the separation towards the upper interface.

References

- [1] Carlson, A., A.M. Bowen, Y. Huang, R.G. Nuzzo, and J.A. Rogers, *Transfer printing techniques for materials assembly and micro/nanodevice fabrication*. Advanced Materials, 2012. **24**(39): p. 5284-5318.
- [2] Widman, M.F., D.T.-F. Wang, and H.A. Dagobert, *Wedge demolding of cast lens mold assemblies*. 1997, Google Patents.
- [3] Larsen, H.-O., *Mold for making contact lenses, either the male or female mold sections being relatively more flexible*. U.S. Patent 4,640,489. 1987
- [4] Madaria, A.R., A. Kumar, F.N. Ishikawa, and C. Zhou, *Uniform, highly conductive, and patterned transparent films of a percolating silver nanowire network on rigid and flexible substrates using a dry transfer technique*. Nano Research, 2010. **3**(8): p. 564-573.
- [5] Martin, W.A., T. Kindt-Larsen, and C.W. Walker, *Method and apparatus for demolding ophthalmic contact lenses*. 1999.
- [6] Watterson, R., R. Leavitt, and M. Litwin, *Methods of demolding ophthalmic lenses*. 2004, Google Patents.
- [7] Gent, A., *Cavitation in rubber: a cautionary tale*. Rubber Chemistry and Technology, 1990. **63**(3): p. 49-53.
- [8] Kaplan, S. and P. Rose, *Plasma surface treatment of plastics to enhance adhesion*. International journal of adhesion and adhesives, 1991. **11**(2): p. 109-113.
- [9] Ansell, S.F., et al., *Decreased lens delamination during ophthalmic lens manufacture*. 2006, Google Patents.
- [10] Larsen, H.-O., *Mold for making contact lenses, either the male or female mold sections being relatively more flexible*. 1987, Google Patents.
- [11] Liechti, K.M. and J.-D. Wu, *Mixed-mode, time-dependent rubber/metal debonding*. Journal of the Mechanics and Physics of Solids, 2001. **49**(5): p. 1039-1072.
- [12] Rahul-Kumar, P., A. Jagota, S. Bennison, and S. Saigal, *Interfacial failures in a compressive shear strength test of glass/polymer laminates*. International Journal of Solids and Structures, 2000. **37**(48): p. 7281-7305.
- [13] Ghatak, A., L. Mahadevan, J.Y. Chung, M.K. Chaudhury, and V. Shenoy, *Peeling from a biomimetically patterned thin elastic film*. Proceedings of the Royal Society of London. Series A: Mathematical, Physical and Engineering Sciences, 2004. **460**(2049): p. 2725-2735.
- [14] Adda-Bedia, M. and L. Mahadevan, *Crack-front instability in a confined elastic film*. Proceedings of the Royal Society A: Mathematical, Physical and Engineering Science, 2006. **462**(2075): p. 3233-3251.
- [15] Mukherjee, B., D.A. Dillard, R.B. Moore, and R.C. Batra, *Debonding of Confined Elastomeric Layer using Cohesive Zone Model*. International Journal of Adhesion and Adhesives, 2016a. **66**: p. 114-127.
- [16] Crosby, A.J., K.R. Shull, H. Lakrout, and C. Creton, *Deformation and failure modes of adhesively bonded elastic layers*. Journal of Applied Physics, 2000. **88**(5): p. 2956-2966.
- [17] Anderson, G., K. DeVries, and M. Williams, *Mixed mode stress field effect in adhesive fracture*. International Journal of Fracture, 1974. **10**(4): p. 565-583.

- [18] Xu, X.-P. and A. Needleman, *Numerical simulations of dynamic crack growth along an interface*. International Journal of Fracture, 1995. **74**(4): p. 289-324.
- [19] Dugdale, D., *Yielding of steel sheets containing slits*. Journal of the Mechanics and Physics of Solids, 1960. **8**(2): p. 100-104.
- [20] Geubelle, P.H. and J.S. Baylor, *Impact-induced delamination of composites: a 2D simulation*. Composites Part B: Engineering, 1998. **29**(5): p. 589-602.
- [21] Hutchinson, J.W. and Z. Suo, *Mixed mode cracking in layered materials*. Advances in applied mechanics, 1992. **29**(63): p. 191.
- [22] Song, S.H., G.H. Paulino, and W.G. Buttlar, *A bilinear cohesive zone model tailored for fracture of asphalt concrete considering viscoelastic bulk material*. Engineering Fracture Mechanics, 2006. **73**(18): p. 2829-2848.
- [23] Hibbitt, K. and Sorensen, *ABAQUS/CAE User's Manual*. 2012: Hibbitt, Karlsson & Sorensen, Incorporated.
- [24] Mukherjee, B., D.A. Dillard, R.B. Moore, and R.C. Batra, *Effect of confinement and interfacial adhesion on peeling of a flexible plate from an elastomeric layer*. In preperation, 2016b.
- [25] Dillard, D., *Bending of plates on thin elastomeric foundations*. Journal of applied mechanics, 1989. **56**(2): p. 382-386.
- [26] Dundurs, J., *Discussion: "Edge-bonded dissimilar orthogonal elastic wedges under normal and shear loading"* (Bogy, DB, 1968, ASME J. Appl. Mech., 35, pp. 460-466). Journal of applied mechanics, 1969. **36**(3): p. 650-652.
- [27] Khaderi, S., N. Fleck, E. Arzt, and R. McMeeking, *Detachment of an adhered micropillar from a dissimilar substrate*. Journal of the Mechanics and Physics of Solids, 2015. **75**: p. 159-183.
- [28] Mukherjee, B., *Interfacial debonding from a sandwiched elastomeric layer*, in *Department of Biomedical Engineering and Mechanics*. 2016, Virginia Polytechnic Institute and State University.
- [29] Chaudhury, M.K., A. Chakrabarti, and A. Ghatak, *Adhesion-induced instabilities and pattern formation in thin films of elastomers and gels*. The European Physical Journal E, 2015. **38**(7): p. 1-26.
- [30] Feng, X., et al., *Competing fracture in kinetically controlled transfer printing*. Langmuir, 2007. **23**(25): p. 12555-12560.
- [31] Mukherjee, B., O. Kaymakci, R.C. Batra, D.A. Dillard, and R.B. Moore. *Understanding bridging of a soft organogel layer by numerical simulations*. in *Adhesion Society Meeting*. 2013. Daytona Beach, FL.
- [32] Murray, K.V., *Characterization of the Interfacial Fracture of Solvated Semi-Interpenetrating Polymer Network (S-IPN) Silicone Hydrogels with a Cyclo-Olefin Polymer (COP)*. 2011, Virginia Polytechnic Institute and State University.
- [33] Tizard III, G.A., *Characterization of the Viscoelastic Fracture of Solvated Semi-Interpenetrating Polymer Network (S-IPN) Silicone Hydrogels*. 2010, Virginia Polytechnic Institute and State University.

6 Conclusions

6.1 Summary:

The thesis is composed of four Chapters (2-5). The contents of Chapter 2 have appeared in the *International Journal of Adhesion and Adhesives*, those of Chapter 3 have been submitted for possible publication in a peer-reviewed journal, those of Chapters 4 and 5 are, respectively, ready and in preparation for submission in peer-reviewed journals.

Understanding the mechanics of interfacial debonding of an elastomeric layer sandwiched between two adherends is of widespread interest due to its relevance in science and technology. Regardless of application-specific requirements, a common need is to control debonding. Motivated by the common need of achieving control of the debonding, we investigated the collective influence of the interfacial adhesion, materials, geometry and loading conditions on interfacial debonding. Methods used in our investigations include analytical and semi-analytical ones, and the finite element method (FEM). A cohesive zone model (CZM) with a bilinear traction separation (TS) relation is used to phenomenologically model the interaction at the interfaces between the elastomer and the adherends.

We first studied the debonding of a confined semi-infinite elastomeric layer bonded perfectly to a rigid base when a rigid adherend is pulled off from the elastomer. The stability analysis of the homogeneous solution (null displacements and constant hydrostatic pressure) of plane strain deformations of the elastomer and the analysis of deformations by the FEM have enabled us to conclude that a necessary condition for a wavy/undulatory debonding to ensue for a rigid semi-infinite adherend is $\phi = T_c^2 h / G_c E_\infty > 4.15$, where T_c is the peak traction and G_c the fracture energy in the TS relation, h the thickness and E_∞ the long-term Young's modulus of the elastomeric layer modeled as linear viscoelastic. Analysis of this problem using the FEM provides details of the interfacial debonding evolution and sheds light on the effects of pulling rate and temperature. These results can help design a materials system for producing/avoiding wavy debonding by choosing thickness of the interlayer and/or altering the interfacial softening by suitable surface treatment. It also serves to tailor the TS relation parameters for simulating spatially undulatory debonding evolution. Motivated by these outcomes, we have also analyzed using the FEM three-dimensional deformations of a thin elastomeric interlayer perfectly bonded to a rigid base when a flexible plate is peeled from it by applying vertical displacements to points on one edge. This analysis predicts, in a

qualitative sense, that the progressive debonding with a fingerlike front is controlled by both the lateral confinement $\alpha = (D_p / \mu h^3)^{1/3}$ and the adhesion parameter, $T_c^2 h / G_c \mu$ where D_p equals the plate bending rigidity and μ the interlayer shear modulus at the operating temperature. This problem is investigated in detail in Chapter 3.

Motivated by the qualitative outcome that interfacial debonding mechanisms during peeling of a flexible plate are dictated by both the geometric confinement (α) and the interfacial adhesion (ϕ), we conducted in Chapter 3 numerical experiments by the FEM to study quantitatively effects of these two quantities on the interfacial debonding mechanisms while approximating deformations as plane strain and assuming linear elastic materials. The computed results suggest that for confinement levels less than a threshold value (~ 9), damage at the interface between the interlayer and the deformable plate initiates at the edge, forms a cohesive zone (CZ), and leads to debonding which propagates with a CZ at its front. When confinement exceeds the threshold value, the damage in addition to occurring at the edge initiates at an internal interface point located at dimensionless distance $\beta^{-1} \sim (\mu / D_p h^3)^{-1/6}$ from the edge, which is proportional to the characteristic stress decay distance (one can also think of this as a shear-lag distance). For such interlayers a wavy debonding occurs over the CZ when the adhesion parameter exceeds a critical value. The spacing between the internal debonds scales with the interlayer thickness. The non-dimensional pull-off force is found to increase with the quantity ϕ / α and depend on the debonding type.

We subsequently studied the edge debonding mechanism for less confined interlayers using a semi-analytical approach built on the previous works of Dillard [1] and Ghatak et al. [2]. The key finding is the single dimensionless number $\psi = (G_c \mu / T_c^2) (D_p / \mu h^6)^{1/3}$ which is shown to govern the debonding behavior, namely, the interfacial opening normalized by δ_f , the debond length and the CZ size normalized by $\beta^{-1} = (12 \mu / D_p h^3)^{-1/6}$, and the load normalized by $D_p \beta^3 \delta_f$. Here $\delta_f = 2 G_c / T_c$ is the debond tip opening. The CZ size decreases as ψ increases; consequently, the response transitions from a strength dominated regime to an energy dominated regime. For small CZ sizes, the predicted pull-off force shows good agreement with the linear elastic fracture mechanics (LEFM) predictions made by Ghatak et

al. [2]. The results of this semi-analytical work agree well with those predicted by the FEM for the edge debonding mechanisms.

We have also explored preferential debonding in a problem that is related to an industrial demolding operation for fabrication of ophthalmic lenses. Demolding during fabrication of a soft ophthalmic lens relies on interfacial separation of an elastomeric interlayer sandwiched between two flexible molds from a desired interface when the molds are pried open. Practical demolding operations use two molds made of the same thermoplastic polymer. With identical adhesion at the two interfaces, engineering of a demolding process is faced with the challenge of understanding and controlling the factors dictating debonding from a desired interface. We analyze using the FEM axisymmetric deformation of an elastomeric layer sandwiched between two molds when the molds are separated by a displacement controlled loading. Debonding occurs preferentially from the edge of the interface with the more flexible mold; however, if the overall confinement of the system is large enough dictated by the absolute values of rigidities of the molds for an elastomeric interlayer of given modulus and thickness, debonding may occur internally in addition to that at the edge due to large peel stresses occurring over the interior of the interface. With the edge debond initiated at the upper interface, the internal initiation may nucleate and grow at the lower interface and thus may cause an erratic debonding process. For a curved mold-assembly and the imposed normal loading conditions, edge peeling is inherently biased towards the interface corresponding with the inner surface of the interlayer. Lastly, it is shown that an option to engineer preferential debonding is to conduct differential preheating of the assembly. Edge peeling becomes biased towards the interface with the mold heated more. However, if the temperature differential between the two molds is large enough dictated by the absolute level of heating, internal debonding begins to ensue. Sensitivities of the predictions of the debonding mechanisms to prescribed biases in the TS parameters (strength and fracture energy) are assessed in a few example problems in light of the speculation that ‘real’ surfaces may have local biases in these parameters due to fabrication issues, roughness and other factors. The computed results suggest that the internal debonding mechanism occurring in mechanical debonding is sensitive to much smaller biases in the TS parameters as compared to the edge debonding mechanism which remains insensitive to a large bias (~200%). It is recommended, therefore, that the molds be so designed that the resulting debonding process does not involve internal debonding. Likewise, the edge debonding mechanism predicted due to differential heating is relatively less sensitive to changes in the TS parameters as compared to the internal debonding mechanism. In essence,

it is shown that debonding becomes biased towards the edge of one interface due to the introduction of additional opening shear [3] induced due to one mold being more flexible than the other, difference in their curvatures, and differential thermal expansion from preheating. However, the initiation of internal debonding in addition to edge debonding occurring for highly confined systems may complicate the debonding process. For an industrial demolding process, it is recommended that the molds be designed against internal debonding to improve process yield since such debonding process is highly sensitive to small variations of interfacial strength/fracture energy.

6.2 Future directions:

6.2.1 Wavy/undulatory debonding:

Whether or not debonding will be undulatory/wavy depends on the amplitude of perturbation to the constant-pressure/zero-deformation field. While in the present work concerning debonding of a rigid semi-infinite adherend, the perturbation is provided by the interlayer free-edge effects, other factors such as the finite dimensions of the adherend, compliance of the adherend or presence of an initial defect/weaker region at the interface may influence the perturbation. Applicability of the derived necessary condition should, therefore, be judged for such departures from the boundary value problem studied in the present work. An example is peeling of a flexible plate, in which the confinement parameter and the adhesion parameter collectively dictate whether or not debonding will be wavy.

Also worth exploring in a future work is the feasibility of using a smeared TS relation in order to lump the effect of undulatory debonding without modeling the elastomeric adhesive layer. Such an analysis may aid development of multiscale modeling techniques for problems involving soft adhesives.

6.2.2 Three-dimensional (3D) effects:

We are aware that the predicted results of our two-dimensional (2D) analyses do not capture the experimentally observed [4-6] out-of-plane variation in deformations. Instead, a predicted in-plane debond implies a long debonding tunnel in the out-of-plane direction. When 3D effects are considered in our simulations, undulations are indeed predicted to occur in the out-of-plane direction for a confined interlayer ($\alpha = 25$) and large enough adhesion parameter ($\phi = 5$). Recalling that an undulatory debonding is triggered by spatial variations in the deformations induced by the free-edge effects, simulations of 3D deformations do not

predict out-of-plane undulations if the bounding surfaces of the assembly parallel to the plane of the paper are constrained in the out-of-plane direction.

Results of several numerical experiments of 3D deformations conducted without constraining the free edges seem to support conclusions drawn from analyses of 2D deformations. However, a comprehensive analysis of 3D deformations is envisioned to be useful in order to strengthen and/or judge the limitations of our conclusions.

The reported results of the 2D analyses are hoped to be valuable in developing models of 3D deformations in a future effort.

6.2.3 Flexible plate on elastomeric foundation:

A major limitation of our analysis reported in Chapter 4 is that it is valid only for the case of edge debonding. In a future effort, one can assume presence of an internal cohesive zone for confined interlayers ($\alpha \gg 9$) and follow the current approach of solving the ordinary differential equations (ODEs) for each region (free/damaged/bonded) by applying pertinent boundary and continuity conditions. Another potential extension could be assuming a smooth TS relation so that one single ODE governs the interfacial peel stress. Then the possibility of fingerlike debonding may be studied by inserting an out-of-plane perturbation in the deformations and following an approach similar to that of Ghatak [7].

6.2.4 Debonding evolution in the demolding problem:

While our investigation of the demolding problem focused on identifying factors that could be tuned to engineer an edge debonding process initiating preferentially at a desired interface, it is important to understand how the debonding evolution could be controlled in the event of bridging occurring for confined interlayers so that complete separation occurs from the desired interface. Preliminary numerical experiments (reported in a conference proceeding [8]) of the demolding process for a viscoelastic hydrogel layer modeled using values of material parameters from [6, 9] reveal that the pulling rate and the operating temperature dictate the final separation interface when internal initiation occurs. While for a lower pulling rate or a higher temperature, the separation is completed from the lower interface, it is completed from the upper interface at fast enough pulling speeds or low enough temperatures. For intermediate values of pulling speed/temperature, there may be significant resistance to crack propagation arising from large viscoelastic dissipations in the interlayer, thereby leading to a pronounced bridging effect. More work is needed in this direction. It is anticipated that details of the debonding evolution are controlled by the

cohesive length scale $G_c\mu/T_c^2$ relative to a characteristic dimension, and the lengths of the external and the internal debonds [10].

The research on preferential debonding in demolding applications should be extended in future by allowing for a number of other factors not accounted for in the present effort. Few examples include spatial variation of interlayer thickness, non-axisymmetric deformations, and coupled thermoviscoelastic effects, as might be appropriate for industrial manufacturing of ophthalmic lenses.

References

- [1] Dillard, D., *Bending of plates on thin elastomeric foundations*. Journal of applied mechanics, 1989. **56**(2): p. 382-386.
- [2] Ghatak, A., L. Mahadevan, and M.K. Chaudhury, *Measuring the work of adhesion between a soft confined film and a flexible plate*. Langmuir, 2005. **21**(4): p. 1277-1281.
- [3] Liechti, K.M. and J.-D. Wu, *Mixed-mode, time-dependent rubber/metal debonding*. Journal of the Mechanics and Physics of Solids, 2001. **49**(5): p. 1039-1072.
- [4] Ghatak, A., M.K. Chaudhury, V. Shenoy, and A. Sharma, *Meniscus instability in a thin elastic film*. Physical Review Letters, 2000. **85**(20): p. 4329.
- [5] Mönch, W. and S. Herminghaus, *Elastic instability of rubber films between solid bodies*. EPL (Europhysics Letters), 2001. **53**(4): p. 525.
- [6] Murray, K.V., *Characterization of the Interfacial Fracture of Solvated Semi-Interpenetrating Polymer Network (S-IPN) Silicone Hydrogels with a Cyclo-Olefin Polymer (COP)*. 2011, Virginia Polytechnic Institute and State University.
- [7] Ghatak, A., *Confinement-induced instability of thin elastic film*. Physical Review E, 2006. **73**(4): p. 041601.
- [8] Mukherjee, B., O. Kaymakci, R.C. Batra, D.A. Dillard, and R.B. Moore. *Understanding bridging of a soft organogel layer by numerical simulations*. in *Adhesion Society Meeting*. 2013. Daytona Beach, FL.
- [9] Tizard III, G.A., *Characterization of the Viscoelastic Fracture of Solvated Semi-Interpenetrating Polymer Network (S-IPN) Silicone Hydrogels*. 2010, Virginia Polytechnic Institute and State University.
- [10] Guan, Y., *Crack path selection and shear toughening effects due to mixed mode loading and varied surface properties in beam-like adhesively bonded joints*. 2014, Virginia Polytechnic Institute and State University.

Appendix J

J.1 Sample input file for debonding of a rigid semi-infinite block (Chapter 2)

```
*Heading
** Job name: Gammaeffect_H_25 Model name: h1
** Generated by: Abaqus/CAE 6.11-2
**Preprint, echo=NO, model=NO, history=NO, contact=NO
**
** PARTS
**
*Part, name=Adherend
*End Part
**
*Part, name=Interlayer
*End Part
**
** ASSEMBLY
**
*Assembly, name=Assembly
**
*Instance, name=Adherend-1, part=Adherend
  4., 0.03125, 0.
*Node
  1, 23.75, 5.
  2, 22.5, 5.
-----
  230, 0., -5.
  231, -1.25, -5.
-----
*Element, type=CPE4R
  1, 1, 2, 23, 22
  2, 2, 3, 24, 23
-----
199, 208, 209, 230, 229
200, 209, 210, 231, 230
-----
*Nset, nset=_PickedSet2, internal, generate
  1, 231, 1
*Elset, elset=_PickedSet2, internal, generate
  1, 200, 1
** Section: Adherend
*Solid Section, elset=_PickedSet2, material=Adherend
,
*End Instance
**
*Instance, name=Interlayer-1, part=Interlayer
 -33.75, -1.29375, 0.
*Node
  1, 60.5, -3.67499995
  2, 60.4425011, -3.67499995
-----
  2405, 37.5574989, -3.95000005
  2406, 37.5, -3.95000005
-----
*Element, type=CPE4H
  1, 1, 2, 403, 402
  2, 2, 3, 404, 403
-----
1999, 2003, 2004, 2405, 2404
2000, 2004, 2005, 2406, 2405
-----
*Nset, nset=_PickedSet2, internal, generate
  1, 2406, 1
*Elset, elset=_PickedSet2, internal, generate
  1, 2000, 1
** Section: Interlayer
*Solid Section, elset=_PickedSet2, material=Elastomer
,
*End Instance
**
*Nset, nset=_PickedSet15, internal, instance=Interlayer-1, generate
2006, 2406, 1
```



```

*Elset, elset=_PickedSet15, internal, instance=Interlayer-1, generate
1601, 2000, 1
*Nset, nset=Interlayer, instance=Interlayer-1, generate
1, 401, 1
*Elset, elset=Interlayer, instance=Interlayer-1, generate
1, 400, 1
*Nset, nset=_PickedSet36, internal, instance=Adherend-1, generate
1, 21, 1
*Elset, elset=_PickedSet36, internal, instance=Adherend-1, generate
1, 20, 1
*Elset, elset=_Adherend_S3, internal, instance=Adherend-1, generate
181, 200, 1
*Surface, type=ELEMENT, name=Adherend
_Adherend_S3, S3
*Elset, elset=_Interlayer_S1, internal, instance=Interlayer-1, generate
1, 400, 1
*Surface, type=ELEMENT, name=Interlayer
_Interlayer_S1, S1
*End Assembly
*Amplitude, name=Amp-1
0., 0., 1., 1.
**
** MATERIALS
**
*Material, name=Adherend
*Elastic
20000., 0.3
*Material, name=Elastomer
*Elastic, moduli=LONG TERM
0.2, 0.5
*Viscoelastic, time=PRONY
0.75, 0., 1e-05
*Material, name=Elastomer-NH
*Hyperelastic, neo hooke, moduli=LONG TERM
0.1,0.
*Viscoelastic, time=PRONY
0.75, 0., 1e-05
**
** INTERACTION PROPERTIES
**
*Surface Interaction, name=CZ
1.,
*Cohesive Behavior, eligibility=SPECIFIED CONTACTS
1e+06, 1e+06, 1e+06
*Damage Initiation, criterion=QUADS
0.09, 0.09, 0.09
*Damage Evolution, type=ENERGY
0.000405,
*Damage Stabilization
1e-08
**
** BOUNDARY CONDITIONS
**
** Name: BC-1 Type: Displacement/Rotation
*Boundary
_PickedSet15, 1, 1
_PickedSet15, 2, 2
**
** INTERACTIONS
**
** Interaction: Int-1
*Contact Pair, interaction=CZ
Interlayer, Adherend
*Initial Conditions, type=CONTACT
Interlayer, Adherend, Interlayer
** -----
**
** STEP: Step-1
**
*Step, name=Step-1, nlgeom=YES, inc=100000
*Visco, cetol=0.0001, creep=EXPLICIT
1e-05, 1., 1e-70, 1.
**
** BOUNDARY CONDITIONS
**

```

```

** Name: BC-2 Type: Displacement/Rotation
*Boundary, amplitude=Amp-1
_PickedSet36, 2, 2, 1.
**
** CONTROLS
**
*Controls, reset
*Controls, parameters=time incrementation
, , 30, , , , 30, , ,
**
** OUTPUT REQUESTS
**
*Restart, write, frequency=0
**
** FIELD OUTPUT: F-Output-1
**
*Output, field, frequency=2
*Node Output
CF, RF, U
*Element Output, directions=YES
CE, CEEQ, CEMAG, LE, PE, PEEQ, PEMAG, S
*Contact Output
CDISP, CSDMG, CSQUADSCRT, CSTRESS
**
** HISTORY OUTPUT: H-Output-1
**
*Output, history, variable=PRESELECT
*End Step

```

J.2 Sample input file for peeling of a flexible plate (Chapter 3)

```

*Heading
** Job name: Alpha100_phi4_mesh2 Model name: Model-1
** Generated by: Abaqus/CAE 6.11-2
*Preprint, echo=NO, model=NO, history=NO, contact=NO
**
** PARTS
**
*Part, name=Film
*End Part
**
*Part, name="flexible plate"
*End Part
**
** ASSEMBLY
**
*Assembly, name=Assembly
**
*Instance, name=Film-1, part=Film
55., 1., 0.
*Node
1, 5.92299986, 9.75
2, 5.91050053, 9.75
-----
49074, -41.2374992, 9.59869099
49075, -41.25, 9.59869099
-----
*Element, type=CPE4H
1, 1, 2, 3777, 3776
2, 2, 3, 3778, 3777
-----
45287, 45298, 45299, 49074, 49073
45288, 45299, 45300, 49075, 49074
-----
*Nset, nset=_PickedSet2, internal, generate
1, 49075, 1
*Elset, elset=_PickedSet2, internal, generate
1, 45288, 1
** Section: Film
*Solid Section, elset=_PickedSet2, material=Adhesive
,
*End Instance

```

```

**
*Instance, name="flexible plate-1", part="flexible plate"
  53.003, 2., 0.
*Node
  1, -39.2529984, 9.75
  2, -39.2529984, 8.75
-----
  5422, -41.1501503, 9.55000019
  5423, -41.1501503, 9.64999962
-----
*Element, type=CPE4
  1, 1, 7, 1014, 966
  2, 7, 8, 1015, 1014
-----
4919, 5422, 5423, 986, 987
4920, 5423, 985, 5, 986
-----
*Nset, nset=_PickedSet2, internal, generate
  1, 5423, 1
*Elset, elset=_PickedSet2, internal, generate
  1, 4920, 1
** Section: plate
*Solid Section, elset=_PickedSet2, material=Plate
,
*End Instance
**
*Nset, nset=_PickedSet23, internal, instance="flexible plate-1"
6,
*Nset, nset=Film, instance=Film-1, generate
  1, 3775, 1
*Elset, elset=Film, instance=Film-1, generate
  1, 3774, 1
*Nset, nset=film_lower, instance=Film-1, generate
45301, 49075, 1
*Elset, elset=film_lower, instance=Film-1, generate
41515, 45288, 1
*Nset, nset=_PickedSet199, internal, instance=Film-1, generate
45301, 49075, 1
*Elset, elset=_PickedSet199, internal, instance=Film-1, generate
41515, 45288, 1
*Elset, elset=_adhredned_S2, internal, instance="flexible plate-1", generate
  10, 4720, 10
*Surface, type=ELEMENT, name=adhredned
  _adhredned_S2, S2
*Elset, elset=_film_S1, internal, instance=Film-1, generate
  1, 3774, 1
*Surface, type=ELEMENT, name=film
  _film_S1, S1
*Elset, elset=_PickedSurf72_S2, internal, instance="flexible plate-1", generate
  10, 4720, 10
*Surface, type=ELEMENT, name=_PickedSurf72, internal
  __PickedSurf72_S2, S2
*Elset, elset=_PickedSurf73_S1, internal, instance=Film-1, generate
  1, 3774, 1
*Surface, type=ELEMENT, name=_PickedSurf73, internal
  __PickedSurf73_S1, S1
*Elset, elset=_film_lower_S3, internal, instance=Film-1, generate
41515, 45288, 1
*Surface, type=ELEMENT, name=film_lower
  _film_lower_S3, S3
*End Assembly
**
** MATERIALS
**
*Material, name=Adhesive
*Elastic
15., 0.5
*Material, name=CZ
*Damage Initiation, criterion=QUADS
0.01,10.,10.
*Damage Evolution, type=ENERGY, mixed mode behavior=POWER LAW, power=1.
0.0002,2000.,2000.
*Damage Stabilization
1e-05
*Elastic, type=TRACTION

```

```

1e+06, 1e+06, 1e+06
*Material, name=Plate
*Elastic
189140., 0.3
**
** INTERACTION PROPERTIES
**
*Surface Interaction, name=IntProp-1
1.,
*Cohesive Behavior, eligibility=SPECIFIED CONTACTS
1e+06, 1e+08, 1e+08
*Damage Initiation, criterion=QUADS
1.265,100.,100.
*Damage Evolution, type=ENERGY, mixed mode behavior=POWER LAW, power=1.
0.00403546,1000.,1000.
*Damage Stabilization
1e-08
*Surface Interaction, name=IntProp-2
1.,
*Cohesive Behavior, eligibility=SPECIFIED CONTACTS
1e+06, 1e+08, 1e+08
*Damage Initiation, criterion=QUADS
0.04,10.,10.
*Damage Evolution, type=ENERGY, mixed mode behavior=POWER LAW, power=1.
1.42656e-05,2000.,2000.
*Damage Stabilization
1e-08
**
** BOUNDARY CONDITIONS
**
** Name: BC-1 Type: Displacement/Rotation
*Boundary
_PickedSet199, 1, 1
_PickedSet199, 2, 2
**
** INTERACTIONS
**
** Interaction: Int-1
*Contact Pair, interaction=IntProp-1
_PickedSurf73, _PickedSurf72
*Initial Conditions, type=CONTACT
_PickedSurf73, _PickedSurf72, Film
** -----
**
** STEP: Step-1
**
*Step, name=Step-1, inc=10000
*Static
0.0001, 0.004466, 1e-50, 0.004466
**
** BOUNDARY CONDITIONS
**
** Name: BC-2 Type: Displacement/Rotation
*Boundary
_PickedSet23, 2, 2, 0.004466
**
** CONTROLS
**
*Controls, reset
*Controls, parameters=time incrementation
, , 30, , , , 30, , ,
**
** OUTPUT REQUESTS
**
*Restart, write, frequency=0
**
** FIELD OUTPUT: F-Output-1
**
*Output, field, frequency=5
*Node Output
CF, RF, U
*Element Output, directions=YES
FV, LE, MFR, PE, PEEQ, PEMAG, S, SDEG, SDV, STATUS, STATUSXFEM, UVARM
*Contact Output
CDISP, CSDMG, CSTRESS

```

```

**
** HISTORY OUTPUT: H-Output-1
**
*Output, history, variable=PRESELECT
*End Step

```

J.3 Sample input file for axisymmetric debonding problem (Chapter 5)

```

*Heading
** Job name: rinf_alpha10_s10_phi3_etap7 Model name: Curved axisymmetric_rinf_alpha10-s10
** Generated by: Abaqus/CAE 6.11-2
** Preprint, echo=NO, model=NO, history=NO, contact=NO
**
** PARTS
**
*Part, name=Interlayer
*End Part
**
*Part, name=Lower
*End Part
**
*Part, name="Upper adherend"
*End Part
**
** ASSEMBLY
**
*Assembly, name=Assembly
**
*Instance, name=Interlayer-1, part=Interlayer
    0., 42.094494, 0.
*Node
    1, 10., 0.
    2, 9.99499989, 0.
-----
47696, 0.0124938171, -0.478480011
47697, 0., -0.478480011
-----
*Element, type=CAX4
    1, 1, 2, 1225, 1224
    2, 2, 3, 1226, 1225
-----
46435, 46472, 46473, 47696, 47695
46436, 46473, 46474, 47697, 47696
-----
*Nset, nset=_PickedSet4, internal, generate
    1, 47697, 1
*Elset, elset=_PickedSet4, internal, generate
    1, 46436, 1
** Section: interlayer
** Solid Section, elset=_PickedSet4, material=Interlayer
,
*End Instance
**
*Instance, name="Upper adherend-1", part="Upper adherend"
    0., 42.0944942764749, 0.
*Node
    1, 11.9949999, 0.
    2, 11.9949999, 1.
-----
5480, 0.0500000007, 0.899999976
5481, 0.0500000007, 0.949999988
-----
*Element, type=CAX4
    1, 1, 9, 599, 124
    2, 9, 10, 600, 599
-----
5199, 5480, 5481, 381, 382
5200, 5481, 380, 7, 381
-----
*Nset, nset=_PickedSet6, internal, generate
    1, 5481, 1
*Elset, elset=_PickedSet6, internal, generate
    1, 5200, 1

```

```

** Section: Adherend
*Solid Section, elset=_PickedSet6, material=Adherend
,
*End Instance
**
**
*Instance, name=Lower-1, part=Lower
0., 40.616014, 0.
*Node
1, 11.9949999, 0.
2, 11.9949999, 1.
-----
5481, 12.9497499, 0.0500000007
-----
*Element, type=CAX4
1, 1, 9, 599, 124
2, 9, 10, 600, 599
5199, 5480, 5481, 561, 562
5200, 5481, 560, 7, 561
*Nset, nset=_PickedSet6, internal, generate
1, 5481, 1
*Elset, elset=_PickedSet6, internal, generate
1, 5200, 1
** Section: Adherend-2
*Solid Section, elset=_PickedSet6, material=Adherend-2
,
*End Instance
**
**
*Nset, nset=_PickedSet144, internal, instance="Upper adherend-1"
1, 5, 125, 126, 127, 128, 129, 130, 131, 132, 133, 134, 135, 136, 137, 138
139, 140, 141, 142, 143
*Elset, elset=_PickedSet144, internal, instance="Upper adherend-1", generate
820, 1200, 20
*Nset, nset=_PickedSet151, internal, instance=Lower-1
2, 8, 580, 581, 582, 583, 584, 585, 586, 587, 588, 589, 590, 591, 592, 593
594, 595, 596, 597, 598
*Elset, elset=_PickedSet151, internal, instance=Lower-1, generate
4801, 5181, 20
*Nset, nset=Interlayer_1, instance=Interlayer-1, generate
46475, 47697, 1
*Elset, elset=Interlayer_1, instance=Interlayer-1, generate
45215, 46436, 1
*Nset, nset=interlayer_u, instance=Interlayer-1, generate
1, 1223, 1
*Elset, elset=interlayer_u, instance=Interlayer-1, generate
1, 1222, 1
*Nset, nset=_PickedSet427, internal, instance="Upper adherend-1", generate
1, 5481, 1
*Elset, elset=_PickedSet427, internal, instance="Upper adherend-1", generate
1, 5200, 1
*Nset, nset=_PickedSet429, internal, instance=Lower-1, generate
1, 5481, 1
*Elset, elset=_PickedSet429, internal, instance=Lower-1, generate
1, 5200, 1
*Elset, elset=_upper_S4, internal, instance="Upper adherend-1", generate
1201, 5181, 20
*Surface, type=ELEMENT, name=upper
_upper_S4, S4
*Elset, elset=_Lower_S2, internal, instance=Lower-1, generate
820, 4800, 20
*Surface, type=ELEMENT, name=Lower
_Lower_S2, S2
*Elset, elset=_Interlayer_L_S3, internal, instance=Interlayer-1, generate
45215, 46436, 1
*Surface, type=ELEMENT, name=Interlayer_L
_Interlayer_L_S3, S3
*Elset, elset=_interlayer_U_S1, internal, instance=Interlayer-1, generate
1, 1222, 1
*Surface, type=ELEMENT, name=interlayer_U
_interlayer_U_S1, S1
*End Assembly
**
** MATERIALS
**
*Material, name=Adherend
*Elastic

```

```

23924.5, 0.3
*Expansion
7e-05,
*Material, name=Adherend-2
*Elastic
8206.1, 0.3
*Expansion
7e-05,
*Material, name=Interlayer
*Elastic
60., 0.5
*Expansion
0.0006,
**
** INTERACTION PROPERTIES
**
*Surface Interaction, name=IntProp-1
1.,
*Cohesive Behavior, eligibility=SPECIFIED CONTACTS
1e+06, 1e+12, 1e+12
*Damage Initiation, criterion=QUADS
0.08,100.,100.
*Damage Evolution, type=ENERGY, mixed mode behavior=POWER LAW, power=1.
1.70126e-05,1000.,1000.
*Damage Stabilization
1e-07
*Surface Interaction, name=IntProp-2
1.,
*Cohesive Behavior, eligibility=SPECIFIED CONTACTS
1e+06, 1e+12, 1e+12
*Damage Initiation, criterion=QUADS
0.08,100.,100.
*Damage Evolution, type=ENERGY, mixed mode behavior=POWER LAW, power=1.
1.70126e-05,1000.,1000.
*Damage Stabilization
1e-07
*Surface Interaction, name=_Int-L-Prop
1.,
*Cohesive Behavior, eligibility=SPECIFIED CONTACTS
1e+06, 1e+12, 1e+12
*Damage Initiation, criterion=QUADS
0.08,100.,100.
*Damage Evolution, type=ENERGY, mixed mode behavior=POWER LAW, power=1.
1.70126e-05,1000.,1000.
*Damage Stabilization
1e-07
**
** BOUNDARY CONDITIONS
**
** Name: BC-1 Type: Displacement/Rotation
*Boundary
_PickedSet151, 2, 2
**
** INTERACTIONS
**
** Interaction: Int-L
*Contact Pair, interaction=_Int-L-Prop
Interlayer_L, Lower
*Initial Conditions, type=CONTACT
Interlayer_L, Lower, Interlayer_1
** Interaction: Int-u
*Contact Pair, interaction=IntProp-1
interlayer_U, upper
*Initial Conditions, type=CONTACT
interlayer_U, upper, interlayer_u
** -----
**
** STEP: Step-1
**
*Step, name=Step-1, inc=10000
*Static
0.001, 0.001, 1e-50, 0.001
**
** BOUNDARY CONDITIONS
**

```

```

** Name: BC-1 Type: Displacement/Rotation
*Boundary
_PickedSet151, 2, 2
**
** INTERACTIONS
**
** Interaction: Int-L
*Change Friction, interaction=_Int-L-Prop
*Friction
0.,
**
** CONTROLS
**
*Controls, reset
*Controls, parameters=time incrementation
, , 30, , , , 30, , ,
**
** OUTPUT REQUESTS
**
*Restart, write, frequency=0
**
** FIELD OUTPUT: F-Output-1
**
*Output, field, frequency=8
*Node Output
CF, RF, U
*Element Output, directions=YES
LE, PE, PEEQ, PEMAG, S
*Contact Output
CDISP, CSDMG, CSTRESS
**
** HISTORY OUTPUT: H-Output-1
**
*Output, history, variable=PRESELECT, frequency=5
*End Step
** -----
**
** STEP: Step-2
**
*Step, name=Step-2, inc=100000
*Static
0.008, 0.008, 1e-50, 0.008
**
** BOUNDARY CONDITIONS
**
** Name: BC-2 Type: Displacement/Rotation
*Boundary
_PickedSet144, 2, 2, 0.008
**
** INTERACTIONS
**
** Interaction: Int-L
*Change Friction, interaction=_Int-L-Prop
*Friction
0.,
**
** OUTPUT REQUESTS
**
*Restart, write, frequency=0
**
** FIELD OUTPUT: F-Output-1
**
*Output, field
*Node Output
CF, RF, U
*Element Output, directions=YES
LE, PE, PEEQ, PEMAG, S
*Contact Output
CDISP, CSDMG, CSTRESS
**
** HISTORY OUTPUT: H-Output-1
**
*Output, history, variable=PRESELECT, frequency=5
*End Step

```